Spin and Heat Transport Beyond Electrons

Ferromagnetic Insulators and Antiferromagnetic Metals

Cover: Baltic Sea in the summer of 2016, by Jiansen Zheng.
In this photo, there are water waves (classical) generated with wavelengths much smaller than the depth of water. They are driven by random fluctuations in the atmospheric pressure on the air-water interface and also a cruise ship's silently spinning propeller beneath the surface.

Printed by ProefschriftMaken

Copyright © 2019 by Jiansen Zheng. All rights reserved.

Spin and Heat Transport Beyond Electrons

Ferromagnetic Insulators and Antiferromagnetic Metals

Spin- en warmtetransport voorbij elektronen

Ferromagnetische isolatoren en antiferromagnetische metalen

(met een samenvatting in het Nederlands)

Proefschrift

ter verkrijging van de graad van doctor
aan de Universiteit Utrecht
op gezag van de rector magnificus, prof. dr. H.R.B.M. Kummeling,
ingevolge het besluit van het college voor promoties
in het openbaar te verdedigen op
maandag 18 maart 2019 des middags te 2.30 uur

door

Jiansen Zheng

geboren op 10 september 1989 te Wenzhou, China

Promotoren: Prof. dr. R.A. Duine
Prof. dr. ir. H.T.C. Stoof

This thesis is dedicated to my parents,
for their love and endless support.

Contents

List of Publications xi

Abbreviations xiii

List of Figures xv

1 Introduction **1**
- 1.1 Magnetism 2
  - 1.1.1 Historical Background 2
  - 1.1.2 Microscopic Origin of Magnetism 2
  - 1.1.3 Paramagnetism and Diamagnetism 4
  - 1.1.4 Ferromagnetism and Antiferromagnetism 5
  - 1.1.5 Spin Wave (Magnon) 6
- 1.2 Spin Transport in Non-magnetic Materials 8
  - 1.2.1 Spin Hall Effect 8
  - 1.2.2 Inverse Spin Hall Effect 8
- 1.3 Spin Transport in Ferromagnetic Materials 9
  - 1.3.1 Ferromagnetic Resonance and Gilbert Damping 9
  - 1.3.2 Ferromagnetic Magnon 10
  - 1.3.3 Ferromagnetic (Ferrimagnetic) Insulators and Metals 12
- 1.4 Spin Transport in Antiferromagnetic Materials 14
  - 1.4.1 Antiferromagnetic Magnon and Antiferromagnetic Resonance . 14
  - 1.4.2 Antiferromagnetic Metals 15
  - 1.4.3 Antiferromagnetic Insulators 15
- 1.5 Outline 16

2 Green's Function Formalism for Spin Transport in Metal-insulator-metal Heterostructures **17**
- 2.1 Introduction 17
- 2.2 Non-equilibrium Green's Function Formalism 20
  - 2.2.1 Model 20
  - 2.2.2 Magnon Density Matrix and Current 21
  - 2.2.3 Landauer-Büttiker Formula 25

2.2.4 Determining the Interface Coupling . . . 26
2.2.5 Summary on Implementation . . . 27
2.3 Numerical Results . . . 28
2.3.1 Clean System . . . 28
2.3.2 Disordered System . . . 29
2.4 Analytical Results . . . 31
2.4.1 Thin Film Regime ($d \ll l$) . . . 33
2.4.2 Thick Film Regime ($d \gg l$) . . . 34
2.4.3 Comparison with Numerical Results . . . 34
2.5 Discussion and Outlook . . . 35
Appendix . . . 36
2.A Evaluation of Magnon Green's Function in the Continuum Limit . . . 36
2.B Stochastic Formalism for Spin Transport in a Ferromagnet . . . 37
2.C Size Dependence of Magnon Current for Various Values of Interface Coupling η . . . 38
2.D Analytic Calculation for Local Magnon Current . . . 38
2.D.1 Density Matrix in the Continuum Limit . . . 39
2.D.2 Contour Integral and Local Magnon Current . . . 40

3 Spin-transfer Mechanism for Magnon Drag in Antiferromagnetic Metals 45
3.1 Introduction . . . 45
3.2 Current-induced Antiferromagnetic Magnetization Dynamics . . . 47
3.2.1 Stochastic Equations of Motion . . . 47
3.2.2 Fourier Transform and Dispersion . . . 50
3.2.3 Correlation Function . . . 51
3.3 Magnon Energy and Spin Current . . . 52
3.3.1 Energy Current . . . 52
3.3.2 Spin Current . . . 56
3.4 Numerical Results and Discussion . . . 56
3.4.1 Energy Transport . . . 57
3.4.2 Spin Transport . . . 60
3.5 Conclusion . . . 63
Appendix . . . 64
3.A Derivation of the Density of Magnon Energy Current . . . 64
3.B Higher-order Total Magnetization Dependent Contributions to the Magnon Energy Current . . . 66

4 Effect of Ellipticity and Dissipation on Magnon Tunneling in a Magnon Spin Valve 69
4.1 Introduction . . . 69
4.2 Deriving the Tunneling Current with Fermi's Golden Rule for Circular Magnons . . . 72
4.2.1 Model Hamiltonian . . . 72
4.2.2 Tunneling Calculation for the Parallel Configuration . . . 73
4.2.3 Tunneling Calculation for the Anti-parallel Configuration . . . 77
4.3 Effects of Ellipticity and Damping . . . 79

4.3.1 Bogoliubov Transformation and Elliptical Magnons 80
4.3.2 Tunneling in the Parallel Configuration 81
4.3.3 Tunneling in the Anti-parallel Configuration 90
4.4 Numerical Results and Discussion 94
4.4.1 K_y Anisotropy Dependence of the Tunneling Thermal Conductance 94
4.4.2 K_y Anisotropy Dependence of the MTC Ratio 96
4.5 Conclusion 98
Appendix 98
4.A Transition Rates for Different Tunneling Processes 98
4.A.1 Parallel Configuration 98
4.A.2 Anti-parallel Configuration 100
4.B K_z Dependence of the MTC Ratio 101

5 Conclusion and Outlook **103**

Bibliography 107

Samenvatting 119

Acknowledgement 121

About the author 123

List of Publications

This Thesis is based on the following publications:

- Chapter 2 is based on J. Zheng, S.A. Bender, J. Armaitis, R.E. Troncoso and R.A. Duine, *Green's function formalism for spin transport in metal-insulator-metal heterostructures*, Physical Review B, 96(17), 174422 (2017).
- Chapter 3 is based on J. Zheng, S.A. Bender, Q. Enneking, Y. Tserkovnyak, B. Flebus and R.A. Duine, *Spin-transfer mechanism for magnon drag in antiferromagnetic metals*, in preparation.
- Chapter 4 is based on J. Zheng, S.A. Bender, A. Rückriegel and R.A. Duine, *Effect of Ellipticity and Dissipation on Magnon Tunneling in a Magnon Spin Valve*, in preparation.

The author also contributed to the following publication which is not part of this Thesis:

- J. Zheng, J. Armaitis and R.A. Duine, *Persistent Spin Current in Spin-orbit Coupled Ultra-cold Atoms*, in preparation.

Abbreviations

SHE : spin Hall effect
ISHE : inverse spin Hall effect
SSE : spin Seebeck effect
LSSE : longitudinal spin Seebeck effect
NM : normal metal
HM : heavy metal
FM : ferromagnet
AFM : antiferromagnet
STT : spin-transfer torque
YIG : yttrium iron garnet
FMR : ferromagnetic resonance
AFMR : antiferromagnetic resonance
LLG : Landau-Lifshitz-Gilbert
BEC : Bose-Einstein condensate
BLS : Brillouin light scattering
SMR : spin Hall magnetoresistance
GMR : giant magnetoresistance
MRAM : magnetoresistive random-acess memory
NEGF : nonequilibrium Green's function
MTC : magnon thermal conductance ratio
FGR : Fermi's golden rule
DOS : density of states
HP : Holstein-Primakoff

List of Figures

1.1 From the pivoting compass needle to a frog floating in strong magnetic field. 2
1.2 Illustration of current loops interacting with an external magnetic field $\boldsymbol{B}$. 3
1.3 Illustration of ferromagnetism and antiferromagnetism. The red and blue arrows denote the localized magnetic moments of ions in the solid system. 5
1.4 Illustration of the spin-flop phase transition of an antiferromagnet. . . 7
1.5 Illustration of the spin wave. The red arrows denote the localized magnetic moments in a ferromagnet. 7
1.6 Illustration of spin Hall effect and inverse spin Hall effect. 9
1.7 Illustration of the terms in the LLG equation. 10
1.8 Dispersion spectrum of magnons in a YIG film magnetized by an in-plane static magnetic field. The arrows illustrate the parametric pumping process, which can be considered as a creation of two magnons with opposite wavevectors by a microwave photon of the pumping field. Figure extracted from Ref. [1]. 11
1.9 Spin Seebeck effect and spin pumping. 13
1.10 Schematic of the non-local measurement geometry of a device. The two platinum strips act as spin injector and detector for the ferromagnetic magnons. On the FM|NM interface, magnons are created and absorbed by the spin-flip scattering of polarized electrons [2]. Figure extracted from Ref. [3] 14

2.1 Illustration of the system where magnon transport in a ferromagnet (orange region) is driven by a spin accumulation difference $\Delta\mu_L - \Delta\mu_R$ and temperature difference $T_L - T_R$ between two normal-metal leads (blue regions). Spin-flip scattering at the interface converts electronic to magnonic spin current. Here, $\mathbf{S}$ is the local spin density in equilibrium. 19

2.2 Schematic for the NM-FM-NM heterostructure and notation for the Green's functions and self-energies. The array of circles denotes the localized magnetic moments, while the two regions outside the parabolic lines denote the leads, i.e., reservoirs of polarized electrons. Moreover, $J^{L/R}_{j;kk'}$ denotes the interface coupling, and $T_{L/R}$ and $\Delta\mu_{L/R}$ denote the temperature and spin accumulation for the leads. The properties of the magnons are encoded in $\mathcal{G}^{(+)}_{j,j'}(t,t')$, the retarded magnon Green's function, and the magnon density matrix $\rho_{j,j'}$. The number of sites in the spin-current direction is N. The self-energies $\Sigma^{FM,(\pm)}$, $\Sigma^{L,(\pm)}$, $\Sigma^{R,(\pm)}$ are due to Gilbert damping, and the left and right lead, respectively. 20

2.3 Feynman diagram for the spin-flip processes emitting and absorbing magnons that are represented by the wavy lines. The two vertices indicate the exchange coupling at one of the interfaces of the magnetic insulator (sites j, j') and normal metal (sites k, k', k'', k'''). $G_{k'k'';\uparrow}$ and $G_{k'''k;\downarrow}$ denotes the electron Keldysh Green's function of one of the leads. 22

2.4 System-size dependence of spin current ejected in the right reservoir for $\alpha = 6.9 \times 10^{-2}, \eta = 8.0$ and various temperatures. 29

2.5 Magnon relaxation length as a function of dimensionless temperature T^* for $\alpha = 6.9 \times 10^{-2}, \eta = 8.0$. The fitted parameters are obtained as $\gamma_0 = 114.33, \gamma_1 = 0.96, \gamma_2 = 0.32$. 30

2.6 Spatial dependence of local magnon current for the case without Gilbert damping and disorder ($\alpha = 0, \delta = 0$), without disorder ($\alpha = 6.9\times10^{-3}, \delta = 0$), without Gilbert damping ($\alpha = 0, \delta = 1.5 \times 10^{-3}$), and both disorder and Gilbert damping ($\alpha = 6.9 \times 10^{-3}, \delta = 1.5 \times 10^{-3}$). The interface coupling parameter is taken equal to $\eta = 0.8$. 31

2.7 Correlation function C_j that characterizes the fluctuations in the spin current for $j = N-1$ as a function of the Gilbert damping constant, for three strengths of the disorder potential. The curves are obtained by performing averaging over 100 realizations of the disorder. The interface coupling parameter is taken equal to $\eta = 0.8$. 32

2.8 Magnon transmission function as a function of energy. The parameters are chosen to be $\Delta/J = 0.2, \alpha = 0.069, \eta = 8.0$. 35

2.9 System-size dependence of spin current ejected in the right reservoir for $\alpha = 6.9 \times 10^{-2}, k_BT/J = 0.048$ and various values of interface coupling η. . . . 39

2.10 Dimensionless local magnon current as a function of system size $l \equiv x_R - x_L = 10\sqrt{A/k_BT}$ for various Gilbert damping values. The units of local magnon current is taken as $j_{m0} \equiv \frac{4\alpha'\hbar^3(k_BT)^{3/2}}{\sqrt{A}\pi}$. Here the temperatures for both leads are equal and kept as constant. The other parameters have the values, $\mu_L/k_BT = 2 \times 10^{-5}$, $\mu_R = 0$, $x_L = 0$. . . . 44

3.1 Schematic illustration for magnon drag in a metallic antiferromagnet with two equivalent sublattices (A, B). The electrical current is flowing in the x direction and drives the magnetization dynamics. An external magnetic field is added in the z direction, with the orange cones and green cones denote the precession of Néel vector. 48

3.2 Magnetic field dependence of the magnon energy current for $H_z/k_BT \in [-1,1]$ and $\sqrt{\frac{Kz}{\chi}}/k_BT = 1.13$. Here the normalization is $j_{\epsilon x0} = \frac{s^2(k_BT)^4 v_{\rm sx}}{24\pi^6\hbar}\left(\frac{\chi}{A}\right)^{3/2}$. 57
3.3 Magnon dispersion relation of the antiferromagnet for different magnetic fields . The red solid curve denotes the case where an electrical current flows in the $\hat{x}$ direction, while the blue dashed curve denotes the one in the absence of an electrical current. Here $\alpha = 0, \beta = 0$. 58
3.4 Temperature dependence of the magnon energy current for different magnetic fields and different temperature range. Here $j_{\epsilon x0} = \frac{s^2 K_z^2 v_{\rm sx}}{384\pi^6\chi^2\hbar}\left(\frac{\chi}{A}\right)^{3/2}$. 59
3.5 Magnetic field dependence of the magnon spin current for various ratio of β/α, where $j^z_{\rm sx0} \equiv \frac{s^2(k_BT)^3 v_{\rm sx}}{24\pi^6}\left(\frac{\chi}{A}\right)^{3/2}$. 61
3.6 Temperature dependence of the magnon spin current for various ratio of β/α for different external magnetic fields, where $j^z_{\rm sx0} \equiv \frac{s^2 v_{\rm sx}}{6(2\pi)^6}\left(\frac{K_z}{A}\right)^{3/2}$. 62

4.1 Illustration of a magnetic junction consisting of two ferromagnetic insulators, which interact with each other with weak exchange coupling J_{ex}. The left(right) insulator has temperature $T_L(T_R)$ and spin accumulation $\mu_L(\mu_R)$. The layer in green is a non-magnetic insulator, and is thin enough for the magnons to tunnel through. The left insulator is the fixed layer, with the red arrow denoting an up spin, while the right insulator is a free layer, who magnetization can be tuned from a parallel configuration (denoted in the red arrow) to an anti-parallel configuration (denoted in the blue arrow). 71
4.2 u^2-addressed density of states (U-DOS) for various Gilbert damping values. α is the Gilbert damping parameter. 89
4.3 v^2-addressed density of states (V-DOS) for various Gilbert damping values. α is the Gilbert damping parameter. 90
4.4 K_y dependence of the tunneling thermal conductance for various Gilbert damping α in the set of $\{0, 0.03, 0.1, 0.15, 0.2\}$ and different configuration of the magnetic junction. Note that the tunneling thermal conductances in both plots are scaled by a constant defined by $\kappa_0 \equiv \frac{2\pi}{\hbar} S^2 \frac{(V_L V_R)^5}{(2\pi)^6} \frac{J^2_{ex,0}}{16\pi^4 T^3}$. 95
4.5 Damping dependence of tunneling density of states for circular magnons in the parallel configuration. α is the Gilbert damping parameter. The y-axis is scaled by $J^2_{ex,0}/(k_BT)^2$ and we take $\bar{K}_z = 1$, $\bar{K}_y = 0$. 96
4.6 Damping dependence of tunneling density of states for circular magnons in the anti-parallel configuration. α is the Gilbert damping parameter. The y-axis is scaled by $J^2_{ex,0}/(k_BT)^2$ and we take $\bar{K}_z = 1$, $\bar{K}_y = 0$. . . 97
4.7 Dependence of MTC ratio on the dimensionless transverse anisotropy $K_y/(k_BT)$ for various damping values. Here we take $K_z/(k_BT) = 1.0$. 97
4.8 MTC ratio as a function of K_z anisotropy for various Gilbert damping values. 102

5.1 Conversion between charge current and magnon spin current with spin Hall effect (SHE) and inverse spin Hall effect (ISHE). 104

CHAPTER 1

Introduction

Magnon spintronics recently emerged as a fascinating topic. This introductory chapter is addressed to readers new to the field. I will introduce magnetism, magnons and other basic concepts in magnon spintronics. Then I will discuss spin and heat transport in different magnetic materials, both ferromagnets and antiferromagnets. I summarize the related materials and effects in Table 1.1, and will explain them in detail in this introduction. Finally, I will briefly give an outline of this Thesis.

Effect	**Reciprocal effect**	**Materials**
spin Hall effect: Transverse spin current induced by charge current.	*inverse spin Hall effect*: Transverse charge current induced by spin current.	NM metal (e.g. Pt) AFM metal (e.g. IrMn)
spin Seebeck effect: spin transport induced by thermal gradient.	*spin Peltier effect*: heat transport induced by spin accumulation.	FM metal (e.g. $Ni_{80}Fe_{20}$) AFM insulator (e.g. NiO) FM insulator (e.g. YIG)
Spin pumping: magnetization dynamics induces spin current	*Spin-transfer torque*: spin current exerts torques on magnetization.	FM metal (e.g. $Ni_{80}Fe_{20}$) FM insulator (e.g. YIG) AFM metal (e.g. IrMn) AFM insulator (e.g. NiO)

Table 1.1: Materials and effects to be discussed in the Introduction.

1.1 Magnetism

1.1.1 Historical Background

Magnetism was first discovered in the ancient world, when people noticed that some magnetized pieces of the mineral magnetite could attract iron. Around 1000 B.C.E., the Olmec people living in the tropical lowlands of south-central Mexico already started manufacturing magnetic compasses from lodestones [4]. In the 13-th century, a French scholar named Petrus Peregrinus de Maricourt, started to discuss in his famous book, *Epistola de magnete* (see Fig. 1.1(a)), about methods for determining the north and south poles of a magnet and the ability to reverse the polarity in an induced magnet such as iron [5]. A proper understanding of magnetism and its connection with other physical phenomena, however, was not possible until the invention of modern physics and calculus. In 1819, Hans Christian Ørsted found that a magnetic field could be generated by an electric current, and Michael Faraday discovered in 1831 that a time-varying magnetic flux through a loop of metallic wire could induce an electric voltage. Decades later James Clerk Maxwell unified the mathematical description of magnetism, electricity, and optics into the field of electromagnetism and the differential equations named after him.

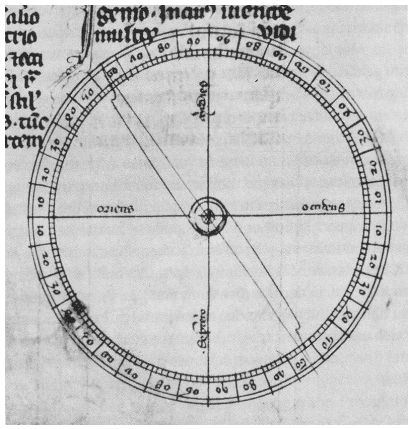

(a) Illustration of a pivoting compass needle in a 14th-century handcopy of *Epistola de magnete*. Ref. [5].

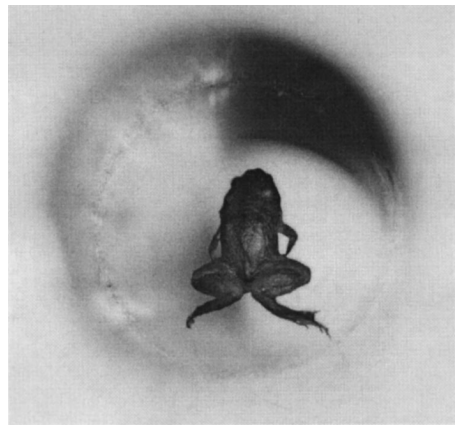

(b) An effectively diamagnetic frog levitated in the stable zone of a 16 tesla magnet in the 20th-century. Picture taken from Ref. [6].

Fig. 1.1: From the pivoting compass needle to a frog floating in strong magnetic field.

1.1.2 Microscopic Origin of Magnetism

The microscopic orgin of magnetism can be considered in its most rudimentary form from a classical toy model. In classical physics, magnetism is due to the magnetic field induced by moving electric charges. For example, magnetic dipoles are induced by tiny current loops, as shown in Fig. 1.2.

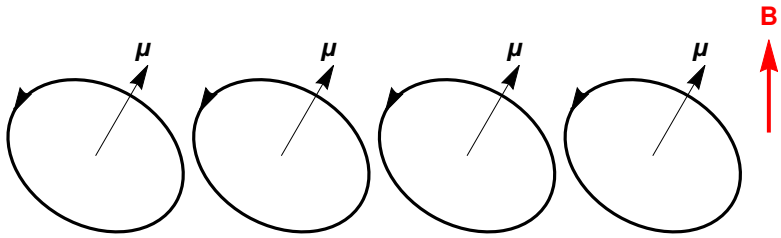

Fig. 1.2: Illustration of current loops interacting with an external magnetic field $\boldsymbol{B}$.

Equation of motion for the magnetic moment — The magnetic moment $\boldsymbol{\mu}$ of a current loop is proportional to the charge current and the area covered by the loop, and therefore also proportional to the total angular momentum $\mathbf{J}$ of the charged particles by a proportionality constant called the *gyromagnetic ratio* γ:

$$\boldsymbol{\mu} = \gamma \mathbf{J} \ , \tag{1.1}$$

which interacts with the externally applied magnetic field $\mathbf{B}$ and performs a *Larmor precession* due to the torque,

$$\boldsymbol{\tau} = \boldsymbol{\mu} \times \mathbf{B} \ . \tag{1.2}$$

Therefore the equation of motion of the magnetic moment is,

$$\frac{d\boldsymbol{J}}{dt} = \boldsymbol{\tau} = -\gamma \boldsymbol{B} \times \boldsymbol{J} \ , \tag{1.3}$$

which shows that the angular precession frequency (*Larmor frequency*) of the magnetic moment is proportional to the strength of the external magnetic field.

In quantum mechanics, the total angular momentum $\boldsymbol{J}$ of electrons consists of two parts, the orbital angular momentum $\boldsymbol{L}$ and the spin angular momentum $\boldsymbol{S}$, which was first discovered by the Stern-Gerlach Experiment for silver atoms in the early 1920s [7]. The spin angular momentum of electrons is quantized, and has two possible eigenvalues, spin-up, $\hbar/2$, and spin-down, $-\hbar/2$, which correspond to the two spin eigenstates that are usually denoted as $|\uparrow\rangle$ and $|\downarrow\rangle$, respectively.

Spintronics — In the past decades, as a subfield of condensed matter physics devoted to the study of active control and manipulation of spin degrees of freedom in solid-state systems [8, 9], spintronics has been developed in parallel with charge-based electronics. A central topic in spintronics is the generation and detection of *spin currents*, which consist of a flux of spin angular momentum. Unlike charge, spin angular momentum is a non-conserved quantity in solids due to spin-orbit coupling [9], which is significant in heavy metals and a main mechanism of manipulating electronic spin [10]. Furthermore, the spin degrees of freedom provide the advantage that they can be switched from one state to another much faster than that switching processes associated with the spatial transport of charge. Moreover, pure spin currents are not accompanied by Joule heating, at least formally [11].

1.1.3 Paramagnetism and Diamagnetism

In solid state systems, magnetic dipoles exist due to the orbital motion of electrons and also their intrinsic spin angular momentum. Paramagnetism is one form of magnetism in which a material produces weak magnetization $\boldsymbol{M} = \chi_w \boldsymbol{B}$ in parallel with the applied magnetic field and does not maintain any magnetization in the absence of an applied magnetic field. Usually it occurs in atoms possessing an odd number of electrons, and the strength of paramagnetism scales with the number of unpaired electrons.

The magnetic moment of an atom can induce a splitting of energy levels in a magnetic field due to the Zeeman coupling. Taking a single spin system where the orbital moment is vanishing as an example, a two-level system is formed and we get a net magnetization resulting from the difference between the separate magnetic moments of both levels. It is well known from the Weiss model that the corresponding magnetic susceptibility satisfies the Curie law,

$$\chi_w = C_w/T \ , \tag{1.4}$$

where T denotes temperature, and C_w is known as the Curie constant, which is proportional to the number of atoms per unit volume and the square of their effective magnetic moments.

One relevant material for this Thesis is platinum (Pt), which is a heavy metal that has gained much popularity among the spintronics community due to its strong spin-orbit coupling [12, 13]. Numerous phenomena in magnon spintronics rely on heterostructures containing heavy transition metals and magnetic insulators [14, 15]. However their magnetic susceptibilities do not obey the Curie law, instead the susceptibility is in general temperature independent. This can be explained by the Pauli paramagnetism of conduction electrons in metals. Denoting the Fermi temperature as T_F, there is only a fraction of T/T_F of electrons that are relevant and form a two-level system as mentioned before. Therefore we have the Pauli paramagnetic susceptibility,

$$\chi_p = \chi_w T/T_F = C_w/T_F \tag{1.5}$$

which is independent of temperature.

Another common phenomenon is diamagnetism, where the change of the orbital dipole moment of a charge current loop is antiparallel to the direction of external magnetic field. Namely, diamagnetic materials have negative magnetic susceptibilities and are repelled by an external magnetic field. Due to this unique property, diamagnets are attracted to the minimum of magnetic field and can achieve stable levitation in free space [6]. Typical examples are superconducting levitation realized due to the perfect diagmagnetism of superconductors when the applied magnetic field is not strong enough to break the Cooper pairing of electrons [16, 17, 18], and a floating frog in a strong magnetic field [6], which is shown in Fig. 1.1(b).

In the classical Langevin theory, the diamagnetic susceptibility is proportional to the number of electrons per atom [19]. Due to the competition with paramagnetism, it is only significant in atoms with lots of complete shells, like copper, whose unpaired single s electron generates only weak paramagnetism. Large diamagnetism also exists in

bismuth, where the band structure of Bloch electrons is renormalized by the magnetic field [20, 21].

1.1.4 Ferromagnetism and Antiferromagnetism

The majority of solids are non-magnetic in the absence of external magnetic fields, since the magnetic dipoles just cancel each other out due to their random orientations caused by thermal fluctuations. Some systems, however, can become spontaneously magnetized. Namely, a net alignment of magnetic dipoles occurs. It is often convenient to introduce the magnetic moment of each atom, which is an integration of the microscopic magnetization over the volume corresponding to one atom. Ferromagnetism arises when a large number of atoms align their spins in the same direction, regardless of whether they are from itinerant conduction electron, or the electrons in the inner atomic shells. The latter allow for a well defined localized magnetic moments in the unit cell of the magnetic material. A special type of magnetic material similar to ferromagnets are *ferrimagnets*. There the microscopic magnetization changes direction or even sign within the smallest possible unit cell of a lattice, but retains a net magnetic moment in the absence of magnetic field.

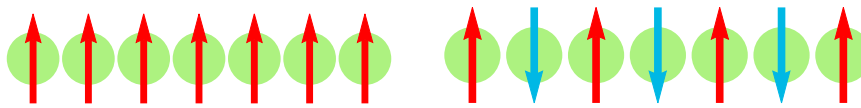

(a) Ferromagnetism (b) Antiferromagnetism

Fig. 1.3: Illustration of ferromagnetism and antiferromagnetism. The red and blue arrows denote the localized magnetic moments of ions in the solid system.

In ferromagnets as illustrated in Fig. 1.3(a), the magnetic moments in the unit cell are aligned in the ground state due to the exchange coupling between nearest neighbors. As temperature increases to be higher than a value called *Curie temperature* (T_C), the magnetic order is destroyed, and the ferromagnet enters the paramagnetic phase. The magnetic susceptibility diverges at T_C, and for a sufficiently high temperature it is described by the Curie-Weiss law,

$$\chi_F = \frac{C_F}{T - T_C}, \quad \text{for} \quad T > T_C \ , \tag{1.6}$$

where C_F is the Curie constant of the ferromagnet.

A typical type of ferromagnetic insulator is yttrium iron garnet (YIG), with a Curie temperature of $T_C = 560\,\mathrm{K}$ [22]. It is actually a ferrimagnet with two sublattices, however, we regard all ferrimagnets as ferromagnets in this Thesis, for the sake of simplicity. Metallic ferromagnets such as permalloy ($Ni_{80}Fe_{20}$), have been widely used in preparing magnetic nanostructures in spintronics [23].

In Nature, most magnetic insulators are antiferromagnetic [24], where the magnetic moments are alternately aligned due to the negative exchange coupling, as shown in

Fig. 1.3(b). For a bipartite antiferromagnet illustrated in this figure, we usually define the directional Néel order parameter $\boldsymbol{n}$ and the total magnetization $\boldsymbol{m}$ to obtain a low-energy theory. These two order parameters are defined locally with respect to two neighboring sites with unit-vector spin orientations $\boldsymbol{m}_1$ and $\boldsymbol{m}_2$ as [25]:

$$\begin{aligned} \boldsymbol{n} &\equiv (\boldsymbol{m}_1 - \boldsymbol{m}_2)/2 \ ; \\ \boldsymbol{m} &\equiv (\boldsymbol{m}_1 + \boldsymbol{m}_2)/2 \ . \end{aligned} \tag{1.7}$$

Like ferromagnetism, antiferromagnetism is a crucial ingredient for the spintronics community. It is robust to stray fields due to the vanishing net magnetization of the ground state, and gives rise to a much faster magnetization dynamics than ferromagnets. The critical temperature for an antiferromagnet to become a paramagnet is called the *Néel temperature* (T_N) [26]. Similar to the Curie-Weiss law, the magnetic susceptibility for an antiferromagnet at the high temperature is given by,

$$\chi_{AF} = \frac{2C_{AF}}{T + T_N}, \quad \text{for} \quad T > T_N \ , \tag{1.8}$$

where C_{AF} is the Curie constant of the antiferromagnet.

The antiferromagnetic insulator NiO has a high Néel temperature of over 500 K [27]. Typical metallic antiferromagnets are CuMnAs with $T_N = 480\,\mathrm{K}$ [28], and Mn_2Au, which is also in antiferromagnetic order at room-temperature [29].

Spin-flop transition — In antiferromagnetic materials with an easy-axis anisotropy, there exists a phase transition as a function of magnetic field where the spins of the two sublattices suddenly rotate and align almost perpendicular to the external field, as illustrated in Fig 1.4. This is called the *spin-flop* transition, and it occurs when the external magnetic field along the spin orientation exceeds a critical value to overcome the anisotropy field. This spin-flop transition field is typically a few Tesla at room-temperature [30]. Study of spin transport around the spin-flop transition is important for developing antiferromagnetic-insulator-based spintronic devices [30, 31].

1.1.5 Spin Wave (Magnon)

An effective Hamiltonian for ferromagnets is the well-known Heisenberg model [32], which illustrates the exchange coupling between neighboring spins,

$$H = -J \sum_{\langle i,j \rangle} \boldsymbol{S}_i \cdot \boldsymbol{S}_j \ , \tag{1.9}$$

where the exchange coupling $J > 0$, the summation is over the nearest neighbors, and $\boldsymbol{S}_i$ denotes the spin on the i-th site.

Its eigenstate can be a state will all spins up

$$|0\rangle = |\ldots\uparrow\uparrow\ldots\rangle \ . \tag{1.10}$$

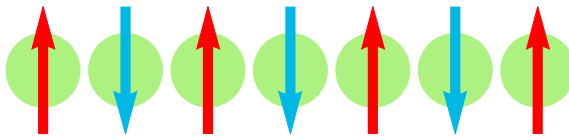

(a) Antiferromagnetic phase. Here the external magnetic field is zero or weaker than the critical field.

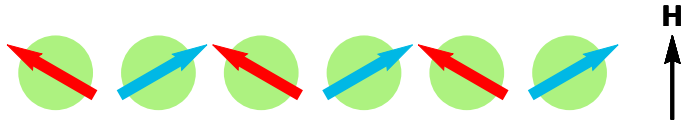

(b) Spin-flop phase. Here the external magnetic field $\boldsymbol{H}$ along the easy-axis is stronger than the critical field.

Fig. 1.4: Illustration of the spin-flop phase transition of an antiferromagnet.

The rotation of all spins is generated by the unitary operator,

$$U(\boldsymbol{\theta}) = \exp(i \sum_i \boldsymbol{S}_i \cdot \boldsymbol{\theta}/\hbar) \ , \tag{1.11}$$

which rotates the spins by the angle $|\boldsymbol{\theta}|$ around the direction $\boldsymbol{\theta}/|\boldsymbol{\theta}|$.

It is easy to show that the Hamiltonian in Eq. 1.9 is invariant under the continuous transformation U, while the eigenstate $|0\rangle$ is not, thus breaking the rotational symmetry. By Goldstone's theorem [33], the invariance under a continuous transformation usually implies the existence of Goldstone modes, since the number of possible ground states is infinitely many, while the actual ground state is only one of them. The Goldstone mode of magnetically ordered systems is called the *spin wave*, while its associated quasi-particle is called the *magnon*. As illustrated in Fig. 1.5, spin waves are wave-like oscillations in a magnet generated by a perturbation in the symmetry-broken phase. In practice, the magnon is not really a Goldstone mode due to anisotropies and external fields, which give rise to a finite energy gap in the magnon dispersion relation. Magnons carry spin angular momentum opposite to the order parameter, so each

Fig. 1.5: Illustration of the spin wave. The red arrows denote the localized magnetic moments in a ferromagnet.

magnon will carry a $+\hbar\,\boldsymbol{z}$ angular momentum when the equilibrium magnetization in a ferromagnet is oriented in the $-\boldsymbol{z}$ direction. In antiferromagnets, the spin wave is described as the propagating precession of two oppositely aligned sublattice magnetic moments, which gives rise to two degenerate magnon branches carrying opposite signs of spin angular momentum in the limit of vanishing external magnetic field.

As mentioned before, spin current is the flow of spin angular momentum. Later we introduce spin transport in magnetic materials in more detail. There can be pure spin currents mediated by magnons, which we refer to as *magnon spin current*. In this Thesis, we focus on magnon spintronics, which is concerned with structures and devices that use magnon spin currents for information processing [34].

1.2 Spin Transport in Non-magnetic Materials

In the following, we are going to introduce spin transport in non-magnetic materials first. By non-magnetic materials, we mean paramagnetic or diamagnetic materials since they do not have macroscopic magnetization in the absence of external magnetic fields.

1.2.1 Spin Hall Effect

The spin Hall effect and inverse spin Hall effect are the two most important effects that help integrate spintronics with conventional electronics based on CMOS technology. When a charge current is applied to a paramagnetic metal with spin-orbit coupling, a transverse spin imbalance will be generated, giving rise to a spin accumulation in the absence of external magnetic fields or ferromagnets. This is the so-called *spin Hall effect* (SHE) [10], which is illustrated in Fig. 1.6(a). It originates from spin-dependent scattering and has been an electrical way to generate spin current in non-magnetic materials with strong spin-orbit coupling, such as the heavy metal Pt. Study on the enhancement of the spin Hall effect is critical to the implementation of functional spintronic devices. The spin Hall effect in Pt is thought to have both an intrinsic origin where a conduction electron acquires Berry-phase based on its unique band structure [35, 36], and an extrinsic origin due to side-jump scattering [37]. Furthermore, one important contribution to the extrinsic spin Hall effect is due to skew scattering of the moving magnetic moments (electrons) with magnetic impurities or phonons [10]. The spin-diffusion length of such types of materials is limited to about 10 nanometers so far [36], which limits the application in electronic-based spintronic devices. Recently, giant spin Hall effects were observed in perpendicularly spin-polarized FePt/Au devices and also in thin film CuBi alloys due to strong skew scattering [14, 38].

1.2.2 Inverse Spin Hall Effect

As the Onsager reciprocal effect to the spin Hall effect, a transverse charge imbalance will also be generated by a flow of spin angular momentum in metals, which is called the *Inverse Spin Hall effect* (ISHE), as illustrated in Fig. 1.6(b). The inverse spin Hall effect has been a powerful way to detect spin current since its discovery in 2006 [39, 40, 41, 42].

The conversion between the generated charge current $\boldsymbol{j}_c$ and the spin current $\boldsymbol{j}_s$ is

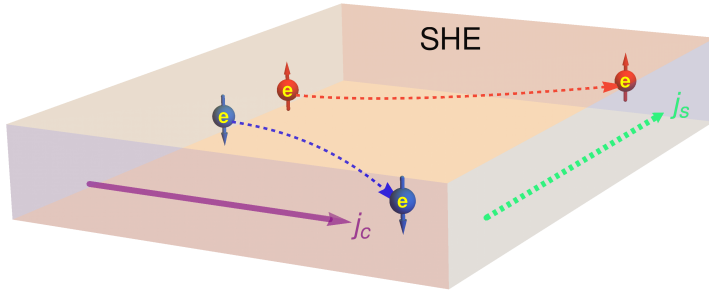

(a) Spin Hall effect. The solid purple arrow denotes the direction of driving charge current $\boldsymbol{j}_c$ and the dashed green arrow denotes the direction of generated spin current $\boldsymbol{j}_s$.

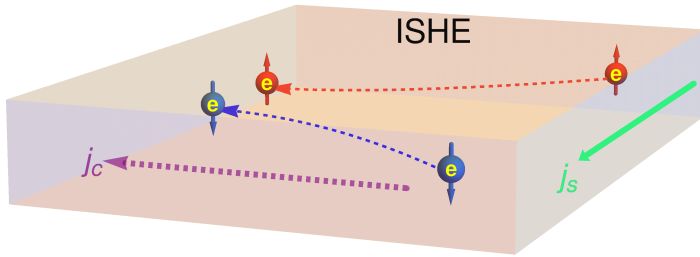

(b) Inverse spin Hall effect. The solid green arrow denotes the direction of the driving spin current $\boldsymbol{j}_s$ and the dashed purple arrow denotes the direction of generated charge current $\boldsymbol{j}_c$.

Fig. 1.6: Illustration of spin Hall effect and inverse spin Hall effect.

expressed as,

$$\boldsymbol{j}_c = \theta_{\mathrm{SH}}(2e/\hbar)\boldsymbol{j}_s \times \boldsymbol{\sigma} \ , \tag{1.12}$$

where $\boldsymbol{\sigma}$ denotes the spin-polarization vector of the conduction electrons, and θ_{SH} is the spin Hall angle, which characterizes the efficiency of the inverse spin Hall effect and can reach the magnitude of ~ 0.05 in Pt [43]. Meanwhile, the topological insulator Bi_2Se_3 also exhibits strong spin-orbit coupling [44], and was reported to host an inverse spin Hall effect with a spin Hall angle of 0.0093 [45]. It can thus play a similar role as Pt in functional spintronic devices.

1.3 Spin Transport in Ferromagnetic Materials

1.3.1 Ferromagnetic Resonance and Gilbert Damping

Ferromagnetic resonance (FMR) is a standard tool for probing spin waves and studying the magnetization dynamics in a ferromagnet. In FMR, the magnetic field component of microwaves exerts a torque on the magnetic moments to cause them to precess

with a frequency depending on the external magnetic field and the magnetization of the ferromagnet [19]. The system loses energy during each precession cycle, which can be characterized by a phenomenological parameter called the *Gilbert damping* constant [46]. Due to the Gilbert damping, the magnons require an external energy source, such as a microwave, to excite. Therefore, low damping materials such as YIG are attractive, for instance, to study spin transport.

Landau-Lifshitz-Gilbert equation — To phenomenologically describe the collective magnetization dynamics during ferromagnetic resonance, we use the Landau-Lifshitz-Gilbert (LLG) equation,

$$\frac{d\boldsymbol{M}}{dt} = -\gamma \boldsymbol{M} \times \boldsymbol{H}_{\text{eff}} + \frac{\alpha}{M_s} \boldsymbol{M} \times \frac{d\boldsymbol{M}}{dt} \ , \tag{1.13}$$

where α is the Gilbert damping parameter, M_s is the saturation magnetization and $\boldsymbol{H}_{\text{eff}}$ is the effective field. The terms of the LLG equation are visualized as shown in Fig. 1.7 to demonstrate the various torques. Here $\boldsymbol{H}_{\text{eff}}$ is determined by the instantaneous magnetic configuration, and can contain contributions from the anisotropy due to spin-orbit interaction, modulation of the exchange energy due to magnetization gradients, and demagnetization field due to dipole-dipole interactions [47].

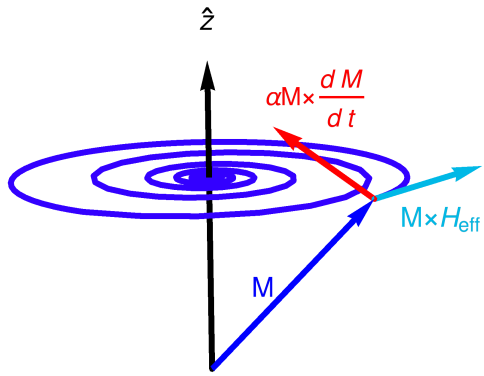

Fig. 1.7: Illustration of the terms in the LLG equation.

1.3.2 Ferromagnetic Magnon

Assuming we have a 1D ferromagnetic spin chain whose lattice constant is a_0, the spin Hamiltonian with an external magnetic field along the $\hat{z}$ axis can be written as

$$H = -\sum_n \left(J\boldsymbol{S}_n \cdot \boldsymbol{S}_{n+1} + g\mu_B H \boldsymbol{S}_n^z \right) \ , \tag{1.14}$$

where $J > 0$ denotes the ferromagnetic couping, which tries to align the neighboring magnetic moments, and H is the magnetic field, g is the Landé factor, μ_B is the Bohr

magneton. Magnons described by linearizing this Hamiltonian are called *exchange magnons*. In the low-energy limit, the dispersion of exchange magnons is found from the Landau-Lifshitz-Gilbert equation,

$$\epsilon(k) = g\mu_B H + 2Jk^2 a_0^2 \,, \tag{1.15}$$

which tells us that it costs at least an energy $g\mu_B H$ to excite magnons in such a system. Consequently we can think about ferromagnetic resonance as exciting magnons with zero momentum.

In realistic materials, the magnon dispersion is strongly affected by magnetic dipole interactions [48], and can be measured by the Brillouin Light Scattering (BLS) experiment, which makes use of the creation and absorption of a magnon by a photon [49].

Taking an in-plane magnetized ferromagnetic film for example, there are two types of magnons, one with wave vector $\boldsymbol{k}$ oriented parallel to the magnetic field, which is called the *backward volume magnetostatic wave*, with opposite directions of its phase and group velocity. The other type has its wave vector perpendicular to the external field, and is called the *magnetostatic surface wave*, since its wave amplitude decays exponentially from the surface of the film [50]. Resulting from the competition between the magnetic dipole interaction and the exchange interaction, there can be a frequency minimum at a nonzero wavevector, which is exploited to realized the Bose–Einstein condensation (BEC) of magnons [1].

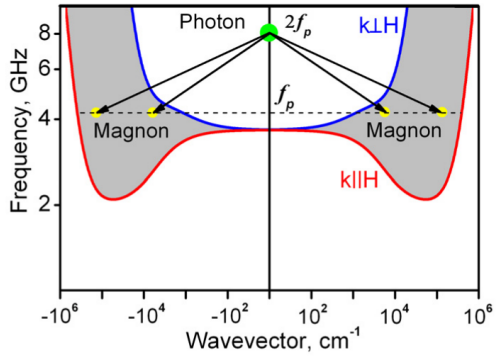

Fig. 1.8: Dispersion spectrum of magnons in a YIG film magnetized by an in-plane static magnetic field. The arrows illustrate the parametric pumping process, which can be considered as a creation of two magnons with opposite wavevectors by a microwave photon of the pumping field. Figure extracted from Ref. [1].

Fig.1.8 illustrates the dispersion of ferromagnetic magnons in a YIG film magnetized by an in-plane static magnetic field. A room-temperature BEC of magnons in such a system has been achieved by applying parametric pumping of the magnon gas to create a strongly non-equilibrium magnon distribution and measuring its redistribution using Brillouin Light Scattering spectroscopy [1]. The non-equilibrium magnons reach a quasi-equilibrium by two-magnon and the four-magnon scattering processes, which evolves to an equilibrium state where magnons accumulate at the minimum magnon frequency of the mode whose wave vector is parallel to the external magnetic field.

Spin Seebeck effect — The coupling of thermoelectric spin and charge transport with magnetization dynamics makes it possible for heat currents to generate spin currents in magnetic structures and transfer the spin angular momentum across the interface with a non-magnetic metal [51, 52]. This is called the *spin Seebeck effect* (SSE), which was initially observed in 2008, when experimentalists used the $Ni_{81}Fe_{19}$|Pt structure to observe the spin current generated by thermal gradient across the interface [53]. They have since then used the longitudinal configuration, where the direction of generated spin current is along the thermal gradient, as shown in Fig. 1.9(a). Therefore this effect is called the longitudinal spin Seebeck effect (LSSE).

1.3.3 Ferromagnetic (Ferrimagnetic) Insulators and Metals

Ferromagnetic insulators can support spin transport with magnons as the spin carriers [34], and a nonlocal spin-Seebeck effect measurement can be utilized to measure the spin diffusion length for magnons [3]. Recently, the longitudinal spin Seebeck signal in a YIG|Pt system was found to peak at a specific temperature that depends on the YIG sample thickness and freeze out at high magnetic fields [54]. A thermoelectric energy harvest technology based on the spin Seebeck effect has also been developed with Bi:YIG|Pt double layer systems [55]. The experimental results of the longitudinal spin Seebeck effect have been well explained by the magnon-driven mechanism, which yields that the interfacial spin current is proportional to the difference between the magnon temperature in the ferromagnet and the electron temperature in the normal metal [52], and that the magnon accumulation in the ferromagnetic insulator pumps the spin current into the NM layer [56]. As a fundamental phenomenon of thermoelectricity, the Peltier effect was observed a long time ago, and converts a charge current into a heat current [11]. The Onsager reciprocal effect to the spin Seebeck effect, the *spin Peltier effect*, has also been discovered in a YIG|Pt bilayer structure, where a magnon heat current is generated in the magnetic insulator by a spin current through the interface with the metal contact [57].

Transfer of spin angular momentum in ferromagnets can also bring other effects. For example, for a bilayer structure of a magnetic insulator and a metal, experimental works have observed that the resistance of the metal can be controlled by orienting the magnetization of the magnetic insulator [58, 59]. This phenomenon is called *Spin Hall Magnetoresistance* (SMR). The measured SMR signal is usually much smaller than the typical values of GMR (giant magnetoresistance), but has a unique angular dependence with respect to the relative orientation of the current and magnetization.

More generally, the interfacial spin Seebeck effect is understood as a manifestation of *spin pumping*, which was first proposed as a mechanism for injecting pure spin current from a ferromagnet to a normal metal [62]. This will be discussed next.

Spin pumping — Spin pumping occurs on the boundary between a normal metal (NM) and a magnet when the magnetization is excited from its equilibrium positions, e.g. by microwaves (ferromagnetic resonance), as shown in Fig. 1.9(b). With the help of interface exchange coupling, the magnetization dynamics transfers spin angular

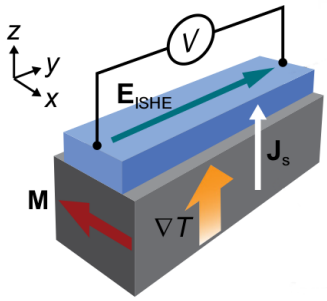

(a) Configuration of longitudinal spin Seebeck effect. Here the gray bulk denotes a ferromagnet, where the magnetization is denoted as $\boldsymbol{M}$. The blue bulk is the attached normal metal with strong spin-orbit coupling. The direction of spin current $\boldsymbol{J}_s$ is parallel to the thermal gradient ∇T. Figure extracted from Ref. [60].

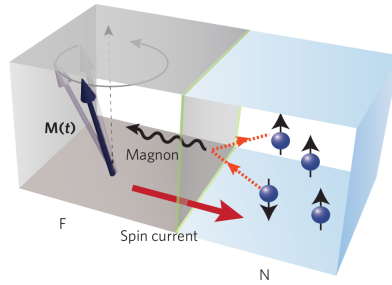

(b) Schematic diagram for spin pumping. The precession of the localized magnetic moment leads to propagation of magnons in the ferromagnet, and pumps spin angular momentum into the normal metal with the electron-magnon scattering on the boundary. Figure extracted from Ref. [61].

Fig. 1.9: Spin Seebeck effect and spin pumping.

momentum which is carried by magnons from the magnetic insulator to the conduction electron system of the NM.

In general, the pumped spin current is expressed as [62],

$$\boldsymbol{I}_{sp} = -\frac{g\mu_B}{4\pi}\mathrm{Re}(2g^{\uparrow\downarrow})\left[\boldsymbol{m}\times\frac{\partial \boldsymbol{m}}{\partial t}\right] \tag{1.16}$$

where $\boldsymbol{m}$ is the unit vector of the magnetization, and $g^{\uparrow\downarrow}$ characterizes the spin pumping efficiency, and is called the *spin-mixing conductance*, of which the real part determines the interface Gilbert damping and its imaginary part is known to be relatively small [63]. For the bilayer structure of Pt/YIG, the spin-mixing conductance is observed to reach $4.56 \times 10^{14}\,\Omega^{-1}m^{-2}$ which gives a large induced inverse spin Hall voltage [64].

Spin-transfer torque — The reciprocal effect of spin pumping is the *spin-transfer torque* (STT), which denotes the driving of magnetization dynamics of a ferromagnetic material by injection of a spin current [65, 2]. In 1996, it was predicted that the spin transfer torque caused by a dc current can make the local magnetization undergo a steady-state precession and lead to emission of spin waves [65, 2].

The current-induced spin-transfer torque has also been observed to be able to switch the magnetic state of a nanoscale magnetic tunnel junction [66, 67]. Therefore it brings potential applications in information technology. In magnetoresistive random-access memory (MRAM) devices, the resistance of a magnetic tunnel junction or a spin-valve determines 1 and 0 states to store information [68]. Spin-transfer Torque MRAM (STT-MRAM), which is aimed at providing a high speed, non-volatile memory, has

been a promising functional spintronic device. In the STT-MRAM, the magnetization is flipped using a spin-polarized current, which is more power efficient and better scalabe than a conventional MRAM device which uses magnetic field-assisted writing [68].

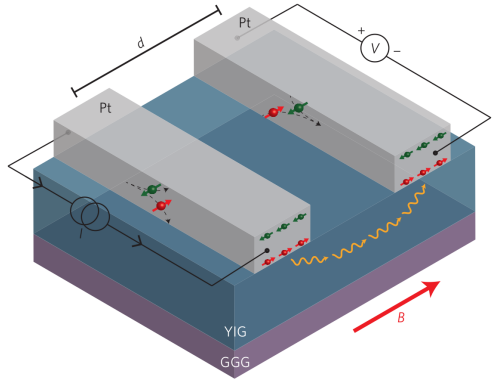

Fig. 1.10: Schematic of the non-local measurement geometry of a device. The two platinum strips act as spin injector and detector for the ferromagnetic magnons. On the FM|NM interface, magnons are created and absorbed by the spin-flip scattering of polarized electrons [2]. Figure extracted from Ref. [3]

Electrical excitation and detection of magnon spin transport — In the full electrical approach of studying magnon transport, excitation and detection of magnons are performed with the non-local geometry [3], as shown in Fig. 1.10. The effect of an external magnetic field on magnon spin transport in the magnetic insulator YIG has been studied using a similar non-local geometry [69]. In these non-local measurements, the spin Hall effect in one normal metal strip (Pt) is utilized to inject into the magnetic insulator a spin current, creating non-equilibrium magnon population in the magnetic insulator, which is then detected by measuring the inverse spin Hall voltage in another attached normal metal.

1.4 Spin Transport in Antiferromagnetic Materials

1.4.1 Antiferromagnetic Magnon and Antiferromagnetic Resonance

Microwave technologies are nowadays restricted to the GHz regime due to the frequency range that can be reached by the ferromagnetic magnetic resonance. To reach the THz regime, one possible approach is utilizing the antiferromagnetic resonance, of which the precession frequency has an exchange-field enhancement as explained below.

The intrinsic ferromagnetic resonance frequency of a ferromagnet is given by,

$$\omega_{\mathrm{FMR}} = \gamma H_{aniso} \ , \tag{1.17}$$

where H_{aniso} denotes the anisotropy field, which yields frequencies on the order of a few GHz.

By modeling the antiferromagnets as two sublattices of magnetizations with opposite orientations and deriving its equations of motion with a transverse magnetic field, the precession frequency for antiferromagnetic resonance (AFMR) is found as [70],

$$\omega_{\mathrm{AFMR}} = \gamma\sqrt{H_{aniso}(H_{aniso} + H_{ex})} \,, \tag{1.18}$$

where H_{ex} denotes the exchange field. In conventional antiferromagnets such as MnO, MnF_2, Cr_2O_3, H_{ex} is usually much larger than than H_{aniso}, thus we have an enhancement in the excitation energy, which can reach several hundred GHz even at zero external field [70].

1.4.2 Antiferromagnetic Metals

Spin transport through the metallic antiferromagnet FeMn has been reported in Ref. [71], where they performed measurements based on spin pumping with the inverse spin Hall effect in $Ni_{80}Fe_{20}$|FeMn|W trilayers and studied the FeMn thickness dependence of the spin currents. In this study, the spin current signals observed for thicknesses well above the electronic spin diffusion length were attributed to the magnonic spin current. In addition, for the metallic antiferromagnet IrMn, an enhanced spin pumping efficiency has been reported during the magnetic phase transition in a heterostructure consisting of NiFe|Cu|IrMn [72].

Antiferromagnetic metals can also be a candidate material for spin-current detection. Recently a large inverse spin Hall voltage has been generated in the polycrystalline $Ir_{20}Mn_{80}$ with a spin Hall angle close to that of Pt [73]. Magnetization dynamics in metallic antiferromagnets driven by spin current attracts wide attention. Recently, a theoretical proposal was made that antiferromagnets driven by dc spin current can be used as tunable detectors and emitters of narrow-band signals operating in the THz range [75].

1.4.3 Antiferromagnetic Insulators

A general system to experimentally study spin transport in antiferromagnetic insulators is the heterostructure of the type FM|AFM|NM, where spin pumping can also happen on the interface between an antiferromagnetic insulator and a normal metal. Robust spin propagation in NiO up to 100-nm thickness is realized by spin injection from YIG. It has also been observed that the insertion of a thin NiO layer between YIG and Pt can create a significant enhancement of the spin currents driven into Pt [27]. Besides, antiferromagnetic resonance close to the spin-flop transition has been detected for a MnF_2|Pt bilayer structure by measuring the dc voltage arising along a thin Pt strip and the microwave transmission through a waveguide underneath the sample [74].

Meanwhile, there is a recent theoretical research on trilayers that consist of one antiferromagnetic insulator and two metals, where spin-transfer torque induced antiferromagnetic resonances have been studied by solving the Landau-Lifshitz-Gilbert equation in the antiferromagnetic insulator and the spin-diffusion equation in the normal metal, indicating that the antiferromagnetic resonance signals are enhanced close to the spin-flop transition [76].

Electrical generation and detection of magnon spin transport — An experimental group recently managed to convey electrically tunable spin information parallel to the antiferromagnetic Néel order over a much longer distance than the thermal approach [30]. They used a non-local geometry of Pt on top of the crystalline antiferromagnetic iron oxide $\alpha - Fe_2O_3$, which has a low anisotropy and Gilbert damping. The magnon spin diffusion lengths were measured for both low and high magnetic fields, and found to be on the order of several micrometers, which is comparable with the spin diffusion length in YIG [3].

Spin Seebeck effect — Antiferromagnetic spin waves can also be an effective carrier of spin angular momentum. The longitudinal spin Seebeck effect has been investigated for a uniaxial antiferromagnetic insulator Cr_2O_3 attached to a Pt layer, where the magnitude of spin current was measured to be proportional to the magnetization in Cr_2O_3 [77]. Longitudinal spin Seebeck effect has also been observed in the non-centrosymmetric antiferromagnet $\alpha - Cu_2V_2O_7$ [78, 79], whose antiferromagnetic ground state is affected by its Dzyaloshinskii-Moriya interaction, which is an antisymmetric exchange interaction due to spin-orbit coupling and the absence of an inversion center between the nearest-neighbor spins [80, 81].

1.5 Outline

The scope of this Thesis is to investigate the spin and thermal transport in ferromagnetic insulators and antiferromagnetic metals with different theoretical approaches.

In Chapter 2, we develop a Green's function formalism for spin transport through heterostructures that contain metallic leads and insulating ferromagnets, such as the structure depicted in Fig. 1.10. We consider ballistic spin transport by exchange magnons in a metal-insulator-metal heterostructure with and without disorder. The developed Green's function formalism is a natural starting point for numerical studies of magnon transport in heterostructures that contain normal metals and magnetic insulators. In Chapter 3, we apply the stochastic Landau-Lifshitz-Gilbert formalism with spin-transfer torques to develop a theory for magnon drag in antiferromagnetic metals. The results show that antiferromagnetic metals might be used as a tunable source of spin current near the spin-flop transition field. In Chapter 4, we study the alignment-dependent thermal transport mediated by magnons across a magnetic junction consisting of two ferromagnetic insulators, which mimics the structure of the recently proposed magnon spin valve [82]. We present the conclusions and outlook of our research in Chapter 5.

CHAPTER 2

Green's Function Formalism for Spin Transport in Metal-insulator-metal Heterostructures

We develop a Green's function formalism for spin transport through heterostructures that contain metallic leads and insulating ferromagnets. While this formalism in principle allows for the inclusion of various magnonic interactions, we focus on Gilbert damping. As an application, we consider ballistic spin transport by exchange magnons in a metal-insulator-metal heterostructure with and without disorder. For the former case, we show that the interplay between disorder and Gilbert damping leads to spin current fluctuations. For the case without disorder, we obtain the dependence of the transmitted spin current on the thickness of the ferromagnet. Moreover, we show that the results of the Green's function formalism agree in the clean and continuum limit with those obtained from the linearized stochastic Landau-Lifshitz-Gilbert equation. The developed Green's function formalism is a natural starting point for numerical studies of magnon transport in heterostructures that contain normal metals and magnetic insulators[1].

2.1 Introduction

Magnons are the bosonic quanta of spin waves, oscillations in the magnetization orientation in magnets [83, 84]. Interest in magnons has recently revived as enhanced

[1]This chapter and its appendix are based on J. Zheng, S.A. Bender, J. Armaitis, R.E. Troncoso and R.A. Duine (2017), Physical Review B, 96(17), 174422. R.A. Duine conceived the project. J. Zheng did all the analytic derivations on the NEGF formalism, performed the related numerical calculations, and wrote the manuscript with the help of all co-authors. S.A. Bender carried out the LLG calculations. All other authors contributed via discussions.

experimental control has made them attractive as potential data carriers of spin information over long distances and without Ohmic dissipation [34]. In general, magnons exist in two regimes. One is the dipolar magnon with long wavelengths that is dominated by long-range dipolar interactions and which can be generated e.g. by ferromagnetic resonance [85, 86]. The other type is the exchange magnon [87], dominated by exchange interactions and which generally has higher frequency and therefore perhaps more potential for applications in magnon based devices [34]. In this chapter, we focus on transport of exchange magnons.

Thermally driven magnon transport has been widely investigated, and is closely related to spin pumping of spin currents across the interface between insulating ferromagnets (FMs) and normal metals (NM) [88, 89, 90] and detection of spin current by the inverse spin Hall Effect [39]. The most-often studied thermal effect in this context is the spin Seebeck effect, which is the generation of a spin current by a temperature gradient applied to a magnetic insulator that is detected in an adjacent normal metal via the inverse spin Hall effect [53, 52]. Here, thermal fluctuations in the NM contacts drive spin transport into the FM, while the dissipation of spin back into the NM by magnetic dynamics is facilitated by the above mentioned spin-pumping mechanism.

The injection of spin into a FM can also be accomplished electrically, via the interaction of spin polarized electrons in the NM and the localized magnetic moments of the FM. Reciprocal to spin-pumping is the spin-transfer torque, which, in the presence of a spin accumulation (typically generated by the spin Hall effect) in the NM, drives magnetic dynamics in the FM [2, 65]. Spin pumping likewise underlies the flow of spin back into the NM contacts, which serve as magnon reservoirs. In two-terminal set-ups based on YIG and Pt, the characteristic length scales and device-specific parameter dependence of magnon transport has attracted enormous attention, both in experiments and theory. Cornelissen *et al.* [3] studied the excitation and detection of high-frequency magnons in YIG and measured the propagating length of magnons, which reaches up to 10 μm in a thin YIG film at room temperature. Other experiments have shown that the polarity reversal of detected spins of thermal magnons in non-local devices of YIG are strongly dependent on temperature, YIG film thickness, and injector-detector separation distance [91]. That the interfaces are crucial can e.g. be seen by changing the interface electron-magnon coupling, which was found to significantly alter the longitudinal spin Seebeck effect [92].

A linear-response transport theory was developed for diffusive spin and heat transport by magnons in magnetic insulators with metallic contacts. Among other quantities, this theory is parameterized by relaxation lengths for the magnon chemical potential and magnon-phonon energy relaxation [93, 94]. In a different but closely-related development, Onsager relations for the magnon spin and heat currents driven by magnetic field and temperature differences were established for insulating ferromagnet junctions, and a magnon analogue of the Wiedemann-Franz law was is also predicted [95, 96]. Wang *et al.* [97] consider ballistic transport of magnons through magnetic insulators with magnonic reservoirs — rather than the more experimentally relevant situation of metallic reservoirs considered here — and use a nonequilibrium Green's function formalism (NEGF) to arrive at Landuaer-Bütikker-type expressions for the magnon current. The above-mentioned works are either in the linear-response regime or do not consider Gilbert damping and/or metallic reservoirs. So far, a complete quantum

mechanical framework to study exchange magnon transport through heterostructures containing metallic reservoirs that can access different regimes, ranging from ballistic to diffusive, large or small Gilbert damping, and/or small or large interfacial magnon-electron coupling, and that can incorporate Gilbert damping, is lacking.

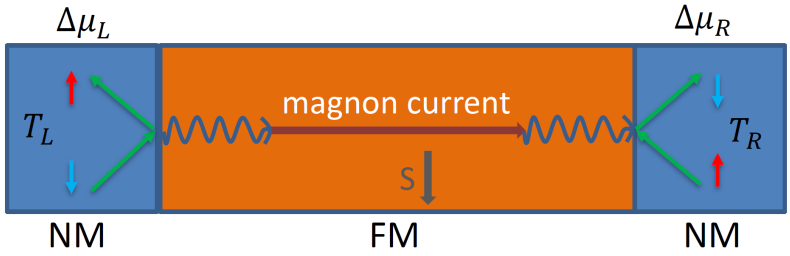

Fig. 2.1: Illustration of the system where magnon transport in a ferromagnet (orange region) is driven by a spin accumulation difference $\Delta\mu_L - \Delta\mu_R$ and temperature difference $T_L - T_R$ between two normal-metal leads (blue regions). Spin-flip scattering at the interface converts electronic to magnonic spin current. Here, **S** is the local spin density in equilibrium.

In this chapter we develop the non-equilibrium Green's function formalism [98] for spin transport through NM-FM-NM heterostructures (see Fig. 2.1). In principle, this formalism straightforwardly allows for adding arbitrary interactions, such as scattering of magnons with impurities and phonons, Gilbert damping, and magnon-magnon interactions, and provides a suitable platform to study magnon spin transport numerically, in particular beyond linear response. Here, we apply the formalism to ballistic magnon transport through a low-dimensional channel in the presence of Gilbert damping. For that case, we compute the magnon spin current as a function of channel length both numerically and analytically. For the clean case in the continuum limit we show how to recover our results from the linearized stochastic Landau-Lifshitz-Gilbert (LLG) equation [99] used previously to study thermal magnon transport in the ballistic regime [100] that applies to to clean systems at low temperatures such that Gilbert damping is the only relaxation mechanism. Using this formalism we also consider the interplay between Gilbert damping and disorder and show that it leads to spin-current fluctuations.

This chapter is organized as follows. In Sec. 2.2, we discuss the non-equilibrium Green's function approach to magnon transport and derive an expression for the magnon spin current. Additionally a Landauer-Büttiker formula for the magnon spin current is derived. In Sec. 2.3, we illustrate the formalism by numerically considering ballistic magnon transport and determine the dependence of the spin current on thickness of the ferromagnet. To further understand these numerical results, we consider the formalism analytically in the continuum limit in Sec. 2.4, and also show that in that limit we obtain the same results using the stochastic LLG equation. We give a further discussion and outlook in section 2.5.

2.2 Non-equilibrium Green's Function Formalism

In this section we describe our model and, using Keldysh theory, arrive at an expression for the density matrix of the magnons from which all observables can be calculated. The reader interested in applying the final result of our formalism may skip ahead to Sec. 2.2.5 where we give a summary on how to implement it.

2.2.1 Model

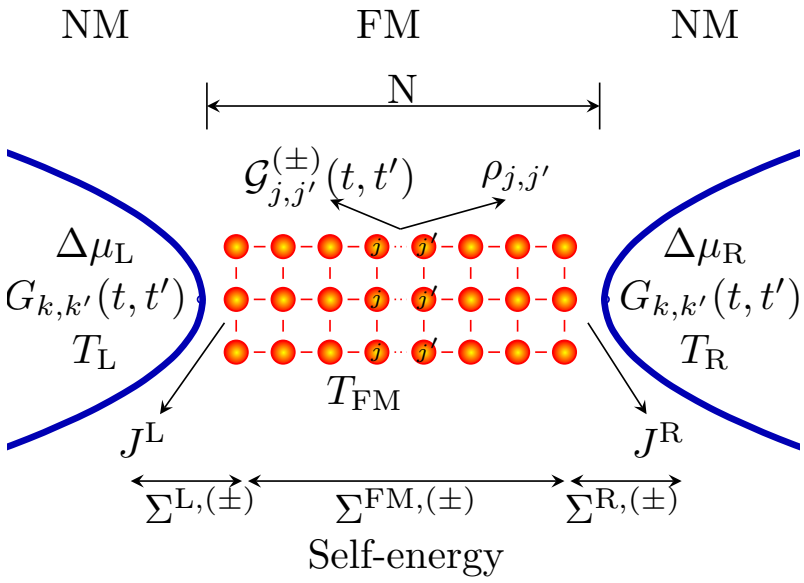

Fig. 2.2: Schematic for the NM-FM-NM heterostructure and notation for the Green's functions and self-energies. The array of circles denotes the localized magnetic moments, while the two regions outside the parabolic lines denote the leads, i.e., reservoirs of polarized electrons. Moreover, $J^{L/R}_{j;kk'}$ denotes the interface coupling, and $T_{L/R}$ and $\Delta\mu_{L/R}$ denote the temperature and spin accumulation for the leads. The properties of the magnons are encoded in $\mathcal{G}^{(+)}_{j,j'}(t,t')$, the retarded magnon Green's function, and the magnon density matrix $\rho_{j,j'}$. The number of sites in the spin-current direction is N. The self-energies $\Sigma^{FM,(\pm)}$, $\Sigma^{L,(\pm)}$, $\Sigma^{R,(\pm)}$ are due to Gilbert damping, and the left and right lead, respectively.

We consider a magnetic insulator connected to two nonmagnetic metallic leads, as shown in Fig. 2.2. For our formalism it is most convenient to consider both the magnons and the electrons as hopping on the lattice for the ferromagnet. Here, we consider the simplest versions of such cubic lattice models; extensions, e.g. to multiple magnon and/or electron bands, and multiple leads are straightforward. The leads have a temperature $T_{L/R}$ and a spin accumulation $\Delta\mu_{L/R}$ that injects spin current from

the non-magnetic metal into the magnetic insulator. This nonzero spin accumulation could, e.g., be established by the spin Hall effect.

The total Hamiltonian is a sum of the uncoupled magnon and lead Hamiltonians together with a coupling term:

$$\hat{H}_{\rm tot} = \hat{H}_{\rm FM} + \hat{H}_{\rm NM} + \hat{H}_C \ . \tag{2.1}$$

Here, $\hat{H}_{\rm FM}$ denotes the free Hamiltonian for the magnons,

$$\hat{H}_{\rm FM} = -\sum_{<j,j'>} J_{j,j'} b_{j'}^\dagger b_j + \sum_j \Delta_j b_j^\dagger b_j \equiv \sum_{<j,j'>} h_{j',j} b_{j'}^\dagger b_j \ . \tag{2.2}$$

where $b_j(b_j^\dagger)$ is a magnon annihilation (creation) operator. This hamiltonian can be derived from a spin hamiltonian using the Holstein-Primakoff transformation [101, 102] and expanding up to second order in the bosonic fields. Eq. (2.2) describes hopping of the magnons with amplitude $J_{j,j'}$ between sites labeled by j and j' on the lattice, with an on-site potential energy Δ_j that, if taken to be homogeneous, would correspond to the magnon gap induced by a magnetic field and anisotropy. We have taken the external field in the $-z$ direction, so that one magnon, created at site j by the operator $\hat{b}_j^\dagger$, corresponds to spin $+\hbar$.

The Hamiltonian for the electrons in the leads is

$$\hat{H}_{\rm NM} = -\sum_{r\in\{L,R\}} \sum_{<k,k'>} \sum_{\sigma\in\uparrow,\downarrow} t^r \hat{\psi}_{k\sigma r}^\dagger \hat{\psi}_{k'\sigma r} + h.c. \tag{2.3}$$

where the electron creation ($\psi_{k\sigma r}^\dagger$) and annihilation ($\psi_{k\sigma r}$) operators are labelled by the lattice position k, spin σ, and an index r distinguishing (L)eft and (R)ight leads. The hopping amplitude for the electrons is denoted by t^r and could in principle be different for different leads. Moreover, terms to describe hopping beyond nearest neighbor can be straightforwardly included. Below we will show that microscopic details will be incorporated in a single parameter per lead that describes the coupling between electrons and magnons.

Finally, the Hamiltonian that describes the coupling between metal and insulator, $\hat{H}_C$, is given by [103]

$$\hat{H}_C = \sum_{r,j;kk'} \left(J_{j;kk'}^r \hat{b}_j^\dagger \hat{\psi}_{k\downarrow r}^\dagger \hat{\psi}_{k'\uparrow r} + \text{h.c.} \right) \ , \tag{2.4}$$

with the matrix elements $J_{j;kk'}^r$ that depend on the microscopic details of the interface. An electron spin that flips from up to down at the interface creates one magnon with spin $+\hbar$ in the magnetic insulator. This form of coupling between electrons and magnons derives from interface exchange coupling between spins in the insulators with electronic spins in the metal [103].

2.2.2 Magnon Density Matrix and Current

Our objective is to calculate the steady-state magnon Green's function $i\mathcal{G}_{j,j'}^<(t,t') = \langle \hat{b}_{j'}^\dagger(t') \hat{b}_j(t) \rangle$, from which all observables are calculated (note that time-dependent operators refer to the Heisenberg picture). This "lesser" Green's function follows from

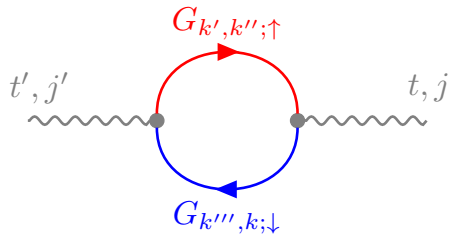

Fig. 2.3: Feynman diagram for the spin-flip processes emitting and absorbing magnons that are represented by the wavy lines. The two vertices indicate the exchange coupling at one of the interfaces of the magnetic insulator (sites j, j') and normal metal (sites k, k', k'', k'''). $G_{k'k'';\uparrow}$ and $G_{k'''k;\downarrow}$ denotes the electron Keldysh Green's function of one of the leads.

the Keldysh Green's function

$$i\mathcal{G}_{j,j'}(t,t') \equiv \mathrm{Tr}\left[\hat{\rho}(t_0)T_{\mathcal{C}^\infty}\left(\hat{b}_j(t)\hat{b}^\dagger_{j'}(t')\right)\right] \ , \tag{2.5}$$

with $\hat{\rho}(t_0)$ the initial (at time t_0) density matrix, and $\mathcal{C}^\infty$ the Keldysh contour, and Tr[...] stands for performing a trace average. The time-ordering operator on this contour is defined by

$$T_{\mathcal{C}^\infty}\left(\hat{O}(t)\hat{O}'(t')\right) \equiv \theta(t,t')\hat{O}(t)\hat{O}'(t') \pm \theta(t',t)\hat{O}'(t')\hat{O}(t) \ , \tag{2.6}$$

with $\theta(t,t')$ the corresponding Heaviside step function and the $+(-)$ sign applies when the operators have bosonic (fermionic) commutation relations. In Fig. 2.2 we schematically indicate the relevant quantities entering our theory.

We compute the magnon self energy due the coupling between magnons and electrons to second order in the coupling matrix elements $J_{j;kk'}$. This implies that the magnons acquire a Keldysh self-energy due to lead r given by

$$\hbar\Sigma^r_{j,j'}(t,t') \ = \ -\frac{i}{\hbar}\sum_{kk'k''k'''} J^r_{j;kk'}\,(J^r)^*_{j';k''k'''}\,G_{k'k'';r\uparrow}(t,t')G_{k'''k;r\downarrow}(t',t) \ , \tag{2.7}$$

where $G_{k'k'';r\sigma}(t,t')$ denotes the electron Keldysh Green's function of lead r, that reads

$$\begin{aligned} G_{kk';r\sigma}(t,t') \ &= \ -i\langle T_{\mathcal{C}^\infty}\hat{\psi}_{kr\sigma}(t)\hat{\psi}^\dagger_{k'r\sigma}(t')\rangle \\ &\equiv \ \Theta(t,t')G^>_{kk';r\sigma}(t,t') + \Theta(t',t)G^<_{kk';r\sigma}(t,t') \ . \end{aligned} \tag{2.8}$$

The Feynman diagram for this self-energy is shown in Fig. 2.3. While this self-energy is computed to second order in $J^r_{j;kk'}$, the magnon Green's function and the magnon spin current, both of which we evaluate below, contain all orders in $J^r_{j;kk'}$, which therefore does not need to be small. In this respect, our approach is different from the work of Ohnuma *et al.* [104], who evaluate the interfacial spin current to second order in the electron-magnon coupling. Irreducible diagrams other than that in Fig. 2.3 involve one or more magnon propagators as internal lines and therefore correspond to magnon-magnon interactions at the interface induced by electrons in the normal metal. For the

small magnon densities of interest to use here these can be safely neglected and the self-energy in Eq. (2.7) thus takes into account the dominant process of spin transfer between metal and insulator.

The lesser and greater component of the electronic Green's functions can be expressed in terms of the spectral functions $A_{kk';r}(\epsilon)$ via

$$\begin{aligned} -iG^{<}_{kk';r\sigma} &= A_{kk';r}(\epsilon) N_F\left(\frac{\epsilon-\mu_{r\sigma}}{k_B T_r}\right) \ ; \\ iG^{>}_{kk';r\sigma} &= A_{kk';r}(\epsilon)\left[1-N_F\left(\frac{\epsilon-\mu_{r\sigma}}{k_B T_r}\right)\right] \ , \end{aligned} \tag{2.9}$$

with $N_F(x)=[e^x+1]^{-1}$ the Fermi distribution function, T_r the temperature of lead r (k_B being Boltzmann's constant) and $\mu_{\sigma,r}$ the chemical potential of spin projection σ in lead r. As we will see later on, the lead chemical potential are taken spin-dependent to be able to implement nonzero spin accumulation. The spectral function is related to the retarded Green's function via

$$A_{kk';r}(\epsilon) = -2\mathrm{Im}\left[G^{(+)}_{kk';r}(\epsilon)\right] \ , \tag{2.10}$$

which does not depend on spin as the leads are taken to be normal metals. While the retarded Green's function of the leads can be determined explicitly for the model that we consider here, we will show below that such a level of detail is not needed but that, instead, we can parameterize the electron-magnon coupling by an effective interface parameter.

As mentioned before, all steady-state properties of the magnon system are determined by the magnon lesser Green's function leading to the magnon density matrix. It is ultimately given by the kinetic equation [98, 105]

$$\rho_{j,j'} \equiv \langle \hat{b}^{\dagger}_{j'}(t)\hat{b}_j(t)\rangle = \int \frac{d\epsilon}{(2\pi)}\left[\mathcal{G}^{(+)}(\epsilon) i\hbar\Sigma^{<}(\epsilon)\mathcal{G}^{(-)}(\epsilon)\right]_{j,j'} \ , \tag{2.11}$$

where $\hbar\Sigma_{j,j'}(t,t')$ is the total magnon self-energy discussed in detail below, of which the "lesser" component enters in the above equation. In the above and what follows, quantities with suppressed site indexes are interpreted as matrices, and matrix multiplication applies for products of these quantities. The retarded $(+)$ and advanced $(-)$ magnon Green's functions satisfy

$$\left[\epsilon^{\pm} - h - \hbar\Sigma^{(\pm)}(\epsilon)\right]\mathcal{G}^{(\pm)}(\epsilon) = 1 \ , \tag{2.12}$$

where $\epsilon^{\pm}=\epsilon\pm i0$. The magnon self-energies have contributions from the leads, as well as a contribution from the bulk denoted by $\hbar\Sigma^{\mathrm{FM}}$:

$$\hbar\Sigma(\epsilon) = \hbar\Sigma^{\mathrm{FM}}(\epsilon) + \sum_{r\in\{L,R\}} \hbar\Sigma^{r}(\epsilon) \ . \tag{2.13}$$

From Eq. (2.7) we find that for the retarded and advanced component, the contribution

due to the leads is given by

$$\hbar\Sigma^{r,(\pm)}_{j,j'}(\epsilon) = \sum_{kk'k''k'''} J^r_{j;kk'} \left(J^r\right)^*_{j';k''k'''} \int \frac{d\epsilon'}{(2\pi)} \int \frac{d\epsilon''}{(2\pi)} \times A_{k'k'';r}(\epsilon') A_{k'''k;r}(\epsilon'') \frac{N_F\left(\frac{\epsilon'-\mu_{r\uparrow}}{k_B T_r}\right) - N_F\left(\frac{\epsilon''-\mu_{r\downarrow}}{k_B T_r}\right)}{-\epsilon^{\pm} + \epsilon' - \epsilon''} , \tag{2.14}$$

whereas the "lesser" self-energy can be shown to be of the form:

$$\hbar\Sigma^{r,<}_{j,j'}(\epsilon) = 2iN_B\left(\frac{\epsilon - \Delta\mu_r}{k_B T_r}\right) \mathrm{Im}\left[\hbar\Sigma^{r,(+)}_{j,j'}(\epsilon)\right] , \tag{2.15}$$

with $N_B(x) = [e^x - 1]^{-1}$ the Bose-Einstein distribution function and $\Delta\mu_r = \mu_{r\uparrow} - \mu_{r\downarrow}$ the spin accumulation in lead r.

Having established the contributions due to the leads, we consider the bulk self-energy $\hbar\Sigma^{\mathrm{FM}}$, which in principle could include various contributions, such as magnon conserving and nonconsering magnon-phonon interactions, or magnon-magnon interactions. Here, we consider magnon non-conserving magnon-phonon coupling as the source of the bulk self-energy and use the Gilbert damping phenomenology to parameterize it by the constant α which for the magnetic insulator YIG is of the order of 10^{-4}. Gilbert damping corresponds to a decay of the magnons into phonons with a rate proportional to their energy. This thus leads to the contributions

$$\begin{aligned} \hbar\Sigma^{\mathrm{FM},<}_{j,j'}(\epsilon) &= 2N_B\left(\frac{\epsilon}{k_B T_{\mathrm{FM}}}\right) \hbar\Sigma^{\mathrm{FM},(+)}_{j,j'}(\epsilon) ; \\ \hbar\Sigma^{\mathrm{FM},(+)}_{j,j'}(\epsilon) &= -i\alpha\,\epsilon\delta_{j,j'} , \end{aligned} \tag{2.16}$$

where T_{FM} is the temperature of phonon bath. We note that in principle the temperature could be taken position dependent to implement a temperature gradient, but we do not consider this situation here.

With the results above, the density-matrix elements $\rho_{j,j'}$ can be explicitly computed from the magnon retarded and advanced Green's function and the "lesser" component of the total magnon self-energy using Eq. (2.11). The magnon self-energy is evaluated using the explicit expression for the retarded and advanced magnon self-energies due to leads and Gilbert damping $\hbar\Sigma^{\mathrm{FM}}$, see Eq. (2.16).

We are interested in the computation of the magnon spin current $\langle j_{m;jj'}\rangle$ in the bulk of the FM from site j to site j', which in terms of the magnon density matrix reads,

$$\langle j_{m;jj'}\rangle = -i(h_{j,j'}\rho_{j',j} - \text{c.c.}) , \tag{2.17}$$

and follows from evaluating the change in time of the local spin density, $\hbar d\langle\hat{b}^\dagger_j\hat{b}_j\rangle/dt$, using the Heisenberg equations of motion. The magnon spin current in the bulk thus follows straightforwardly from the magnon density matrix.

While the formalism presented so far provides a complete description of the magnon spin transport driven by metallic reservoirs, we discuss two simplifying developments

below. First, we derive a Landauer-Bütikker-like formula for the spin current from metallic reservoirs to the magnon system. Second, we discuss how to replace the matrix elements $J^r_{j;k,k'}$ by a single phenomenological parameter that characterizes the interface between metallic reservoirs and the magnetic insulator.

2.2.3 Landauer-Büttiker Formula

In this section we derive a Landauer-Büttiker formula for the magnon transport. Using the Heisenberg equations of motion for the local spin density, we find that the spin current from the left reservoir into the magnon system is given by

$$\begin{aligned} j_s^L &\equiv -\frac{\hbar}{2}\left\langle \frac{d}{dt}\sum_k \left(\hat{\psi}^\dagger_{k\uparrow L}\psi_{k\uparrow L} - \psi^\dagger_{k\downarrow L}\psi_{k\downarrow L}\right)\right\rangle \\ &= -\frac{2}{\hbar}\sum_{j;kk'} \mathrm{Re}[\left(J^L\right)^*_{j;kk'} g^<_{j;kk'}(t,t')] \ , \end{aligned} \tag{2.18}$$

in terms of the Green's function

$$g^<_{j;kk'}(t,t') \equiv i\langle \hat{\psi}^\dagger_{k'\uparrow L}(t')\hat{\psi}_{k\downarrow L}(t')\hat{b}_j(t)\rangle \ . \tag{2.19}$$

This "lesser" coupling Green's function $g^<_{j;kk'}(t,t')$ is calculated using Wick's theorem and standard Keldysh methods as described below.

We introduce the spin-flip operator for lead r

$$\hat{d}^\dagger_{kk';r}(t) = \hat{\psi}^\dagger_{k'\uparrow r}(t)\hat{\psi}_{k\downarrow r}(t) \ , \tag{2.20}$$

so that the coupling Green's function becomes

$$g^<_{j;kk'}(t,t') \equiv i\langle \hat{d}^\dagger_{kk';L}(t')\hat{b}_j(t)\rangle \ . \tag{2.21}$$

The Keldysh Green's function for the spin-flip operator is given by

$$\Pi^r_{kk'k''k'''}(t,t') = -i\langle T_{\mathcal{C}\infty}\hat{d}_{kk';r}(t)\hat{d}^\dagger_{k''k''';r}(t')\rangle \tag{2.22}$$

and using Wick's theorem we find that

$$\begin{aligned} \Pi^{r,>}_{kk'k''k'''}(t,t') &= -i\, G^>_{kk''';r\downarrow}(t,t')G^<_{k'k'';r\uparrow}(t',t) \ ; \\ \Pi^{r,<}_{kk'k''k'''}(t,t') &= -i\, G^>_{k'k'';r\uparrow}(t',t)G^<_{kk''';r\downarrow}(t,t') \ ; \\ \Pi^{r,(+)}_{kk'k''k'''}(t,t') &= -i\theta(t-t')\Big[G^>_{kk''';r\downarrow}(t,t')G^<_{k'k'';r\uparrow}(t',t) \\ &\quad -G^>_{k'k'';r\uparrow}(t',t)G^<_{kk''';r\downarrow}(t,t')\Big] \ , \end{aligned} \tag{2.23}$$

where we used the definition for the electron Green's function in Eq. (2.8).

Applying the Langreth theorem [105] and Fourier transforming, we write down the lesser coupling Green's function in terms of the spin-flip Green's function and magnon

Green's function

$$g^{<}_{j;kk'}(\epsilon) = \sum_{j';k''k'''} J^{L}_{j';k''k'''}\left(\mathcal{G}^{(+)}_{j,j'}(\epsilon)\Pi^{L,<}_{kk'k''k'''}(\epsilon) + \mathcal{G}^{<}_{j',j}(\epsilon)\Pi^{L,(-)}_{kk'k''k'''}(\epsilon)\right) , \tag{2.24}$$

where the retarded and "lesser" magnon Green's function are given by Eq. (2.11) and Eq. (2.12). Using these results, we ultimately find that

$$\begin{aligned} j^{L}_{s} &= \int \frac{d\epsilon}{2\pi}\left[N_B\left(\frac{\epsilon-\Delta\mu_L}{k_BT_L}\right) - N_B\left(\frac{\epsilon-\Delta\mu_R}{k_BT_R}\right)\right]\mathrm{T}(\epsilon) \\ &+ \int \frac{d\epsilon}{2\pi}\left[N_B\left(\frac{\epsilon-\Delta\mu_L}{k_BT_L}\right) - N_B\left(\frac{\epsilon}{k_BT_{\mathrm{FM}}}\right)\right] \\ &\quad \times \mathrm{Tr}\left[\hbar\Gamma^{L}(\epsilon)\mathcal{G}^{(+)}(\epsilon)\hbar\Gamma^{\mathrm{FM}}(\epsilon)\mathcal{G}^{(-)}(\epsilon)\right] , \end{aligned} \tag{2.25}$$

with the transmission function

$$\mathrm{T}(\epsilon) \equiv \mathrm{Tr}\left[\hbar\Gamma^{L}(\epsilon)\mathcal{G}^{(+)}(\epsilon)\hbar\Gamma^{R}(\epsilon)\mathcal{G}^{(-)}(\epsilon)\right] . \tag{2.26}$$

In the above, the rates $\hbar\Gamma^{L/R}(\epsilon)$ are defined by

$$\hbar\Gamma^{r}(\epsilon) \equiv -2\mathrm{Im}\left[\hbar\Sigma^{r,(+)}(\epsilon)\right] , \tag{2.27}$$

and

$$\hbar\Gamma^{\mathrm{FM}}(\epsilon) \equiv -2\mathrm{Im}\left[\hbar\Sigma^{\mathrm{FM},(+)}(\epsilon)\right] , \tag{2.28}$$

and correspond to the decay rates of magnons with energy ϵ due to interactions with electrons in the normal metal at the interfaces, and phonons in the bulk, respectively. This result is similar to the Laudauer-Büttiker formalism [98] for electronic transport using single-particle scattering theory. In the present context, a Landauer-Büttiker-like for spin transport was first derived by Bender *et al.* [103] for a single NM-FM interface. In the absence of Gilbert damping, the spin current would correspond to the expected result from Landauer-Bütikker theory, i.e., the spin current from left to the right lead is then given by the first line of Eq. (2.25). The presence of damping gives leakage of spin current due to the coupling with the phononic reservoir, as the second term shows. Finally, we note that the spin current from the right reservoir into the system is obtained by interchanging labels L and R in the first term, and the label L replaced by R in the second one. Due to the presence of Gilbert damping, however, we have in general that $j^{L}_{s} \neq -j^{R}_{s}$.

2.2.4 Determining the Interface Coupling

We now proceed to express the magnon spin current (Eq. (2.25)) in terms of a macroscopic, measurable quantity rather than the interfacial exchange constants $J^{r}_{j;k,k'}$. For $\Delta\mu_r \ll \epsilon_F$ (with ϵ_F the Fermi energy of the metallic leads), which is in practice always

obeyed, we have for low energies and temperatures that

$$\hbar\Sigma^{r,(\pm)}_{j,j'}(\epsilon) \simeq \mp i\frac{1}{4\pi}\sum_{kk'k''k'''} J^r_{j;kk'}\,(J^r)^*_{j';k''k'''}\,A_{k',k'';r}(\epsilon_F)A_{k''',k;r}(\epsilon_F)(\epsilon-\Delta\mu_r)\ . \tag{2.29}$$

Here, we also neglected the real part of this self-energy which provides a small renormalization of the magnon energies but is otherwise unimportant. The expansion for small energies in Eq. (2.29) is valid as long as $\epsilon \ll \epsilon_F$, which applies since ϵ is a magnon energy, and therefore at most on the order of the thermal energy. Typically, the above self-energy is strongly peaked for j, j' at the interface because the magnon-electron interactions occur at the interface. For j, j' at the interface we have that the self-energy depends weakly on varying j, j' along the interface provided that the properties of the interface do not vary substantially from position to position. We can thus make the identification:

$$\hbar\Sigma^{r,(\pm)}_{j,j'}(\epsilon) \simeq \mp i\eta^r(\epsilon-\Delta\mu_r)\delta_{j,j'}\delta_{j,j_r}\ , \tag{2.30}$$

with j_r the positions of the sites at the r-th interface, and η^r parametrizing the coupling between electrons and magnons at the interface. Note that η^r can be read off from Eq. (2.29). Rather than evaluating this parameter in terms of the matrix elements $J^r_{j;kk'}$ and the electronic spectral functions of the leads $A_{k,k';r}(\epsilon)$, we determine it in terms of the real part of the spin-mixing conductance $g^{\uparrow\downarrow;r}$, a phenomenological parameter that characterizes the spin-transfer efficiency at the interface [106]. This can be done by noting that in the classical limit the self-energy in Eq. (2.30) leads to an interfacial contribution, determined by the damping constant η^r/N, to the Gilbert damping of the homogeneous mode, where N is the number of sites of the system perpendicular to the leads, as indicated in Fig. 2.2. In terms of the spin-mixing conductance, we have that this contribution is given by [62] $g^{\uparrow\downarrow;r}/4\pi s_r N$, with s_r the saturation spin density per area of the ferromagnet at the interface with the r-th lead. Hence, we find that

$$\eta^r = \frac{g^{\uparrow\downarrow;r}}{4\pi s_r}\ , \tag{2.31}$$

which is used to express the reservoir contributions to the magnon self-energies in terms of measurable quantities. The spin-mixing conductance can be up to $5\hbar$ nm^{-2} for YIG-Pt interfaces [107], leading to the conclusion that η can be of the order $1-10$ for that case.

2.2.5 Summary on Implementation

We end this section with some summarizing remarks on implementation that may facilitate the reader who is interested in applying the formalism presented here.

First, one determines the retarded and advanced magnon Green's functions. This can be done given a magnon hamiltonian characterized by matrix elements $h_{j,j'}$ in Eq. (2.2), mixing conductances for the metal-insulator interfaces $g^{\uparrow\downarrow;r}$, and a value

Table 2.1: Parameters chosen for numerical calculations based on the NEGF formalism (unless otherwise noted).

	Quantity	Value
	J	$0.05\,eV$
	$\Delta\mu_L/J$	2.0×10^{-5}
	$\Delta\mu_R/J$	0.0
	η	8
	Δ/J	2.0×10^{-3}
	$k_B T_{\mathrm{FM}}/J$	0.60

for the Gilbert damping constant α, from which one computes the retarded self-energies at the interfaces in Eq. (2.30) with Eq. (2.31), and Eq. (2.16). The retarded and advanced magnon Green's functions are then computed via Eq. (2.12), which amounts to a matrix inversion. The next step is to calculate the density matrix for the magnons using Eq. (2.11), with as input the expressions for the "lesser" self-energies in Eqs. (2.15) and (2.16). Finally, the spin current is evaluated using Eq. (2.17) in the bulk of the FM or Eq. (2.25) at the NM-FM interface. In the next sections, we discuss some applications of our formalism.

2.3 Numerical Results

In this section, we present results of numerical calculations using the formalism presented in the previous section.

2.3.1 Clean System

For simplicity, we consider now the situation where the leads and magnetic insulators are one dimensional. The values of various parameters are displayed in Table 2.1, where we take the hopping amplitudes $J_{j,j'} = J(\delta_{j,j'+1} + \delta_{j,j'-1})$, i.e., $J_{j,j'}$ is equal to J between nearest neighbours, and zero otherwise. We focus on transport driven by spin accumulation in the leads and set all temperatures equal, i.e., $T_L = T_R = T_{\mathrm{FM}} \equiv T$. We also assume both interfaces to have equal properties, i.e., for the magnon-electron coupling parameters to obey $\eta^L = \eta^R \equiv \eta$. First we consider the case without disorder and take $\Delta_j = \Delta$.

We are interested in how the Gilbert damping affects the magnon spin current. In particular, we calculate the spin current injected in the right reservoir as a function of system size. The results of this calculation are shown in Fig. 2.4 for various temperatures, which indicates that for a certain fixed spin accumulation, the injected spin current decays with the thickness of the system for $N > 25$, for the parameters we have chosen. We come back to the various regimes of thickness dependence when we present analytical results for clean systems in the continuum limit in Sec. 2.4. From

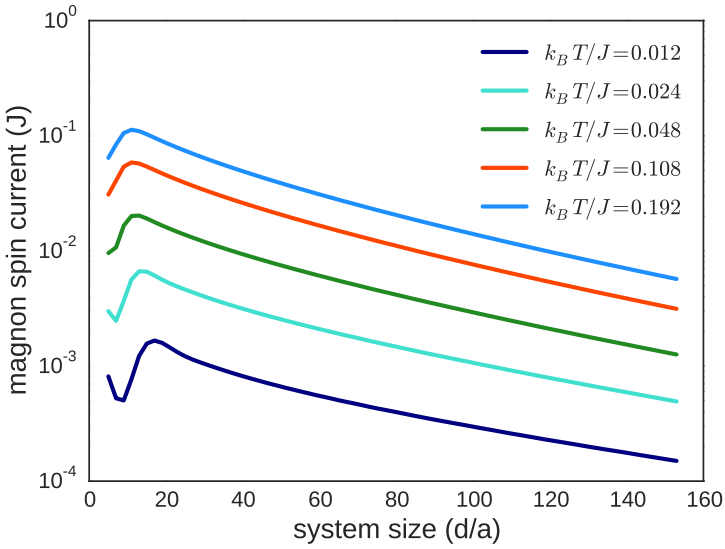

Fig. 2.4: System-size dependence of spin current ejected in the right reservoir for $\alpha = 6.9 \times 10^{-2}, \eta = 8.0$ and various temperatures.

these results we define a magnon relaxation length d_{relax} using the definition

$$j_m(d) \propto \exp(-d/d_{\text{relax}}) \ , \tag{2.32}$$

applied to the region $N > 25$ and where $d = \text{N}a$ with a the lattice constant. The magnon relaxation length depends on system temperature and is shown in Fig. 2.5. We attempt to fit the temperature dependence with

$$d_{\text{relax}}(T^*) = a(\gamma_0 + \frac{\gamma_1}{\sqrt{T^*}} + \frac{\gamma_2}{T^*}) \ , \tag{2.33}$$

with $\gamma_0, \gamma_1, \gamma_2$ constants and T^* defined as the dimensionless temperature $T^* \equiv k_BT/J$. The term proportional to γ_1 is expected for quadratically dispersing magnons with Gilbert damping as the only relaxation mechanism [100, 3]. The terms proportional to γ_0 and γ_2 are added to characterize the deviation from this expected form. Our results show that the relaxation length has not only $\sim 1/\sqrt{T}$ behaviour. This is due to the finite system size, the contact resistance that the spin current experiences at the interface between metal and magnetic insulator, and the deviation of the magnon dispersion from a quadratic one due to the presence of the lattice.

2.3.2 Disordered System

We now consider the effects of disorder on the spin current as a function of the thickness of the FM. We consider a one-dimensional system with a disorder potential implemented by taking $\Delta_j = \Delta(1+\delta_j)$, where δ_j is a random number evenly distributed

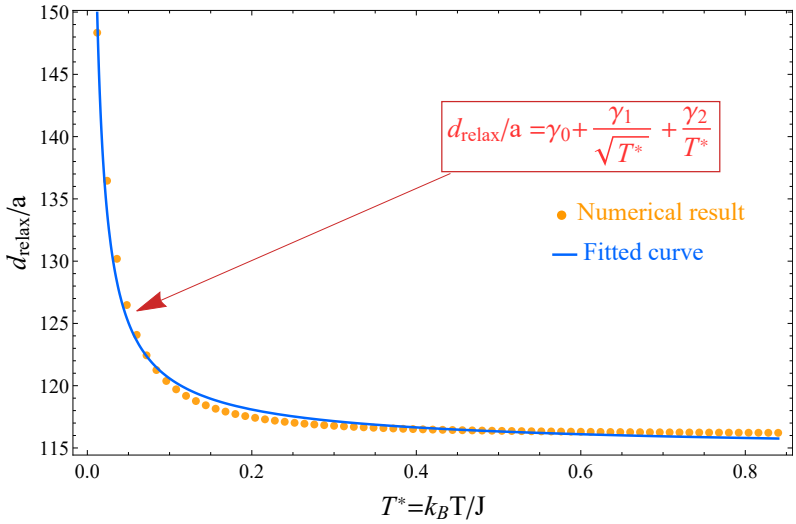

Fig. 2.5: Magnon relaxation length as a function of dimensionless temperature T^* for $\alpha = 6.9 \times 10^{-2}, \eta = 8.0$. The fitted parameters are obtained as $\gamma_0 = 114.33, \gamma_1 = 0.96, \gamma_2 = 0.32$.

between $-\delta$ and δ (with $\delta \ll 1$ and positive) that is uncorrelated between different sites. In one dimension, all magnon states are Anderson localized [108]. Since this is an interference phenomenon, it is expected that Gilbert damping diminishes such localization effects. The effect of disorder on spin waves was investigated using a classical model in Ref. [109], whereas Ref. [110] presents a general discussion of the effect of dissipation on Anderson localization. Very recently, the effect of Dzyaloshinskii-Moriya interactions on magnon localization was studied [111]. Here we consider how the interplay between Gilbert damping and the disorder affects the magnon transport.

For a system without Gilbert damping the spin current carried by magnons is conserved and therefore independent of position regardless of the presence or absence of disorder. Due to the presence of Gilbert damping the spin current decays as a function of position. Adding disorder on top of the dissipation due to Gilbert damping causes the spin current to fluctuate from position to position. For large Gilbert damping, however, the effects of disorder are suppressed as the Gilbert damping suppresses the localization of magnon states. In Fig. 2.6 we show numerical results of the position dependence of the magnon current for different combinations of disorder and Gilbert damping constants. The plots clearly show that the spin current fluctuates in position due to the combined effect of disorder and Gilbert damping, whereas it is constant without Gilbert damping, and decays in the case with damping but without disorder. Note that for the two cases without Gilbert damping the magnitude of the spin current is different because the disorder alters the conductance of the system and each curve in Fig. 2.6 corresponds to a different realization of disorder.

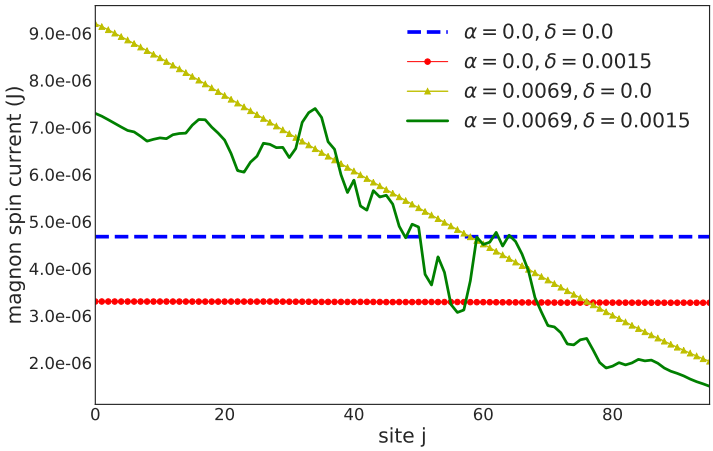

Fig. 2.6: Spatial dependence of local magnon current for the case without Gilbert damping and disorder ($\alpha = 0, \delta = 0$), without disorder ($\alpha = 6.9 \times 10^{-3}, \delta = 0$), without Gilbert damping ($\alpha = 0, \delta = 1.5 \times 10^{-3}$), and both disorder and Gilbert damping ($\alpha = 6.9 \times 10^{-3}, \delta = 1.5 \times 10^{-3}$). The interface coupling parameter is taken equal to $\eta = 0.8$.

To characterize the fluctuations in the spin current, we define the correlation function

$$C_j = \sqrt{\frac{\overline{\left(j_{m;j,j+1} - \overline{j_{m;j,j+1}}\right)^2}}{\left(\overline{j_{m;j,j+1}}\right)^2}} \,, \tag{2.34}$$

where the bar stands for performing averaging over the realizations of disorder. Fig. (2.7) shows this correlation function for $j = N - 1$ as a function of Gilbert damping for various strengths of the disorder. As we expect, based on the previous discussion, the fluctuations become small as the Gilbert damping becomes very large or zero, leaving an intermediate range where there are sizeable fluctuations in the spin current.

2.4 Analytical Results

In this section we analytically compute the magnon transmission function in the continuum limit $a \to 0$ for a clean system. We consider again the situation of a magnon hopping amplitude $J_{j,j'}$ that is equal to J and nonzero only for nearest neighbors, and a constant magnon gap $\Delta_j = \Delta$. We compute the magnon density matrix, denoted by $\rho(\boldsymbol{x}, \boldsymbol{x}')$, and retarded and advanced Green's functions, denoted by $\mathcal{G}^{(\pm)}(\boldsymbol{x}, \boldsymbol{x}''; \epsilon)$. Here, the spatial coordinates in the continuum are denoted by $\boldsymbol{x}, \boldsymbol{x}', \boldsymbol{x}'', \cdots$. We take the system to be translationally invariant in the $y - z$-plane and the current direction as shown in Fig. 2.1 to be x.

In the continuum limit, the imaginary part of the various self-energies acquired by the

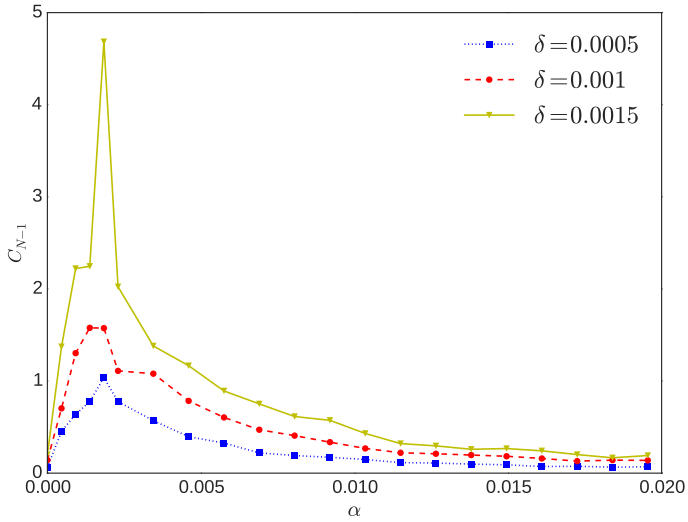

Fig. 2.7: Correlation function C_j that characterizes the fluctuations in the spin current for $j = N - 1$ as a function of the Gilbert damping constant, for three strengths of the disorder potential. The curves are obtained by performing averaging over 100 realizations of the disorder. The interface coupling parameter is taken equal to $\eta = 0.8$.

magnons have the form:

$$\begin{aligned} \mathrm{Im}\left[\hbar\Sigma^{r,(+)}(\boldsymbol{x},\boldsymbol{x}';\epsilon)\right] &= -\tilde{\eta}^r(\epsilon-\mu_r)\delta(x-x_r)\delta(\boldsymbol{x}-\boldsymbol{x}')\ ; \\ \mathrm{Im}\left[\hbar\Sigma^{\mathrm{FM},(+)}(\boldsymbol{x},\boldsymbol{x}';\epsilon)\right] &= -\alpha\,\epsilon\,\delta(\boldsymbol{x}-\boldsymbol{x}')\,, \end{aligned} \tag{2.35}$$

where x_r is the position of the r-th lead, and where $\tilde{\eta}^r$ is the parameter that characterizes the interfacial coupling between magnons and electrons. We use a different notation for this parameter as in the continuum situation its dimension is different with respect to the discrete case. To express $\tilde{\eta}^r$ in terms of the spin-mixing conductance we have that $\tilde{\eta}^r = g^{\uparrow\downarrow}/4\pi\tilde{s}^r$ where $\tilde{s}^r$ is now the three-dimensional saturated spin density of the ferromagnet.

We proceed by evaluating the magnon transmission function from Eq. (2.26). We compute the rates in Eq. (2.27) from the self-energies Eqs. (2.35) and find for the transmission function in the first instance that

$$\mathrm{T}(\epsilon) = 4\tilde{\eta}^L\tilde{\eta}^R(\epsilon-\Delta\mu_L)(\epsilon-\Delta\mu_R)\int\frac{d\mathbf{q}}{(2\pi)^2}g^{(+)}(x_L,x_R,\mathbf{q};\epsilon)g^{(-)}(x_R,x_L,\mathbf{q};\epsilon)\ , \tag{2.36}$$

where $\mathbf{q}$ is the two-dimensional momentum that results from Fourier transforming in

the $y-z$-plane. The Green's functions $g^{(\pm)}(x,x',\mathbf{q};\epsilon)$ obey [compare Eq. (2.12)]

$$\left[(1\pm i\alpha)\epsilon + A\frac{d^2}{dx^2} - A\mathbf{q}^2 - \Delta \pm i\sum_{r\in\{L,R\}}\tilde{\eta}^r(\epsilon-\Delta\mu_r)\delta(x-x_r)\right] g^{(\pm)}(x,x',\mathbf{q};\epsilon) = \delta(x-x') \ , \tag{2.37}$$

where $A = Ja^2$. This Green's function is evaluated using standard techniques for inhomogeneous boundary value problems (see Appendix 2.A) to ultimately yield

$$\mathrm{T}(\epsilon) = 4\tilde{\eta}^2(\epsilon-\Delta\mu_L)(\epsilon-\Delta\mu_R)\int\frac{d\mathbf{q}}{(2\pi)^2}|t(\mathbf{q},\epsilon)|^2 \ , \tag{2.38}$$

with

$$\begin{aligned} t(\mathbf{q},\epsilon) &= A\kappa\left[\left(A^2\kappa^2 - \tilde{\eta}^2(\epsilon-\Delta\mu_L)(\epsilon-\Delta\mu_R)\right)\sinh(\kappa d)\right. \\ &\quad \left. -iA\tilde{\eta}\kappa(2\epsilon-\Delta\mu_L-\Delta\mu_R)\cosh(\kappa d)\right]^{-1} , \end{aligned} \tag{2.39}$$

with $\kappa = \sqrt{(A\mathbf{q}^2+\Delta-\epsilon-i\alpha\epsilon)/A}$ and where $d = x_R - x_L$. Note that we have at this point taken both interfaces equal for simplicity, so that $\tilde{\eta}^L = \tilde{\eta}^R \equiv \tilde{\eta}$. In terms of an interfacial Gilbert damping parameter α' we have that $\tilde{\eta} = d\alpha'$.

Let us identify the magnon decay length

$$l \equiv \frac{\lambda}{\alpha},$$

where $\lambda = \sqrt{A/k_BT}$ is proportional to the thermal de Broglie wavelength. Equipped with a closed, analytic expression, we may now, in an analogous way as Hoffman *et al.* [100], investigate the behavior of Eq. (2.38) in the thin FM ($d \ll l$) and thick FM ($d \gg l$) regimes. In order to do so, we take $\mu_L = 0$ so that the second term in Eq. (2.25) vanishes and the spin current is fully determined by the transmission coefficient $\mathrm{T}(\epsilon)$. Before analyzing the result for the spin current more closely, we remark that the result for the transmission function may also be obtained from the linearized stochastic Landau-Lifshitz-Gilbert equation, as shown in Appendix 2.B.

2.4.1 Thin Film Regime ($d \ll l$)

In the thin film regime, the transmission coefficient $\mathrm{T}(\epsilon)$ exhibits scattering resonances near $\epsilon = \epsilon_{n\mathbf{q}}$ for given $\mathbf{q}$, where

$$\frac{\epsilon_{n\mathbf{q}}}{A} = \mathbf{q}^2 + \frac{1}{\xi^2} + \frac{n^2\pi^2}{d^2}$$

and n is an integer and where $\xi = \sqrt{A/\Delta}$ is the coherence length of the ferromagnet. When the ferromagnet is sufficiently thin ($d \ll \lambda/\alpha^{1/2} = \sqrt{\alpha}l$), one finds that these peaks are well separated, and the transmission coefficient is approximated as a sum of Lorentzians: $\mathrm{T} = \sum_{n=0}^{\infty}\mathrm{T}_n$, where:

$$\mathrm{T}_n(\epsilon) \approx A_{n\mathbf{q}}\frac{\Gamma_n^L\Gamma_n^R}{\Gamma_n^L+\Gamma_n^R+\Gamma_n^{\mathrm{FM}}} \tag{2.40}$$

with

$$A_{n\mathbf{q}}(\epsilon) = \frac{\Gamma_n}{\left(\epsilon - \epsilon_{n\mathbf{q}}\right)^2 + \left(\Gamma_n/2\right)^2} \tag{2.41}$$

as the spin wave spectral density. The broadening rates are given by $\Gamma_n^{\mathrm{FM}} = 2\alpha\epsilon$, $\Gamma_0^L = 2\alpha'\epsilon$, $\Gamma_0^R = 2\alpha'(\epsilon - \mu_R)$, $\Gamma_{n\neq 0}^L = 4\alpha'\epsilon$, $\Gamma_{n\neq 0}^R = 4\alpha'(\epsilon - \mu_R)$ and $\Gamma_n = \Gamma_n^{\mathrm{FM}} + \Gamma_n^L + \Gamma_n^R$. In the extreme small dissipation limit (i.e. neglecting spectral broadening by the Gilbert damping), one has:

$$A_{n\mathbf{q}}(\epsilon) \to 2\pi\delta\left(\epsilon - \epsilon_{n\mathbf{q}}\right), \tag{2.42}$$

and the current has the simple form, $j_s^L = \sum_{n=0}^{\infty} j_n$, where

$$j_n = a^2 \int \frac{d^2q}{(2\pi)^2} \frac{\Gamma_n^L \Gamma_n^R}{\Gamma_n} \left[N_B\left(\frac{\epsilon_{n\mathbf{q}}}{k_B T}\right) - N_B\left(\frac{\epsilon_{n\mathbf{q}} - \Delta\mu_R}{k_B T}\right)\right] \tag{2.43}$$

where Γ_n^L, Γ_n^R and Γ_n^{FM} are all evaluated at $\epsilon = \epsilon_{n\mathbf{q}}$. Eq. (2.43) allows one to estimate the thickness dependence of the signal. Supposing $\mu_R \lesssim \epsilon_{n\mathbf{q}}$, when $d \ll g^{\uparrow\downarrow}/s\alpha$, then $\alpha' \gg \alpha$, and $\Gamma_n^L\Gamma_n^R/\Gamma_n^{\mathrm{FM}} \sim j_{s,\mathrm{cl}}^L \sim 1/d$; when $d \gg g^{\uparrow\downarrow}/s\alpha$, then $\alpha' \ll \alpha$, and $j_{s,\mathrm{cl}}^L \sim 1/d^2$. The enhancement of the spin current for small d is in rough agreement with our numerical results in the previous section as shown in Fig. 2.4.

2.4.2 Thick Film Regime ($d \gg l$)

In the thick film regime, the transmission function becomes

$$\mathrm{T}(\epsilon) \approx \frac{(4Ad)^2 \Gamma_x^L \Gamma_x^R \sqrt{(\epsilon - \epsilon_{0\mathbf{q}})^2 + (\Gamma_x^{\mathrm{FM}}/2)^2}\, e^{-2\kappa_r d}}{\left|(4A\kappa)^2 - (d)^2 \Gamma_x^L \Gamma_x^R - i4dA\Gamma_x^R \kappa S(\kappa_r)\right|^2}$$

where $\Gamma_x^{L/R/\mathrm{FM}} = \Gamma_{n\neq 0}^{L/R/\mathrm{FM}}$, $\kappa_r = \mathrm{Re}[\kappa]$, and $S(\kappa_r)$ is the sign of κ_r. For $\alpha \ll 1$, we have $\kappa = ik_x\left(1 + i\alpha\epsilon/2Ak_x^2\right)$, where $k_x = \sqrt{\mathbf{q}^2 + \xi^{-2} - \epsilon/A}$. For energies $\epsilon > A(\mathbf{q}^2 + \xi^{-2})$, k_x is imaginary, and the contribution to the spin current decays rapidly with d. When, however, $\epsilon < A(\mathbf{q}^2 + \xi^{-2})$, k_x is real, and $\kappa_r = -\alpha\left(\mathbf{q}^2 + \xi^{-2}\right)/2k_x \sim \alpha/\lambda$ (for thermal magnons), so that the signal decays over a length scale $l \propto 1/\sqrt{T}$, in agreement with our numerical results as shown in Fig. 2.5.

2.4.3 Comparison with Numerical Results

In order to compare the numerical with the analytical results we plot in Fig. 2.8 the transmission function as a function of energy. Here, the numerical result is evaluated for a clean system using Eq. (2.26) while the analytical result is that of Eq. (2.38). While they agree in the appropriate limit ($N \to \infty, a \to 0$), for finite N there are substantial deviations that are due to the increased importance of interfacing coupling relative to the Gilbert damping for small systems and the deviations of the dispersion from a quadratic one.

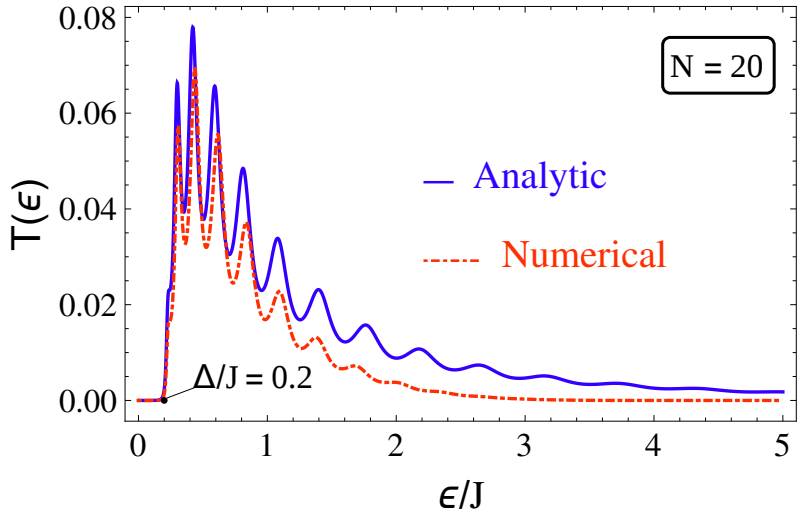

Fig. 2.8: Magnon transmission function as a function of energy. The parameters are chosen to be $\Delta/J = 0.2, \alpha = 0.069, \eta = 8.0$.

2.5 Discussion and Outlook

We have developed a NEGF formalism for exchange magnon transport in a NM-FM-NM heterostructure. We have illustrated the formalism with numerical and analytical calculations and determined the thickness dependence of the magnon spin current. We have also considered magnon disorder scattering and shown that the interplay between disorder and Gilbert damping leads to spin-current fluctuations.

We have also demonstrated that for a clean system, i.e., without disorder, in the continuum limit the results obtained from the NEGF formalism agree with those from the stochastic LLG formalism. The latter is suitable for a clean system in the continuum limit where the various boundary conditions on the solutions of the stochastic equations are easily imposed. The NEGF formalism is geared towards real-space implementation, such that, e.g., disorder scattering due to impurities are more straightforwardly included as illustrated by our example application. The NEGF formalism is also more flexible for systematically including self-energies due to additional physical processes [112], such as magnon-conserving magnon-phonon scattering and magnon-magnon scattering, or, for example, for treating strong-coupling regimes into which the stochastic Landau-Lifshitz-Gilbert formalism has no natural extension.

Using our formalism, a variety of mesoscopic transport features of magnon transport can be investigated including, e.g., magnon shot noise [113]. The generalization of our formalism to elliptical magnons and magnons in antiferromagnets is an attractive direction for future research.

Appendix

2.A Evaluation of Magnon Green's Function in the Continuum Limit

In this appendix we evaluate the magnon Green's function in the continuum limit that is determined by Eq. (2.37). For simplicity we take the momentum $\mathbf{q}$ equal to zero and suppress it in the notation, as it can be trivially restored afterwards. The Green's function is then determined by

$$\left[\epsilon \pm i\alpha\epsilon \pm i \sum_{r\in\{L,R\}} \tilde{\eta}^r(\epsilon - \Delta\mu_r)\delta(x - x_r) + A\frac{d^2}{dx^2} - H\right] g^{(\pm)}(x, x'; \epsilon) = \delta(x - x') \ . \tag{2.44}$$

To determine this Green's function we first solve for the states $\chi^{\pm}(x)$ that obey:

$$\left[\epsilon \pm i\alpha\epsilon \pm i \sum_{r\in\{L,R\}} \tilde{\eta}^r(\epsilon - \Delta\mu_r)\delta(x - x_r) + A\frac{d^2}{dx^2} - H\right] \chi^{\pm}(x) = 0 \ . \tag{2.45}$$

Integrating this equation across $x = x_L$ and $x = x_R$ leads to the boundary conditions:

$$x = x_L \quad : \qquad \pm i\tilde{\eta}^L(\epsilon - \Delta\mu_L)\chi^{\pm}(x_L) + A\frac{d\chi^{\pm}(x)}{dx}|_{x=x_L} = 0; \tag{2.46}$$

$$x = x_R \quad : \qquad \pm i\tilde{\eta}^R(\epsilon - \Delta\mu_R)\chi^{\pm}(x_R) - A\frac{d\chi^{\pm}(x)}{dx}|_{x=x_R} = 0 \ . \tag{2.47}$$

For $x_L < x < x_R$, the general solution is:

$$\chi^{\pm}(x) = Be^{ik_{\pm}x} + Ce^{-ik_{\pm}x} \ , \tag{2.48}$$

with $k_{\pm} = \sqrt{(\epsilon \pm i\alpha\epsilon - H)/A}$. We write the solution obeying the boundary condition at $x = x_L$ as

$$\chi^{\pm}_L(x) = e^{ik_{\pm}x} + C_{\pm}e^{-ik_{\pm}x} \ , \tag{2.49}$$

With the boundary condition at $x = x_L$ (Eq.2.47), we find that

$$C_{\pm} = \left[\frac{Ak_{\pm} \pm \tilde{\eta}^L(\epsilon - \Delta\mu_L)}{Ak_{\pm} \mp \tilde{\eta}^L(\epsilon - \Delta\mu_L)}\right] e^{2ik_{\pm}x_L} \ .$$

For the solution obeying the boundary condition at $x = x_R$, we write

$$\chi^{\pm}_R(x) = B_{\pm}e^{ik_{\pm}x} + e^{-ik_{\pm}x} \ . \tag{2.50}$$

With the boundary condition at $x = x_R$ (Eq.2.47), we have:

$$A(iB_{\pm}k_{\pm}e^{ik_{\pm}x_R} - ik_{\pm}e^{-ik_{\pm}x_R}) = \pm i\tilde{\eta}^R(\epsilon - \mu_R)(B_{\pm}e^{ik_{\pm}x_R} + e^{-ik_{\pm}x_R}) \ ,$$

so that

$$B_{\pm} = \left[\frac{Ak_{\pm} \pm \tilde{\eta}^R(\epsilon - \Delta\mu_R)}{Ak_{\pm} \mp \tilde{\eta}^R(\epsilon - \Delta\mu_R)}\right] e^{-2ik_{\pm}x_R} \ .$$

The Green's function is now given by [114]

$$g^{(\pm)}(x,x';\epsilon)=\begin{cases}\frac{\chi_L^{(\pm)}(x')\chi_R^{(\pm)}(x)}{A\,W^{(\pm)}(x')} & \text{for } x>x'\ ;\\ \frac{\chi_L^{(\pm)}(x)\chi_R^{(\pm)}(x')}{A\,W^{(\pm)}(x')} & \text{for } x<x'\ .\end{cases} \tag{2.51}$$

with the Wronskian

$$W^{\pm}(x')=\chi_L^{\pm}(x')\frac{d\chi_R^{\pm}(x')}{dx'}-\chi_R^{\pm}(x')\frac{d\chi_L^{\pm}(x')}{dx'}\ .$$

Inserting the result for the Green's function in Eq. (2.36) and using that $k_+=i\kappa$ and $k_-=(k_+)^*$, we obtain Eqs. (2.38) and (2.39) after restoring the $\mathbf{q}$-dependence and taking $\tilde{\eta}^R=\tilde{\eta}^L=\tilde{\eta}$.

2.B Stochastic Formalism for Spin Transport in a Ferromagnet

Here, we show how to recover our analytical results from the stochastic Landau-Lifshitz-Gilbert equation, generalizing the results of Ref. [100] to the case of nonzero spin accumulation in the metallic reservoirs. The dynamics of the spin density unit vector $\mathbf{n}$ is governed by:

$$(1+\alpha\mathbf{n}\times)\,\hbar\dot{\mathbf{n}}+\mathbf{n}\times(\mathbf{H}+\mathbf{h})-A\mathbf{n}\times\nabla^2\mathbf{n}=0, \tag{2.52}$$

where $\mathbf{H}=\Delta\hat{\mathbf{z}}$ is the effective applied magnetic field (in units of energy) and $\mathbf{h}$ is the bulk stochastic field [99]. We assume a spin accumulation $\boldsymbol{\mu}'=\Delta\mu_R\mathbf{z}$ in the right normal metal, while the spin accumulation in the left lead is taken zero. The boundary condition at $x=0$ reads

$$\begin{aligned}\mathbf{j}_s\,(x=0)&=-\,A\tilde{s}\mathbf{n}\times\partial_x\mathbf{n}|_{x=0}\\&=\left[\frac{g^{\uparrow\downarrow}}{4\pi}\,(\mathbf{n}\times(\mathbf{n}\times\boldsymbol{\mu}')+\mathbf{n}\times\hbar\dot{\mathbf{n}})+\mathbf{n}\times\mathbf{h}_L'\right]_{x=0}\end{aligned} \tag{2.53}$$

and at $x=d$:

$$\begin{aligned}\mathbf{j}_s\,(x=d)&=-\,A\tilde{s}\mathbf{n}\times\partial_x\mathbf{n}|_{x=d}\\&=-\left[\frac{g^{\uparrow\downarrow}}{4\pi}\,(\mathbf{n}\times\hbar\dot{\mathbf{n}})+\mathbf{n}\times\mathbf{h}_R'\right]_{x=d}\ .\end{aligned} \tag{2.54}$$

Defining $\psi\,(\mathbf{x},t)=n\,(\mathbf{x},t)\,\sqrt{\tilde{s}/2}$, where $n\equiv n_x-in_y$, we linearize the dynamics around the equilibrium orientation $\mathbf{n}=-\mathbf{z}$. Fourier transforming:

$$\psi\,(x,\mathbf{q},\epsilon)=\int\frac{dt}{2\pi\hbar}\int\frac{d^2\boldsymbol{r}_\perp}{2\pi}e^{i\epsilon t/\hbar}e^{-i\boldsymbol{r}_\perp\cdot\mathbf{q}}\psi\,(x,\boldsymbol{r}_\perp,t)\,,$$

the bulk equation of motion reads:

$$A\left(\partial_x^2-\kappa^2\right)\psi=h\sqrt{\tilde{s}}\ . \tag{2.55}$$

The bulk transformed stochastic field $h = h_x - ih_y$ obeys the fluctuation dissipation theorem:

$$\langle h^* (x, \mathbf{q}, \epsilon) h (x', \mathbf{q}', \epsilon') \rangle = 2 (2\pi)^3 \alpha(\hbar^2/\tilde{s})\epsilon \frac{\delta (x - x') \delta (\mathbf{q} - \mathbf{q}') \delta (\epsilon - \epsilon')}{\tanh [\epsilon/2k_B T]} \quad (2.56)$$

The boundary conditions, Eqs. (2.53) and (2.54), become respectively:

$$A\partial_x \psi - i\frac{g^{\uparrow\downarrow}}{4\pi\tilde{s}} (\epsilon - \Delta\mu_R) = \frac{h_R}{\sqrt{2\tilde{s}}} \quad (2.57)$$

at $x = 0$ and

$$A\partial_x \psi + i\frac{g^{\uparrow\downarrow}}{4\pi\tilde{s}} \epsilon\psi = \frac{h_L}{\sqrt{2\tilde{s}}} \quad (2.58)$$

at $x = d$, where we have taken the coupling at both interfaces equal. Similarly, the interfacial stochastic fields obey:

$$\left\langle h_R^{'*} (\mathbf{q}, \epsilon) h_R' (\mathbf{q}', \epsilon') \right\rangle = \frac{2 (2\pi)^3 \alpha' d\hbar^2 \tilde{s} (\epsilon - \Delta\mu_R) \delta (\mathbf{q} - \mathbf{q}') \delta (\epsilon - \epsilon')}{\tanh [(\epsilon - \Delta\mu_R)/2k_B T]} \quad (2.59)$$

and

$$\left\langle h_L^{'*} (\mathbf{q}, \epsilon') h_L' (\mathbf{q}', \epsilon) \right\rangle = \frac{2 (2\pi)^3 \alpha' d\hbar^2 \tilde{s}\epsilon\delta (\mathbf{q} - \mathbf{q}') \delta (\epsilon - \epsilon')}{\tanh [\epsilon/2k_B T]}. \quad (2.60)$$

Using Eqs. (2.55)-(2.60), one finds the current on the left side of the structure: $j_s^L \equiv \mathbf{z} \cdot \mathbf{j}_s (x = 0)$ to be of the form:

$$j_s^L = \int \frac{d\epsilon}{2\pi} \left[N_B \left(\frac{\epsilon}{k_B T} \right) - N_B \left(\frac{\epsilon - \Delta\mu_R}{k_B T} \right) \right] \mathrm{T}(\epsilon) \quad (2.61)$$

where $\mathrm{T}(\epsilon)$ is the transmission coefficient in Eq. (2.38). Hence, for a clean system and in the continuum limit the results of the stochastic Landau-Lifshitz-Gilbert equation coincide with those of the NEGF formalism given by Eq. (2.25).

2.C Size Dependence of Magnon Current for Various Values of Interface Coupling η

Fig. 2.9 demonstrates the size dependence of magnon current.

2.D Analytic Calculation for Local Magnon Current

Besides numerical calculations based on NEGF theory as demonstrated, we would like to have an analytic explanation of local magnon current as well. Therefore we perform the calculations in the continuum limit as below.

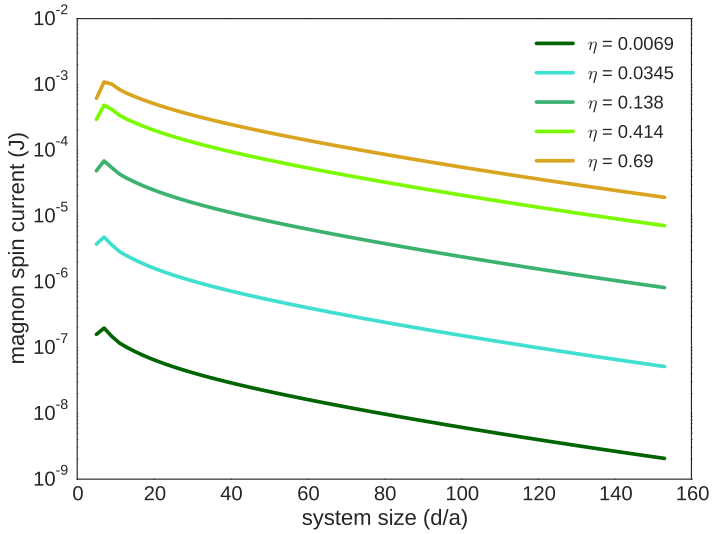

Fig. 2.9: System-size dependence of spin current ejected in the right reservoir for $\alpha = 6.9 \times 10^{-2}, k_B T/J = 0.048$ and various values of interface coupling η.

2.D.1 Density Matrix in the Continuum Limit

We rewrite the density matrix as below, where $\rho^{L,R}_{j,j'}$ comes from the contributions of s-d exchange coupling with the left lead or the right lead, and $\rho^{C}_{j,j'}$ denotes the one from interacting with the phonon bath in the central scattering region.

$$\begin{aligned}
\rho^{L/R}_{j,j'} &= -2\int \frac{d\epsilon}{2\pi} n_B(\epsilon-\mu_{L/R}) \sum_{j'',j'''} [\mathcal{G}^{+}_{j',j''}(\epsilon) \mathrm{Im}\left(\hbar\Sigma^{+}_{j'',j'''}(\epsilon)\right)^{L/R} \mathcal{G}^{-}_{j''',j'}(\epsilon)] \; ; \\
\rho^{C}_{j,j'} &= -2\int \frac{d\epsilon}{2\pi} n_B(\epsilon) \sum_{j'',j'''} [\mathcal{G}^{+}_{j',j''}(\epsilon) \mathrm{Im}\left(\hbar\Sigma^{+}_{j'',j'''}(\epsilon)\right)^{C} \mathcal{G}^{-}_{j''',j'}(\epsilon)] \; .
\end{aligned} \tag{2.62}$$

Their continuum limits become,

$$\begin{aligned}
\rho^{L/R}_{x,x'} &= -2\int \frac{d\epsilon}{2\pi} n_B(\epsilon-\mu_{L/R}) \int dx'' \int dx''' \Big[g^{+}(x,x'';\epsilon) \\
&\quad \times \mathrm{Im}\left(\hbar\Sigma^{+}(x'',x''';\epsilon)\right)^{L/R} g^{-}(x''',x';\epsilon) \Big] \; ; \\
\rho^{C}_{x,x'} &= -2\int \frac{d\epsilon}{2\pi} n_B(\epsilon) \int dx'' \int dx''' \Big[g^{+}(x,x'';\epsilon) \\
&\quad \times \mathrm{Im}\left(\hbar\Sigma^{+}(x'',x''';\epsilon)\right)^{C} g^{-}(x''',x';\epsilon) \Big] \; .
\end{aligned} \tag{2.63}$$

Note that in the NM|FM|NM heterostructure, the total density matrix for magnons

is a summation over the three contributions,

$$\rho_{x,x'} \equiv \rho^L_{x,x'} + \rho^R_{x,x'} + \rho^C_{x,x'} \ . \tag{2.64}$$

Under the condition that the energy scale of spin accumulation is small compared to the Fermi level, and in the low temperature limit, the imaginary part of the Keldysh self-energy acquired by magnon is given as,

$$\begin{aligned} \mathrm{Im}\left(\hbar\Sigma^+(x'',x''';\epsilon)\right)^{L,R} &= -\alpha'(\epsilon-\mu_{L,R})\delta(x''-x_{L,R})\delta(x'''-x_{L,R}) \ ; \\ \mathrm{Im}\left(\hbar\Sigma^+(x'',x''';\epsilon)\right)^{C} &= -\alpha\,\epsilon\,\delta(x''-x''') \ . \end{aligned} \tag{2.65}$$

The retarded (+) and advanced (−) magnon Green's function are expressed in real space as below,

$$g^{\pm}(x,x_{L/R};\epsilon) = \int \frac{dk}{2\pi} e^{ik(x-x_{L/R})} \frac{\hbar}{\epsilon \pm i\alpha\epsilon - \epsilon_k} \ ; \tag{2.66}$$

and α is the bulk Gilbert damping, with α' the interfacial coupling parameter.

Substituting Eq. 2.65 and Eq. 2.66 into the continuum form of density matrices in Eq. 2.63 , we get,

$$\begin{aligned} & \rho^{L/R}_{x,x'} \\ = \ & 2\alpha' \int \frac{d\epsilon}{2\pi} n_B(\epsilon-\mu_{L/R})(\epsilon-\mu_{L/R}) \\ & \times \int \frac{dk_1\,dk_2}{(2\pi)^2} e^{ik_1(x-x_{L/R})} e^{ik_2(x'-x_{L/R})} \frac{\hbar^2}{(\epsilon+i\alpha\epsilon-\epsilon_{k_1})(\epsilon-i\alpha\epsilon-\epsilon_{k_2})} \ , \end{aligned} \tag{2.67}$$

and

$$\begin{aligned} & \rho^{C}_{x,x'} \\ = \ & \frac{\alpha}{\pi} \int d\epsilon n_B(\epsilon)\epsilon \left[\int \frac{dk_6}{2\pi} e^{ik_6(x'-x)} \frac{\hbar^2}{(\epsilon+i\alpha\epsilon-\epsilon_{-k_6})(\epsilon-i\alpha\epsilon-\epsilon_{k_6})} \right] \\ = \ & \frac{\alpha}{\pi} \int d\epsilon n_B(\epsilon)\epsilon \left[\int \frac{dk_6}{2\pi} e^{ik_6(x'-x)} \frac{\hbar^2}{(\epsilon+i\alpha\epsilon-\epsilon_{k_6})(\epsilon-i\alpha\epsilon-\epsilon_{k_6})} \right] \ , \end{aligned} \tag{2.68}$$

where in the last step we take the quadratic dispersion for ferromagnetic magnons. In the calculation below, we assume an energy dispersion $\epsilon_k = \epsilon_0 + Ak^2$, where A is the spin stiffness constant in the continuum limit.

2.D.2 Contour Integral and Local Magnon Current

We first perform contour integrations for Eq. 2.67 over k_1 and k_2 as below.

Considering an integral as

$$\mathcal{M} = \int \frac{dk}{2\pi} e^{ik(x-x_L)} \frac{\hbar}{\epsilon + i\alpha\epsilon - (\epsilon_0 + A\,k^2)} \ , \tag{2.69}$$

The integrand has two poles

$$k^\star = \pm\frac{1}{\sqrt{A}}\sqrt{\epsilon-\epsilon_0+i\alpha\epsilon}\ . \tag{2.70}$$

Since $x > x_L$, we take the pole in the upper half-plane, and define the contour that goes along the real line from $-\infty$ to ∞ and then counterclockwise along a semicircle back from ∞ to $-\infty$.

With the residue theorem, we get,

$$\mathcal{M} \;=\; \frac{-\hbar\, i}{2\sqrt{A}}\frac{e^{i\frac{1}{\sqrt{A}}\left(\sqrt{\epsilon-\epsilon_0+i\alpha\epsilon}\right)(x-x_L)}}{\sqrt{\epsilon-\epsilon_0+i\alpha\epsilon}}\ . \tag{2.71}$$

Therefore we get the contribution to density matrix from the left lead,

$$\begin{aligned}\rho^L_{x_1,x_2} \;=\; & \frac{\hbar^2\alpha'}{2A}\int\frac{d\epsilon}{2\pi}\frac{n_B(\epsilon-\mu_L)(\epsilon-\mu_L)}{\sqrt{(\epsilon-\epsilon_0)^2+\epsilon^2\alpha^2}} \\ & \times e^{i\frac{1}{\sqrt{A}}(\sqrt{\epsilon-\epsilon_0-i\alpha\epsilon}-\sqrt{\epsilon-\epsilon_0+i\alpha\epsilon})x_L}e^{i\frac{1}{\sqrt{A}}(x_1\sqrt{\epsilon-\epsilon_0+i\alpha\epsilon}-x_2\sqrt{\epsilon-\epsilon_0-i\alpha\epsilon})}\ ,\end{aligned} \tag{2.72}$$

and similar the contribution from the right lead,

$$\begin{aligned}\rho^R_{x_1,x_2} \;=\; & \frac{\hbar^2\alpha'}{2A}\int\frac{d\epsilon}{2\pi}\frac{n_B(\epsilon-\mu_R)(\epsilon-\mu_R)}{\sqrt{(\epsilon-\epsilon_0)^2+\epsilon^2\alpha^2}} \\ & \times e^{i\frac{1}{\sqrt{A}}(\sqrt{\epsilon-\epsilon_0+i\alpha\epsilon}-\sqrt{\epsilon-\epsilon_0-i\alpha\epsilon})x_R}e^{i\frac{1}{\sqrt{A}}(-x_1\sqrt{\epsilon-\epsilon_0+i\alpha\epsilon}+x_2\sqrt{\epsilon-\epsilon_0-i\alpha\epsilon})}\ .\end{aligned} \tag{2.73}$$

For the contribution from the phonon bath in Eq. 2.68, a summation over the residues of two poles in the upper plane is required if we take $x' > x$, and we get,

$$\rho^C_{x_1,x_2} = \frac{\hbar^2}{2\pi\sqrt{A}}\int d\epsilon n_B(\epsilon)\mathrm{Re}\left(\frac{e^{-i(x_2-x_1)\sqrt{(\epsilon-\epsilon_0-i\alpha\epsilon)/A}}}{\sqrt{\epsilon-\epsilon_0-i\alpha\epsilon}}\right)\ . \tag{2.74}$$

Plugging Eq. 2.72, Eq. 2.73, Eq. 2.74 into Eq. 2.64 gives the expression for the total density matrix as an integral over magnon energy,

$$\begin{aligned}&\rho_{x_1,x_2} \\ &= \frac{\hbar^2\alpha'}{2A}\int\frac{d\epsilon}{2\pi\sqrt{(\epsilon-\epsilon_0)^2+\epsilon^2\alpha^2}} \\ &\times\Big(n_B(\epsilon-\mu_L)(\epsilon-\mu_L)e^{i\frac{1}{\sqrt{A}}(\sqrt{\epsilon-\epsilon_0-i\alpha\epsilon}-\sqrt{\epsilon-\epsilon_0+i\alpha\epsilon})x_L}e^{i\frac{1}{\sqrt{A}}(x_1\sqrt{\epsilon-\epsilon_0+i\alpha\epsilon}-x_2\sqrt{\epsilon-\epsilon_0-i\alpha\epsilon})} \\ &+n_B(\epsilon-\mu_R)(\epsilon-\mu_R)e^{i\frac{1}{\sqrt{A}}(\sqrt{\epsilon-\epsilon_0+i\alpha\epsilon}-\sqrt{\epsilon-\epsilon_0-i\alpha\epsilon})x_R}e^{i\frac{1}{\sqrt{A}}(-x_1\sqrt{\epsilon-\epsilon_0+i\alpha\epsilon}+x_2\sqrt{\epsilon-\epsilon_0-i\alpha\epsilon})}\Big) \\ &+\frac{\hbar^2}{2\pi\sqrt{A}}\int d\epsilon n_B(\epsilon)\mathrm{Re}\left(\frac{e^{-i(x_2-x_1)\sqrt{(\epsilon-\epsilon_0-i\alpha\epsilon)/A}}}{\sqrt{\epsilon-\epsilon_0-i\alpha\epsilon}}\right)\ .\end{aligned} \tag{2.75}$$

Local Magnon Current

The local magnon current can be calculated from the density matrix $\rho_{x,x'}$ by,

$$j_m(x) = \frac{2J\,a^2\hbar}{i}\lim_{x'\to x}\left[\nabla_x\rho_{x,x'} - \nabla_{x'}\rho_{x,x'}\right] \ . \tag{2.76}$$

Performing the derivative over spatial coordinate for the phase factor gives the final energy integral,

$$\begin{aligned} & j_m(x) \\ & = \frac{\alpha'\hbar^3}{\sqrt{A}}\int\frac{d\epsilon}{2\pi}\frac{\sqrt{\epsilon-\epsilon_0+i\alpha\epsilon}+\sqrt{\epsilon-\epsilon_0-i\alpha\epsilon}}{\sqrt{(\epsilon-\epsilon_0)^2+\epsilon^2\alpha^2}} \\ & \times\Big[n_B(\epsilon-\mu_L)(\epsilon-\mu_L)e^{i\frac{x-x_L}{\sqrt{A}}(\sqrt{\epsilon-\epsilon_0+i\alpha\epsilon}-\sqrt{\epsilon-\epsilon_0-i\alpha\epsilon})} \\ & -n_B(\epsilon-\mu_R)(\epsilon-\mu_R)e^{i\frac{x_R-x}{\sqrt{A}}(\sqrt{\epsilon-\epsilon_0+i\alpha\epsilon}-\sqrt{\epsilon-\epsilon_0-i\alpha\epsilon})}\Big] \ . \end{aligned} \tag{2.77}$$

Note that the fact that the contribution from the phonon bath to the density matrix does not directly affect the expression of the local magnon current is making sense, since the Gilbert damping only acts locally, and does not act on the magnon hopping process. This is different from the case in the expression of interface magnon current, in which there is the spin angular momentum loss due to coupling with the phonon bath.

Taking the zero Gilbert damping limit, we get,

$$\boxed{j_m(x) = \frac{2\alpha'\hbar^3}{\sqrt{A}}\int_{\epsilon_0}^{\infty}\frac{d\epsilon}{2\pi}\left[\frac{n_B(\epsilon-\mu_L)(\epsilon-\mu_L)-n_B(\epsilon-\mu_R)(\epsilon-\mu_R)}{\sqrt{\epsilon-\epsilon_0}}\right]} \tag{2.78}$$

which is a constant function of the spatial coordinate x.

Performing linear response theory for a small μ_R and μ_L compared with the thermal energy, we obtain the high-temperature limit of the local magnon spin conductivity defined as $\sigma_m(x) \equiv \frac{j_m(x)}{\mu_R-\mu_L}$,

$$\begin{aligned} \sigma_m(x) &\approx \frac{\alpha'\hbar^3(k_BT)^{3/2}}{\sqrt{\pi A}}e^{-\frac{\epsilon_0}{k_BT}}(1-2\frac{\epsilon_0}{k_BT}) \\ &\approx \frac{\alpha'\hbar^3(k_BT)^{3/2}}{\sqrt{\pi A}} \ , \end{aligned} \tag{2.79}$$

where in the last step we take a small magnon gap so that $\epsilon_0/k_BT \to 0$.

Case in the presence of finite Gilbert damping — We rewrite the magnon current as into a summation of four integrals,

$$j_m(x) \equiv \frac{2\alpha'\hbar^3}{\sqrt{A}}\left(j_m^{L,+}(x) + j_m^{L,-}(x) + j_m^{R,+}(x) + j_m^{R,-}(x)\right) \ , \tag{2.80}$$

where we defined

$$\begin{aligned} j_m^{L,\pm}(x) &= \int \frac{d\epsilon}{2\pi} \frac{1}{\sqrt{\epsilon-\epsilon_0 \pm i\alpha\epsilon}} n_B(\epsilon-\mu_L)(\epsilon-\mu_L) e^{i\frac{x-x_L}{\sqrt{A}}(\sqrt{\epsilon-\epsilon_0+i\alpha\epsilon}-\sqrt{\epsilon-\epsilon_0-i\alpha\epsilon})} \\ j_m^{R,\pm}(x) &= -\int \frac{d\epsilon}{2\pi} \frac{1}{\sqrt{\epsilon-\epsilon_0 \pm i\alpha\epsilon}} n_B(\epsilon-\mu_R)(\epsilon-\mu_R) e^{i\frac{x_R-x}{\sqrt{A}}(\sqrt{\epsilon-\epsilon_0+i\alpha\epsilon}-\sqrt{\epsilon-\epsilon_0-i\alpha\epsilon})} . \end{aligned} \tag{2.81}$$

To calculate the integrals, we take its high temperature limit by replacing the Bose-Einstein distribution function $n_B(\epsilon-\mu_L)$ with a Boltzmann one, therefore,

$$j_m^{L,+}(x) = \int \frac{d\epsilon}{2\pi} \frac{1}{\sqrt{\epsilon-\epsilon_0+i\alpha\epsilon}} (\epsilon-\mu_L) e^{-\frac{\epsilon-\mu_L}{k_BT}+i\frac{x-x_L}{\sqrt{A}}(\sqrt{\epsilon-\epsilon_0+i\alpha\epsilon}-\sqrt{\epsilon-\epsilon_0-i\alpha\epsilon})} . \tag{2.82}$$

Defining dimensionless variables as $\tilde{\mu}_L = \mu_L/k_BT$, $\tilde{\epsilon}_0 = \epsilon_0/k_BT\tilde{\mu}_L$, and also making the energy integral dimensionless by taking the replacement $\epsilon \to \tilde{\epsilon}k_BT$, we have

$$\begin{aligned} & j_m^{L,+}(x) \\ = \; & \frac{(k_BT)^{3/2}}{2\pi} \int_0^\infty d\tilde{\epsilon} \frac{\tilde{\epsilon}-\tilde{\mu}_L}{\sqrt{(1+i\alpha)\tilde{\epsilon}-\tilde{\epsilon}_0}} \\ & \times \exp\left[-(\tilde{\epsilon}-\tilde{\mu}_L) - \frac{2\alpha\tilde{\epsilon}(x-x_L)\sqrt{k_BT/A}}{\sqrt{(1+i\alpha)\tilde{\epsilon}-\tilde{\epsilon}_0}+\sqrt{(1-i\alpha)\tilde{\epsilon}-\tilde{\epsilon}_0}}\right] \\ \approx \; & \frac{(k_BT)^{3/2}}{2\pi} \int_0^\infty d\tilde{\epsilon} \frac{\tilde{\epsilon}-\tilde{\mu}_L}{\sqrt{\tilde{\epsilon}-\tilde{\epsilon}_0}} \exp\left[-(\tilde{\epsilon}-\tilde{\mu}_L) - \frac{\alpha\tilde{\epsilon}(x-x_L)\sqrt{k_BT/A}}{\sqrt{\tilde{\epsilon}-\tilde{\epsilon}_0}}\right] , \end{aligned} \tag{2.83}$$

where in the last step we approximate the integral by taking the Gilbert damping to be much smaller than 1.

Taking $u = \sqrt{\tilde{\epsilon}-\tilde{\epsilon}_0}$ gives,

$$\begin{aligned} & j_m^{L,+}(x) \\ & = \frac{(k_BT)^{3/2}}{\pi} \int_0^\infty du(u^2+\tilde{\epsilon}_0-\tilde{\mu}_L) \\ & \times \exp\left[-(u^2+\tilde{\epsilon}_0-\tilde{\mu}_L) - \frac{\alpha(u^2+\tilde{\epsilon}_0)(x-x_L)\sqrt{k_BT/A}}{u}\right] . \end{aligned} \tag{2.84}$$

With a similar approach, we calculate the other three integrals and obtain,

$$
\begin{aligned}
& j_m(x) \\
& = \frac{4\alpha'\hbar^3(k_BT)^{3/2}}{\sqrt{A}\pi}\Big(\int_0^\infty du(u^2+\tilde{\epsilon}_0-\tilde{\mu}_L) \\
& \times \exp\left[-(u^2+\tilde{\epsilon}_0-\tilde{\mu}_L)-\frac{\alpha(u^2+\tilde{\epsilon}_0)(x-x_L)\sqrt{k_BT/A}}{u}\right] \\
& -\int_0^\infty du(u^2+\tilde{\epsilon}_0-\tilde{\mu}_R)\exp\left[-(u^2+\tilde{\epsilon}_0-\tilde{\mu}_R)-\frac{\alpha(u^2+\tilde{\epsilon}_0)(x_R-x)\sqrt{k_BT/A}}{u}\right]\Big)\,.
\end{aligned}
\tag{2.85}
$$

It is clear from Eq. 2.85 that the Gilbert damping gives the dependence of local magnon current on the spatial coordinate, as shown in previous numerical plots.

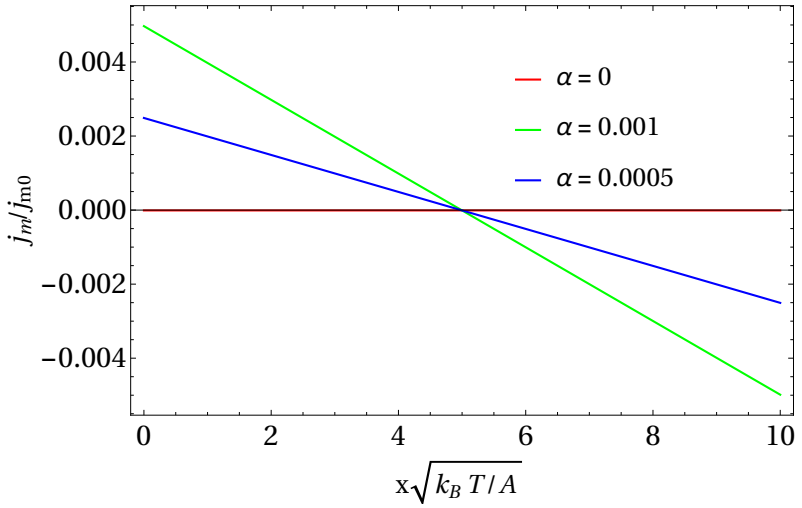

Fig. 2.10: Dimensionless local magnon current as a function of system size $l \equiv x_R - x_L = 10\sqrt{A/k_BT}$ for various Gilbert damping values. The units of local magnon current is taken as $j_{m0} \equiv \frac{4\alpha'\hbar^3(k_BT)^{3/2}}{\sqrt{A}\pi}$. Here the temperatures for both leads are equal and kept as constant. The other parameters have the values, $\mu_L/k_BT = 2\times10^{-5}$, $\mu_R = 0$, $x_L = 0$.

We numerically calculate the dimensionless integral over u above and plot the spatial dependence of the local magnon current as shown in Fig. 2.10.

CHAPTER 3

Spin-transfer Mechanism for Magnon Drag in Antiferromagnetic Metals

The magnon-drag thermopower, the contribution to the Seebeck effect due to magnons dragging electrons, has been extensively investigated in conducting ferromagnets. In this chapter, we apply the stochastic Landau-Lifshitz-Gilbert formalism with spin-transfer torques to develop a theory for magnon drag in antiferromagnetic metals. We evaluate the magnon spin and heat current driven by an electric current, both as a function of magnetic field and temperature. In particular, we find that the magnon spin current is enhanced near the spin-flop transition. This result shows that antiferromagnetic metals may be used as a tunable source of spin current[2].

3.1 Introduction

Over the last half century, physics phenomena associated with "drag" have been attracting wide interest in the field of solid-state systems. The effects of various type of drags on the transport properties of electrons have been a subject of much scrutiny. Coulomb drag, caused by electron-electron interaction, is defined as a frictional coupling between electric currents flowing in spatially separated conducting layers. Gramila *et al.* [115] first observed the Coulomb drag between barrier-separated two-dimensional electron gases in GaAlAs heterostructures, and showed agreement of the magnitude and temperature dependence of the drag voltage with theoretical

[2]This chapter and its appendix are based on J. Zheng, S.A. Bender, Q. Enneking Y. Tserkovnyak, B. Flebus and R. A. Duine, *Spin-transfer mechanism for magnon drag in antiferromagnetic metals*, in preparation. J. Zheng conceived the project, did all the analytic derivations, performed the related numerical calculations, and wrote the manuscript with the help of all co-authors.

predictions [116]. Recently, Coulomb drag was probed in the strong-coupling limit in graphene-boron-nitride heterostructures, showing a quadratic temperature dependence of the drag resistivity for a sufficiently high charge carrier density [117].

Besides the drag due to interactions among themselves, electrons can feel a drag force due to the coupling with phonons. A phonon flow driven by a temperature gradient can cause a steep rise in the thermopower at low temperatures by dragging electrons [118, 119, 120]. This is referred to as the phonon-drag mechanism, and occurs in various semiconductors and metals. One example of recent work is that of Kubakaddi *et al.* [121], who developed a theory of low-temperature phonon-drag thermopower in three-dimensional Dirac semimetals. They found that the thermopower increases with decreasing electron concentration at low temperatures and that screening effects of the electron-phonon interaction strongly affect its temperature dependence. Phonons can also drag other quasi-particle excitations, e.g. magnons, which are the quanta of spin-orientation oscillations in magnetic materials. Magnons have recently been envisioned to be a promising information carrier for spintronics due to their long relaxation length [34, 3]. A gigantic enhancement of the spin Seebeck effect has been experimentally observed in the magnetic insulator $LaY_2Fe_5O_{12}$ at low temperatures [122], and can be explained by an extra contribution to the spin-current injection due to the phonon-drag mechanism. Here, the non-equilibrium phonons feel the temperature gradient in the magnetic insulator and drag the low-energy spin excitations via the magnon-phonon interaction. Magnons and electrons also have mutual interactions both in the bulk of a ferromagnetic metal, and near interfaces between normal metals and ferromagnets. For example, excitation and detection of magnon spin transport in a magnetic insulator have been demonstrated fully electrically using a non-local measurement geometry [3]. Recently, Cornelissen *et al.* [123] achieved efficient manipulation of magnon spin transport in a three terminal device based on the magnetic insulator yttrium iron garnet (YIG), where the magnon spin current in the YIG channel is modulated by tuning the magnon density with a dc electrical current driven through a platinum electrode. Wu *et al.* [124] experimentally studied the magnon-mediated transport in a spin-valve-like trilayer structure where two heavy metal (HM) layers are sandwiching a ferrimagnetic insulator. In these experiments, the charge/spin current in one HM layer is observed to drag a charge/spin current in the other at room temperature.

In conducting magnets, magnon-electron interactions give rise to additional contributions, on top of the diffusive ones, to the Seebeck effect and its reciprocal, the Peltier effect. The magnon-drag contributions to the Peltier effect of Ni-Cu alloy and the p-type antiferromagnetic semiconductor MnTe have been separately measured long time ago [125, 126]. Since magnon drag can be exploited to increase the thermopower of metals, intense efforts have been recently devoted to the experimental and theoretical study of magnon-drag in ferromagnets, especially on the temperature dependence. A thermopile device formed by pairs of ferromagnetic wires has been demonstrated in an experimental study, in which it was found that due to the magnon-magnon and magnon-phonon interactions the contribution from magnon-drag to the thermopower decreases at high temperatures [127]. Watzman *et al.* [128] measured the thermopower of Fe, Co and Ni, and found that the magnon-drag effect dominates the thermopower in these materials over a wide range of temperature. At the same time, there have been various theoretical studies of magnon drag. Lucassen *et al.* [129] proposed a spin-

transfer contribution to the magnon-drag thermopower, in which the electric current density induced by a time-dependent magnetization via the process reciprocal to spin transfer, namely spin pumping. Building upon this work, Flebus *et al.* [130] proposed a Berry-phase correction to the thermopower in conducting ferromagnets by solving the stochastic Landau-Lifshitz-Gilbert equation and evaluating the pumped current. A hydrodynamic theory based on Galilean spin-preserving electron-magnon scattering has also been presented to quantitatively explain the observed thermopower of Fe and Co [128]. Note that the hydrodynamic and spin-transfer based theories are very different from each other, since the hydrodynamic theory starts from a spin-conserving scattering between the electron fluid and the magnon fluid, while the spin-transfer mechanism requires the existence of spin-orbit coupling [128].

Next to developments with ferromagnets, some of which are mentioned above, antiferromagnets have recently gained attention in spintronics. The latter represents a promising platform for the future of spintronic applications, e.g. in race-track memories and THz oscillators, due to their robustness against magnetic perturbation and intrinsic ultrafast dynamics [25, 131, 132, 133, 134]. This motivates us to investigate magnon drag in antiferromagnetic metals. In particular, we consider a current driven through a conducting antiferromagnet and calculate the magnon spin and heat current generated by this electric current using the stochastic Landau-Lifhistz-Gilbert formalism that includes spin transfer torques [130, 135]. As a result, we evaluate the contribution to the Peltier effect due to magnon drag. We find, moreover, that the magnon spin current driven by the electric current is strongly enhanced near the spin-flop transition (see Section 1.1.4 in the introduction chapter for the definition). This paves the way for field-tunable spin current generation by antiferromagnetic metals.

The remainder of this chapter is organized as follows. In Section 3.2, we introduce a free-energy functional for a bipartite antiferromagnet, and derive the magnon energy and spin current from the appropriate continuity equation. We evaluate the magnon energy current and magnon spin current and present analytical and numerical results. We finally summarize our findings in Section 3.5, and discuss possible directions for future research.

3.2 Current-induced Antiferromagnetic Magnetization Dynamics

In this section we introduce the stochastic equations of motion for the magnetization dynamics of an antiferromagnet. We include current-induced torques to investigate how an electric current affects the transport of magnons.

3.2.1 Stochastic Equations of Motion

We consider a three-dimensional antiferromagnetic metal with two equivalent sublattices, as Fig. 3.1 shows. Electrons propagates through a magnetic texture characterized by the Néel order unit vector $\boldsymbol{n}$ and the dimensionless magnetization density $\boldsymbol{m}$, which

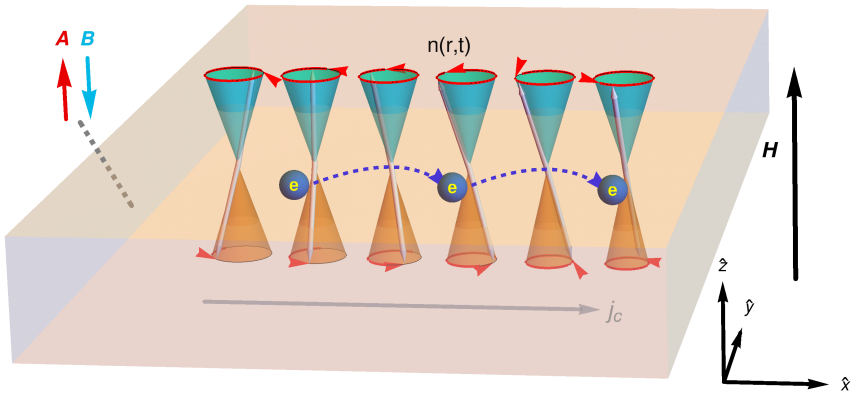

Fig. 3.1: Schematic illustration for magnon drag in a metallic antiferromagnet with two equivalent sublattices (A, B). The electrical current is flowing in the x direction and drives the magnetization dynamics. An external magnetic field is added in the z direction, with the orange cones and green cones denote the precession of Néel vector.

are constrained to satisfy $|\boldsymbol{n}| = 1$ and $\boldsymbol{n} \cdot \boldsymbol{m} = 0$. An effective long-wavelength theory of these two fields gives the following free-energy functional [135]

$$\begin{aligned} F &= s \int_{\mathcal{V}} d\boldsymbol{r} \left(\frac{\boldsymbol{m}^2}{2\chi} + \frac{A}{2} \sum_{i=1}^{3} (\partial_i \boldsymbol{n})^2 - \frac{K_z}{2} (\boldsymbol{n} \cdot \hat{z})^2 - \boldsymbol{H} \cdot \boldsymbol{m} \right) \\ &\equiv \int_{\mathcal{V}} d\boldsymbol{r} \epsilon(\boldsymbol{r}) \end{aligned} \tag{3.1}$$

where we have introduced the energy density $\epsilon(\boldsymbol{r})$ and the saturated spin density s (in units of $\hbar$). Furthermore, χ is the transverse spin susceptibility, A is the Néel order exchange stiffness, and $K_z (> 0)$ is the easy-axis anisotropy. We take the orientation of external magnetic field $\boldsymbol{H}$ along $\hat{z}$ direction, $\boldsymbol{H} = (0, 0, H_z)$.

The dynamics without dissipation and electric current is governed by the following equations,

$$\begin{aligned} \hbar \dot{\boldsymbol{n}} &= \boldsymbol{f}_m \times \boldsymbol{n} \; ; \\ \hbar \dot{\boldsymbol{m}} &= \boldsymbol{f}_n \times \boldsymbol{n} + \boldsymbol{f}_m \times \boldsymbol{m} \; , \end{aligned} \tag{3.2}$$

where $\boldsymbol{f}_n$ and $\boldsymbol{f}_m$ are the effective fields given by [136],

$$\begin{aligned} \boldsymbol{f}_m &\equiv -s^{-1} \delta_{\boldsymbol{n}} F \\ &= -\frac{\boldsymbol{m}}{\chi} + \boldsymbol{n} \times (\boldsymbol{H} \times \boldsymbol{n}) \; ; \\ \boldsymbol{f}_n &\equiv -s^{-1} \delta_{\boldsymbol{m}} F \\ &= A \boldsymbol{n} \times (\nabla^2 \boldsymbol{n} \times \boldsymbol{n}) + K_z (\boldsymbol{n} \cdot \hat{z}) \boldsymbol{n} \times (\hat{z} \times \boldsymbol{n}) - (\boldsymbol{n} \cdot \boldsymbol{H}) \boldsymbol{m} \; . \end{aligned} \tag{3.3}$$

To linearize the equations of motion and evaluate the energy density up to the second order we write

$$\begin{aligned} \boldsymbol{n} &= (n_x, n_y, 1 - n_x^2/2 - n_y^2/2) \ ; \\ \boldsymbol{m} &= (m_x, m_y, -n_x m_x - n_y m_y) \ , \end{aligned} \tag{3.4}$$

which obeys the constraints mentioned earlier in this subsection, and applies to the antiferromagnetic phase when the external magnetic field is sufficiently small, $|H_z| \leq H_c \equiv \sqrt{K_z/\chi}$, to prevent the formation of a spin-flop phase [137].

Substituting Eq. 3.4 to Eq. 3.2 and Eq. 3.3, and switching to complex variables by means of

$$n \equiv n_x - i n_y, \quad m \equiv m_x - i m_y \ , \tag{3.5}$$

we get the linearized equations of motion

$$\begin{aligned} i\hbar\partial_t m &= K_z n + H_z m - A\nabla^2 n \ ; \\ i\hbar\partial_t n &= \frac{m}{\chi} + H_z n \ . \end{aligned} \tag{3.6}$$

Similarly, the energy density is found as

$$E_0 = s\Big(\frac{m * m}{2\chi} + \frac{A}{2}\nabla n^*\nabla n - \frac{K_z}{2}(1 - n^* n) + \frac{H_z}{2}(n^* m + m^* n)\Big) \ . \tag{3.7}$$

We proceed to add to the equations of motion Eq. 3.2 the contribution from reactive spin-transfer torques, following the approach of Ref. [138]. This amounts to substitute the time derivative with $\partial_t \to \partial_t + \boldsymbol{v}_s \cdot \nabla$, where $\boldsymbol{v}_s$ is a phenomenological parameter proportional to the drift velocity of the conduction electrons in the antiferromagnetic metal [139]. This reactive torque essentially comes from the component of the spin density generated by the current and that is perpendicular to the magnetization. In the simplest microscopic picture, this spin density exerts a torque via the $s-d$ exchange coupling [138]. Including the reactive spin-transfer torques leads to

$$\begin{aligned} i\hbar\big(\partial_t + (\boldsymbol{v}_s \cdot \nabla)\big)m &= K_z n + H_z m - A\nabla^2 n \ ; \\ i\hbar\big(\partial_t + (\boldsymbol{v}_s \cdot \nabla)\big)n &= \frac{m}{\chi} + H_z n \ . \end{aligned} \tag{3.8}$$

These equations follow from the Lagrangian density

$$\begin{aligned} L_{AF} = \frac{s}{2}\Big[& i\hbar\Big(m^*(\partial_t + (\boldsymbol{v}_s \cdot \nabla))n - m(\partial_t + (\boldsymbol{v}_s \cdot \nabla)n^*)\Big) \\ & -\Big(\frac{m * m}{\chi} + A\nabla n^*\nabla n - K_z(1 - n^* n) + H_z(n^* m + m^* n)\Big)\Big] \ . \end{aligned} \tag{3.9}$$

In conducting magnets, there is another contribution to the dynamics of magnetization density $\boldsymbol{m}$. Namely, the dissipative spin-transfer torque proportional to the dimensionless parameter β and has the form $\beta \boldsymbol{n} \times (\boldsymbol{v}_s \cdot \nabla)\boldsymbol{n}$. It breaks time-reversal symmetry and arises from spin dephasing processes [140, 141]. We also include Gilbert damping and fluctuating torques to account for thermal fluctuations. To derive them, we start from the fluctuating and dissipative torques for the $\zeta = A, B$ sub-lattice that

can be written as $\boldsymbol{\tau}_\zeta = (\boldsymbol{h}^b_\zeta - \alpha\hbar\boldsymbol{\Omega}_\zeta) \times \boldsymbol{\Omega}_\zeta$, where $\boldsymbol{\Omega}_\zeta$ is a unit vector in the direction of the magnetization of ζ sublattice, α is the bulk Gilbert damping. $\boldsymbol{h}^b_\zeta$ denotes the fluctuating forces, which satisfy the fluctuation-dissipation relation [142]:

$$\langle h^{b,(i)}_\zeta(\boldsymbol{r},\omega) h^{b,(i')}_{\zeta'}(\boldsymbol{r}',\omega')\rangle = \frac{2\pi\alpha s\hbar\omega\delta_{\zeta\zeta'}\delta_{ii'}\delta(\boldsymbol{r}-\boldsymbol{r}')\delta(\omega-\omega')}{\tanh(\hbar\omega/2k_BT(\boldsymbol{r}))} \ , \qquad (3.10)$$

where ω is the frequency of the magnons, T is the temperature function, and $\langle ... \rangle$ denotes the average over realizations of the noise. Here $\langle h^{b,(i)}_\zeta(\boldsymbol{r},t) h^{b,(i')}_{\zeta'}(\boldsymbol{r}',t')\rangle$ contains contributions from both the classical and quantum fluctuations [143]. Later on we will slightly modify the form of this relation for the computation of the correlation function of the Néel order parameter.

After some rewriting (see the supplemental material of Ref. [135]), we have

$$\begin{aligned} \boldsymbol{\tau}_m &= \big((\boldsymbol{h}^b_A + \boldsymbol{h}^b_B)/2 - \alpha\hbar\dot{\boldsymbol{m}}\big) \times \boldsymbol{m} + ((\boldsymbol{h}^b_A - \boldsymbol{h}^b_B)/2 - \alpha\hbar\dot{\boldsymbol{n}}) \times \boldsymbol{n} \ ; \qquad (3.11)\\ \boldsymbol{\tau}_n &= \big((\boldsymbol{h}^b_A + \boldsymbol{h}^b_B)/2 - \alpha\hbar\dot{\boldsymbol{m}}\big) \times \boldsymbol{n} \ , \qquad (3.12)\end{aligned}$$

where the fluctuating force is expressed as a Cartesian vector, $\boldsymbol{h}^b_A = (h^{b,x}_A, h^{b,y}_A, h^{b,z}_A)$, $\boldsymbol{h}^b_B = (h^{b,x}_B, h^{b,y}_B, h^{b,z}_B)$.
From this, we find the complex stochastic fields as,

$$\begin{aligned} h^b_B &\equiv h^{b,x}_B - i h^{b,y}_B \ ; \\ h^b_A &\equiv h^{b,x}_A - i h^{b,y}_A \ . \qquad (3.13)\end{aligned}$$

Expanding Eq. 3.12 with Eq. 3.4, and switching to the complex variable using Eq. 3.13, we add the damping torques and the stochastic fields illustrated above. Including also the dissipative spin transfer torques, we find the final form for the equations of motion as:

$$\begin{aligned} \hbar\frac{\partial n}{\partial t} &= i h^b_A/2 + i h^b_B/2 - iH_z n - i\frac{m}{\chi} - i\alpha\hbar\frac{\partial m}{\partial t} - \hbar(\boldsymbol{v}_s\cdot\nabla)n \ ; \qquad (3.14)\\ \hbar\frac{\partial m}{\partial t} &= i h^b_A/2 - i h^b_B/2 - iH_z m - iK_z n - i\alpha\hbar\frac{\partial n}{\partial t} \\ &\quad + iA\nabla^2 n - \hbar(\boldsymbol{v}_s\cdot\nabla)m - i\beta\hbar(\boldsymbol{v}_s\cdot\nabla)n \ . \qquad (3.15)\end{aligned}$$

3.2.2 Fourier Transform and Dispersion

Consider the Fourier transform in the circular basis with respect to the y and z axes:

$$\mathcal{O}(x,\boldsymbol{\rho},t) = \int d^2\mathbf{q}d\omega \, e^{-i\omega t + i\mathbf{q}\cdot\boldsymbol{\rho}}\mathcal{O}(x,\mathbf{q},\omega) \ , \qquad (3.16)$$

where $\boldsymbol{\rho}$ is the transverse coordinate $\boldsymbol{\rho} = y\hat{\boldsymbol{y}} + z\hat{\boldsymbol{z}}$ and $\mathbf{q}$ is the transverse wave vector $\mathbf{q} = q_y\hat{\boldsymbol{q}}_y + q_z\hat{\boldsymbol{q}}_z$. Therefore we have the equations of motion in the frequency space,

$$\begin{aligned}
\big(-\hbar\omega + H_z - \hbar(iv_{sx}\partial_x - v_{sy}q_y - v_{sz}q_z)\big)n(x,\mathbf{q},\omega) &+ (\frac{1}{\chi} - i\alpha\hbar\omega)m(x,\mathbf{q},\omega) \\
&= h^b_m(x,\mathbf{q},\omega)\ ; \\
\big(-\hbar\omega + H_z - \hbar(iv_{sx}\partial_x - v_{sy}q_y - v_{sz}q_z)\big)m(x,\mathbf{q},\omega) &+ \big(K_z - i\alpha\hbar\omega + A(\mathbf{q}^2 - \partial_x^2) \\
+\beta\hbar(v_{sx}\partial_x + iv_{sy}q_y + iv_{sz}q_z)\big)n(x,\mathbf{q},\omega) &= h^b_n(x,\mathbf{q},\omega)\ . \qquad (3.17)
\end{aligned}$$

where for the stochastic fields we define, $h^b_m(x,\mathbf{q},\omega) \equiv h^b_A(x,\mathbf{q},\omega)/2 + h^b_B(x,\mathbf{q},\omega)/2$, $h^b_n(x,\mathbf{q},\omega) \equiv h^b_A(x,\mathbf{q},\omega)/2 - h^b_B(x,\mathbf{q},\omega)/2$. Combining Eq. 3.17 with the Fourier transform $\mathcal{O}(x,\mathbf{q},\omega) = \int dk\, \mathcal{O}(k,\mathbf{q},\omega)e^{ikx}$, where k is the wave vector along the $\hat{x}$ axis, we obtain

$$n(k,\mathbf{q},\omega) = \frac{h^b_n(k,\mathbf{q},\omega) - \frac{\chi(-\hbar\omega+H_z+\hbar v_{sx}k)h^b_m(k,\mathbf{q},\omega)}{(1-i\alpha\hbar\chi\omega)}}{Ak^2 + (\beta\hbar i - \frac{2\chi\hbar(-\hbar\omega+H_z)}{1-i\alpha\hbar\chi\omega})v_{sx}k + \mu^2}\ , \qquad (3.18)$$

where

$$\mu^2 \equiv Aq^2 + K_z - i\alpha\hbar\omega - \chi\frac{(-\hbar\omega + H_z)^2 + (\hbar v_{sx}k)^2}{1 - i\alpha\hbar\chi\omega}\ , \qquad (3.19)$$

and we have taken $v_{sy}q_y + v_{sz}q_z \to 0$, since we focus on the case where the electrical current is applied in x-direction.

Neglecting dissipations, $\alpha = \beta = 0$, the equation for the poles of Eq. 3.18 yields the dispersion of the antiferromagnetic magnons

$$\hbar\omega^{(\pm)} = H_z + \hbar v_{sx}k \pm \sqrt{(K_z + A(k^2 + \mathbf{q}^2))/\chi}\ , \qquad (3.20)$$

which is consistent with the conventional results [136]. Assuming $H_z > 0$, the zero wavelength limit of the two branches is thus given as,

$$\begin{aligned}
\mathcal{E}^{(+)}_{k,\mathbf{q}=0} &= H_z + \sqrt{K_z/\chi} \\
\mathcal{E}^{(-)}_{k,\mathbf{q}=0} &= H_z - \sqrt{K_z/\chi}\ . \qquad (3.21)
\end{aligned}$$

The two types of magnons are influenced differently by the external magnetic field. As the external magnetic field H_z increases from zero, the energy of the (+) branch $\mathcal{E}^{(+)}_{k,\mathbf{q}=0}$ keep increasing, while the energy of the other branch $\mathcal{E}^{(-)}_{k,\mathbf{q}=0}$ vanishes when H_z reaches $\sqrt{K_z/\chi}$. For a large enough magnetic field which satisfies $|H_z| \geq \sqrt{K_z/\chi}$, our theory breaks down, since the ground state Néel order is no longer pointing in the z-direction, but enters the spin-flop phase. For the sake of simplicity, we only consider fields $|H_z| < \sqrt{K_z/\chi}$.

3.2.3 Correlation Function

In order to evaluate the magnon spin and heat current, we need the correlation function $\langle n(k,\mathbf{q},\omega)n^*(k',\mathbf{q}',\omega')\rangle$. This function is obtained by invoking the relation between

Néel order parameter n and the stochastic field h in Eq. 3.18 and the fluctuation-dissipation theorem in Eq. 3.10, to yield

$$\langle n(k,\mathbf{q},\omega)n^*(k',\mathbf{q}',\omega')\rangle = \frac{\alpha s\hbar\omega\delta(k-k')\delta(\mathbf{q}-\mathbf{q}')\delta(\omega-\omega')\left(1+\frac{\chi^2[(-\hbar\omega+H_z)^2+2\hbar v_{sx}k(-\hbar\omega+H_z)]}{1+(\alpha\hbar\chi\omega)^2}\right)}{2(2\pi)^2\tanh(\frac{\hbar\omega}{2k_BT})|Ak^2+(\beta\hbar i-\frac{2\chi\hbar(-\hbar\omega+H_z)}{1-i\alpha\hbar\chi\omega})v_{sx}k+\mu^2|^2} . \tag{3.22}$$

Taking the exchange approximation that the spin susceptibility χ is tiny and also assuming the electrical current is small,

$$\chi H_z \ll 1, \quad \chi\omega \ll 1, \quad |\hbar v_{sx}k\chi| \ll 1 , \tag{3.23}$$

we find

$$\langle n(k,\mathbf{q},\omega)n^*(k',\mathbf{q}',\omega')\rangle = \frac{\alpha s\hbar\omega\delta(k-k')\delta(\mathbf{q}-\mathbf{q}')\delta(\omega-\omega')/\tanh(\frac{\hbar\omega}{2k_BT})}{|Ak^2+(\beta\hbar i-2\chi\hbar(-\hbar\omega+H_z))\,v_{sx}k+\mu^2|^2 2(2\pi)^2} , \tag{3.24}$$

which will be used in later calculations of the magnon energy current.

3.3 Magnon Energy and Spin Current

In this section we discuss the magnon energy and spin current, and derive the expressions for these that are evaluated numerically in the next section.

3.3.1 Energy Current

We derive the energy current from the appropriate continuity equation that follows after taking $\alpha = \beta = 0$, i.e., neglecting dissipations. Starting from Eq. 3.9, we first obtain an expression for the energy density that contains the reactive torques,

$$\begin{aligned} E &= \frac{s}{2}\Big(\frac{m^*m}{\chi} + A\nabla n^*\nabla n - K_z(1-n^*n) + H_z(n^*m+m^*n) \\ &\quad -i\hbar\big(m^*(\boldsymbol{v}_s\cdot\nabla)n - m(\boldsymbol{v}_s\cdot\nabla)n^*\big)\Big) . \end{aligned} \tag{3.25}$$

We find from the equations of motion that,

$$\nabla\cdot\boldsymbol{j}_\epsilon + \frac{\partial E}{\partial t} = 0 , \tag{3.26}$$

which defines the magnon energy current $\boldsymbol{j}_\epsilon$. After some tedious algebra (see Appendix 3.A), we have

$$\begin{aligned} \boldsymbol{j}_\epsilon &= \frac{s}{2}\Big[-A(\frac{\partial n}{\partial t}\nabla n^* + \frac{\partial n^*}{\partial t}\nabla n) + A\big(\nabla n^*(\boldsymbol{v}_s\cdot\nabla)n + \nabla n(\boldsymbol{v}_s\cdot\nabla)n^*\big) \\ &\quad +\frac{2}{\chi}(\boldsymbol{v}_s m^*m) - i\boldsymbol{v}_s\hbar(m\frac{\partial n^*}{\partial t} - m^*\frac{\partial n}{\partial t})\Big] . \end{aligned} \tag{3.27}$$

It is easy to show from Eq. 3.8 that $m \propto \chi$. Assuming $\chi \ll A$, we can neglect the last line in Eq. 3.27 (for more details see Appendix 3.B). Therefore the energy current to be evaluated becomes,

$$\boldsymbol{j}_\epsilon \;=\; \frac{s}{2}\Big[- A(\frac{\partial n}{\partial t}\nabla n^* + \frac{\partial n^*}{\partial t}\nabla n) + A\big(\nabla n^*(\boldsymbol{v}_s\cdot\nabla)n + \nabla n(\boldsymbol{v}_s\cdot\nabla)n^*\big)\Big] \,. \tag{3.28}$$

Performing Fourier transform over Eq. 3.28, we find,

$$\begin{aligned}\langle \hat{\boldsymbol{x}}\cdot\boldsymbol{j}_\epsilon\rangle \;=\; & \frac{As}{2(2\pi)^6}\int d^3\boldsymbol{Q}\int d\omega\int d^3\boldsymbol{Q}'\int d\omega'[k\omega'+k'\omega]\langle n^*(\boldsymbol{Q},\omega)n(\boldsymbol{Q}',\omega')\rangle \\ & \times e^{-i(\boldsymbol{Q}-\boldsymbol{Q}')\cdot\boldsymbol{r}}e^{i(\omega-\omega')t} \\ & + \frac{-As}{2(2\pi)^6}\int d^3\boldsymbol{Q}\int d\omega\int d^3\boldsymbol{Q}'\int d\omega'[-2v_{sx}kk']\langle n^*(\boldsymbol{Q},\omega)n(\boldsymbol{Q}',\omega')\rangle \\ & \times e^{-i(\boldsymbol{Q}-\boldsymbol{Q}')\cdot\boldsymbol{r}}e^{i(\omega-\omega')t} \,,\end{aligned} \tag{3.29}$$

where $\boldsymbol{Q} = (k, \mathbf{q})$ is the wave vector of the magnons and ω is their frequency. This intermediate result expresses the energy current in terms of the correlation function $\langle n^*(\boldsymbol{Q},\omega)n(\boldsymbol{Q}',\omega')\rangle$ that we considered before in Eq. 3.24. Since we take the electric current in the x-direction, only the energy current in the x-direction is nonzero.

Plugging the correlation function as given in Eq. 3.24, we have

$$\begin{aligned}\langle \hat{\boldsymbol{x}}\cdot\boldsymbol{j}_\epsilon\rangle \;=\; & \frac{\alpha s^2\hbar A}{2(2\pi)^8}\int d^2\mathbf{q}\int d\boldsymbol{k}\int d\omega\frac{\omega(k\omega+v_{sx}k^2)}{\tanh(\frac{\hbar\omega}{2k_BT})} \\ & \times\frac{1}{|Ak^2+(\beta\hbar i-2\chi\hbar(-\hbar\omega+H_z))\,v_{sx}k+\mu^2|^2} \,,\end{aligned} \tag{3.30}$$

where μ^2 is given by Eq. 3.19. Performing Fourier transform over Eq. 3.28, we find,

$$\mu^2 \;\approx\; Aq^2 + K_z - i\alpha\hbar\omega - \chi\left((-\hbar\omega+H_z)^2 + (\hbar v_{sx}k)^2\right) \,, \tag{3.31}$$

which transforms the energy current into,

$$\begin{aligned}\langle \hat{\boldsymbol{x}}\cdot\boldsymbol{j}_\epsilon\rangle \;=\; & \frac{\alpha s^2\hbar A}{2(2\pi)^8}\int d^2\mathbf{q}\int dk\int d\omega\frac{\omega(k\omega+v_{sx}k^2)}{\tanh(\frac{\hbar\omega}{2k_BT})} \\ & \times\frac{1}{|[A-\chi(\hbar v_{sx})^2]k^2+(\beta\hbar i-2\chi\hbar(-\hbar\omega+H_z))\,v_{sx}k+\mu_0^2|^2} \,,\end{aligned} \tag{3.32}$$

where

$$\mu_0^2 = Aq^2 + K_z - i\alpha\hbar\omega - \chi(-\hbar\omega+H_z)^2 \,. \tag{3.33}$$

We proceed to evaluate the integral over the momentum space. Let us first look at the denominator in the last line in Eq. 3.32. Taking a small χ and weak longitudinal electric current v_{sx} to have $\chi(\hbar v_{sx})^2 \ll A$, we approximate for the denominator of Eq. 3.32 as below,

$$\begin{aligned} & |[A-\chi(\hbar v_{sx})^2]k^2 + \big(\beta\hbar i - 2\chi\hbar(-\hbar\omega+H_z)\big)v_{sx}k + \mu_0^2|^2 \\ \approx\; & \Big(Ak^2 - 2\chi\hbar(-\hbar\omega+H_z)v_{sx}k + A\mathbf{q}^2 + K_z - \chi(-\hbar\omega+H_z)^2\Big)^2 \\ & + (-\beta v_{sx}k+\alpha\omega)^2\hbar^2 \\ \equiv\; & A^2\left[g(k)^2+\zeta(k)^2\right] \,,\end{aligned} \tag{3.34}$$

where in the last step above we defined the following two functions $\zeta(k), g(k)$,

$$\zeta(k) \equiv -a\beta k + \alpha\tilde{\omega} \; ; \tag{3.35}$$

$$g(k) \equiv k^2 - 2\tilde{\chi}(-\tilde{\omega} + \tilde{H})ak + \mathbf{q}^2 + \tilde{K} - \tilde{\chi}(-\tilde{\omega} + \tilde{H})^2 \; . \tag{3.36}$$

Here, the new variables $a, \tilde{\omega}, \tilde{K}, \tilde{H}, \tilde{\chi}$ in Eq. 3.35 and Eq. 3.36 are defined as

$$a \equiv \frac{\hbar v_{sx}}{A}, \tilde{\omega} \equiv \frac{\hbar\omega}{A}, \tilde{K} \equiv \frac{K_z}{A}, \tilde{H} \equiv \frac{H_z}{A}, \tilde{\chi} \equiv \chi A \; . \tag{3.37}$$

Since the correlation function in Eq. 3.10 is defined only for the classical stochastic field, we replace the tanh function by means of

$$\frac{1}{\tanh(\frac{\hbar\omega}{2k_BT})} \to \mathrm{sgn}(\omega)\coth(\frac{\hbar\omega}{2k_BT}) - 1 \tag{3.38}$$

to remove the contribution from quantum fluctuations [143]. Here, sgn() denotes the sign function.

Putting Eq. 3.32, Eq. 3.34, Eq. 3.38 together, we have for the magnon energy current

$$\langle \hat{\boldsymbol{x}} \cdot \boldsymbol{j}_\epsilon \rangle = \frac{\alpha s^2 \hbar A}{2(2\pi)^8} \int d^2\mathbf{q} \int dk \int d\omega \frac{\omega(k\omega + v_{sx}k^2)(\mathrm{sgn}(\omega)\coth(\frac{\hbar\omega}{2k_BT}) - 1)}{A^2\left[g(k)^2 + \zeta(k)^2\right]} \; . \tag{3.39}$$

We proceed to integrate out k in Eq. 3.39 in the low damping limit $\alpha \to 0$. Note that in general the dissipative parameter β is of the same order of magnitude as α [144, 145], therefore β also vanishes in the low damping limit.

Considering these limits for Eq. 3.35 and Eq. 3.36, we find that,

$$\begin{aligned} \lim_{\alpha,\beta\to 0} \zeta(k) &= 0 \; ; \\ \lim_{\epsilon\to 0} \frac{\epsilon}{g(k)^2 + \epsilon^2} &= \pi\delta(g(k)) \; , \end{aligned} \tag{3.40}$$

where δ denotes the Dirac-delta function. Within this approximation we find

$$\begin{aligned} &\langle \hat{\boldsymbol{x}} \cdot \boldsymbol{j}_\epsilon \rangle \\ = \; & \frac{\alpha s^2 \hbar A^2}{2(2\pi)^8\hbar^2} \int d^2\mathbf{q} \int dk \int d\tilde{\omega} \frac{\tilde{\omega}(k\tilde{\omega} + ak^2)}{\hbar\zeta(k)} \frac{\zeta(k)}{(g(k)^2 + \zeta(k)^2)} \left(\mathrm{sgn}(\tilde{\omega})\coth(\frac{A\tilde{\omega}}{2k_BT}) - 1\right) \\ \approx \; & \frac{\alpha s^2 \hbar A^2}{2(2\pi)^8\hbar^2} \int d^2\mathbf{q} \int dk \int d\tilde{\omega} \frac{\tilde{\omega}(k\tilde{\omega} + ak^2)}{\hbar\zeta(k)} \pi \left(\frac{\delta(k - k_0^+)}{|g'(k_0^+)|} + \frac{\delta(k - k_0^-)}{|g'(k_0^-)|}\right) \\ & \times \left(\mathrm{sgn}(\tilde{\omega})\coth(\frac{A\tilde{\omega}}{2k_BT}) - 1\right) \; , \end{aligned} \tag{3.41}$$

where in the last step we have used the identity $\delta(g(k)) = \sum_i \frac{\delta(k-k_i)}{|g'(k_i)|}$, where $k_i = k_0^\pm$ are the roots resulting from $g(k) = 0$. Thus,

$$k_0^\pm = \tilde{\chi}(-\tilde{\omega} + \tilde{H})a \pm \sqrt{\tilde{\chi}^2(-\tilde{\omega} + \tilde{H})^2a^2 - (\mathbf{q}^2 + \tilde{K} - \tilde{\chi}(-\tilde{\omega} + \tilde{H})^2)} \; ; \tag{3.42}$$

$$|g'(k_0^{+/-})| = \sqrt{\tilde{\chi}^2(-\tilde{\omega} + \tilde{H})^2a^2 - (\mathbf{q}^2 + \tilde{K} - \tilde{\chi}(-\tilde{\omega} + \tilde{H})^2)} \; . \tag{3.43}$$

After performing the k integral in the above, we obtain

$$\begin{aligned}\langle \hat{\boldsymbol{x}} \cdot \boldsymbol{j}_\epsilon \rangle &= \frac{\pi\alpha s^2\hbar A^2}{2(2\pi)^8\hbar^2}\int d^2\mathbf{q}\int d\tilde{\omega}\tilde{\omega}(\mathrm{sgn}(\tilde{\omega})\coth(\frac{A\tilde{\omega}}{2k_BT})-1)\\ &\times\frac{\Theta[(-\tilde{\omega}+\tilde{H})^2-(\mathbf{q}^2+\tilde{K})/(\tilde{\chi}^2a^2+\tilde{\chi})]}{\sqrt{\tilde{\chi}^2(-\tilde{\omega}+\tilde{H})^2a^2-(\mathbf{q}^2+\tilde{K}-\tilde{\chi}(-\tilde{\omega}+\tilde{H})^2)}}\\ &\times\left[\frac{\tilde{\omega}}{\hbar}(\frac{k_0^+}{\zeta(k_0^+)}+\frac{k_0^-}{\zeta(k_0^-)})+\frac{a}{\hbar}(\frac{(k_0^+)^2}{\zeta(k_0^+)}+\frac{(k_0^-)^2}{\zeta(k_0^-)})\right]. \end{aligned} \tag{3.44}$$

Let us insert Eq. 3.35, Eq. 3.43, Eq. 3.42 into Eq. 3.44, and expand everything to the leading order in a, since we are interested in the linear response of the magnetic system. Therefore, we obtain

$$\begin{aligned}&\langle \hat{\boldsymbol{x}} \cdot \boldsymbol{j}_\epsilon \rangle\\ =\ & \frac{\pi\alpha s^2\hbar A^2}{2(2\pi)^8\hbar^2}\int d^2\mathbf{q}\int d\tilde{\omega}\tilde{\omega}\left(\mathrm{sgn}(\tilde{\omega})\coth(\frac{A\tilde{\omega}}{2k_BT})-1\right)\\ &\times\frac{2a\Theta[(-\tilde{\omega}+\tilde{H})^2-(\mathbf{q}^2+\tilde{K})/\tilde{\chi}]}{\alpha^2\tilde{\omega}\hbar\sqrt{-(\mathbf{q}^2+\tilde{K}-\tilde{\chi}(-\tilde{\omega}+\tilde{H})^2)}}\\ &\times\left[\beta\left(\tilde{\chi}(\tilde{H}-\tilde{\omega})^2-\tilde{K}^2-q^2\right)+\alpha\left(\tilde{\chi}\tilde{H}(\tilde{H}-\tilde{\omega})-\tilde{K}-q^2\right)\right], \end{aligned} \tag{3.45}$$

where there is still a two-fold integral over the wave vector $\mathbf{q}$. Transforming the integral over $\mathbf{q}$ inside Eq. 3.45 by defining $W \equiv \tilde{K}+\mathbf{q}^2$ and performing the integration over W, we have

$$\begin{aligned}&\langle \hat{\boldsymbol{x}} \cdot \boldsymbol{j}_\epsilon \rangle\\ =\ & \frac{a\pi s^2A^2}{(2\pi)^7\hbar^2}\int d\tilde{\omega}(\mathrm{sgn}(\tilde{\omega})\coth(\frac{A\tilde{\omega}}{2k_BT})-1)\sqrt{\tilde{\chi}(\tilde{H}-\tilde{\omega})^2-\tilde{K}}\Theta[\tilde{\chi}(-\tilde{\omega}+\tilde{H})^2-\tilde{K}]\\ &\times\frac{\tilde{\chi}(\tilde{H}-\tilde{\omega})\big(\tilde{H}(\alpha+\beta)+\tilde{\omega}(2\alpha-\beta)\big)-\tilde{K}(\alpha+\beta)}{3\alpha}. \end{aligned} \tag{3.46}$$

To make the integral over $\tilde{\omega}$ above dimensionless, we introduce the dimensionless variable y such that $\tilde{\omega} \equiv 2k_BTy/A$, and also switch $\tilde{H}, \tilde{\chi}, \tilde{K}$ to the following dimensionless variables,

$$H_p \equiv \tilde{H}\frac{A}{2k_BT},\ \chi_p \equiv \tilde{\chi}\frac{2k_BT}{A},\ K_p \equiv \tilde{K}\frac{A}{2k_BT}. \tag{3.47}$$

Therefore the magnon energy current is transformed into the form as

$$\begin{aligned}&\langle \hat{\boldsymbol{x}} \cdot \boldsymbol{j}_\epsilon \rangle\\ =\ & \frac{a\pi s^2A^2}{3(2\pi)^7\hbar^2}\left(\frac{2k_BT}{A}\right)^{\frac{5}{2}}(\chi_p)^{\frac{3}{2}}\int dy(\mathrm{sgn}(y)\coth(y)-1)\sqrt{(H_p-y)^2-\frac{K_p}{\chi_p}}\\ &\times\Big[(-2+\frac{\beta}{\alpha})(H_p-y)^2+3H_p(H_p-y)-(1+\frac{\beta}{\alpha})\frac{K_p}{\chi_p}\Big]\Theta[\chi_p(H_p-y)^2-K_p]. \end{aligned} \tag{3.48}$$

The result Eq. 3.48 is one of the main analytical results of this chapter. The final integral over the dimensionless variable y, which is actually integrating over the magnon frequency, will be evaluated in the next section.

3.3.2 Spin Current

The expression for the spin current is found by rewriting the equation of motion for the magnetization density $\boldsymbol{m}$ as a continuity equation for spin density, i.e.,

$$\frac{ds_z}{dt} + \nabla \cdot \boldsymbol{j}_s^z = 0 \ , \tag{3.49}$$

where the spin density is given by $s_z = s\hbar m_z$. This result defines the spin current $\boldsymbol{j}_s^z$. Since the magnetic field is applied in the z-direction, we are only interested in the dynamics of z-component of the spin density. From the equations of motion we find

$$\boldsymbol{j}_s^z = \hbar s \left(\frac{A}{\hbar} (\mathrm{Im}[n^* \nabla n]) + \mathrm{Re}[\boldsymbol{v}_s (m n^*)] \right) \ , \tag{3.50}$$

in which the first term is due to exchange interaction, and the second is an advective contribution. Note that the latter term does not contribute because we take the spin susceptibility to be small. This expression is evaluated in a similar way as the expression for the energy current. By using Eq. 3.4 and Eq. 3.5, we ultimately obtain for the thermally-averaged spin current that flows in the x-direction as

$$\langle \hat{\boldsymbol{x}} \cdot \boldsymbol{j}_s^z \rangle = \frac{sA}{2(2\pi)^8} \int d\omega \int d^2\mathbf{q} \int dk \frac{k \alpha s \hbar \omega / \tanh(\hbar\omega / 2k_B T)}{|Ak^2 + (\beta \hbar i - 2\chi\hbar(-\hbar\omega + H_z)) v_{sx} k + \mu_0^2|^2} \ , \tag{3.51}$$

where μ_0 is defined as in Eq. 3.33. Performing the integral over k and $\mathbf{q}$ as done in the previous section, and treating the thermal fluctuations according to Eq. 3.38 we find

$$\begin{aligned} &\langle \hat{\boldsymbol{x}} \cdot \boldsymbol{j}_s^z \rangle \\ = \ & \frac{2s^2 a \pi A}{(2\pi)^7 \hbar} \int d\tilde{\omega} \frac{\mathrm{sgn}(\tilde{\omega}) \coth(\frac{A\tilde{\omega}}{2k_B T}) - 1}{\tilde{\omega}} \frac{3\alpha\tilde{\chi}\tilde{\omega}(\tilde{H} - \tilde{\omega}) + \beta\left(\tilde{\chi}(-\tilde{\omega} + \tilde{H})^2 - \tilde{K}\right)}{3\alpha} \\ & \times \sqrt{\tilde{\chi}(\tilde{H} - \tilde{\omega})^2 - \tilde{K}} \Theta[\tilde{\chi}(-\tilde{\omega} + \tilde{H})^2 - \tilde{K}] \ , \end{aligned} \tag{3.52}$$

which is an integral over the precession frequency of the two magnon modes and will be left for further discussion in the next section.

3.4 Numerical Results and Discussion

In this section, we present results for the temperature dependence of both magnon energy and spin current when the external magnetic field is zero, and discuss the scenario when the magnetic field is finite but smaller than the critical field for the spin-flop phase transition. We also report numerical results on the dependence on different physical parameters.

3.4.1 Energy Transport

Magnetic Field Dependence

We first calculate the dependence of the magnon energy current on the dimensionless external magnetic field H_z/k_BT. The results are shown in Fig. 3.2. Similar to the case for ferromagnets [130], the energy current does not vanish when the external magnetic field is taken to be zero, since the contributions from the two different AFM magnon modes with opposite polarizations add up for the energy current. In the case with non-zero magnetic field, the degeneracy between the two magnons modes is lifted. We note that the magnitude of the magnon energy current in the direction of charge current increases monotonically with the magnetic field until the spin-flop field is reached.

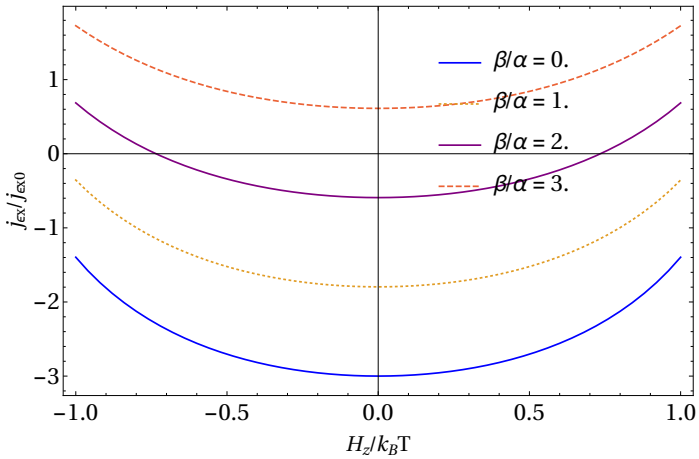

Fig. 3.2: Magnetic field dependence of the magnon energy current for $H_z/k_BT \in [-1, 1]$ and $\sqrt{\frac{Kz}{\chi}}/k_BT = 1.13$. Here the normalization is $j_{\epsilon x0} = \frac{s^2(k_BT)^4 v_{sx}}{24\pi^6\hbar}\left(\frac{\chi}{A}\right)^{3/2}$.

To understand the magnetic field dependence of the magnon energy current, we perform a Taylor expansion around zero magnetic field of the energy current, and keep the terms up to the quadratic order in the dimensionless magnetic field H_p

$$\langle \hat{\boldsymbol{x}} \cdot \boldsymbol{j}_\epsilon \rangle \equiv j_{\epsilon,0} + j_{\epsilon,2} + \mathcal{O}(H_p^4) \ , \tag{3.53}$$

where we defined the zero-order and the quadratic order term as $j_{\epsilon,0}$ and $j_{\epsilon,2}$, which are respectively given by

$$\begin{aligned} j_{\epsilon,0} \quad &\equiv \quad 4f_e(T)\,(\chi_p)^{\frac{3}{2}} \int_{\sqrt{K_p/\chi_p}}^{+\infty} dy' n_B(2y') \sqrt{y'^2 - (K_p/\chi_p)} \\ &\quad \times \Big[-(2y'^2 + \frac{K_p}{\chi_p}) + \frac{\beta}{\alpha}\left(y'^2 - (K_p/\chi_p)\right) \Big] \ ; \end{aligned} \tag{3.54}$$

$$j_{\epsilon,2} \quad \equiv \quad 24f_e(T)\,(\chi_p)^{\frac{3}{2}} \int_{\sqrt{K_p/\chi_p}}^{+\infty} dy' n_B(2y') \sqrt{y'^2 - (K_p/\chi_p)}\,(n_B(2y') + 1)\, y' H_p^2 \ . \tag{3.55}$$

The temperature dependent prefactor $f_e(T)$ is defined by $f_e(T) \equiv \frac{a\pi s^2 A^2}{3(2\pi)^7\hbar^2}(\frac{2k_BT}{A})^{\frac{5}{2}}$, and $n_B(x)$ denotes the Bose distribution function as $n_B(x) \equiv 1/(e^x - 1)$. The zeroth-order contribution as displayed in Eq. 3.54 has a term proportional to β/α. This shows that the energy current changes sign when we tune the ratio β/α from zero to some large value while fixing the external magnetic field. Note that the quadratic order term does not depend on β/α. When taking a small spin-flop field strength compared with the thermal energy, the quadratic order term becomes proportional to $\left(\frac{2k_BT}{A}\right)^{\frac{5}{2}}(\chi_p)^{\frac{3}{2}} H_p^2 \sim (k_BT)^2 H_z^2$. Therefore, the deviation of the magnon energy current from the one at the zero magnetic field point acquires a temperature dependence to the second order.

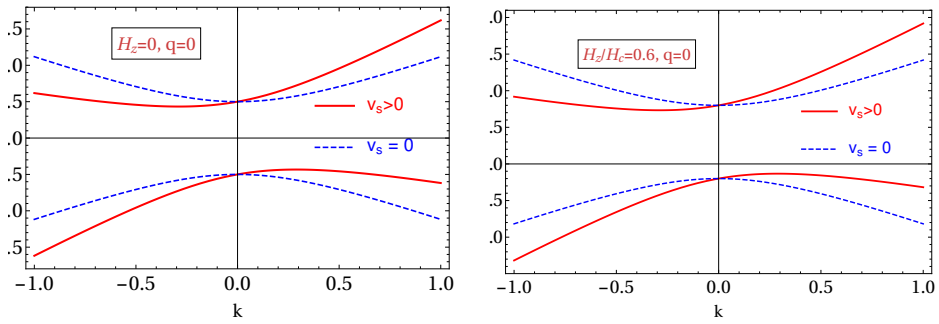

(a) $H_z = 0$ (b) $H_z \neq 0$

Fig. 3.3: Magnon dispersion relation of the antiferromagnet for different magnetic fields . The red solid curve denotes the case where an electrical current flows in the $\hat{x}$ direction, while the blue dashed curve denotes the one in the absence of an electrical current. Here $\alpha = 0, \beta = 0$.

The finite magnon energy current driven by a charge current in the absence of an external magnetic field can be understood with the energy dispersion of magnons in Eq. 3.20, which is plotted in Fig. 3.3. We have two different modes of antiferromagnetic magnons, one precesses in the anti-clockwise orientation, say $\omega^{(+)}$, the other precesses in the clockwise orientation, say $\omega^{(-)}$. They carry the same amount of magnon energy $\hbar|\omega^{\pm}|$ due to the degeneracy. The v_s-term in the dispersion plays the role of a Doppler shift for the two magnon modes, and both anti-clockwise and clockwise polarized modes shift in the same direction in momentum space. Thus the energy currents carried by the two branches of magnons add up together, giving rise to a finite magnon current when the external magnetic field H_z is vanishing, as the results in Fig. 3.4(b) demonstrates.

Temperature dependence

We plot the magnon energy current for various β/α as a function of dimensionless temperature defined as $T^* = \frac{k_BT}{\sqrt{K_z/\chi}}$ in Fig. 3.4.

Firstly, taking the derivative of the magnon energy current with respect to the β/α

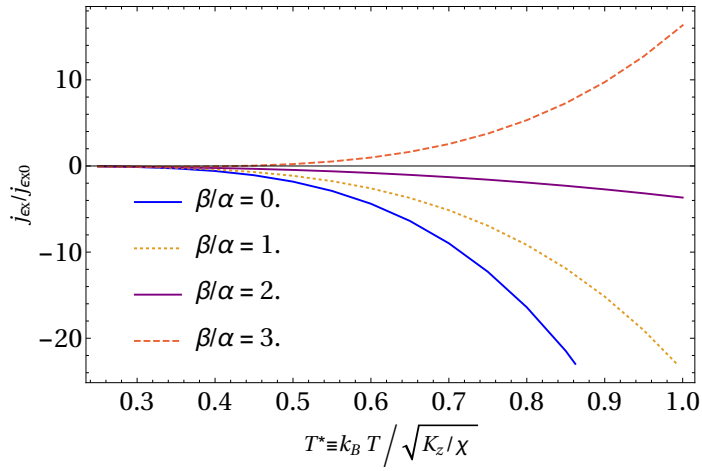

(a) $H_z/H_c = 0.5$

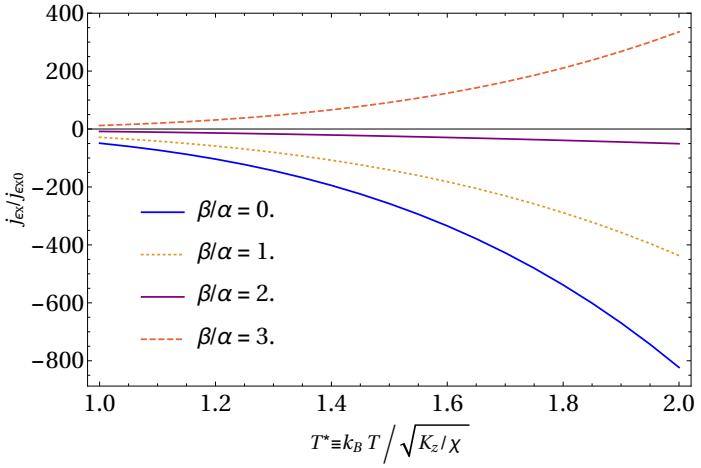

(b) $H_z = 0$

Fig. 3.4: Temperature dependence of the magnon energy current for different magnetic fields and different temperature range. Here $j_{\epsilon x0} = \frac{s^2 K_z^2 v_{sx}}{384\pi^6 \chi^2 \hbar} \left(\frac{\chi}{A}\right)^{3/2}$.

ratio gives,

$$\begin{aligned} &\frac{\partial \langle \hat{\boldsymbol{x}} \cdot \boldsymbol{j}_\epsilon \rangle}{\partial(\beta/\alpha)} \\ &= f_e(T) \chi_p^{3/2} \int_{\sqrt{K_p/\chi_p}}^{\infty} dy' \Big[n_B(2(y' + H_p)) + n_B(2(y' - H_p)) \Big] \left(y'^2 - \frac{K_p}{\chi_p} \right)^{3/2} . \end{aligned} \tag{3.56}$$

Therefore $\frac{\partial \langle \hat{\boldsymbol{x}} \cdot \boldsymbol{j}_\epsilon \rangle}{\partial(\beta/\alpha)}$ has the same sign as v_s, and a larger value of β/α increases the magnon energy current.

Taking the high temperature limit where $H_c/k_BT \to 0$ and also taking the magnetic field to zero gives,

$$\langle \hat{\boldsymbol{x}} \cdot \boldsymbol{j}_\epsilon \rangle|_{H_c/k_BT\to 0, H_z=0} = (\frac{\beta}{\alpha} - 2)\frac{s^2 a}{360(2\pi)^2\hbar^2}(\frac{\chi^3}{A})^{1/2}(k_BT)^4 \ . \tag{3.57}$$

In this limit, the magnon energy current gets a sign change when we tune the parameter around $\beta/\alpha = 2$, which is consistent with Fig. 3.4(b).

From Eq. 3.57 we extract the magnon-drag contribution to the Peltier coefficient in antiferromagnetic metal, which is proportional to the fourth order of temperature at zero magnetic field:

$$\Pi_m|_{H_c/k_BT\to 0, H_z=0} \propto T^4 \ . \tag{3.58}$$

Furthermore, from the Kelvin relation [11], we conclude that the magnon-drag thermopower acquires a cubic temperature dependence.

3.4.2 Spin Transport

Magnetic Field Dependence

We now consider the spin current, starting from the expression in Eq. 3.52. Switching to the dimensionless variables defined in Eq. 3.47 gives the spin current as

$$\begin{aligned} \langle \hat{x} \cdot \boldsymbol{j}_s^z \rangle \ &= \ f_s(T)(\chi_p)^{\frac{3}{2}} \int dy \frac{\mathrm{sgn}(y)\coth(y) - 1}{y} \sqrt{(y - H_p)^2 - (K_p/\chi_p)} \\ &\quad \times \big[(\frac{\beta}{\alpha} - 3)(y - H_p)^2 + 3H_p(H_p - y) - \frac{\beta}{\alpha}\frac{K_p}{\chi_p}\big] \ , \end{aligned} \tag{3.59}$$

where we defined the prefactor $f_s(T) \equiv \frac{2\pi a s^2 A}{3(2\pi)^7\hbar}(\frac{2k_BT}{A})^{\frac{3}{2}}$. When $H_p = 0$, the integrand on the right side is an odd function of the integration variable, showing that the contributions from the two magnon modes cancel each other in the degenerate case, thus giving a vanishing spin current,

$$\langle \hat{\boldsymbol{x}} \cdot \boldsymbol{j}_s^z \rangle|_{\tilde{H}=0} = 0 \ . \tag{3.60}$$

In the absence of an external magnetic field, the magnetization $M_z \propto \langle m^* n \rangle$ vanishes as well due to the degeneracy of the magnons with opposite spin. To have a complete picture of the magnetic field dependence, we plot the spin current as a function of external magnetic field, which is displayed in Fig. 3.5. From this figure we observe that, there are different signs of spin current around the zero magnetic field point for different values of β/α.

In order to analytically study the response to a finite magnetic field, we perform an expansion of the spin current around the zero magnetic field to the linear order, which

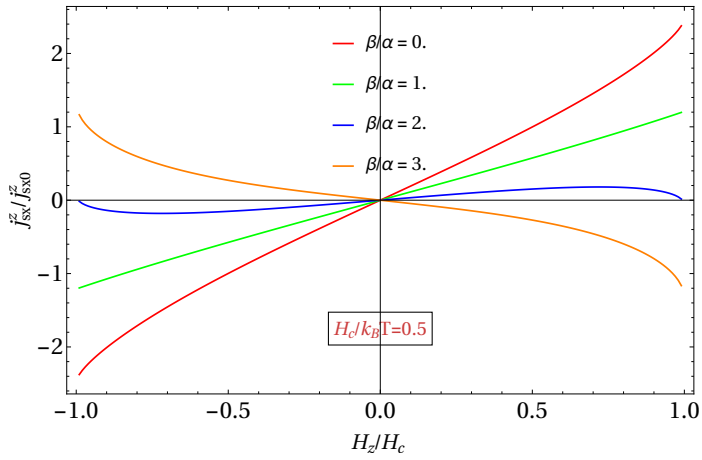

Fig. 3.5: Magnetic field dependence of the magnon spin current for various ratio of β/α, where $j^z_{\rm sx0} \equiv \frac{s^2(k_BT)^3 v_{\rm sx}}{24\pi^6}\left(\frac{\chi}{A}\right)^{3/2}$.

gives,

$$\begin{aligned}\langle \hat{x}\cdot \boldsymbol{j}^z_s\rangle &= 4f_s(T)(\chi_p)^{\frac{3}{2}}\int_{\sqrt{K_p/\chi_p}}^{+\infty} dy' n_B(2y')\sqrt{y'^2-(K_p/\chi_p)} \\ &\quad\times\left[6y'\left(n_B(2y')+1\right)+\frac{\beta}{\alpha}\left(\frac{K_p/\chi_p}{y'^2}-1\right)\left(1+2y'\left(n_B(2y')+1\right)\right)\right]H_p \\ &\quad+\mathcal{O}(H_p^2)\ . \end{aligned} \tag{3.61}$$

As given in Eq. 3.61, the linear response to magnetic field combines two competing terms in the integrand with opposite signs. The first contribution does not depend on β and comes from the adiabatic torque, while the second contribution is proportional to the ratio β/α and reflects the addition spin current flow due to the non-adiabatic torque. The competition between these two contributions qualitatively gives what we observe from Fig. 3.5.

When the field approaches the spin-flop field, i.e., when $|H_p| \to \sqrt{K_p/\chi_p}$, one of the magnon modes becomes gapless, thus dominating the spin transport. This results in a divergence of the spin current

$$\begin{aligned}&\langle \hat{x}\cdot \boldsymbol{j}^z_s\rangle|_{|H_p|\to\sqrt{K_p/\chi_p}} \\ =\ & 2f_s(T)\int_{\sqrt{K_p/\chi_p}}^{+\infty} dy' n_B(2(y'-H_p))\sqrt{y'^2-(K_p/\chi_p)}\left[3y'-\frac{\beta}{\alpha}\frac{y'^2-\frac{K_p}{\chi_p}}{y'-H_p}\right] \\ \sim\ & \frac{3-2\frac{\beta}{\alpha}}{|H_c-H_z|^{1/2}}\ . \end{aligned} \tag{3.62}$$

Therefore we have a strong enhancement for the spin current around the spin-flop field. As seen from Eq. 3.62, this enhancement of spin current depends on the ratio

β/α, and changes sign at $\beta/\alpha = 3/2$. A similar enhancement was found in previous work for a thin-film insulating antiferromagnet [135]. Here, we find that the ratio β/α strongly affects the sign of the divergence, which is unique for a metallic system.

Temperature Dependence

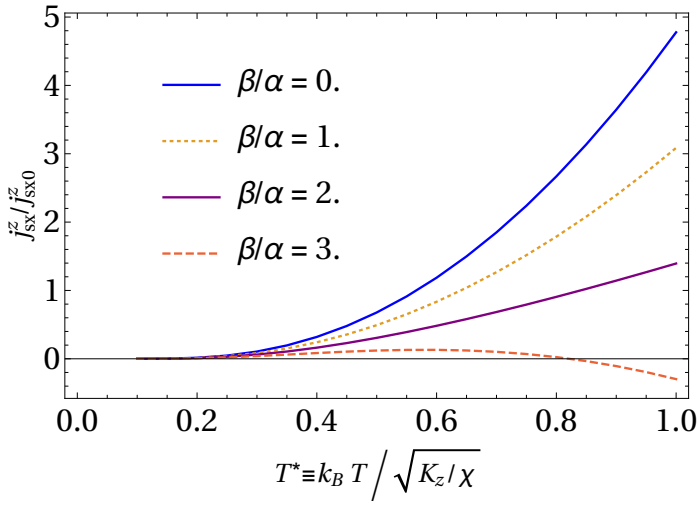

(a) $H_z/H_c = 0.4$

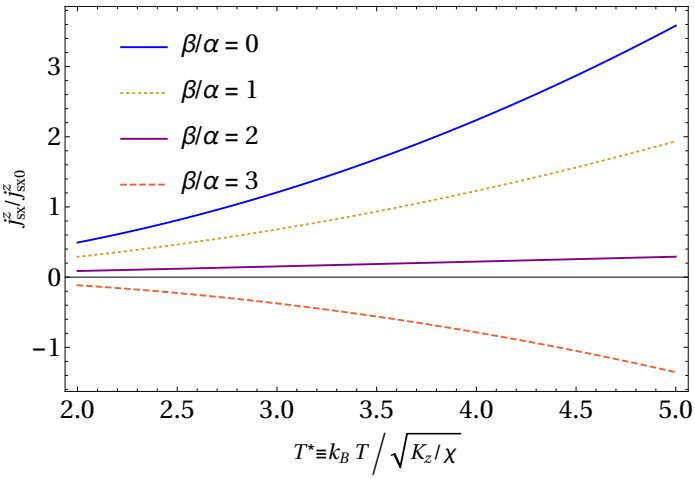

(b) $H_z/H_c = 0.004$

Fig. 3.6: Temperature dependence of the magnon spin current for various ratio of β/α for different external magnetic fields, where $j^z_{\rm sx0} \equiv \frac{s^2 v_{\rm sx}}{6(2\pi)^6}\left(\frac{K_z}{A}\right)^{3/2}$.

Taking the derivative of the magnon spin current with respect to β/α gives

$$\begin{aligned}&\frac{\partial\langle\hat{\boldsymbol{x}}\cdot\boldsymbol{j}_s^z\rangle}{\partial(\beta/\alpha)}\\ =\;& 2f_s(T)\chi_p^{3/2}\int_{\sqrt{K_p/\chi_p}}^{\infty}dy'\Big(\frac{n_B(2(y'+H_p))}{y'+H_p}-\frac{n_B(2(y'-H_p))}{y'-H_p}\Big)\left(y'^2-\frac{K_p}{\chi_p}\right)^{3/2}.\end{aligned} \tag{3.63}$$

As shown in Eq. 3.63, increasing β/α linearly decreases the magnon spin current, as shown in Fig. 3.6(a), where we have plotted the magnon spin current as a function of the dimensionless temperature T^*.

With Eq. 3.61 as the magnon spin current in linear response to an external magnetic field, we further take the high temperature limit where $K_p/\chi_p \to 0$, and obtain its quadratic temperature dependence as

$$\langle\hat{x}\cdot\boldsymbol{j}_s^z\rangle|_{H_c/k_BT\to 0,H_z=0} = (2-\frac{\beta}{\alpha})\frac{s^2a}{6(2\pi)^4\hbar}\left(\frac{\chi^3}{A}\right)^{1/2}(k_BT)^2H_z\,. \tag{3.64}$$

Therefore, we obtain the condition for sign change at $\beta/\alpha = 2$, which is exactly the same as for the magnon energy current, given in Eq. 3.57. Finally we plot Fig. 3.6(b) for the numerical result of the spin current at high temperatures for various values of β/α, which qualitatively matches with the sign change point given in Eq. 3.64.

3.5 Conclusion

In summary, we have presented a stochastic Landau-Lifshitz-Gilbert formalism for magnon drag in a three-dimensional antiferromagnetic metal. The numerical results demonstrate that tailoring the sign and magnitude of an easy-axis AFM metal based Peltier-cooling device might be possible via the manipulation of the external magnetic field, the dissipation parameter β, and the anisotropy K_z. Recently A. Prakash *et al.* [146] observed that ferromagnetic magnons impede the phonon-electron drag dynamics at the metallic interface in the heterostructure of normal-metal |YIG, thus making the phonon drag peaks in thermopower of the Ag, Al films vanish, and the thermopower in Pt film decrease. In order to fully unlock the potential of AFM based thermoelectric device studied here, a future work should investigate the influence of magnetization dynamics on the phonon-electron drag in an AFM metal. Finally, the use of antiferromagnets in thermoelectric devices could avoid the interaction between neighboring modules due to the inherent stray fields in ferromagnetic device, thus making a high integration density of tunable thermocouples possible.

We also found that the magnon spin current driven by the electric current is strongly enhanced near the spin-flop transition. This result may motivate the use of antiferromagnetic metals as tunable sources of spin current, for example, in heterostructures with normal metals.

Appendix

3.A Derivation of the Density of Magnon Energy Current

In this appendix, we present the derivation of the energy current expression. Taking the time derivative of the energy density of Eq. 3.25, we get

$$\begin{aligned}\frac{\partial E}{\partial t} &= \frac{s}{2}\Big[\frac{1}{\chi}(\frac{\partial m^*}{\partial t}m+\frac{\partial m}{\partial t}m^*)+A(\nabla(\frac{\partial n^*}{\partial t})\nabla n+\nabla n^*\nabla(\frac{\partial n}{\partial t}))\\ &\quad +K_z(\frac{\partial n^*}{\partial t}n+\frac{\partial n}{\partial t}n^*)+H_z(\frac{\partial n^*}{\partial t}m+n^*\frac{\partial m}{\partial t}+\frac{\partial m^*}{\partial t}n+m^*\frac{\partial n}{\partial t})\\ &\quad -i\hbar\big[\frac{\partial m^*}{\partial t}(\boldsymbol{v}_s\cdot\nabla)n+m^*(\boldsymbol{v}_s\cdot\nabla)\frac{\partial n}{\partial t}-\frac{\partial m}{\partial t}(\boldsymbol{v}_s\cdot\nabla)n^*-m(\boldsymbol{v}_s\cdot\nabla)\frac{\partial n^*}{\partial t}\big]\Big]\ ;\\ &\equiv (\frac{\partial E}{\partial t})_0+(\frac{\partial E}{\partial t})_J\ , \end{aligned} \tag{3.65}$$

where we defined

$$\begin{aligned}(\frac{\partial E}{\partial t})_0 &= \frac{s}{2}\Big[\frac{1}{\chi}(\frac{\partial m^*}{\partial t}m+\frac{\partial m}{\partial t}m^*)+A(\nabla(\frac{\partial n^*}{\partial t})\nabla n+\nabla n^*\nabla(\frac{\partial n}{\partial t}))\\ &\quad +K_z(\frac{\partial n^*}{\partial t}n+\frac{\partial n}{\partial t}n^*)+H_z(\frac{\partial n^*}{\partial t}m+n^*\frac{\partial m}{\partial t}+\frac{\partial m^*}{\partial t}n+m^*\frac{\partial n}{\partial t})\Big]\ , \end{aligned} \tag{3.66}$$

and

$$(\frac{\partial E}{\partial t})_J = \frac{-i\hbar s}{2}\big[\frac{\partial m^*}{\partial t}(\boldsymbol{v}_s\cdot\nabla)n+m^*(\boldsymbol{v}_s\cdot\nabla)\frac{\partial n}{\partial t}-\frac{\partial m}{\partial t}(\boldsymbol{v}_s\cdot\nabla)n^*-m(\boldsymbol{v}_s\cdot\nabla)\frac{\partial n^*}{\partial t}\big]\ . \tag{3.67}$$

From the equations of motion in Eq. 3.8, we have,

$$\begin{aligned}\frac{\partial n}{\partial t} &= \frac{H_z n+\frac{m}{\chi}-i\hbar(\boldsymbol{v}_s\cdot\nabla)n}{i\hbar}\ ;\\ \frac{\partial m}{\partial t} &= \frac{H_z m+K_z n-A\nabla^2 n-i(\boldsymbol{v}_s\cdot\nabla)m}{i\hbar}\ ;\\ \frac{\partial n^*}{\partial t} &= \frac{H_z n^*+\frac{m^*}{\chi}+i\hbar(\boldsymbol{v}_s\cdot\nabla)n^*}{-i\hbar}\ ;\\ \frac{\partial m^*}{\partial t} &= \frac{H_z m^*+K_z n^*-A\nabla^2 n^*+i(\boldsymbol{v}_s\cdot\nabla)m^*}{-i\hbar}\ , \end{aligned} \tag{3.68}$$

with which we transform Eq. 3.66 and Eq. 3.67 to find,

$$
\begin{aligned}
&(\frac{\partial E}{\partial t})_0 \\
= \;& \frac{s}{2}\Bigg[\frac{1}{\chi}\big[\frac{K_z}{i\hbar}(m^*n-n^*m)+\frac{A}{i\hbar}(m\nabla^2n^*-m^*\nabla^2n)-m(\boldsymbol{v}_s\cdot\nabla)m^*-m^*(\boldsymbol{v}_s\cdot\nabla)m\big] \\
&+\frac{A}{i\hbar\chi}\big(\nabla n^*\nabla m-\nabla m^*\nabla n\big)-A\big[\nabla((\boldsymbol{v}_s\cdot\nabla)n^*)\nabla n+\nabla n^*\nabla((\boldsymbol{v}_s\cdot\nabla)n)\big] \\
&+\frac{K_z}{i\hbar\chi}(mn^*-m^*n)-K_z\big[n(\boldsymbol{v}_s\cdot\nabla)n^*+n^*(\boldsymbol{v}_s\cdot\nabla)n\big] \\
&-H_z(n^*(\boldsymbol{v}_s\cdot\nabla)m+n(\boldsymbol{v}_s\cdot\nabla)m^*)+\frac{H_zA}{i\hbar}(n\nabla^2n^*-n^*\nabla^2n) \\
&-H_z\big(m^*(\boldsymbol{v}_s\cdot\nabla)n+m(\boldsymbol{v}_s\cdot\nabla)n^*\big)\Bigg]\;; \\
= \;& \frac{s}{2}\Bigg[\frac{A}{i\hbar\chi}\nabla\cdot\big(m\nabla n^*-m^*\nabla n\big)+\frac{AH_z}{i\hbar}\nabla\cdot\big(n\nabla n^*-n^*\nabla n\big)-\frac{1}{\chi}\nabla\cdot\big(\boldsymbol{v}_sm^*m\big) \\
&-A\nabla\cdot\big(\boldsymbol{v}_s\nabla n^*\nabla n\big)-K_z\nabla\cdot\big(\boldsymbol{v}_sn^*n\big)-H_z\nabla\cdot\big(\boldsymbol{v}_s(mn^*+m^*n)\big)\Bigg]\;. \qquad (3.69)
\end{aligned}
$$

and,

$$
\begin{aligned}
&(\frac{\partial E}{\partial t})_J \\
= \;& \frac{s}{2}\Bigg[-\big[\frac{1}{\chi}\big(m^*(\boldsymbol{v}_s\cdot\nabla)m+m(\boldsymbol{v}_s\cdot\nabla)m^*\big)-K_z(n^*(\boldsymbol{v}_s\cdot\nabla)n+n(\boldsymbol{v}_s\cdot\nabla)n^*) \\
&+A\left(\nabla^2n^*(\boldsymbol{v}_s\cdot\nabla)n+\nabla^2n(\boldsymbol{v}_s\cdot\nabla)n^*\right)\big]-i\hbar\left(m^*(\boldsymbol{v}_s\cdot\nabla)^2n-m(\boldsymbol{v}_s\cdot\nabla)^2n^*\right) \\
&+i\hbar\left((\boldsymbol{v}_s\cdot\nabla)m^*(\boldsymbol{v}_s\cdot\nabla)n-(\boldsymbol{v}_s\cdot\nabla)m(\boldsymbol{v}_s\cdot\nabla)n^*\right)\Bigg]\;; \\
= \;& \frac{s}{2}\big[-\frac{1}{\chi}\nabla\cdot\big(\boldsymbol{v}_sm^*m\big)+K_z\nabla\cdot\big(\boldsymbol{v}_sn^*n\big)-A\left(\nabla n^*(\boldsymbol{v}_s\cdot\nabla)n+\nabla n(\boldsymbol{v}_s\cdot\nabla)n^*\right) \\
&+A\nabla\cdot\big(\boldsymbol{v}_s\nabla n^*\cdot\nabla n\big)+i\hbar\nabla\cdot\left(\boldsymbol{v}_s\left[n(\boldsymbol{v}_s\cdot\nabla)m^*-m(\boldsymbol{v}_s\cdot\nabla)n^*\right]\right)\Big]\;; \\
\approx \;& \frac{s}{2}\big[-\frac{1}{\chi}\nabla\cdot\big(\boldsymbol{v}_sm^*m\big)+K_z\nabla\cdot\big(\boldsymbol{v}_sn^*n\big)-A\left(\nabla n^*(\boldsymbol{v}_s\cdot\nabla)n+\nabla n(\boldsymbol{v}_s\cdot\nabla)n^*\right) \\
&+A\nabla\cdot\big(\boldsymbol{v}_s\nabla n^*\cdot\nabla n\big)\big]\;, \qquad (3.70)
\end{aligned}
$$

where in the last step we neglected the term

$$
i\hbar\nabla\cdot\left(\boldsymbol{v}_s\left[n(\boldsymbol{v}_s\cdot\nabla)m^*-m(\boldsymbol{v}_s\cdot\nabla)n^*\right]\right)\;,
$$

since only the linear response to external electric field is considered in this chapter and this term is a second-order term. Combining the results from Eq. 3.69 and Eq. 3.70,

we get the time derivative of the energy density,

$$\begin{aligned}\frac{\partial E}{\partial t} &= \frac{s}{2}\Big[\frac{A}{i\hbar\chi}\nabla\cdot\big(m\nabla n^* - m^*\nabla n\big) + \frac{AH_z}{i\hbar}\nabla\cdot\big(n\nabla n^* - n^*\nabla n\big) \\ &\quad -A\nabla\cdot\big(\boldsymbol{v}_s\nabla n^*\nabla n\big) - K_z\nabla\cdot\big(\boldsymbol{v}_s n^* n\big) - H_z\nabla\cdot\big(\boldsymbol{v}_s(mn^* + m^* n)\big) \\ &\quad -\frac{2}{\chi}\nabla\cdot\big(\boldsymbol{v}_s m^* m\big) + K_z\nabla\cdot\big(\boldsymbol{v}_s n^* n\big) - A\left(\nabla n^*(\boldsymbol{v}_s\cdot\nabla)n + \nabla n(\boldsymbol{v}_s\cdot\nabla)n^*\right) \\ &\quad +A\nabla\cdot\big(\boldsymbol{v}_s\nabla n^*\cdot\nabla n\big)\Big]\,, \end{aligned} \tag{3.71}$$

which is plugged back to the continuity equation as in Eq. 3.26 to obtain the magnon energy current

$$\begin{aligned}\boldsymbol{j}_\epsilon &= \frac{s}{2}\Big(\frac{A}{\chi\hbar}\left(m\nabla n^* - m^*\nabla n\right) + iH_z\frac{A}{\hbar}\left(n\nabla n^* - n^*\nabla n\right) + \frac{2\boldsymbol{v}_s}{\chi}(m^* m) \\ &\quad +A\left(\nabla n^*(\boldsymbol{v}_s\cdot\nabla)n + \nabla n(\boldsymbol{v}_s\cdot\nabla)n^*\right) + H_z\boldsymbol{v}_s(mn^* + m^* n)\Big)\,. \end{aligned} \tag{3.72}$$

Furthermore, replacing the H_z above with the relations from the equation of motion in Eq. 3.68 gives

$$\begin{aligned}\boldsymbol{j}_\epsilon &= \frac{s}{2}\Big(-A(\frac{\partial n}{\partial t}\nabla n^* + \frac{\partial n^*}{\partial t}\nabla n) + A\big(\nabla n^*(\boldsymbol{v}_s\cdot\nabla)n + \nabla n(\boldsymbol{v}_s\cdot\nabla)n^*\big) \\ &\quad +\frac{2}{\chi}(\boldsymbol{v}_s m^* m) - i\boldsymbol{v}_s\hbar\left(m(\frac{\partial n^*}{\partial t} + (\boldsymbol{v}_s\cdot\nabla)n^*) - m^*(\frac{\partial n}{\partial t} + (\boldsymbol{v}_s\cdot\nabla)n)\right)\Big)\,. \end{aligned} \tag{3.73}$$

Finally, we neglect the second-order term in $\boldsymbol{v}_s$ in the expression above, which yields

$$\begin{aligned}\boldsymbol{j}_\epsilon &= \frac{s}{2}\Big[-A(\frac{\partial n}{\partial t}\nabla n^* + \frac{\partial n^*}{\partial t}\nabla n) + A\big(\nabla n^*(\boldsymbol{v}_s\cdot\nabla)n + \nabla n(\boldsymbol{v}_s\cdot\nabla)n^*\big) \\ &\quad +\frac{2}{\chi}(\boldsymbol{v}_s m^* m) - i\boldsymbol{v}_s\hbar\left(m\frac{\partial n^*}{\partial t} - m^*\frac{\partial n}{\partial t}\right)\Big]\,. \end{aligned} \tag{3.74}$$

3.B Higher-order Total Magnetization Dependent Contributions to the Magnon Energy Current

First we rewrite the relation between the transverse Néel order parameter and the stochastic field as

$$n(k,\mathbf{q},\omega) = \frac{h_n^b(k,\mathbf{q},\omega) - \frac{\chi(-\hbar\omega + H_z + \hbar v_{sx}k)h_m^b(k,\mathbf{q},\omega)}{(1-i\alpha\hbar\chi\omega)}}{Ak^2 + (\beta\hbar i - \frac{2\chi\hbar(-\hbar\omega+H_z)}{1-i\alpha\hbar\chi\omega})v_{sx}k + \mu^2}\,, \tag{3.75}$$

where

$$\mu^2 \equiv Aq^2 + K_z - i\alpha\hbar\omega - \chi\frac{(-\hbar\omega + H_z)^2 + (\hbar v_{sx}k)^2}{1 - i\alpha\hbar\chi\omega}\,, \tag{3.76}$$

and we have taken $v_{sy}q_y + v_{sz}q_z \to 0$,

Since the Gilbert damping α is small and the spin susceptibility χ is also tiny, we get $\alpha\chi\hbar\omega \ll 1$, therefore,

$$n(k,\mathbf{q},\omega) = \frac{h_n^b(k,\mathbf{q},\omega) - \chi(-\hbar\omega + H_z + \hbar v_{sx}k)h_m^b(k,\mathbf{q},\omega)}{Ak^2 + (\beta\hbar i - 2\chi\hbar(-\hbar\omega + H_z))v_{sx}k + \mu_0^2} \ . \tag{3.77}$$

Similarly, from the equation of motion in Eq. 3.17, we obtained the relation between magnetization density m and the stochastic field h as the following,

$$\begin{aligned} & m(k,\mathbf{q},\omega) \\ = & \frac{1}{(-\hbar\omega + H_z + \hbar v_{sx}k)^2 - (\frac{1}{\chi} - i\alpha\hbar\omega)\left(K_z - i\alpha\hbar\omega + A(\mathbf{q}^2 + k^2) + i\beta\hbar v_{sx}k\right)} \\ & \times[(-\hbar\omega + H_z + \hbar v_{sx}k)h_n^b(k,\mathbf{q},\omega) \\ & -(K_z - i\alpha\hbar\omega + A(\mathbf{q}^2 + k^2) + i\beta\hbar v_{sx}k)h_m^b(k,\mathbf{q},\omega)] \ . \end{aligned} \tag{3.78}$$

which can be simplified to,

$$\begin{aligned} & m(k,\mathbf{q},\omega) \\ = & \frac{-\chi}{Ak^2 + (\beta\hbar i - 2\chi\hbar(-\hbar\omega + H_z))v_{sx}k + \mu_0^2}[(-\hbar\omega + H_z + \hbar v_{sx}k)h_n^b(k,\mathbf{q},\omega) \\ & -(K_z - i\alpha\hbar\omega + A(\mathbf{q}^2 + k^2) + i\beta\hbar v_{sx}k)h_m^b(k,\mathbf{q},\omega)] \ , \end{aligned} \tag{3.79}$$

where

$$\mu_0^2 \approx Aq^2 + K_z - i\alpha\hbar\omega - \chi\left((-\hbar\omega + H_z)^2 + (\hbar v_{sx}k)^2\right) \ . \tag{3.80}$$

With Eq. 3.79 and Eq. 3.77, the corresponding correlation functions are found,

$$\begin{aligned} & \langle m^*(k,\mathbf{q},\omega)n(k',\mathbf{q}',\omega')\rangle \\ = & \frac{(-\chi)(-\hbar\omega + H_z + \hbar v_{sx}k)(1 + \chi(K_z + A(\mathbf{q}^2 + k^2)))\alpha s\hbar\omega}{|Ak^2 + (\beta\hbar i - 2\chi\hbar(-\hbar\omega + H_z))\, v_{sx}k + \mu_0^2|^2 2(2\pi)^2} \\ & \times\delta(k - k')\delta(\mathbf{q} - \mathbf{q}')\delta(\omega - \omega')/\tanh(\frac{\hbar\omega}{2k_BT}) \ ; \end{aligned} \tag{3.81}$$

$$\begin{aligned} & \langle m^*(k,\mathbf{q},\omega)m(k',\mathbf{q}',\omega')\rangle \\ = & \chi^2\frac{\left(|-\hbar\omega + H_z + \hbar v_{sx}k|^2 + |K_z + A(\mathbf{q}^2 + k^2)|^2\right)\alpha s\hbar\omega}{|Ak^2 + (\beta\hbar i - 2\chi\hbar(-\hbar\omega + H_z))\, v_{sx}k + \mu_0^2|^2 2(2\pi)^2} \\ & \times\delta(k - k')\delta(\mathbf{q} - \mathbf{q}')\delta(\omega - \omega')/\tanh(\frac{\hbar\omega}{2k_BT}) \ . \end{aligned} \tag{3.82}$$

Finally we obtain other contribution to the magnon energy current $\langle \boldsymbol{j}_\epsilon\rangle_{III}$ and $\langle \boldsymbol{j}_\epsilon\rangle_{IV}$

as below,

$$
\begin{aligned}
& \langle \boldsymbol{j}_\epsilon \rangle_{III} \\
\equiv\ & \frac{s}{2}\langle -\frac{2}{\chi}(\boldsymbol{v}_s m^* m)\rangle \\
=\ & \frac{s v_{sx}}{\chi(2\pi)^6}\int d^3\boldsymbol{Q}\int d\omega \int d^3\boldsymbol{Q}'\int d\omega' \langle m^*(\boldsymbol{Q},\omega)m(\boldsymbol{Q}',\omega')\rangle e^{-i(\boldsymbol{Q}-\boldsymbol{Q}')\cdot\boldsymbol{r}} e^{i(\omega-\omega')t}\ ; \\
=\ & \frac{s^2 v_{sx}\chi}{(2\pi)^6}\int d^3\boldsymbol{Q}\int d\omega \frac{\alpha\hbar\omega}{|\,(K_z - i\alpha\hbar\omega + A(\mathbf{q}^2+k^2) - i\beta\hbar v_{sx}k)\,|^2 2(2\pi)^2\tanh(\frac{\hbar\omega}{2k_BT})} \\
& \times\left[(-\hbar\omega + H_z + \hbar v_{sx}k)^2 + |K_z - i\alpha\hbar\omega + A(\mathbf{q}^2+k^2) - i\beta\hbar v_{sx}k|^2\right]\ , \qquad (3.83)
\end{aligned}
$$

$$
\begin{aligned}
& \langle \boldsymbol{j}_\epsilon \rangle_{IV} \\
\equiv\ & \langle i\boldsymbol{v}_s\hbar(m\frac{\partial n^*}{\partial t} - m^*\frac{\partial n}{\partial t})\rangle \\
=\ & \frac{s}{2}\frac{v_{sx}\hbar}{(2\pi)^6}\int d^3\boldsymbol{Q}\int d\omega\int d^3\boldsymbol{Q}'\int d\omega'(-2\omega')e^{-i(\boldsymbol{Q}-\boldsymbol{Q}')\cdot\boldsymbol{r}}e^{i(\omega-\omega')t} \\
& \langle m(\boldsymbol{Q},\omega)n^*(\boldsymbol{Q}',\omega') + m^*(\boldsymbol{Q},\omega)n(\boldsymbol{Q}',\omega')\rangle\ ; \\
=\ & \frac{-s v_{sx}\hbar}{(2\pi)^6}\int d^3\boldsymbol{Q}\int d\omega\frac{(-2\omega)\chi(-\hbar\omega + H_z + \hbar v_{sx}k)\alpha s\hbar\omega}{2(2\pi)^2\tanh(\frac{\hbar\omega}{2k_BT})} \\
& \mathrm{Re}[\frac{1}{\left(Ak^2 + (\beta\hbar i - 2\chi\hbar(-\hbar\omega + H_z))v_{sx}k + \mu^2\right)} \\
& \times\frac{1}{\left(K_z + i\alpha\hbar\omega + A(\mathbf{q}^2+k^2) + i\beta\hbar v_{sx}k\right)}]\ . \qquad (3.84)
\end{aligned}
$$

By taking the small spin susceptibility limit $\chi \to 0$, the contributions to the energy current from related correlations are found to be vanish, therefore the last line in Eq. 3.27 of the energy current expression can be neglected.

CHAPTER 4

Effect of Ellipticity and Dissipation on Magnon Tunneling in a Magnon Spin Valve

In this chapter, we study the alignment-dependent thermal transport mediated by magnons across a junction consisting of two ferromagnetic insulators, which mimics the structure of the recently proposed magnon spin valve. Under the assumption of a weak exchange coupling between the two insulators, the ellipticity of magnon precession is found to open a channel for magnons to tunnel through in the anti-parallel configuration. We define the magnon thermal conductance (MTC) ratio to determine the relative change of thermal conductance due to a change of magnetization orientation from a parallel configuration to an anti-parallel one. The dependence of the MTC ratio on both the Gilbert damping and ellipticity is studied for various parameters, revealing a clear difference in their roles in magnon thermal transport. Finally this theoretical study indicates the potential of a thermal diode based on a ferromagnetic junction that is tunable by magnetic field[3].

4.1 Introduction

Spintronics based on spin-polarized charge currents has been witnessing remarkable achievements in information storage technology since the discovery of giant magnetoresistance effect (GMR) in antiferromagnetically coupled Fe/Cr super-lattices [147, 148].

[3]This chapter and its appendix are based on J. Zheng, S.A. Bender, A. Rückriegel and R. A. Duine, *Effect of Ellipticity and Dissipation on Magnon Tunneling in Magnon Spin Valve*, in preparation. R.A. Duine conceived the project. J. Zheng did all the analytic derivations, performed the related numerical calculations, and wrote the manuscript with the help from all co-authors. All other authors contributed via discussions.

This effect is known to arise from the spin-dependent transmission of the conduction electrons. The quanta of collective excitation in magnetically ordered system, magnons, can carry pure spin currents that lead to, e.g., the spin-Seebeck effect [42]. In magnetic insulators, these pure spin currents may dramatically improve the power efficiency of logic devices due to the absence of Joule heating [34, 149, 150], and become candidates for information carriers in neuromorphic computing [151, 152].

Magnon spin valve, the insulating analogue of the spin valve, has become a fascinating topic for both experimental and theoretical communities. H. Wu *et al* have observed the magnon valve effect in a heterostructure made of two ferromagnetic insulators (YIG) separated by a nonmagnetic heavy metal layer [82]. The magnon valve ratio, which measures the relative change of spin current signal due to a change of magnetization orientations, is observed to decreases significantly as the temperature drops. In a recent theoretical work, a Green's function formalism for the magnon tunneling driven by temperature bias in a ferromagnetic junction has been developed and applied to compute the diode property of the tunneling spin current [153]. A key aspect of this study is the consideration of many-body magnon interaction that is exploited for the emergence of rectification and negative differential spin Seebeck effects. Furthermore, a tunable spin Seebeck diode based on the magnetic junction structure in which the tunneling spin current can be turned on and off by controlling the magnetization orientation has also been theoretically studied [154].

In this work, we study the alignment-dependent thermal transport across a heterostructure consisting of two ferromagnet insulators, where the ferromagnets have their magnetization orientations aligned parallel or anti-parallel to each other, as schematically shown in Fig. 4.1. The ferromagnetic insulators act as reservoirs for magnons, which can be driven coherently by ferromagnetic resonance or incoherently with an electrical or thermal bias [155]. In order to investigate the factors affecting the magnon tunneling for different alignment configurations, we will focus on the effect of the ellipticity of magnon precession, which is usually caused by anisotropies, and also the Gilbert damping, which is a phenomenological parameter characterizing the decay of magnons. The ellipticity of precession has been shown to strongly affect the parametric excitation of magnons in ferromagnetic resonance experiments [156], and plays a role in Rayleigh-Jeans condensation of pumped magnons in thin-film ferromagnets [157]. Meanwhile, a low Gilbert damping has also been demonstrated to result in a long-distance spin transport in magnetic materials, such as yttrium iron garnet [3]. However, neither damping nor ellipticity has been considered for magnon tunneling inside the magnetic spin valve structure proposed here.

In our model, magnons tunnel between the ferromagnets due to exchange coupling at the magnetic interface and they carry heat currents in response to an applied temperature gradient which is normal to the interface. As illustrated in Fig. 4.1, the temperatures of the left reservoir and the right reservoir are denoted as T_L, T_R separately. The magnon chemical potential for the two insulators are denoted as μ_L, μ_R. In each insulator, the magnon chemical potential is considered to be homogeneous in the bulk and could be in principle different from each other.

When the temperature difference between the two insulators is small compared to the average temperature, the magnon heat current flowing from the left to the right can

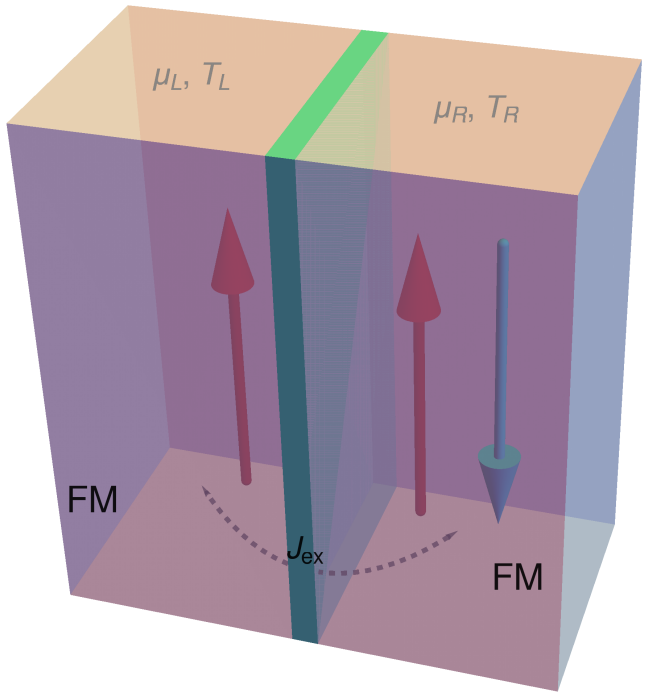

Fig. 4.1: Illustration of a magnetic junction consisting of two ferromagnetic insulators, which interact with each other with weak exchange coupling J_{ex}. The left(right) insulator has temperature $T_L(T_R)$ and spin accumulation $\mu_L(\mu_R)$. The layer in green is a non-magnetic insulator, and is thin enough for the magnons to tunnel through. The left insulator is the fixed layer, with the red arrow denoting an up spin, while the right insulator is a free layer, who magnetization can be tuned from a parallel configuration (denoted in the red arrow) to an anti-parallel configuration (denoted in the blue arrow).

be expressed as

$$j_m = (T_L - T_R)\kappa \ , \tag{4.1}$$

where κ is the interfacial tunneling thermal conductance, which is the central quantity to be computed in this chapter. Furthermore, we define a quantity named *magneto-thermal conductance* (MTC) ratio derived from the thermal conductance as below,

$$\text{MTC} = \frac{\kappa_P - \kappa_{AP}}{\kappa_P} \ , \tag{4.2}$$

where $\kappa_P(\kappa_{AP})$ is the thermal conductance for the parallel (anti-parallel) configuration. For the circularly polarized magnons with zero Gilbert damping, our calculation shows that the tunneling is forbidden in the anti-parallel configuration, which yields MTC = 1, while the tunneling of elliptical magnons makes the MTC ratio deviate from one. As seen from numerical calculations, the MTC ratio for the magnetic junction proposed here is strongly affected by the transverse anisotropy and the resulting precession ellipticity of magnons. In addition, a finite Gilbert damping is also found to enhance the influence of ellipticity.

The remainder of the chapter is organized as follows. In Section 4.2, we introduce the Fermi's Golden Rule (FGR) method [158] and derive the magnon tunneling currents for both parallel and anti-parallel configurations for the circularly polarized magnons without dissipation. In Section 4.3, we analytically derive the magnon tunneling currents with the consideration of precession ellipticity and Gilbert damping, whose effects on the magnon density of states (DOS) are visualized and discussed. In Section 4.4, we demonstrate the results by numerically calculating the tunneling thermal conductance and consider the dependences of MTC ratio on the magnon ellipticity and dissipation. In Section 4.5, we conclude our theoretical findings.

4.2 Deriving the Tunneling Current with Fermi's Golden Rule for Circular Magnons

4.2.1 Model Hamiltonian

The magnetization dynamics in the bulk of each insulator with a cubic lattice is modeled by the following Hamiltonian,

$$\mathcal{H}_F = -\frac{J}{2}\sum_l\sum_{\boldsymbol{\delta}} \boldsymbol{S}_l\cdot\boldsymbol{S}_{l,\boldsymbol{\delta}} - \Delta\sum_l S_l^z - \frac{K_z}{2}\sum_l (S_l^z)^2 \ , \tag{4.3}$$

where we defined the Zeeman energy $\Delta \equiv g\mu_B h$, and h is the external magnetic field, K_z is the strength of easy-axis anisotropy ($K_z > 0$), $\boldsymbol{S}$ is the localized magnetic moment, l denotes the site number of a certain lattice point. Here we only consider the nearest neighboring coupling, $\boldsymbol{\delta}$ is one vector to one of the nearest neighbors, and $\boldsymbol{S}_{l,\boldsymbol{\delta}}$ denotes one nearest neighbor to the magnetic moment at site l. With the magnetic order parameter pointing in the +z direction ($h > 0$), we performs the Holstein-Primakoff (HP) transformation,

$$S_l^+ = (2S)^{1/2} b_l, S_l^- = (2S)^{1/2} b_l^\dagger, S_l^z = S - b_l^\dagger b_l \ , \tag{4.4}$$

where $b_l(b_l^\dagger)$ annihilates (creates) a circular magnon on site l. Keeping the anisotropy terms to the linear order in $b^\dagger b$, we get,

$$H_{aniso} = -\frac{K_z}{2}\sum_l (S - b_l^\dagger b_l)^2 \approx K_z S\sum_l b_l^\dagger b_l \ . \tag{4.5}$$

Therefore the Hamiltonian becomes,

$$\begin{aligned}\mathcal{H}_F &= \sum_l \Big[-\frac{J}{2}S\sum_{\boldsymbol{\delta}} (b_l^\dagger b_{l,\boldsymbol{\delta}} + b_l b_{l,\boldsymbol{\delta}}^\dagger) + (\Delta + SK) b_l^\dagger b_l + \frac{J}{2}S\sum_{\boldsymbol{\delta}} \Big(b_{l,\boldsymbol{\delta}}^\dagger b_{l,\boldsymbol{\delta}} + b_l^\dagger b_l \Big) \Big] \\ &= \sum_{\boldsymbol{k}} \epsilon_{\boldsymbol{k}}^{(+)} b_{\boldsymbol{k}}^\dagger b_{\boldsymbol{k}} \ ,\end{aligned} \tag{4.6}$$

where the energy dispersion reads,

$$\epsilon_{\boldsymbol{k}}^{(+)} \equiv \Delta + JSa^2\boldsymbol{k}^2 + SK_z \ . \tag{4.7}$$

Here $b_{\boldsymbol{k}} = \sum_l \frac{1}{\sqrt{\Lambda}} e^{-i\boldsymbol{k}\cdot\boldsymbol{x}_l} b_l$ is the Fourier transform of b_l, Λ is the number of sites in the insulator, $\boldsymbol{x}_l$ is the position vector of the magnetic moment at site l, a is the lattice constant, s is the saturation spin density.

When the magnetic order parameter points in the $-$z direction ($h < 0$), we apply the HP transformation as,

$$S_l^+ = (2S)^{1/2} b_l^\dagger, \quad S_l^- = (2S)^{1/2} b_l, \quad S_l^z = -S + b_l^\dagger b_l \ , \tag{4.8}$$

and obtain for the Hamiltonian,

$$\mathcal{H}_F = \sum_{\boldsymbol{k}} \epsilon_{\boldsymbol{k}}^{(-)} b_{\boldsymbol{k}}^\dagger b_{\boldsymbol{k}} \ , \tag{4.9}$$

where

$$\epsilon_{\boldsymbol{k}}^{(-)} \equiv -\Delta + JSa^2\boldsymbol{k}^2 + SK_z \ . \tag{4.10}$$

To summarize, the Hamiltonian for the bulk insulator can be written as,

$$\mathcal{H}_F = \sum_{\boldsymbol{k}} \epsilon_{\boldsymbol{k}}^{(\pm)} b_{\boldsymbol{k}}^\dagger b_{\boldsymbol{k}} \ . \tag{4.11}$$

The interface interaction between the two ferromagnetic insulators is modeled as the 3D coupling Hamiltonian below,

$$\mathcal{H}_C = -\int J_{ex}(\boldsymbol{r}, \boldsymbol{r}') S_L(\boldsymbol{r}) \cdot S_R(\boldsymbol{r}') d^3\boldsymbol{r} d^3\boldsymbol{r}' \ , \tag{4.12}$$

where the localized magnetic moments are denoted as S_L and S_R in the left and right ferromagnetic insulator, and $\boldsymbol{r}$ denotes the position vector in the magnet. Here we assume a weak exchange coupling, and the coupling function $J_{ex}(\boldsymbol{r}, \boldsymbol{r}')$ will give finite values only when the locations of both spins $\boldsymbol{r}, \boldsymbol{r}'$ are close to the interface.

4.2.2 Tunneling Calculation for the Parallel Configuration

Taking the HP transformation as in Eq. 4.4 and neglecting the constant term and higher-order terms, one has the coupling Hamiltonian,

$$\mathcal{H}_C = -S \int J_{ex}(\boldsymbol{r}, \boldsymbol{r}') \left(b_L^\dagger(\boldsymbol{r}) b_R(\boldsymbol{r}') + b_R^\dagger(\boldsymbol{r}') b_L(\boldsymbol{r}) \right) d^3\boldsymbol{r} d^3\boldsymbol{r}' \ . \tag{4.13}$$

We have also neglected the energy shift due to the interfacial exchange coupling which is small compared to the bulk exchange interactions and anisotropy.

We define,

$$\begin{aligned} \mathcal{H}_{C,L} &= -S \int J_{ex}(\boldsymbol{r}, \boldsymbol{r}') \left(b_L^\dagger(\boldsymbol{r}) b_R(\boldsymbol{r}') \right) d^3\boldsymbol{r} d^3\boldsymbol{r}' \ , \\ \mathcal{H}_{C,R} &= -S \int J_{ex}(\boldsymbol{r}, \boldsymbol{r}') \left(b_R^\dagger(\boldsymbol{r}') b_L(\boldsymbol{r}) \right) d^3\boldsymbol{r} d^3\boldsymbol{r}' \ . \end{aligned} \tag{4.14}$$

Here $b^\dagger_{L/R}(b_{L/R})$ denotes the creation (annihilation) operator of a magnon on the interface. $\mathcal{H}_{C,L}$ describes the process in which a magnon tunnels from right to left, and $\mathcal{H}_{C,R}$ describing the process in which a magnon tunnels from left to right. Therefore $\mathcal{H}_C \equiv \mathcal{H}_{C,L} + \mathcal{H}_{C,R}$ changes the magnon numbers in the left and right insulators, and induces the process of magnon tunneling.

Performing the Fourier transform as

$$a(\boldsymbol{r}) = V \int \frac{d^3\boldsymbol{k}}{(2\pi)^3} e^{i\boldsymbol{k}\cdot\boldsymbol{r}} a_{\boldsymbol{k}} \ , \tag{4.15}$$

where V denotes the system volume, we get

$$\begin{aligned} \mathcal{H}_{C,L} &= -S(V_L V_R)^2 \int \frac{d^3\boldsymbol{k}_1}{(2\pi)^3}\frac{d^3\boldsymbol{k}_2}{(2\pi)^3} J_{ex}^{\boldsymbol{k}_1,-\boldsymbol{k}_2} b^\dagger_{\boldsymbol{k}_1,L} b_{\boldsymbol{k}_2,R} \ , \\ \mathcal{H}_{C,R} &= -S(V_L V_R)^2 \int \frac{d^3\boldsymbol{k}_1}{(2\pi)^3}\frac{d^3\boldsymbol{k}_2}{(2\pi)^3} J_{ex}^{-\boldsymbol{k}_1,\boldsymbol{k}_2} b^\dagger_{\boldsymbol{k}_2,R} b_{\boldsymbol{k}_1,L} \ . \end{aligned} \tag{4.16}$$

Here V_L, V_R denote the volume of the left and right insulators respectively.

Transition Rate Calculation with Fermi's Golden Rule

The transition rate for a magnon tunneling through the interface can be written as below with the tunneling Hamiltonian as a perturbation, similar to the treatment in modeling Coloumb blockade of a quantum dot system [159, 158]:

$$\Gamma = \frac{2\pi}{\hbar} \sum_{i,f} |\langle f|H_C|i\rangle|^2 W_i \delta(E_i - E_f) \ , \tag{4.17}$$

where $|f\rangle$ and $|i\rangle$ denote the final state and initial state for the transition separately, W_i denotes the thermal probability of initial state i, which can be decomposed as $W_i = W_{i,1}(n_L)W_{i,2}(n_R)$, where n_L and n_R are the magnon occupation numbers of the left (L) and right (R) insulator, and $W_{i,v}(n)$ is given by

$$W_{i,v}(n) = \frac{e^{-n(\epsilon_v - \mu_v)\beta}}{\sum_j e^{-j(\epsilon_v-\mu_v)\beta}} \ . \tag{4.18}$$

Here μ_v denotes the magnon chemical potential of a magnon with energy ϵ_v, and $\beta \equiv 1/k_B T$. In the following we consider the energy conservation condition and the specification of the initial/final states with Fock states.

Energy conservation condition during tunneling — Assuming an ensemble where we have a ferromagnetic junction where there are n_L magnons with $\boldsymbol{k}_1$ as the wave vector in the left insulator and n_R magnons with $\boldsymbol{k}_2$ as the wave vector in the right insulator, the total energy of the initial state i before the tunneling is expressed as

$$E_i = n_L \epsilon_{\boldsymbol{k}_1} + n_R \epsilon_{\boldsymbol{k}_2} \ . \tag{4.19}$$

The final state for the tunneling process described by $\mathcal{H}_{C,L}$ is labeled as f_+ and the final state for the process described by $\mathcal{H}_{C,R}$ as f_-. The total energies of the two different final states are given separately as

$$\begin{aligned} E_{f_+} &= (n_L+1)\epsilon_{\boldsymbol{k}_1} + (n_R-1)\epsilon_{\boldsymbol{k}_2} \ , \\ E_{f_-} &= (n_L-1)\epsilon_{\boldsymbol{k}_1} + (n_R+1)\epsilon_{\boldsymbol{k}_2} \ . \end{aligned} \tag{4.20}$$

Energy conservation, $\epsilon_{\boldsymbol{k}_1} = \epsilon_{\boldsymbol{k}_2}$, appears as a a Dirac-delta function factor in the calculation of transition rate from Fermi's Golden Rule.

Initial state and final state — The initial state is a product state of the Fock state in each insulator, $|i\rangle = |n_L\rangle|n_R\rangle$, where $|n_L\rangle$ and $|n_R\rangle$ denote the Fock states for magnons in the left terminal and right terminal respectively, and is written as $|n_{L/R}\rangle = \Pi_{\boldsymbol{k}}|n_{\boldsymbol{k},L/R}\rangle$. However there is only one certain final state contributing to the matrix element of tunneling Hamiltonian for each type of tunneling processes specified by $\mathcal{H}_{C,L}$ and $\mathcal{H}_{C,R}$.

The final state after a transition that a magnon tunnels from the right insulator to the left insulator, $|f_+\rangle \propto b^\dagger_{\boldsymbol{k}_1,L} b_{\boldsymbol{k}_2,R}|i\rangle$, is normalized to,

$$|f_+\rangle = \frac{1}{\sqrt{n_{\boldsymbol{k}_2,R}(n_{\boldsymbol{k}_1,L}+1)}} b^\dagger_{\boldsymbol{k}_1,L} b_{\boldsymbol{k}_2,R}|i\rangle \ . \tag{4.21}$$

Similarly, the final state for the process where a magnon tunnels from left to right becomes,

$$|f_-\rangle = \frac{1}{\sqrt{n_{\boldsymbol{k}_1,L}(n_{\boldsymbol{k}_2,R}+1)}} b^\dagger_{\boldsymbol{k}_2,R} b_{\boldsymbol{k}_1,L}|i\rangle \ . \tag{4.22}$$

The summation over the final states in Eq. 4.17 is taken as the summation over the corresponding momenta, which is later converted into an integration over momenta. To constrain the final state $|f\rangle$ to the one given by Eq. 4.21 or Eq. 4.22 for a given tunneling between magnons parameterized by wave vector $\boldsymbol{k}_1$ and $\boldsymbol{k}_2$, we have

$$\sum_f \to V_L V_R \int \frac{d^3\boldsymbol{p}_1 d^3\boldsymbol{p}_2}{(2\pi)^6} \delta^3(\boldsymbol{p}_1 - \boldsymbol{k}_1)\delta^3(\boldsymbol{p}_2 - \boldsymbol{k}_2) \ , \tag{4.23}$$

where $\boldsymbol{p}_1$ and $\boldsymbol{p}_2$ are momenta of the magnons of the tunneling. Combining the results given above, especially Eq. 4.18, Eq. 4.23, the transition rate for the tunneling process

described by $\mathcal{H}_{C,L}$ can be calculated as,

$$\begin{aligned}
&\Gamma_L \\
\equiv\ & \frac{2\pi}{\hbar}\sum_{i,f}|\langle f|S(V_LV_R)^2\int\frac{d^3\boldsymbol{k}_1}{(2\pi)^3}\frac{d^3\boldsymbol{k}_2}{(2\pi)^3}J_{ex}^{\boldsymbol{k}_1,-\boldsymbol{k}_2}b^\dagger_{\boldsymbol{k}_1,L}b_{\boldsymbol{k}_2,R}|i\rangle|^2W_i\delta(E_i-E_f) \\
=\ & \frac{2\pi}{\hbar}S^2(V_LV_R)^5\sum_i\int\frac{d^3\boldsymbol{p}_1d^3\boldsymbol{p}_2}{(2\pi)^6}W_i\delta(\epsilon_{\boldsymbol{k}_1,L}-\epsilon_{\boldsymbol{k}_2,R}) \\
&\times|\langle i|\int\frac{d^3\boldsymbol{k}_1}{(2\pi)^3}\frac{d^3\boldsymbol{k}_2}{(2\pi)^3}J_{ex}^{\boldsymbol{k}_1,-\boldsymbol{k}_2}\frac{\delta^3(\boldsymbol{p}_1-\boldsymbol{k}_1)\delta^3(\boldsymbol{p}_2-\boldsymbol{k}_2)}{\sqrt{n_{\boldsymbol{k}_2,R}(n_{\boldsymbol{k}_1,L}+1)}}b^\dagger_{\boldsymbol{p}_2,R}b_{\boldsymbol{p}_1,L}b^\dagger_{\boldsymbol{k}_1,L}b_{\boldsymbol{k}_2,R}|i\rangle|^2 \\
=\ & \frac{2\pi}{\hbar}S^2(V_LV_R)^5\int\frac{d^3\boldsymbol{p}_1d^3\boldsymbol{p}_2}{(2\pi)^{12}}|J_{ex}^{\boldsymbol{p}_1,-\boldsymbol{p}_2}|^2\delta(\epsilon_{\boldsymbol{p}_1,L}-\epsilon_{\boldsymbol{p}_2,R}) \\
&\times n_B((\epsilon_{\boldsymbol{p}_2,R}-\mu_R)\beta_R)\left(1+n_B((\epsilon_{\boldsymbol{p}_1,L}-\mu_L)\beta_L)\right)\ , \qquad (4.24)
\end{aligned}$$

where we denote the Bose-Einstein distribution function as $n_B(x)\equiv 1/(e^x-1)$. The tunneling rate described by $\mathcal{H}_{C,R}$ is calculated as,

$$\begin{aligned}
&\Gamma_R \\
\equiv\ & \frac{2\pi}{\hbar}\sum_{i,f}|\langle f|S(V_LV_R)^2\int\frac{d^3\boldsymbol{k}_1}{(2\pi)^3}\frac{d^3\boldsymbol{k}_2}{(2\pi)^3}J_{ex}^{-\boldsymbol{k}_1,\boldsymbol{k}_2}b^\dagger_{\boldsymbol{k}_2,R}b_{\boldsymbol{k}_1,L}|i\rangle|^2W_i\delta(E_i-E_f) \\
=\ & \frac{2\pi}{\hbar}S^2(V_LV_R)^5\int\frac{d^3\boldsymbol{p}_1d^3\boldsymbol{p}_2}{(2\pi)^{12}}|J_{ex}^{-\boldsymbol{p}_1,\boldsymbol{p}_2}|^2\delta(\epsilon_{\boldsymbol{p}_1,L}-\epsilon_{\boldsymbol{p}_2,R}) \\
&\times n_B((\epsilon_{\boldsymbol{p}_1,L}-\mu_L)\beta_L)\left(1+n_B((\epsilon_{\boldsymbol{p}_2,R}-\mu_R)\beta_R)\right)\ . \qquad (4.25)
\end{aligned}$$

This defines the momentum resolved transition rate as,

$$\begin{aligned}
&\Gamma_{L,I}(\boldsymbol{p}_1,\boldsymbol{p}_2) \\
=\ & \frac{2\pi}{\hbar}S^2(V_LV_R)^5\frac{|J_{ex}^{\boldsymbol{p}_1,-\boldsymbol{p}_2}|^2}{(2\pi)^6}\delta(\epsilon_{\boldsymbol{p}_1,L}-\epsilon_{\boldsymbol{p}_2,R})n_B((\epsilon_{\boldsymbol{p}_2,R}-\mu_R)\beta_R) \\
&\times\big(1+n_B((\epsilon_{\boldsymbol{p}_1,L}-\mu_L)\beta_L)\big)\ ; \\
&\Gamma_{R,I}(\boldsymbol{p}_1,\boldsymbol{p}_2) \\
=\ & \frac{2\pi}{\hbar}S^2(V_LV_R)^5\frac{|J_{ex}^{-\boldsymbol{p}_1,\boldsymbol{p}_2}|^2}{(2\pi)^6}\delta(\epsilon_{\boldsymbol{p}_1,L}-\epsilon_{\boldsymbol{p}_2,R})n_B((\epsilon_{\boldsymbol{p}_1,L}-\mu_L)\beta_L) \\
&\times\big(1+n_B((\epsilon_{\boldsymbol{p}_2,R}-\mu_R)\beta_R)\big)\ .
\end{aligned} \qquad (4.26)$$

Taking $J_{ex}(\boldsymbol{r},\boldsymbol{r}')=\sum_{\boldsymbol{r}_0}J_{ex,0}\delta_{\boldsymbol{r},\boldsymbol{r}_0}\delta_{\boldsymbol{r}',\boldsymbol{r}_0}$, where $\boldsymbol{r}_0$ denotes the position vector on the interface, its Fourier transform becomes,

$$\begin{aligned}
J_{ex}^{\boldsymbol{k}_1,\boldsymbol{k}_2} &= \sum_{\boldsymbol{r},\boldsymbol{r}'}J_{ex}(\boldsymbol{r},\boldsymbol{r}')e^{i\boldsymbol{k}_1\cdot\boldsymbol{r}+i\boldsymbol{k}_2\cdot\boldsymbol{r}'} \\
&= J_{ex,0}\delta_{\boldsymbol{k}_1,-\boldsymbol{k}_2}\ . \qquad (4.27)
\end{aligned}$$

The momentum dependence of interface coupling above will be removed when taking the limit of a rough interface, which is usually found in realistic systems. By noting

that the Fermi's Golden Rule usually applies to the regime which is far away from the interface, this also can be seen as taking the lowest order contribution in the interface coupling at $\boldsymbol{k} = 0$, which just neglects all the fine details of the interface. Namely, we take the approximation that $J_{ex}^{\boldsymbol{k}_1,\boldsymbol{k}_2} = J_{ex,0}$.

Tunneling current

The energy current from the left FM to the right FM by tunneling of magnons is obtained by summing over all the magnon modes,

$$j_\epsilon^P = \int \frac{d^3\boldsymbol{p}_1 d^3\boldsymbol{p}_2}{(2\pi)^6}\Big(\Gamma_{R,I}(\boldsymbol{p}_1,\boldsymbol{p}_2)\epsilon_{\boldsymbol{p}_2,R} - \Gamma_{L,I}(\boldsymbol{p}_1,\boldsymbol{p}_2)\epsilon_{\boldsymbol{p}_1,L}\Big) . \tag{4.28}$$

Further using the identity $\int_{-\infty}^{\infty} d\epsilon\delta(\epsilon-\epsilon_0) = 1$ gives,

$$j_\epsilon^P = \frac{2\pi}{\hbar}S^2\frac{(V_L V_R)^5}{(2\pi)^6}J_{ex,0}^2\int d\epsilon\epsilon g_L(\epsilon)g_R(\epsilon)\Big[n_B((\epsilon-\mu_L)\beta_L) - n_B((\epsilon-\mu_R)\beta_R)\Big] . \tag{4.29}$$

In agreement with the analytical result by Ref. [153], Eq. 4.29 shows that the magnon tunneling current is determined by the overlap between the magnon density of states of the left and right insulator, and the magnon number density difference between them.

Here we defined the density of states for magnons $g(\epsilon)$ as,

$$g_{L/R}(\epsilon) \equiv \int \frac{d^3\boldsymbol{k}}{(2\pi)^3}\delta(\epsilon - \epsilon_{\boldsymbol{k},L/R}) , \tag{4.30}$$

where the dispersion relation $\epsilon_{\boldsymbol{k},L/R}$ is given as in Eq. 4.11, and the subscript L/R denotes the left (L) or right (R) insulator.

Eq. 4.29 is the expression for the magnon tunneling for the parallel case, next we are going to calculate for the anti-parallel case.

4.2.3 Tunneling Calculation for the Anti-parallel Configuration

We take the HP transformation in Eq. 4.8 to transform the coupling Hamiltonian as given in Eq. 4.12. Therefore we get,

$$\begin{aligned}\mathcal{H}_C^{AP} = & -S\int J_{ex}(\boldsymbol{r},\boldsymbol{r}')\Big(b_L^\dagger(\boldsymbol{r})b_R^\dagger(\boldsymbol{r}') + b_R(\boldsymbol{r}')b_L(\boldsymbol{r}) \\ & + b_L^\dagger(\boldsymbol{r})b_L(\boldsymbol{r}') + b_R^\dagger(\boldsymbol{r}')b_R(\boldsymbol{r})\Big)d^3\boldsymbol{r}d^3\boldsymbol{r}' .\end{aligned} \tag{4.31}$$

Neglecting, as before, the constant term and energy shift due to interfacial exchange interaction, we find the tunneling Hamiltonian written in the following after performing

the Fourier transform given in Eq. 4.15,

$$\begin{aligned}\mathcal{H}_{C,L}^{AP} &= -S(V_L V_R)^2 \int \frac{d^3\boldsymbol{k}_1}{(2\pi)^3}\frac{d^3\boldsymbol{k}_2}{(2\pi)^3} J_{ex}^{\boldsymbol{k}_1,\boldsymbol{k}_2} b_{\boldsymbol{k}_1,L}^{\dagger} b_{\boldsymbol{k}_2,R}^{\dagger} \ , \\ \mathcal{H}_{C,R}^{AP} &= -S(V_L V_R)^2 \int \frac{d^3\boldsymbol{k}_1}{(2\pi)^3}\frac{d^3\boldsymbol{k}_2}{(2\pi)^3} J_{ex}^{-\boldsymbol{k}_1,-\boldsymbol{k}_2} b_{\boldsymbol{k}_1,L} b_{\boldsymbol{k}_2,R} \ , \end{aligned} \tag{4.32}$$

with $\mathcal{H}_{C,L}^{AP}$ describing the tunneling process in which two magnon are created simultaneously in the left and right insulator, and $\mathcal{H}_{C,R}^{AP}$ describing the process where two magnons are annihilated simultaneously.

Transition rates — The transition rate for a magnon tunneling through the interface can be written as,

$$\Gamma^{AP} = \frac{2\pi}{\hbar}\sum_{i,f} |\langle f|H_C^{AP}|i\rangle|^2 W_i \delta(E_i - E_{f^{AP}}) \ , \tag{4.33}$$

where the energy conservation condition for a magnon with energy ϵ_1 to tunnel into a magnon with energy ϵ_2 in the other side is enforced as a a Dirac-delta function as,

$$\begin{aligned}\delta(E_i - E_{f_+^{AP}}) &= \delta(\epsilon_1 + \epsilon_2) \ , \\ \delta(E_i - E_{f_-^{AP}}) &= \delta(\epsilon_1 + \epsilon_2) \ , \end{aligned} \tag{4.34}$$

where $|f\rangle$, $|i\rangle$, W_i have the same definitions as given in the parallel configuration.

The initial state for the ferromagnetic insulating junction can be represented as $|i\rangle = |n_L\rangle|n_R\rangle$, where $|n_L\rangle$ and $|n_R\rangle$ denote the Fock states for magnons in the left insulator and right insulator respectively. The final state which gives a non-zero matrix element of this tunneling Hamiltonian is of a certain form. The normalized final state corresponding to the $\mathcal{H}_{C,L}^{AP}$ process is given as,

$$|f_+^{AP}\rangle = |n_L + 1\rangle|n_R + 1\rangle \ , \tag{4.35}$$

while the one for the $\mathcal{H}_{C,R}^{AP}$ process is

$$|f_-^{AP}\rangle = |n_L - 1\rangle|n_R - 1\rangle \ . \tag{4.36}$$

As done similarly in the parallel configuration, the momentum resolved transition rates for $\mathcal{H}_{C,L}^{AP}$ and $\mathcal{H}_{C,R}^{AP}$ can be derived as,

$$\begin{aligned} &\Gamma_{L,II}(\boldsymbol{p}_1,\boldsymbol{p}_2) \\ =\ & \frac{2\pi}{\hbar} S^2 (V_L V_R)^5 \frac{|J_{ex}^{\boldsymbol{p}_1,\boldsymbol{p}_2}|^2}{(2\pi)^6} \delta(\epsilon_{\boldsymbol{p}_1,L} + \epsilon_{\boldsymbol{p}_2,R}) \big(1 + n_B((\epsilon_{\boldsymbol{p}_2,R} - \mu_R)\beta_R)\big) \\ & \times \big(1 + n_B((\epsilon_{\boldsymbol{p}_1,L} - \mu_L)\beta_L)\big) \ ; \\ &\Gamma_{R,II}(\boldsymbol{p}_1,\boldsymbol{p}_2) \\ =\ & \frac{2\pi}{\hbar} S^2 (V_L V_R)^5 \frac{|J_{ex}^{-\boldsymbol{p}_1,-\boldsymbol{p}_2}|^2}{(2\pi)^6} \delta(\epsilon_{\boldsymbol{p}_1,L} + \epsilon_{\boldsymbol{p}_2,R}) n_B\big((\epsilon_{\boldsymbol{p}_1,L} - \mu_L)\beta_L\big) \\ & \times n_B\big((\epsilon_{\boldsymbol{p}_2,R} - \mu_R)\beta_R\big) \ . \end{aligned} \tag{4.37}$$

Magnon tunneling current — With similar calculations as done for the parallel case, we get the energy current transferred from the left FM to the right FM by summing over all the magnons modes,

$$j_\epsilon^{AP} = \int \frac{d^3\boldsymbol{p}_1 d^3\boldsymbol{p}_2}{(2\pi)^6}\Big(-\Gamma_{R,II}(\boldsymbol{p}_1,\boldsymbol{p}_2)\epsilon_{\boldsymbol{p}_2,R} + \Gamma_{L,II}(\boldsymbol{p}_1,\boldsymbol{p}_2)\epsilon_{\boldsymbol{p}_2,R}\Big) . \quad (4.38)$$

Furthermore we have

$$\begin{aligned} & j_\epsilon^{AP} \\ = \; & \frac{2\pi}{\hbar} S^2 \frac{(V_L V_R)^5}{(2\pi)^6} J_{ex,0}^2 \int d\epsilon(-\epsilon) g_L(\epsilon) g_R(-\epsilon)\Big[n_B((\epsilon-\mu_L)\beta_L) - n_B((\epsilon+\mu_R)\beta_R)\Big] , \end{aligned} \quad (4.39)$$

where $g(\epsilon)$ is the same density of states of magnons as defined in Eq. 4.30.

Performing the momentum integration for both $g_L(\epsilon)$ and $g_R(\epsilon)$ in Eq. 4.30, we derive the density of states as below,

$$g_{L/R}(\epsilon) = \frac{1}{2\pi^2(JSa^2)^{3/2}}\sqrt{\epsilon - (|\Delta_{L/R}| + SK_{z,L/R})}\Theta(\epsilon - (|\Delta_{L/R}| + SK_{z,L/R})) . \quad (4.40)$$

Assuming that the magnitude of external magnetic field and anisotropy are equal for both insulators, we substitute Eq. 4.40 into Eq. 4.39 and get

$$\begin{aligned} & j_\epsilon^{AP} \\ = \; & \frac{2\pi}{\hbar} S^2 \frac{(V_L V_R)^5}{(2\pi)^6} \frac{J_{ex,0}^2}{4\pi^4(JSa^2)^3}\Theta(-(|\Delta| + SK_z)) \\ & \times \int d\epsilon(-\epsilon)\sqrt{\epsilon - (|\Delta| + SK_z)}\sqrt{-\epsilon - (|\Delta| + SK_z)}\Big[n_B((\epsilon-\mu_L)\beta_L) \\ & -n_B((\epsilon+\mu_R)\beta_R)\Big]\Theta((|\Delta| + SK_z)^2 - \epsilon^2) . \end{aligned} \quad (4.41)$$

Therefore, the tunneling energy current j_ϵ^{AP} vanishes since the density of states of both insulators do not overlap with each other in an anti-parallel configuration. Later we will show that by adding dissipation to the magnetic system, the process of magnon tunneling becomes possible again for such configuration.

4.3 Effects of Ellipticity and Damping

In this section we calculate the magnon tunneling current by taking account of precession ellipticity and a finite lifetime of magnons due to the Gilbert damping.

4.3.1 Bogoliubov Transformation and Elliptical Magnons

We add the following anisotropy terms to introduce ellipticity to the precession of spin waves in these two ferromagnetic insulators,

$$H^{xy}_{aniso} = -\frac{1}{2}\sum_l \left[K_x (S^x_l)^2 + K_y (S^y_l)^2\right] \ . \tag{4.42}$$

Taking the HP expansion as defined in Eq. 4.8, we get,

$$H^{xy}_{aniso} \ = \ -\frac{S}{4}\sum_l \left[(K_x - K_y)(b^\dagger_l b^\dagger_l + b_l b_l) + (K_x + K_y)(b^\dagger_l b_l + b_l b^\dagger_l)\right] \ . \tag{4.43}$$

Adding H^{xy}_{aniso} into the original bulk Hamiltonian, we obtain,

$$\begin{aligned}\mathcal{H}_F \ \approx \ & \sum_l \Big[-\frac{J}{2} S \sum_{\boldsymbol{\delta}} (b^\dagger_l b_{l,\boldsymbol{\delta}} + b_l b^\dagger_{l,\boldsymbol{\delta}}) + \frac{J}{2} S \sum_{\boldsymbol{\delta}} (b^\dagger_{l,\boldsymbol{\delta}} b_{l,\boldsymbol{\delta}} + b^\dagger_l b_l) \\ & + \left(|\Delta| + SK_z - \frac{S}{2}(K_x + K_y) \right) b^\dagger_l b_l \Big] - \frac{S}{4}\sum_l (K_x - K_y)(b^\dagger_l b^\dagger_l + b_l b_l) \ ,\end{aligned} \tag{4.44}$$

where we dropped a constant term as done before and $\sum_{\boldsymbol{\delta}}$ is a summation over the vectors to the nearest neighbors of a lattice point.

After Fourier transform, we have the Hamiltonian in the low energy limit,

$$\begin{aligned}\mathcal{H}_F \ = \ & \sum_{\boldsymbol{k}} \left(|\Delta| + JSa^2 \boldsymbol{k}^2 - \frac{S}{2}(K_x + K_y) + SK_z \right) b^\dagger_{\boldsymbol{k}} b_{\boldsymbol{k}} \\ & - \frac{S}{4}\sum_{\boldsymbol{k}} (K_x - K_y)(b^\dagger_{\boldsymbol{k}} b^\dagger_{-\boldsymbol{k}} + b_{\boldsymbol{k}} b_{-\boldsymbol{k}}) \ ,\end{aligned} \tag{4.45}$$

which is rewritten into

$$\mathcal{H}_F \ \equiv \ 2 {\sum_{\boldsymbol{k}}}' \left(\frac{A_1}{2}(b^\dagger_{\boldsymbol{k}} b_{\boldsymbol{k}} + b^\dagger_{-\boldsymbol{k}} b_{-\boldsymbol{k}}) + A_2 (b^\dagger_{\boldsymbol{k}} b^\dagger_{-\boldsymbol{k}} + b_{\boldsymbol{k}} b_{-\boldsymbol{k}}) \right) \ , \tag{4.46}$$

where ${\sum_{\boldsymbol{k}}}'$ denotes the summation for half of the momentum space and we define,

$$\begin{aligned} A_1 \ &\equiv \ |\Delta| + JSa^2 \boldsymbol{k}^2 + SK_z - \frac{S}{2}(K_x + K_y) \ , \\ A_2 \ &\equiv \ -\frac{S}{4}(K_x - K_y) \ . \end{aligned} \tag{4.47}$$

where we take the long-wavelength limit in defining A_1. To diagonalize the Hamiltonian, we apply the Bogoliubov transformation,

$$\begin{bmatrix} \beta_{\boldsymbol{k}} \\ \beta^\dagger_{-\boldsymbol{k}} \end{bmatrix} = \begin{bmatrix} u_{\boldsymbol{k}} & v_{\boldsymbol{k}} \\ v_{\boldsymbol{k}} & u_{\boldsymbol{k}} \end{bmatrix} \begin{bmatrix} b_{\boldsymbol{k}} \\ b^\dagger_{-\boldsymbol{k}} \end{bmatrix} \ , \tag{4.48}$$

with the momentum dependent real-valued parameters $u_{\boldsymbol{k}}$ and $v_{\boldsymbol{k}}$ satisfying,

$$\begin{aligned} u_{\boldsymbol{k}}^2 &= \frac{1}{2}(\frac{A_1}{\epsilon_{\boldsymbol{k}}}+1) \ , \\ v_{\boldsymbol{k}}^2 &= \frac{1}{2}(\frac{A_1}{\epsilon_{\boldsymbol{k}}}-1) \ , \\ \epsilon_{\boldsymbol{k}} &= \sqrt{A_1^2-4A_2^2} \ . \end{aligned} \tag{4.49}$$

The dispersion relation for the elliptical magnons is thus given as,

$$\epsilon_{\boldsymbol{k}} = \Big[\Big(|\Delta| + JSa^2\boldsymbol{k}^2 + SK_z - \frac{S}{2}(K_x+K_y) \Big)^2 - \Big(\frac{S}{2}(K_x-K_y) \Big)^2 \Big]^{1/2} \ , \tag{4.50}$$

which demonstrates a competition between the exchange interaction and anisotropies.

The Hamiltonian is finally given by,

$$\begin{aligned} \mathcal{H}_F &= {\sum_{\boldsymbol{k}}}' \Big(\epsilon_{\boldsymbol{k}}(\beta_{\boldsymbol{k}}^\dagger\beta_{\boldsymbol{k}} + \beta_{-\boldsymbol{k}}^\dagger\beta_{-\boldsymbol{k}}) + (\epsilon_{\boldsymbol{k}}-A_1) \Big) \\ &= \sum_{\boldsymbol{k}} \Big(\epsilon_{\boldsymbol{k}}\beta_{\boldsymbol{k}}^\dagger\beta_{\boldsymbol{k}} + (\epsilon_{\boldsymbol{k}}-A_1) \Big) \ , \end{aligned} \tag{4.51}$$

where in the last step we recovered the summation over the whole momentum space, and $\sum_{\boldsymbol{k}}(\epsilon_{\boldsymbol{k}}-A_1)$ denotes the ground state energy and is negative. This shows that the new elementary excitations are the Bogoliubov quasi-particles created by $\beta_{\boldsymbol{k}}^\dagger$.

4.3.2 Tunneling in the Parallel Configuration

Effect of Ellipticity

As derived before, the tunneling Hamiltonian $\mathcal{H}_C$ is given as below,

$$\mathcal{H}_C = -S(V_LV_R)^2 \int \frac{d^3\boldsymbol{k}_1}{(2\pi)^3}\frac{d^3\boldsymbol{k}_2}{(2\pi)^3} \big(J_{ex}^{\boldsymbol{k}_1,-\boldsymbol{k}_2} b_{\boldsymbol{k}_1,L}^\dagger b_{\boldsymbol{k}_2,R} + J_{ex}^{-\boldsymbol{k}_1,\boldsymbol{k}_2} b_{\boldsymbol{k}_2,R}^\dagger b_{\boldsymbol{k}_1,L} \big) \ . \tag{4.52}$$

Plugging the Bogoliubov transformation into Eq. 4.52 , we get

$$\mathcal{H}_C \equiv \mathcal{H}_{C,1} + \mathcal{H}_{C,2} + \mathcal{H}_{C,3} + \mathcal{H}_{C,4} \ , \tag{4.53}$$

where we defined,

$$
\begin{aligned}
&\mathcal{H}_{C,1}\\
\equiv\ & -S(V_LV_R)^2\int\frac{d^3\boldsymbol{k}_1}{(2\pi)^3}\frac{d^3\boldsymbol{k}_2}{(2\pi)^3}u_{\boldsymbol{k}_1,L}u_{\boldsymbol{k}_2,R}\left(J_{ex}^{\boldsymbol{k}_1,-\boldsymbol{k}_2}\beta^\dagger_{\boldsymbol{k}_1,L}\beta_{\boldsymbol{k}_2,R}+J_{ex}^{-\boldsymbol{k}_1,\boldsymbol{k}_2}\beta_{\boldsymbol{k}_1,L}\beta^\dagger_{\boldsymbol{k}_2,R}\right);\\
&\mathcal{H}_{C,2}\\
\equiv\ & S(V_LV_R)^2\int\frac{d^3\boldsymbol{k}_1}{(2\pi)^3}\frac{d^3\boldsymbol{k}_2}{(2\pi)^3}v_{\boldsymbol{k}_1,L}u_{\boldsymbol{k}_2,R}\left(J_{ex}^{\boldsymbol{k}_1,-\boldsymbol{k}_2}\beta_{-\boldsymbol{k}_1,L}\beta_{\boldsymbol{k}_2,R}+J_{ex}^{-\boldsymbol{k}_1,\boldsymbol{k}_2}\beta^\dagger_{-\boldsymbol{k}_1,L}\beta^\dagger_{\boldsymbol{k}_2,R}\right);\\
&\mathcal{H}_{C,3}\\
\equiv\ & S(V_LV_R)^2\int\frac{d^3\boldsymbol{k}_1}{(2\pi)^3}\frac{d^3\boldsymbol{k}_2}{(2\pi)^3}u_{\boldsymbol{k}_1,L}v_{\boldsymbol{k}_2,R}\left(J_{ex}^{\boldsymbol{k}_1,-\boldsymbol{k}_2}\beta^\dagger_{\boldsymbol{k}_1,L}\beta^\dagger_{-\boldsymbol{k}_2,R}+J_{ex}^{-\boldsymbol{k}_1,\boldsymbol{k}_2}\beta_{\boldsymbol{k}_1,L}\beta_{-\boldsymbol{k}_2,R}\right);\\
&\mathcal{H}_{C,4}\\
\equiv\ & -S(V_LV_R)^2\int\frac{d^3\boldsymbol{k}_1}{(2\pi)^3}\frac{d^3\boldsymbol{k}_2}{(2\pi)^3}v_{\boldsymbol{k}_1,L}v_{\boldsymbol{k}_2,R}\Big(J_{ex}^{\boldsymbol{k}_1,-\boldsymbol{k}_2}\beta_{-\boldsymbol{k}_1,L}\beta^\dagger_{-\boldsymbol{k}_2,R}\\
&+J_{ex}^{-\boldsymbol{k}_1,\boldsymbol{k}_2}\beta^\dagger_{-\boldsymbol{k}_1,L}\beta_{-\boldsymbol{k}_2,R}\Big)\ .
\end{aligned}
\tag{4.54}
$$

Here the u, v coefficients in the Bogoliubov transformation are given as in Eq. 4.49 and Eq. 4.47. Note that we take the same energy dispersion relation as the one previously derived for the bulk, this applies to the case where the two semi-infinite insulators are weakly attached to each other.

For the tunneling process described by $\mathcal{H}_{C,1}$, we define the momentum resolved transition rates as $\Gamma_{I,e1}(\boldsymbol{p}_1,\boldsymbol{p}_2)$ for the tunneling to the left and $\Gamma_{II,e1}(\boldsymbol{p}_1,\boldsymbol{p}_2)$ for the tunneling to the right. $\boldsymbol{p}_1$ is the wave vector of the magnon in the left insulator, $\boldsymbol{p}_2$ is the one for the magnon in the right insulator. For $\mathcal{H}_{C,2}$, we define $\Gamma_{I,e2}(\boldsymbol{p}_1,\boldsymbol{p}_2)$ for the tunneling where the magnon number decreases by one for both insulators and $\Gamma_{II,e2}(\boldsymbol{p}_1,\boldsymbol{p}_2)$ for the tunneling where the magnon number increases by one for both insulators. For $\mathcal{H}_{C,3}$, we define $\Gamma_{I,e3}(\boldsymbol{p}_1,\boldsymbol{p}_2)$ for the tunneling where the magnon number increases by one for both insulators and $\Gamma_{II,e3}(\boldsymbol{p}_1,\boldsymbol{p}_2)$ for the tunneling where the magnon number decreases by one for both insulators. For $\mathcal{H}_{C,4}$, we define $\Gamma_{I,e4}(\boldsymbol{p}_1,\boldsymbol{p}_2)$ for the tunneling to the right, and $\Gamma_{II,e4}(\boldsymbol{p}_1,\boldsymbol{p}_2)$ for the tunneling to the left. Detailed expressions for these transition rates in the parallel configuration are given in Appendix 4.A.1.

Magnon Tunneling Current — In the absence of any dissipation in the magnetic system, due to the energy conservation condition constrained by the Dirac-delta function and the fact that magnons have non-negative energies, the only terms giving rise to finite contributions in the magnon tunneling are $\Gamma_{I,e1}(\boldsymbol{p}_1,\boldsymbol{p}_2)$, $\Gamma_{II,e1}(\boldsymbol{p}_1,\boldsymbol{p}_2)$, $\Gamma_{I,e4}(\boldsymbol{p}_1,\boldsymbol{p}_2)$, $\Gamma_{II,e4}(\boldsymbol{p}_1,\boldsymbol{p}_2)$, as demonstrated from the comparison of Eq. 4.29 and Eq. 4.41.

Therefore we obtain the expression for the total magnon tunneling current from the

left insulator to the right insulator in the parallel (P) configuration,

$$j_\epsilon^P = \int \frac{d^3\boldsymbol{p}_1 d^3\boldsymbol{p}_2}{(2\pi)^6}\Big(-\Gamma_{I,e1}(\boldsymbol{p}_1,\boldsymbol{p}_2)\epsilon_{\boldsymbol{p}_2,R} + \Gamma_{II,e1}(\boldsymbol{p}_1,\boldsymbol{p}_2)\epsilon_{\boldsymbol{p}_1,L} + \Gamma_{I,e4}(\boldsymbol{p}_1,\boldsymbol{p}_2)\epsilon_{-\boldsymbol{p}_1,L} - \Gamma_{II,e4}(\boldsymbol{p}_1,\boldsymbol{p}_2)\epsilon_{-\boldsymbol{p}_2,R}\Big) , \tag{4.55}$$

which is rewritten as,

$$j_\epsilon^P = \frac{2\pi}{\hbar} S^2 \frac{(V_L V_R)^5}{(2\pi)^6} \int d\epsilon \epsilon D^P(\epsilon)\Big[n_B((\epsilon-\mu_L)\beta_L) - n_B((\epsilon-\mu_R)\beta_R)\Big] , \tag{4.56}$$

where we defined the *tunneling density of states* in the parallel configuration as,

$$D^P(\epsilon) \equiv \int \frac{d^3\boldsymbol{p}_1 d^3\boldsymbol{p}_2}{(2\pi)^6} |J_{ex}^{-\boldsymbol{p}_1,\boldsymbol{p}_2}|^2 \delta(\epsilon-\epsilon_{\boldsymbol{p}_1,L})\delta(\epsilon-\epsilon_{\boldsymbol{p}_2,R})\left((u_{\boldsymbol{p}_1,L}u_{\boldsymbol{p}_2,R})^2 + (v_{\boldsymbol{p}_1,L}v_{\boldsymbol{p}_2,R})^2\right) . \tag{4.57}$$

In the following, we first go to compute the momentum integral inside $D^P(\epsilon)$, and then compute the energy integral to obtain the magnon tunneling current. Taking the rough interface limit as Eq. 4.27,

$$D^P(\epsilon) = J_{ex,0}^2 \int \frac{d^3\boldsymbol{p}_1 d^3\boldsymbol{p}_2}{(2\pi)^6} \delta(\epsilon-\epsilon_{\boldsymbol{p}_1,L})\delta(\epsilon-\epsilon_{\boldsymbol{p}_2,R})\left((u_{\boldsymbol{p}_1,L}u_{\boldsymbol{p}_2,R})^2 + (v_{\boldsymbol{p}_1,L}v_{\boldsymbol{p}_2,R})^2\right) . \tag{4.58}$$

For the following calculations, we take the material parameters, such as magnetic field strength and anisotropy, to be the same for both magnets, thus we have $u_{\boldsymbol{p},L} \equiv u_{\boldsymbol{p},R}$ and $v_{\boldsymbol{p},L} \equiv v_{\boldsymbol{p},R}$.

Removing the momentum dependence of u, v coefficients of the Bogoliubov transformation by taking the low temperature limit gives,

$$(u_{\boldsymbol{p}_1,L}u_{\boldsymbol{p}_2,R})^2 + (v_{\boldsymbol{p}_1,L}v_{\boldsymbol{p}_2,R})^2 = 1 + \frac{(\bar{K}_x-\bar{K}_y)^2/2}{\left(2\left(\bar{\Delta}+\bar{K}_z\right)-(\bar{K}_x+\bar{K}_y)\right)^2 - (\bar{K}_x-\bar{K}_y)^2} , \tag{4.59}$$

where we defined the dimensionless anisotropy and magnetic field as,

$$\bar{K}_x = K_x/k_BT,\ \bar{K}_y = K_y/k_BT,\ \bar{K}_z = K_z/k_BT,\ \bar{\Delta} = \Delta/k_BT . \tag{4.60}$$

We also define the dimensionless stiffness constant $\bar{A}$ by taking $\bar{A} \equiv SA/(k_BT) \equiv JSa^2/(k_BT)$, which gives the dimensionless energy dispersion scaled by the thermal energy,

$$\xi_p \equiv \epsilon_p/(k_BT) = \sqrt{\left(\bar{\Delta}+\bar{A}p^2+\bar{K}_z-\frac{\bar{K}_x+\bar{K}_y}{2}\right)^2 - \frac{(\bar{K}_x-\bar{K}_y)^2}{4}} , \tag{4.61}$$

where p denotes the magnitude of the wave vector $\boldsymbol{p}$.

With this, we evaluate the momentum integral involved using,

$$\int \frac{d^3\boldsymbol{p}}{(2\pi)^3}\delta(\epsilon-\epsilon_{\boldsymbol{p}}) = \frac{1}{2\pi^2}\sum_{p_j}\frac{p_j^2}{|\epsilon'_{\boldsymbol{p}}(p_j)|}\ , \tag{4.62}$$

where we need to perform the summation over the roots p_j of the equation $\epsilon-\epsilon_p=0$. Defining the dimensionless energy ξ,

$$\xi \equiv \epsilon/(k_BT)\ . \tag{4.63}$$

the physically relevant p_j is given by,

$$p_j = \frac{1}{\bar{A}}\sqrt{\frac{\bar{K}_x+\bar{K}_y}{2}-\bar{\Delta}-\bar{K}_z+\sqrt{\frac{(\bar{K}_x-\bar{K}_y)^2}{4}+\xi^2}}\ , \tag{4.64}$$

Noting that,

$$\int \frac{d^3\boldsymbol{p}_1 d^3\boldsymbol{p}_2}{(2\pi)^6}\delta(\epsilon-\epsilon_{\boldsymbol{p}_1,L})\delta(\epsilon-\epsilon_{\boldsymbol{p}_2,R}) \quad = \quad \left[\int \frac{d^3\boldsymbol{p}}{(2\pi)^3}\delta(\epsilon-\epsilon_{\boldsymbol{p}})\right]^2\ , \tag{4.65}$$

we plug Eq. 4.64 and Eq. 4.62 into Eq. 4.65, and get,

$$\begin{aligned}&\int \frac{d^3\boldsymbol{p}_1 d^3\boldsymbol{p}_2}{(2\pi)^6}\delta(\epsilon-\epsilon_{\boldsymbol{p}_1,L})\delta(\epsilon-\epsilon_{\boldsymbol{p}_2,R})\\ = \quad &\frac{(\bar{K}_x+\bar{K}_y)-2(\bar{\Delta}+\bar{K}_z)+\sqrt{(\bar{K}_x-\bar{K}_y)^2+4\xi^2}}{(\bar{K}_x-\bar{K}_y)^2+4\xi^2}\frac{\xi^2}{8\pi^4\bar{A}^3(k_BT)^2}\ .\end{aligned} \tag{4.66}$$

Linear response to temperature difference: tunneling thermal conductance — We go to calculate the tunneling thermal conductance by taking the temperatures in the two insulators to be very close to each other, namely $|(T_L-T_R)/(T_L+T_R)|<1$ and defining the mean of temperatures as $T\equiv(T_L+T_R)/2$. The spin accumulations μ_L,μ_R are always smaller than their corresponding magnon gaps, and are taken to be zero in the following derivations and numerical calculations. Thus the difference of the Bose-Einstein factors is approximated by,

$$n_B\left(\frac{\epsilon}{k_BT_L}\right)-n_B\left(\frac{\epsilon}{k_BT_R}\right)\approx\frac{\xi e^{\xi}(T_L-T_R)}{(e^{\xi}-1)^2T}\ . \tag{4.67}$$

The tunneling thermal conductance is defined as $\kappa_P\equiv j_\epsilon^P/(T_L-T_R)$. Plugging Eq. 4.58 and Eq. 4.59 into Eq. 4.56, with the consideration of Eq. 4.66 and Eq. 4.67, we get the

tunneling thermal conductance in the parallel configuration,

$$\begin{aligned}\kappa_P &= \frac{2\pi}{\hbar} S^2 \frac{(V_L V_R)^5}{(2\pi)^6} \frac{J_{ex,0}^2}{8\pi^4 \bar{A}^3 T} \int_{\xi_0}^{\infty} d\xi \frac{\xi^4 e^\xi}{(e^\xi - 1)^2} \\ &\times \Big[1 + \frac{(\bar{K}_x - \bar{K}_y)^2/2}{\left(2\left(\bar{\Delta} + \bar{K}_z\right) - \left(\bar{K}_x + \bar{K}_y\right)\right)^2 - (\bar{K}_x - \bar{K}_y)^2}\Big] \\ &\times \frac{(\bar{K}_x + \bar{K}_y) - 2(\bar{\Delta} + \bar{K}_z) + \sqrt{(\bar{K}_x - \bar{K}_y)^2 + 4\xi^2}}{(\bar{K}_x - \bar{K}_y)^2 + 4\xi^2} \ , \end{aligned} \tag{4.68}$$

which is an integral over the dimensionless energy ξ, with the lower limit starting from the dimensionless gap defined as

$$\xi_0 \equiv \sqrt{\left(\bar{\Delta} + \bar{K}_z - \frac{\bar{K}_x + \bar{K}_y}{2}\right)^2 - \frac{(\bar{K}_x - \bar{K}_y)^2}{4}} \ . \tag{4.69}$$

Recovering the momentum dependence — Note that in the calculations above, the $u_{\boldsymbol{k}}, v_{\boldsymbol{k}}$ functions are approximated to be independent of momenta. Recovering the momentum dependence, we have,

$$D_{\alpha=0}^P(\epsilon) = J_{ex,0}^2 \left(\mathcal{I}_u(\epsilon)^2 + \mathcal{I}_v(\epsilon)^2\right) \ , \tag{4.70}$$

where we defined the u^2-addressed density of states (U-DOS) and v^2-addressed density of states (V-DOS) in the absence of damping,

$$\begin{aligned}\mathcal{I}_u(\epsilon) &\equiv \int \frac{d^3\boldsymbol{p}}{(2\pi)^3} u_{\boldsymbol{p}}^2 \delta(\epsilon - \epsilon_{\boldsymbol{p}}) \ , \\ \mathcal{I}_v(\epsilon) &\equiv \int \frac{d^3\boldsymbol{p}}{(2\pi)^3} v_{\boldsymbol{p}}^2 \delta(\epsilon - \epsilon_{\boldsymbol{p}}) \ , \end{aligned} \tag{4.71}$$

with $u_{\boldsymbol{p}}^2$, $v_{\boldsymbol{p}}^2$ given by,

$$\begin{aligned} u_{\boldsymbol{p}}^2 &= \frac{1}{2}\left[\sqrt{\frac{\left(\bar{\Delta} + \bar{A}\boldsymbol{p}^2 + \bar{K}_z - \frac{\bar{K}_x + \bar{K}_y}{2}\right)^2}{\left(\bar{\Delta} + \bar{A}\boldsymbol{p}^2 + \bar{K}_z - \frac{\bar{K}_x + \bar{K}_y}{2}\right)^2 - \left(\frac{\bar{K}_x - \bar{K}_y}{2}\right)^2}} + 1\right] \ , \\ v_{\boldsymbol{p}}^2 &= \frac{1}{2}\left[\sqrt{\frac{\left(\bar{\Delta} + \bar{A}\boldsymbol{p}^2 + \bar{K}_z - \frac{\bar{K}_x + \bar{K}_y}{2}\right)^2}{\left(\bar{\Delta} + \bar{A}\boldsymbol{p}^2 + \bar{K}_z - \frac{\bar{K}_x + \bar{K}_y}{2}\right)^2 - \left(\frac{\bar{K}_x - \bar{K}_y}{2}\right)^2}} + 1\right] \ . \end{aligned} \tag{4.72}$$

Performing the momentum integral gives,

$$\begin{aligned}
\mathcal{I}_u(\epsilon) &= \frac{1}{4\pi^2}\sum_j \frac{p_j^2}{|\epsilon'_{\boldsymbol{p}}(p_j)|}\left[\sqrt{\frac{\left(2(\bar{\Delta}+\bar{A}p_j^2+\bar{K}_z)-(\bar{K}_x+\bar{K}_y)\right)^2}{\left(2(\bar{\Delta}+\bar{A}p_j^2+\bar{K}_z)-(\bar{K}_x+\bar{K}_y)\right)^2-(\bar{K}_x-\bar{K}_y)^2}}+1\right], \\
\mathcal{I}_v(\epsilon) &= \frac{1}{4\pi^2}\sum_j \frac{p_j^2}{|\epsilon'_{\boldsymbol{p}}(p_j)|}\left[\sqrt{\frac{\left(2(\bar{\Delta}+\bar{A}p_j^2+\bar{K}_z)-(\bar{K}_x+\bar{K}_y)\right)^2}{\left(2(\bar{\Delta}+\bar{A}p_j^2+\bar{K}_z)-(\bar{K}_x+\bar{K}_y)\right)^2-(\bar{K}_x-\bar{K}_y)^2}}-1\right],
\end{aligned} \tag{4.73}$$

where p_j and $\epsilon'_{\boldsymbol{p}}(p_j)$ have the same meaning as given in Eq. 4.64 and Eq. 4.62.

Plugging Eq. 4.73 into Eq. 4.70 gives,

$$\begin{aligned}
\mathcal{I}_u(\epsilon) &= \frac{1}{8\sqrt{2}\pi^2\bar{A}^{3/2}k_BT}\frac{2\xi+\sqrt{((\bar{K}_x-\bar{K}_y)^2+4\xi^2}}{\sqrt{((\bar{K}_x-\bar{K}_y)^2+4\xi^2}} \\
&\quad \sqrt{\sqrt{(\bar{K}_x-\bar{K}_y)^2+4\xi^2}-2(\bar{\Delta}+\bar{K}_z)+(\bar{K}_x+\bar{K}_y)}\,, \\
\mathcal{I}_v(\epsilon) &= \frac{1}{8\sqrt{2}\pi^2\bar{A}^{3/2}k_BT}\frac{-2\xi+\sqrt{((\bar{K}_x-\bar{K}_y)^2+4\xi^2}}{\sqrt{((\bar{K}_x-\bar{K}_y)^2+4\xi^2}} \\
&\quad \sqrt{\sqrt{(\bar{K}_x-\bar{K}_y)^2+4\xi^2}-2(\bar{\Delta}+\bar{K}_z)+(\bar{K}_x+\bar{K}_y)}\,.
\end{aligned} \tag{4.74}$$

therefore,

$$\begin{aligned}
&D^P_{\alpha=0}(\epsilon) \\
&= \frac{J^2_{ex,0}((\bar{K}_x-\bar{K}_y)^2+8\xi^2)}{64\pi^4\bar{A}^3(k_BT)^2((\bar{K}_x-\bar{K}_y)^2+4\xi^2}\Big[\sqrt{(\bar{K}_x-\bar{K}_y)^2+4\xi^2}-2(\bar{\Delta}+\bar{K}_z) \\
&\quad +(\bar{K}_x+\bar{K}_y)\Big]\Theta\left(\sqrt{(\bar{K}_x-\bar{K}_y)^2+4\xi^2}-2(\bar{\Delta}+\bar{K}_z)+(\bar{K}_x+\bar{K}_y)\right).
\end{aligned} \tag{4.75}$$

Inserting Eq. 4.75 into Eq. 4.56 with the combination of Eq. 4.67, we find the tunneling thermal conductance,

$$\begin{aligned}
\kappa_P|_{\alpha=0} &= \frac{2\pi}{\hbar}S^2\frac{(V_LV_R)^5}{(2\pi)^6}\frac{J^2_{ex,0}}{64\pi^4\bar{A}^3T}\int_{\xi_0}^{\infty}d\xi\frac{\xi^2e^{\xi}}{(e^{\xi}-1)^2}\frac{\left((\bar{K}_x-\bar{K}_y)^2+8\xi^2\right)}{\left((\bar{K}_x-\bar{K}_y)^2+4\xi^2\right)} \\
&\quad \times\Big[\sqrt{(\bar{K}_x-\bar{K}_y)^2+4\xi^2}-2(\bar{\Delta}+\bar{K}_z)+(\bar{K}_x+\bar{K}_y)\Big]\,.
\end{aligned} \tag{4.76}$$

where ξ_0 is given in Eq. 4.69.

Effect of Gilbert Damping

In the presence of finite Gilbert damping, the broadening of spectral function will give rise to the overlap of density of states in the two insulators. Therefore, the other terms of transition rates as given in Eq. 4.105 and Eq. 4.106 will also contribute in this case.

We write down the extra term to the tunneling energy current in the parallel configuration as,

$$\begin{aligned} j^{P}_{\epsilon,\text{extra}} &= \int \frac{d^3\boldsymbol{p}_1 d^3\boldsymbol{p}_2}{(2\pi)^6}\Big(\Gamma_{I,e2}(\boldsymbol{p}_1,\boldsymbol{p}_2)\epsilon_{-\boldsymbol{p}_1,L} - \Gamma_{II,e2}(\boldsymbol{p}_1,\boldsymbol{p}_2)\epsilon_{-\boldsymbol{p}_1,L} \\ &\quad +\Gamma_{I,e3}(\boldsymbol{p}_1,\boldsymbol{p}_2)\epsilon_{-\boldsymbol{p}_2,R} - \Gamma_{II,e3}(\boldsymbol{p}_1,\boldsymbol{p}_2)\epsilon_{-\boldsymbol{p}_2,R}\Big) \ , \end{aligned} \tag{4.77}$$

which can be rewritten as,

$$j^{P}_{\epsilon,\text{extra}} = \frac{2\pi}{\hbar} S^2 \frac{(V_L V_R)^5}{(2\pi)^6} \int d\epsilon \epsilon D^{P}_{extra}(\epsilon)\Big[n_B((\epsilon-\mu_L)\beta_L) - n_B((\epsilon+\mu_R)\beta_R)\Big] \ , \tag{4.78}$$

where we defined the extra contribution to the tunneling density of states as,

$$\begin{aligned} D^{P}_{\text{extra}}(\epsilon) &= -\int \frac{d^3\boldsymbol{p}_1 d^3\boldsymbol{p}_2}{(2\pi)^6} |J_{ex}^{-\boldsymbol{p}_1,\boldsymbol{p}_2}|^2 \delta(\epsilon-\epsilon_{\boldsymbol{p}_1,L})\delta(\epsilon+\epsilon_{\boldsymbol{p}_2,R}) \\ &\quad \times \left((u_{\boldsymbol{p}_1,L} v_{\boldsymbol{p}_2,R})^2 + (v_{\boldsymbol{p}_1,L} u_{\boldsymbol{p}_2,R})^2\right) \ . \end{aligned} \tag{4.79}$$

Meanwhile, to take account of dissipation in the magnon tunneling process, we use the substitution in the following,

$$\delta(\epsilon-\epsilon_{\boldsymbol{k}}) \to \frac{1}{\pi}\frac{\alpha\epsilon}{(\epsilon-\epsilon_{\boldsymbol{k}})^2+(\alpha\epsilon)^2} \ , \tag{4.80}$$

where α denotes the Gilbert damping constant. Note that the Lorentzian type function in the right-hand side of Eq. 4.80 is consistent with the spectral line shape of a ferromagnetic resonance [50], and can be derived using the Green's function formalism as well [160, 161].

Adding the original contribution from Eq. 4.58 by the extra contribution in Eq. 4.79 gives the total tunneling density of states,

$$D^{P}_{\alpha\neq 0}(\epsilon) = J^2_{ex,0}\left(\mathcal{M}_u(\epsilon)^2 + \mathcal{M}_v(\epsilon)^2 - \mathcal{M}_u(\epsilon)\mathcal{M}_v(-\epsilon) - \mathcal{M}_v(\epsilon)\mathcal{M}_u(-\epsilon)\right) \ . \tag{4.81}$$

Here, we define the u^2-addressed density of states (U-DOS) and v^2-addressed density of states (V-DOS) in the case of finite damping,

$$\begin{aligned} \mathcal{M}_u(\epsilon) &\equiv \frac{\alpha\epsilon}{\pi}\int \frac{d^3\boldsymbol{p}}{(2\pi)^3}\frac{u^2_{\boldsymbol{p}}}{(\epsilon-\epsilon_{\boldsymbol{p}})^2+(\alpha\epsilon)^2} \ , \\ \mathcal{M}_v(\epsilon) &\equiv \frac{\alpha\epsilon}{\pi}\int \frac{d^3\boldsymbol{p}}{(2\pi)^3}\frac{v^2_{\boldsymbol{p}}}{(\epsilon-\epsilon_{\boldsymbol{p}})^2+(\alpha\epsilon)^2} \ , \end{aligned} \tag{4.82}$$

where $u^2_{\boldsymbol{p}}$, $v^2_{\boldsymbol{p}}$ are given in Eq. 4.72, the energy dispersion $\epsilon_{\boldsymbol{p}}$ is given in Eq. 4.61. We take the Gilbert damping to be equal for both ferromagnetic insulators. Therefore

$\mathcal{M}_u(\epsilon), \mathcal{M}_v(\epsilon)$ are transformed as,

$$\begin{aligned}\mathcal{M}_u(\epsilon) &= \int \frac{p^2 dp}{4\pi^2} \frac{\alpha\xi}{\pi(k_B T)} \frac{\sqrt{1+\frac{(\bar{K}_x-\bar{K}_y)^2/4}{\xi_p^2}}+1}{(\xi-\xi_p)^2+(\alpha\xi)^2} \,, \\ \mathcal{M}_v(\epsilon) &= \int \frac{p^2 dp}{4\pi^2} \frac{\alpha\xi}{\pi(k_B T)} \frac{\sqrt{1+\frac{(\bar{K}_x-\bar{K}_y)^2/4}{\xi_p^2}}-1}{(\xi-\xi_p)^2+(\alpha\xi)^2} \,, \end{aligned} \tag{4.83}$$

where ξ_p is defined as before in Eq. 4.61 and ξ is given in Eq. 4.63.

Noting that $\bar{A}$ has a dimension of length square, we define a dimensionless momentum q by taking $q \equiv \sqrt{\bar{A}}p$ in order to convert the momentum integral above into a dimensionless one.

Therefore the tunneling thermal conductance in the presence of finite Gilbert damping can be expressed as,

$$\begin{aligned}&\kappa_P|_{\alpha\neq 0} \\ =\ & \frac{2\pi}{\hbar} S^2 \frac{(V_L V_R)^5}{(2\pi)^6} \frac{J_{ex,0}^2}{16\pi^4 T \bar{A}^3} \int_{-\infty}^{\infty} d\xi \frac{\xi^2 e^\xi}{(e^\xi-1)^2} \left(\frac{\alpha\xi}{\pi}\right)^2 \\ &\times \left(\left[\int_0^\infty dq\ q^2 \frac{\sqrt{1+\frac{(\bar{K}_x-\bar{K}_y)^2/4}{\zeta_q^2}}+1}{(\xi-\zeta_q)^2+(\alpha\xi)^2} \right]^2 + \left[\int_0^\infty dq\ q^2 \frac{\sqrt{1+\frac{(\bar{K}_x-\bar{K}_y)^2/4}{\zeta_q^2}}-1}{(\xi-\zeta_q)^2+(\alpha\xi)^2} \right]^2 \right. \\ &+ \left[\int_0^\infty dq\ q^2 \frac{\sqrt{1+\frac{(\bar{K}_x-\bar{K}_y)^2/4}{\zeta_q^2}}+1}{(\xi-\zeta_q)^2+(\alpha\xi)^2} \right] \left[\int_0^\infty dq\ q^2 \frac{\sqrt{1+\frac{(\bar{K}_x-\bar{K}_y)^2/4}{\zeta_q^2}}-1}{(\xi+\zeta_q)^2+(\alpha\xi)^2} \right] \\ &\left. + \left[\int_0^\infty dq\ q^2 \frac{\sqrt{1+\frac{(\bar{K}_x-\bar{K}_y)^2/4}{\zeta_q^2}}+1}{(\xi+\zeta_q)^2+(\alpha\xi)^2} \right] \left[\int_0^\infty dq\ q^2 \frac{\sqrt{1+\frac{(\bar{K}_x-\bar{K}_y)^2/4}{\zeta_q^2}}-1}{(\xi-\zeta_q)^2+(\alpha\xi)^2} \right] \right) \end{aligned} \tag{4.84}$$

where we defined another dimensionless dispersion relation as

$$\zeta_q \equiv \frac{1}{2}\sqrt{\left(2(\bar{\Delta}+q^2+\bar{K}_z)-(\bar{K}_x+\bar{K}_y)\right)^2-(\bar{K}_x-\bar{K}_y)^2} \,. \tag{4.85}$$

We perform the energy integration starting from minus infinity rather than the magnon gap, since the contribution from energy below the gap also contributes to the density of states when the Gilbert damping is non-zero.

In the following, we integrate over momentum numerically to obtain the density of state and discuss its damping dependence.

Gilbert Damping Dependence of the u^2 and v^2 Addressed Density of States

We now compute the u^2-addressed density of states (U-DOS) and v^2-addressed density of states (V-DOS), as defined in Eq. 4.71 in the case with zero Gilbert damping, and

in Eq. 4.82 for the case with finite damping. The U-DOS and V-DOS are plotted with the expressions derived in Eq. 4.74 and Eq. 4.83 as functions of dimensionless energy for various Gilbert damping values, as shown in Fig. 4.2 and Fig. 4.3. The two plots have the same scale in the y-axis. From the plots, we see that both U-DOS and V-DOS gradually converge to the case with zero dissipation when the damping value decreases from a larger value as 0.2 to a small value as 0.03.

The Gilbert damping intrinsically is the broadening effect for magnons to acquire a finite lifetime. As the damping becomes larger, the details of dispersion relation become less important, which allows us to find particles within a small band around the energy given by the dispersion relation. Therefore the U-DOS monotonically increases with Gilbert damping, as shown in Fig. 4.2.

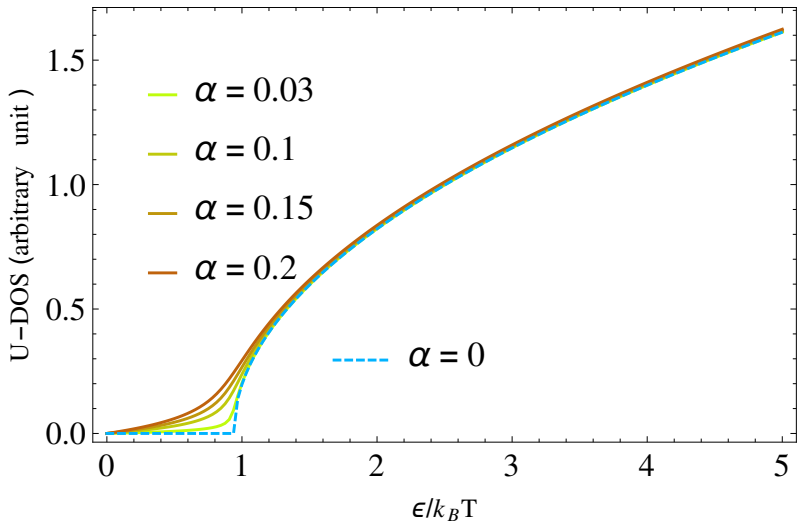

Fig. 4.2: u^2-addressed density of states (U-DOS) for various Gilbert damping values. α is the Gilbert damping parameter.

For the V-DOS, its damping dependence is more versatile. The central peak close to the gap of V-DOS can be attributed to that it is an integral over the product of a finite DOS and v^2 coefficient, whose value is large for a low energy mode. In the low energy regime, the V-DOS increases with the damping, while in the high energy regime, the V-DOS decreases with the damping. Therefore, the Gilbert damping effectively redistributes the contributions to the total V-DOS from the higher energy regime to the lower one, which can be explained by the fact that the magnon lifetime with a Gilbert-type dissipation is inversely proportional to its energy.

In the next, we will perform further derivations to obtain the expression of tunneling thermal conductance for the anti-parallel configuration.

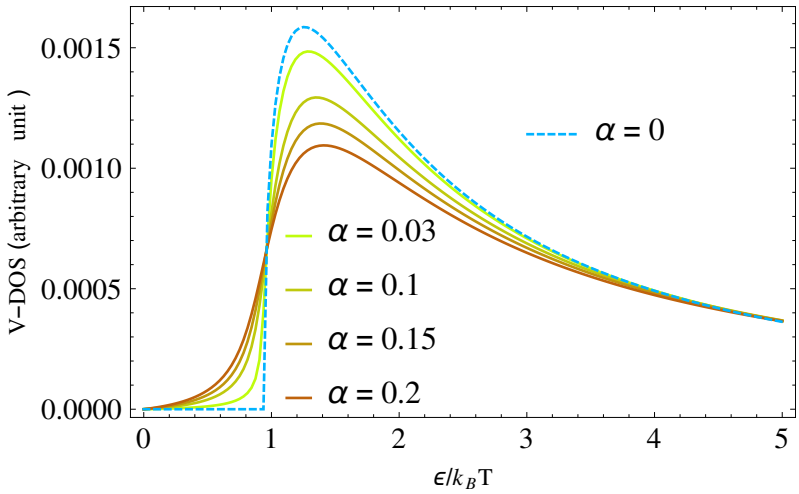

Fig. 4.3: v^2-addressed density of states (V-DOS) for various Gilbert damping values. α is the Gilbert damping parameter.

4.3.3 Tunneling in the Anti-parallel Configuration

Effect of Ellipticity

The tunneling Hamiltonian for the anti-parallel (AP) case is given as,

$$\mathcal{H}_C^{AP} = -S(V_L V_R)^2 \int \frac{d^3\boldsymbol{k}_1}{(2\pi)^3}\frac{d^3\boldsymbol{k}_2}{(2\pi)^3}\left(J_{ex}^{\boldsymbol{k}_1,\boldsymbol{k}_2} b^\dagger_{\boldsymbol{k}_1,L} b^\dagger_{\boldsymbol{k}_2,R} + J_{ex}^{-\boldsymbol{k}_1,-\boldsymbol{k}_2} b_{\boldsymbol{k}_1,L} b_{\boldsymbol{k}_2,R}\right) . \tag{4.86}$$

Plugging the Bogoliubov transformation into Eq. 4.86, we get

$$\mathcal{H}_C^{AP} \equiv \mathcal{H}_{C,1}^{AP} + \mathcal{H}_{C,2}^{AP} + \mathcal{H}_{C,3}^{AP} + \mathcal{H}_{C,4}^{AP} , \tag{4.87}$$

where we defined,

$$\begin{aligned}
\mathcal{H}_{C,1}^{AP} &\equiv -S(V_L V_R)^2 \int \frac{d^3\boldsymbol{k}_1}{(2\pi)^3}\frac{d^3\boldsymbol{k}_2}{(2\pi)^3} u_{\boldsymbol{k}_1,L} u_{\boldsymbol{k}_2,R}\left(J_{ex}^{\boldsymbol{k}_1,\boldsymbol{k}_2}\beta^\dagger_{\boldsymbol{k}_1,L}\beta^\dagger_{\boldsymbol{k}_2,R} + J_{ex}^{-\boldsymbol{k}_1,-\boldsymbol{k}_2}\beta_{\boldsymbol{k}_1,L}\beta_{\boldsymbol{k}_2,R}\right);\\
\mathcal{H}_{C,2}^{AP} &\equiv S(V_L V_R)^2 \int \frac{d^3\boldsymbol{k}_1}{(2\pi)^3}\frac{d^3\boldsymbol{k}_2}{(2\pi)^3} v_{\boldsymbol{k}_1,L} u_{\boldsymbol{k}_2,R}\left(J_{ex}^{\boldsymbol{k}_1,\boldsymbol{k}_2}\beta_{-\boldsymbol{k}_1,L}\beta^\dagger_{\boldsymbol{k}_2,R} + J_{ex}^{-\boldsymbol{k}_1,-\boldsymbol{k}_2}\beta^\dagger_{-\boldsymbol{k}_1,L}\beta_{\boldsymbol{k}_2,R}\right);\\
\mathcal{H}_{C,3}^{AP} &\equiv S(V_L V_R)^2 \int \frac{d^3\boldsymbol{k}_1}{(2\pi)^3}\frac{d^3\boldsymbol{k}_2}{(2\pi)^3} u_{\boldsymbol{k}_1,L} v_{\boldsymbol{k}_2,R}\left(J_{ex}^{\boldsymbol{k}_1,\boldsymbol{k}_2}\beta^\dagger_{\boldsymbol{k}_1,L}\beta_{-\boldsymbol{k}_2,R} + J_{ex}^{-\boldsymbol{k}_1,-\boldsymbol{k}_2}\beta_{\boldsymbol{k}_1,L}\beta^\dagger_{-\boldsymbol{k}_2,R}\right);\\
\mathcal{H}_{C,4}^{AP} &\equiv -S(V_L V_R)^2 \int \frac{d^3\boldsymbol{k}_1}{(2\pi)^3}\frac{d^3\boldsymbol{k}_2}{(2\pi)^3} v_{\boldsymbol{k}_1,L} v_{\boldsymbol{k}_2,R}\Big(J_{ex}^{\boldsymbol{k}_1,\boldsymbol{k}_2}\beta_{-\boldsymbol{k}_1,L}\beta_{-\boldsymbol{k}_2,R}\\
&\quad + J_{ex}^{-\boldsymbol{k}_1,-\boldsymbol{k}_2}\beta^\dagger_{-\boldsymbol{k}_1,L}\beta^\dagger_{-\boldsymbol{k}_2,R}\Big) .
\end{aligned} \tag{4.88}$$

The tunneling process $\mathcal{H}_{C,1}^{AP}$ gives the momentum resolved transition rate defined as $\Gamma_{I,e1}^{AP}(\boldsymbol{p}_1,\boldsymbol{p}_2)$ for the tunneling where the magnon number increases by one for both

insulators and $\Gamma^{AP}_{II,e1}(\boldsymbol{p}_1,\boldsymbol{p}_2)$ for the tunneling where the magnon number decreases by one for both insulators. For $\mathcal{H}^{AP}_{C,2}$, we define $\Gamma^{AP}_{I,e2}(\boldsymbol{p}_1,\boldsymbol{p}_2)$ for the tunneling towards the right and $\Gamma^{AP}_{II,e2}(\boldsymbol{p}_1,\boldsymbol{p}_2)$ for the tunneling towards the left. For $\mathcal{H}^{AP}_{C,3}$, we define $\Gamma^{AP}_{I,e3}(\boldsymbol{p}_1,\boldsymbol{p}_2)$ for the tunneling towards the left and $\Gamma^{AP}_{II,e3}(\boldsymbol{p}_1,\boldsymbol{p}_2)$ for the tunneling towards the right. For $\mathcal{H}^{AP}_{C,4}$, we define $\Gamma^{AP}_{I,e4}(\boldsymbol{p}_1,\boldsymbol{p}_2)$ for the tunneling where the magnon number decreases by one for both insulators, and $\Gamma^{AP}_{II,e4}(\boldsymbol{p}_1,\boldsymbol{p}_2)$ for the tunneling where the magnon number increases by one for both insulators. Detailed expressions for these transition rates in the anti-parallel configuration are given in Appendix 4.A.2.

Magnon Tunneling Current — Similar to the calculations for the parallel configuration, we first consider the tunneling for a system without Gilbert damping. Due to the energy conservation condition constrained by the Dirac-delta function and the fact that magnons have non-negative energies, the only terms giving rise to finite contributions in the magnon tunneling are $\Gamma^{AP}_{I,e2}(\boldsymbol{p}_1,\boldsymbol{p}_2)$, $\Gamma^{AP}_{II,e2}(\boldsymbol{p}_1,\boldsymbol{p}_2)$, $\Gamma^{AP}_{I,e3}(\boldsymbol{p}_1,\boldsymbol{p}_2)$, $\Gamma^{AP}_{II,e3}(\boldsymbol{p}_1,\boldsymbol{p}_2)$. Therefore we obtain the expression for the total magnon tunneling current from the left insulator to the right insulator,

$$\begin{aligned} j^{AP}_{\epsilon} &= \int \frac{d^3\boldsymbol{p}_1 d^3\boldsymbol{p}_2}{(2\pi)^6}\Big(\Gamma^{AP}_{I,e2}(\boldsymbol{p}_1,\boldsymbol{p}_2)\epsilon_{-\boldsymbol{p}_1,L} - \Gamma^{AP}_{II,e2}(\boldsymbol{p}_1,\boldsymbol{p}_2)\epsilon_{\boldsymbol{p}_2,R} \\ &\quad -\Gamma^{AP}_{I,e3}(\boldsymbol{p}_1,\boldsymbol{p}_2)\epsilon_{\boldsymbol{p}_2,R} + \Gamma^{AP}_{II,e3}(\boldsymbol{p}_1,\boldsymbol{p}_2)\epsilon_{\boldsymbol{p}_1,L}\Big)\ . \end{aligned} \tag{4.89}$$

Introducing the identity $\int_{-\infty}^{\infty} d\epsilon\delta(\epsilon-\epsilon_0)=1$ again, we get,

$$j^{AP}_{\epsilon} = \frac{2\pi}{\hbar}S^2\frac{(V_LV_R)^5}{(2\pi)^6}\int d\epsilon\epsilon D^{AP}(\epsilon)\Big[n_B\big((\epsilon-\mu_L)\beta_L\big)-n_B\big((\epsilon-\mu_R)\beta_R\big)\Big]\ , \tag{4.90}$$

where we defined *tunneling density of states* in the anti-parallel configuration,

$$\begin{aligned} &D^{AP}(\epsilon) \\ \equiv\ &\int \frac{d^3\boldsymbol{p}_1 d^3\boldsymbol{p}_2}{(2\pi)^6}|J^{-\boldsymbol{p}_1,\boldsymbol{p}_2}_{ex}|^2\delta(\epsilon-\epsilon_{\boldsymbol{p}_1,L})\delta(\epsilon-\epsilon_{\boldsymbol{p}_2,R})\left((v_{\boldsymbol{p}_1,L}u_{\boldsymbol{p}_2,R})^2+(u_{\boldsymbol{p}_1,L}v_{\boldsymbol{p}_2,R})^2\right)\ . \end{aligned} \tag{4.91}$$

Taking again the rough interface limit, we find,

$$\begin{aligned} &D^{AP}(\epsilon) \\ =\ &J^2_{ex,0}\int \frac{d^3\boldsymbol{p}_1 d^3\boldsymbol{p}_2}{(2\pi)^6}\delta(\epsilon-\epsilon_{\boldsymbol{p}_1,L})\delta(\epsilon-\epsilon_{\boldsymbol{p}_2,R})\left((v_{\boldsymbol{p}_1,L}u_{\boldsymbol{p}_2,R})^2+(u_{\boldsymbol{p}_1,L}v_{\boldsymbol{p}_2,R})^2\right)\ . \end{aligned} \tag{4.92}$$

In the low temperature limit, we have

$$(v_{\boldsymbol{p}_1,L}u_{\boldsymbol{p}_2,R})^2+(u_{\boldsymbol{p}_1,L}v_{\boldsymbol{p}_2,R})^2 = \frac{(\bar{K}_x-\bar{K}_y)^2/2}{\big(2(\bar{\Delta}+\bar{K}_z)-(\bar{K}_x+\bar{K}_y)\big)^2-(\bar{K}_x-\bar{K}_y)^2}\ . \tag{4.93}$$

With similar calculations as done for the parallel case, we obtain the thermal conductance defined by $\kappa_{AP} \equiv j_\epsilon^{AP}/(T_L - T_R)$,

$$\begin{aligned}\kappa_{AP} &= \frac{2\pi}{\hbar} S^2 \frac{(V_L V_R)^5}{(2\pi)^6} \frac{J_{ex,0}^2}{8\pi^4 \bar{A}^3 T} \int_{\xi_0}^{\infty} d\xi \frac{\xi^4 e^\xi}{(e^\xi - 1)^2} \\ &\times \frac{(\bar{K}_x - \bar{K}_y)^2/2}{\left(2\left(\bar{\Delta} + \bar{K}_z\right) - (\bar{K}_x + \bar{K}_y)\right)^2 - (\bar{K}_x - \bar{K}_y)^2} \\ &\times \frac{(\bar{K}_x + \bar{K}_y) - 2(\bar{\Delta} + \bar{K}_z) + \sqrt{(\bar{K}_x - \bar{K}_y)^2 + 4\xi^2}}{(\bar{K}_x - \bar{K}_y)^2 + 4\xi^2} \ , \end{aligned} \tag{4.94}$$

where the lower bound ξ_0 for the dimensionless energy integral is the same as given in Eq. 4.69.

Recovering the momentum dependence — Note that in the calculations above, the $u_{\boldsymbol{k}}, v_{\boldsymbol{k}}$ functions are approximated to be independent of momenta. Recovering the momentum dependence gives,

$$D_{\alpha=0}^{AP}(\epsilon) = 2J_{ex,0}^2 \mathcal{I}_u(\epsilon)\mathcal{I}_v(\epsilon) \ , \tag{4.95}$$

where $\mathcal{I}_u(\epsilon)$ and $\mathcal{I}_v(\epsilon)$ have the same definitions as Eq. 4.71.

Therefore we have

$$\begin{aligned} & D_{\alpha=0}^{AP}(\epsilon) \\ = \ & \frac{J_{ex,0}^2 (\bar{K}_x - \bar{K}_y)^2}{64\pi^4 \bar{A}^3 (k_B T)^2 ((\bar{K}_x - \bar{K}_y)^2 + 4\xi^2} \Big[\sqrt{(\bar{K}_x - \bar{K}_y)^2 + 4\xi^2} - 2(\bar{\Delta} + \bar{K}_z) \\ & + (\bar{K}_x + \bar{K}_y)\Big] \Theta\left(\sqrt{(\bar{K}_x - \bar{K}_y)^2 + 4\xi^2} - 2(\bar{\Delta} + \bar{K}_z) + (\bar{K}_x + \bar{K}_y)\right) \ . \end{aligned} \tag{4.96}$$

Inserting Eq. 4.96 into Eq. 4.90 with the combination of Eq. 4.67, we have for the thermal conductance,

$$\begin{aligned}\kappa_{AP}|_{\alpha=0} &= \frac{2\pi}{\hbar} S^2 \frac{(V_L V_R)^5}{(2\pi)^6} \frac{J_{ex,0}^2}{64\pi^4 \bar{A}^3 T} \int_{\xi_0}^{\infty} d\xi \frac{\xi^2 e^\xi}{(e^\xi - 1)^2} \frac{(\bar{K}_x - \bar{K}_y)^2}{\left((\bar{K}_x - \bar{K}_y)^2 + 4\xi^2\right)} \\ &\times \Big[\sqrt{(\bar{K}_x - \bar{K}_y)^2 + 4\xi^2} - 2(\bar{\Delta} + \bar{K}_z) + (\bar{K}_x + \bar{K}_y)\Big] \ . \end{aligned} \tag{4.97}$$

Effect of Gilbert Damping

Similar to what has been illustrated for the parallel configuration, the other terms of transition rates as given in Eq. 4.108 and Eq. 4.111 will also contribute to the tunneling current in the case with dissipation added.

Therefore we have the extra contribution to the tunneling current in the anti-parallel configuration,

$$\begin{aligned} j^{AP}_{\epsilon,\text{extra}} &= \int \frac{d^3\boldsymbol{p}_1 d^3\boldsymbol{p}_2}{(2\pi)^6}\Big(-\Gamma^{AP}_{I,e1}(\boldsymbol{p}_1,\boldsymbol{p}_2)\epsilon_{\boldsymbol{p}_1,L} + \Gamma^{AP}_{II,e1}(\boldsymbol{p}_1,\boldsymbol{p}_2)\epsilon_{\boldsymbol{p}_1,L} \\ &\quad -\Gamma^{AP}_{I,e4}(\boldsymbol{p}_1,\boldsymbol{p}_2)\epsilon_{-\boldsymbol{p}_2,R} + \Gamma^{AP}_{II,e4}(\boldsymbol{p}_1,\boldsymbol{p}_2)\epsilon_{-\boldsymbol{p}_2,R}\Big) , \end{aligned} \tag{4.98}$$

which is worked out to yield,

$$j^{AP}_{\epsilon,\text{extra}} = \frac{2\pi}{\hbar}S^2\frac{(V_L V_R)^5}{(2\pi)^6}\int d\epsilon\epsilon D^{AP}_{\text{extra}}(\epsilon)\Big[n_B((\epsilon-\mu_L)\beta_L) - n_B((\epsilon+\mu_R)\beta_R)\Big] , \tag{4.99}$$

where $D^{AP}_{\text{extra}}(\epsilon)$ denotes the extra contribution to the tunneling density of states,

$$\begin{aligned} & D^{AP}_{\text{extra}}(\epsilon) \\ \equiv\ & -\int \frac{d^3\boldsymbol{p}_1 d^3\boldsymbol{p}_2}{(2\pi)^6}|J_{ex}^{-\boldsymbol{p}_1,\boldsymbol{p}_2}|^2\delta(\epsilon-\epsilon_{\boldsymbol{p}_1,L})\delta(\epsilon+\epsilon_{\boldsymbol{p}_2,R})\left((u_{\boldsymbol{p}_1,L}u_{\boldsymbol{p}_2,R})^2 + (v_{\boldsymbol{p}_1,L}v_{\boldsymbol{p}_2,R})^2\right) . \end{aligned} \tag{4.100}$$

To account for the Gilbert damping for the magnon tunneling process, we take the substitution for the Dirac-delta function as done in Eq. 4.80, therefore the quantity $D^{AP}_{\text{extra}}(\epsilon)$ from this extra contribution due to broadening reads,

$$D^{AP}_{\text{extra}}(\epsilon) = -J^2_{ex,0}\big(\mathcal{M}_u(\epsilon)\mathcal{M}_u(-\epsilon) + \mathcal{M}_v(\epsilon)\mathcal{M}_v(-\epsilon)\big) , \tag{4.101}$$

where $\mathcal{M}_u$ and $\mathcal{M}_v$ are the density of states as given in Eq. 4.82. The Gilbert damping is again taken to be the same for both ferromagnetic insulators.

With numerical calculations, it turns out that such extra contribution for the anti-parallel configuration can be significantly larger than the original term if the Gilbert damping is large enough, which is very different from the case in the parallel configuration.

The total tunneling density of states in the anti-parallel configuration is thus obtained by combining Eq. 4.92 and Eq. 4.101,

$$D^{AP}_{\alpha\neq 0}(\epsilon) = J^2_{ex,0}\big(2\mathcal{M}_u(\epsilon)\mathcal{M}_v(\epsilon) - \mathcal{M}_u(\epsilon)\mathcal{M}_u(-\epsilon) - \mathcal{M}_v(\epsilon)\mathcal{M}_v(-\epsilon)\big) . \tag{4.102}$$

Therefore the tunneling thermal conductance in the case with finite Gilbert damping

is given as,

$$
\begin{aligned}
&\kappa_{AP}|_{\alpha\neq 0} \\
= \;& \frac{2\pi}{\hbar} S^2 \frac{(V_L V_R)^5}{(2\pi)^6} \frac{J_{ex,0}^2}{16\pi^4 T \bar{A}^3} \int_{-\infty}^{\infty} d\xi \frac{\xi^2 e^{\xi}}{(e^{\xi}-1)^2} \left(\frac{\alpha\xi}{\pi}\right)^2 \\
&\times \Bigg(2 \left[\int_0^{\infty} dq\; q^2 \frac{\sqrt{1+\frac{(\bar{K}_x-\bar{K}_y)^2/4}{\zeta_q^2}}+1}{\left(\xi-\zeta_q\right)^2+(\alpha\xi)^2} \right] \left[\int_0^{\infty} dq\; q^2 \frac{\sqrt{1+\frac{(\bar{K}_x-\bar{K}_y)^2/4}{\zeta_q^2}}-1}{\left(\xi-\zeta_q\right)^2+(\alpha\xi)^2} \right] \\
&+ \left[\int_0^{\infty} dq\; q^2 \frac{\sqrt{1+\frac{(\bar{K}_x-\bar{K}_y)^2/4}{\zeta_q^2}}+1}{\left(\xi-\zeta_q\right)^2+(\alpha\xi)^2} \right] \left[\int_0^{\infty} dq\; q^2 \frac{\sqrt{1+\frac{(\bar{K}_x-\bar{K}_y)^2/4}{\zeta_q^2}}+1}{\left(\xi+\zeta_q\right)^2+(\alpha\xi)^2} \right] \\
&+ \left[\int_0^{\infty} dq\; q^2 \frac{\sqrt{1+\frac{(\bar{K}_x-\bar{K}_y)^2/4}{\zeta_q^2}}-1}{\left(\xi-\zeta_q\right)^2+(\alpha\xi)^2} \right] \left[\int_0^{\infty} dq\; q^2 \frac{\sqrt{1+\frac{(\bar{K}_x-\bar{K}_y)^2/4}{\zeta_q^2}}-1}{\left(\xi+\zeta_q\right)^2+(\alpha\xi)^2} \right] \Bigg) ,
\end{aligned}
\tag{4.103}
$$

where ζ_q is the dimensionless dispersion relation as defined in Eq. 4.85.

4.4 Numerical Results and Discussion

In the following, we will first numerically evaluate the momentum integral and energy integral to calculate the tunneling density of states and tunneling thermal conductance for different configurations based on the expression as derived in Eq. 4.90 and Eq. 4.56. With this, the MTC ratio is obtained. All plots below are based on a fixed magnetic field as $|\Delta|/(k_B T) = 0.1$. Meanwhile, for all the numerical results shown below, the system temperature is fixed, and the stiffness constant scaled by thermal energy is taken to be $\bar{A} = 0.1$, the magnitude of the K_x is taken zero.

4.4.1 K_y Anisotropy Dependence of the Tunneling Thermal Conductance

We plot the K_y transverse anisotropy dependence of the tunneling thermal conductance for various damping values, as shown in Fig. 4.4. Since the Gilbert damping values of thin film metallic magnets can be very large [162], we take $\alpha = 0.2$ as the maximum. Note that the concept of quasi-particle magnon will not be well-defined when the damping is too large.

For both parallel and anti-parallel configurations, the thermal conductance increases with the increasing of precession ellipticity, e.g. the increasing of K_y, because the magnon population increases as the gap decreases to zero. The tunneling conductances

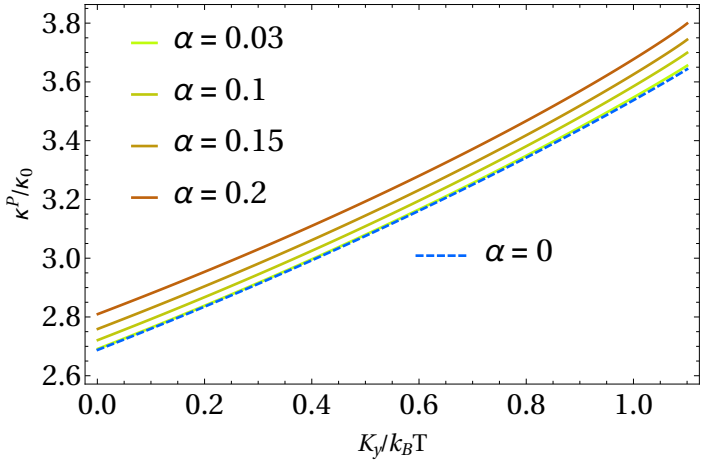

(a) Parallel configuration

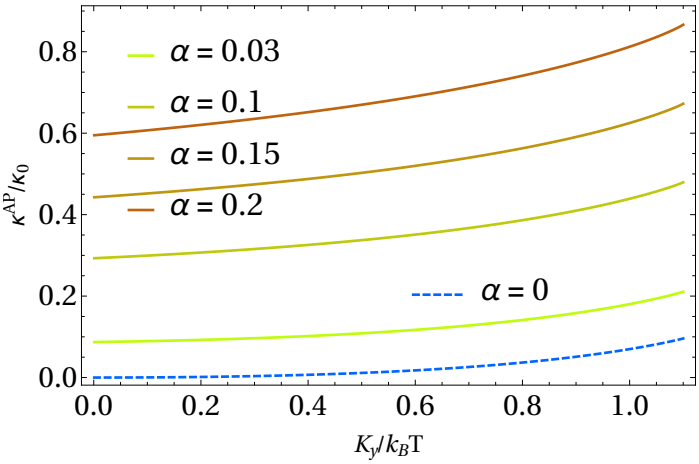

(b) Anti-parallel configuration

Fig. 4.4: K_y dependence of the tunneling thermal conductance for various Gilbert damping α in the set of $\{0, 0.03, 0.1, 0.15, 0.2\}$ and different configuration of the magnetic junction. Note that the tunneling thermal conductances in both plots are scaled by a constant defined by $\kappa_0 \equiv \frac{2\pi}{\hbar} S^2 \frac{(V_L V_R)^5}{(2\pi)^6} \frac{J_{ex,0}^2}{16\pi^4 T^3}$.

increase with Gilbert damping as well, due to the broadening of density of states. The thermal conductance in the anti-parallel configuration increases faster than the parallel case. As seen from the plot, the thermal conductance vanishes for a zero damping value in the case where magnons are circularly polarized by taking $K_y = 0$, which is consistent with Eq. 4.41. However with a finite Gilbert damping introduced, the tunneling conductance acquires a non-zero value even at $K_y = 0$, as shown in Fig. 4.4(b). This can be qualitatively understood by the finite overlap of magnon density of states from the left and right insulator, which is characterized by the tunneling density of

states $D^{P/AP}(\epsilon)$ as defined previously for deriving the magnon tunneling current. In the next, we will find that Gilbert damping has a much larger effect on the tunneling density of states in the anti-parallel configuration than the parallel configuration.

We plot the tunneling density of states for circular magnons in the parallel configuration based on the analytical results in Eq. 4.75 and Eq. 4.81, as shown in Fig. 4.5. In this configuration, we see that Gilbert damping weakly affects the tunneling density of states, which is consistent with the weak dependence in tunneling thermal conductance, as shown in Fig. 4.4(a). Fig. 4.6 shows the tunneling density of states for circular magnons in the anti-parallel configuration, which is based on the results in Eq. 4.96 and Eq. 4.102. We notice that a finite Gilbert damping gives rise to a finite tunneling density of states to circular magnons in the anti-parallel configuration, which explain the finite thermal conductance at $K_y = 0$ observed in Fig. 4.4(b).

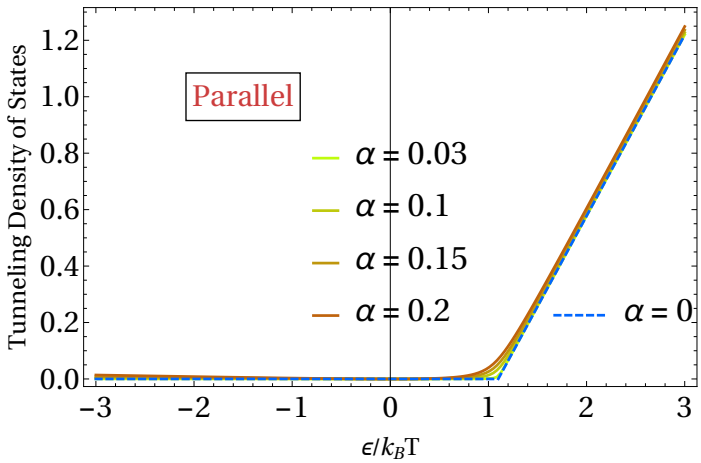

Fig. 4.5: Damping dependence of tunneling density of states for circular magnons in the parallel configuration. α is the Gilbert damping parameter. The y-axis is scaled by $J_{ex,0}^2/(k_BT)^2$ and we take $\bar{K}_z = 1$, $\bar{K}_y = 0$.

4.4.2 K_y Anisotropy Dependence of the MTC Ratio

We plot the K_y dependence of the MTC ratio as shown in Fig. 4.7. By defining the precession ellipticity as the ratio of transverse anisotropy strength K_y over the z-axis anisotropy strength, namely K_y/K_z, we find that the MTC ratio is equal to 1 when both Gilbert damping and the ellipticity are zero, which shows that the magnons are forbidden to tunnel through in the anti-parallel configuration, as illustrated previously in Fig. 4.4(b). We can explain this by the conservation of magnon polarization, which forbids the circular magnons to tunnel in the anti-parallel configuration, since they need to preserve their precession orientation. In the presence of ellipticity or Gilbert damping, the magnon tunneling process becomes possible again for the anti-parallel configuration, as shown in the deviation of the MTC ratio from 1.0 in this plot.

When K_y increases or K_z decreases, a stronger deviation of the MTC ratio from 1 is

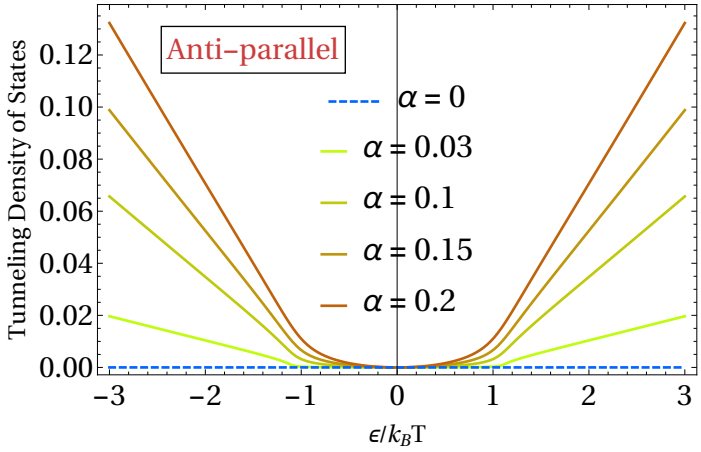

Fig. 4.6: Damping dependence of tunneling density of states for circular magnons in the anti-parallel configuration. α is the Gilbert damping parameter. The y-axis is scaled by $J_{ex,0}^2/(k_BT)^2$ and we take $\bar{K}_z = 1$, $\bar{K}_y = 0$.

obtained due to a faster increase of tunneling current in the anti-parallel configuration than the one in the parallel configuration, which can be seen by comparing the two subplots in Fig. 4.4.

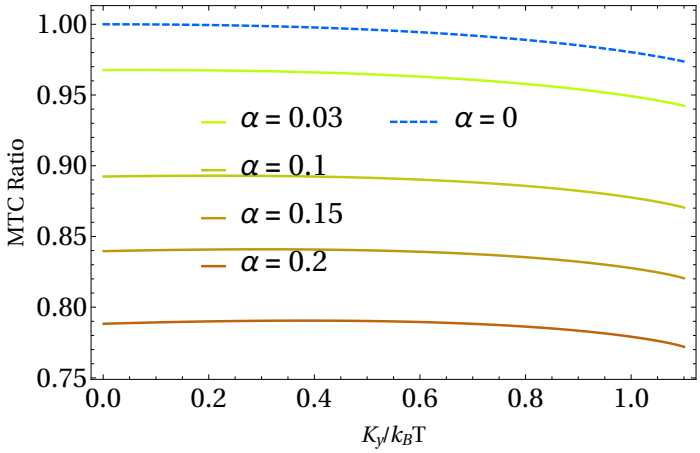

Fig. 4.7: Dependence of MTC ratio on the dimensionless transverse anisotropy $K_y/(k_BT)$ for various damping values. Here we take $K_z/(k_BT) = 1.0$.

Discussion

As Gilbert damping of magnons usually implies spin non-conserving scattering with the lattice vibrations, it effectively plays the role of driving the tunneling of elliptical magnons with energy below the gap with the assistance of phonons. Therefore we

could regard this effect as the *phonon-assisted magnon tunneling*. As seen from the numerical results above, a tunneling of circularly polarized magnons can also occur in the anti-parallel configuration, although this tunneling current can be very small if the damping is taken as the usual value 2.3×10^{-4} for realistic magnetic materials such as yttrium iron garnet [163]. Moreover, in spite of taking a larger K_y value or dissipation strength, the MTC ratio for such a magnonic system is still close to 1.0, which is in contrast with the case of an electronic system. Finally, the K_z dependence of the MTC ratio is also discussed, as shown in Appendix 4.B.

4.5 Conclusion

We have studied the magnon spin valve effect by calculating the magnon tunneling current using the Fermi's Golden Rule method. By applying the Holstein-Primakoff transformation to the Heisenberg Hamiltonian, we derived the magnon Hamiltonian, where the transverse easy-axis anisotropy terms introduce ellipticity to the magnon precession. We manually add Gilbert damping to the magnon spectral function and study the dissipation effect to the magnon tunneling, in addition to the effect of precession ellipticity, which brings new physics into the magnetization-dependent tunneling. We not only find that the magneto-thermal conductance ratio decreases with both Gilbert damping and the ellipticity of magnon precession, but also reveal a clear difference in its sensitivity over these two quantities. This relative change of magneto-thermal conductance with respect to different magnetization orientation is large for a much wider parameter space than its electronic counterpart. In the future our results presented here could provide important theoretical guidance for the experimental design of magnon spin valve devices.

Appendix

4.A Transition Rates for Different Tunneling Processes

4.A.1 Parallel Configuration

For the tunneling process described by $\mathcal{H}_{C,1}$, the momentum resolved transition rates are calculated with the Fermi's Golden Rule as, with one tunneling to the left and the

other tunneling to the right,

$$\begin{aligned}
&\Gamma_{I,e1}(\boldsymbol{p}_1,\boldsymbol{p}_2)\\
\equiv\;& \frac{2\pi}{\hbar}S^2(V_LV_R)^5\frac{|J_{ex}^{\boldsymbol{p}_1,-\boldsymbol{p}_2}|^2}{(2\pi)^6}(u_{\boldsymbol{p}_1,L}u_{\boldsymbol{p}_2,R})^2\delta(\epsilon_{\boldsymbol{p}_1,L}-\epsilon_{\boldsymbol{p}_2,R})\\
&\times(1+n_B((\epsilon_{\boldsymbol{p}_1,L}-\mu_L)\beta_L))\,n_B((\epsilon_{\boldsymbol{p}_2,R}-\mu_R)\beta_R)\ ,\\
&\Gamma_{II,e1}(\boldsymbol{p}_1,\boldsymbol{p}_2)\\
\equiv\;& \frac{2\pi}{\hbar}S^2(V_LV_R)^5\frac{|J_{ex}^{-\boldsymbol{p}_1,\boldsymbol{p}_2}|^2}{(2\pi)^6}(u_{\boldsymbol{p}_1,L}u_{\boldsymbol{p}_2,R})^2\delta(\epsilon_{\boldsymbol{p}_1,L}-\epsilon_{\boldsymbol{p}_2,R})\\
&\times n_B((\epsilon_{\boldsymbol{p}_1,L}-\mu_L)\beta_L)\,(1+n_B((\epsilon_{\boldsymbol{p}_2,R}-\mu_R)\beta_R))\ .
\end{aligned}\tag{4.104}$$

For the tunneling process described by $\mathcal{H}_{C,2}$, the transition rates are calculated as in Eq. 4.105, with one case in which the magnon number increase by one for both insulators and the other case with which the magnon number decreases by one for both insulators,

$$\begin{aligned}
&\Gamma_{I,e2}(\boldsymbol{p}_1,\boldsymbol{p}_2)\\
\equiv\;& \frac{2\pi}{\hbar}S^2(V_LV_R)^5\frac{|J_{ex}^{\boldsymbol{p}_1,-\boldsymbol{p}_2}|^2}{(2\pi)^6}(v_{\boldsymbol{p}_1,L}u_{\boldsymbol{p}_2,R})^2\delta(\epsilon_{-\boldsymbol{p}_1,L}+\epsilon_{\boldsymbol{p}_2,R})\\
&\times n_B((\epsilon_{-\boldsymbol{p}_1,L}-\mu_L)\beta_L)n_B((\epsilon_{\boldsymbol{p}_2,R}-\mu_R)\beta_R)\ ,\\
&\Gamma_{II,e2}(\boldsymbol{p}_1,\boldsymbol{p}_2)\\
\equiv\;& \frac{2\pi}{\hbar}S^2(V_LV_R)^5\frac{|J_{ex}^{-\boldsymbol{p}_1,\boldsymbol{p}_2}|^2}{(2\pi)^6}(v_{\boldsymbol{p}_1,L}u_{\boldsymbol{p}_2,R})^2\delta(\epsilon_{-\boldsymbol{p}_1,L}+\epsilon_{\boldsymbol{p}_2,R})\\
&\times(1+n_B((\epsilon_{-\boldsymbol{p}_1,L}-\mu_L)\beta_L))\,(1+n_B((\epsilon_{\boldsymbol{p}_2,R}-\mu_R)\beta_R))\ .
\end{aligned}\tag{4.105}$$

For the tunneling process described by $\mathcal{H}_{C,3}$, the transition rates are calculated as in Eq. 4.106, with one case in which the magnon number increase by one for both insulators and the other case with which the magnon number decreases by one for both insulators,

$$\begin{aligned}
&\Gamma_{I,e3}(\boldsymbol{p}_1,\boldsymbol{p}_2)\\
\equiv\;& \frac{2\pi}{\hbar}S^2(V_LV_R)^5\frac{|J_{ex}^{\boldsymbol{p}_1,-\boldsymbol{p}_2}|^2}{(2\pi)^6}(u_{\boldsymbol{p}_1,L}v_{\boldsymbol{p}_2,R})^2\delta(\epsilon_{\boldsymbol{p}_1,L}+\epsilon_{-\boldsymbol{p}_2,R})\\
&\times(1+n_B((\epsilon_{\boldsymbol{p}_1,L}-\mu_L)\beta_L))\,(1+n_B((\epsilon_{-\boldsymbol{p}_2,R}-\mu_R)\beta_R))\ ,\\
&\Gamma_{II,e3}(\boldsymbol{p}_1,\boldsymbol{p}_2)\\
\equiv\;& \frac{2\pi}{\hbar}S^2(V_LV_R)^5\frac{|J_{ex}^{-\boldsymbol{p}_1,\boldsymbol{p}_2}|^2}{(2\pi)^6}(u_{\boldsymbol{p}_1,L}v_{\boldsymbol{p}_2,R})^2\delta(\epsilon_{\boldsymbol{p}_1,L}+\epsilon_{-\boldsymbol{p}_2,R})\\
&\times n_B((\epsilon_{\boldsymbol{p}_1,L}-\mu_L)\beta_L)n_B((\epsilon_{-\boldsymbol{p}_2,R}-\mu_R)\beta_R)\ .
\end{aligned}\tag{4.106}$$

For the tunneling process described by $\mathcal{H}_{C,4}$, the transition rates are calculated as in Eq. 4.107, with one tunneling to the left and the other tunneling to the right,

$$\begin{aligned}
&\Gamma_{I,e4}(\boldsymbol{p}_1,\boldsymbol{p}_2)\\
\equiv\ &\frac{2\pi}{\hbar}S^2(V_LV_R)^5\frac{|J_{ex}^{\boldsymbol{p}_1,-\boldsymbol{p}_2}|^2}{(2\pi)^6}(v_{\boldsymbol{p}_1,L}v_{\boldsymbol{p}_2,R})^2\delta(\epsilon_{-\boldsymbol{p}_1,L}-\epsilon_{-\boldsymbol{p}_2,R})\\
&\times n_B((\epsilon_{-\boldsymbol{p}_1,L}-\mu_L)\beta_L)\left(1+n_B((\epsilon_{-\boldsymbol{p}_2,R}-\mu_R)\beta_R)\right)\ ,\\
\\
&\Gamma_{II,e4}(\boldsymbol{p}_1,\boldsymbol{p}_2)\\
\equiv\ &\frac{2\pi}{\hbar}S^2(V_LV_R)^5\frac{|J_{ex}^{-\boldsymbol{p}_1,\boldsymbol{p}_2}|^2}{(2\pi)^6}(v_{\boldsymbol{p}_1,L}v_{\boldsymbol{p}_2,R})^2\delta(\epsilon_{-\boldsymbol{p}_1,L}-\epsilon_{-\boldsymbol{p}_2,R})\\
&\times\left(1+n_B((\epsilon_{-\boldsymbol{p}_1,L}-\mu_L)\beta_L)\right)n_B((\epsilon_{-\boldsymbol{p}_2,R}-\mu_R)\beta_R)\ .
\end{aligned}\tag{4.107}$$

4.A.2 Anti-parallel Configuration

For the tunneling process described by $\mathcal{H}_{C,1}^{AP}$, the momentum resolved transition rate is calculated with the Fermi's Golden Rule as the following with one case in which the magnon number increase by one for both insulators and the other case with which the magnon number decreases by one for both insulators,

$$\begin{aligned}
&\Gamma_{I,e1}^{AP}(\boldsymbol{p}_1,\boldsymbol{p}_2)\\
\equiv\ &\frac{2\pi}{\hbar}S^2(V_LV_R)^5\int\frac{d^3\boldsymbol{p}_1d^3\boldsymbol{p}_2}{(2\pi)^{12}}|J_{ex}^{\boldsymbol{p}_1,\boldsymbol{p}_2}|^2(u_{\boldsymbol{p}_1,L}u_{\boldsymbol{p}_2,R})^2\\
&\times\left(1+n_B((\epsilon_{\boldsymbol{p}_1,L}-\mu_L)\beta_L)\right)\left(1+n_B((\epsilon_{\boldsymbol{p}_2,R}-\mu_R)\beta_R)\right)\delta(\epsilon_{\boldsymbol{p}_1,L}+\epsilon_{\boldsymbol{p}_2,R})\ ,\\
\\
&\Gamma_{II,e1}^{AP}(\boldsymbol{p}_1,\boldsymbol{p}_2)\\
\equiv\ &\frac{2\pi}{\hbar}S^2(V_LV_R)^5\int\frac{d^3\boldsymbol{p}_1d^3\boldsymbol{p}_2}{(2\pi)^{12}}|J_{ex}^{-\boldsymbol{p}_1,-\boldsymbol{p}_2}|^2(u_{\boldsymbol{p}_1,L}u_{\boldsymbol{p}_2,R})^2\\
&\times n_B((\epsilon_{\boldsymbol{p}_1,L}-\mu_L)\beta_L)n_B((\epsilon_{\boldsymbol{p}_2,R}-\mu_R)\beta_R)\delta(\epsilon_{\boldsymbol{p}_1,L}+\epsilon_{\boldsymbol{p}_2,R})\ .
\end{aligned}\tag{4.108}$$

For the tunneling process described by $\mathcal{H}_{C,2}^{AP}$, the transition rates are calculated as in Eq. 4.109, with one tunneling to the left and the other tunneling to the right,

$$\begin{aligned}
&\Gamma_{I,e2}^{AP}(\boldsymbol{p}_1,\boldsymbol{p}_2)\\
\equiv\ &\frac{2\pi}{\hbar}S^2(V_LV_R)^5\int\frac{d^3\boldsymbol{p}_1d^3\boldsymbol{p}_2}{(2\pi)^{12}}|J_{ex}^{\boldsymbol{p}_1,\boldsymbol{p}_2}|^2(v_{\boldsymbol{p}_1,L}u_{\boldsymbol{p}_2,R})^2\\
&\times n_B((\epsilon_{-\boldsymbol{p}_1,L}-\mu_L)\beta_L)\left(1+n_B((\epsilon_{\boldsymbol{p}_2,R}-\mu_R)\beta_R)\right)\delta(\epsilon_{-\boldsymbol{p}_1,L}-\epsilon_{\boldsymbol{p}_2,R})\ ,\\
\\
&\Gamma_{II,e2}^{AP}(\boldsymbol{p}_1,\boldsymbol{p}_2)\\
\equiv\ &\frac{2\pi}{\hbar}S^2(V_LV_R)^5\int\frac{d^3\boldsymbol{p}_1d^3\boldsymbol{p}_2}{(2\pi)^{12}}|J_{ex}^{-\boldsymbol{p}_1,-\boldsymbol{p}_2}|^2(v_{\boldsymbol{p}_1,L}u_{\boldsymbol{p}_2,R})^2\\
&\times\left(1+n_B((\epsilon_{-\boldsymbol{p}_1,L}-\mu_L)\beta_L)\right)n_B((\epsilon_{\boldsymbol{p}_2,R}-\mu_R)\beta_R)\delta(\epsilon_{-\boldsymbol{p}_1,L}-\epsilon_{\boldsymbol{p}_2,R})\ .
\end{aligned}\tag{4.109}$$

For the tunneling process described by $\mathcal{H}_{C,3}^{AP}$, the transition rates are calculated as in Eq. 4.110, with one tunneling to the left and the other tunneling to the right,

$$\begin{aligned}
&\Gamma_{I,e3}^{AP}(\boldsymbol{p}_1,\boldsymbol{p}_2)\\
\equiv\ &\frac{2\pi}{\hbar}S^2(V_LV_R)^5\int\frac{d^3\boldsymbol{p}_1d^3\boldsymbol{p}_2}{(2\pi)^{12}}|J_{ex}^{\boldsymbol{p}_1,\boldsymbol{p}_2}|^2(u_{\boldsymbol{p}_1,L}v_{\boldsymbol{p}_2,R})^2\\
&\times\left(1+n_B((\epsilon_{\boldsymbol{p}_1,L}-\mu_L)\beta_L)\right)n_B((\epsilon_{-\boldsymbol{p}_2,R}-\mu_R)\beta_R)\delta(\epsilon_{\boldsymbol{p}_1,L}-\epsilon_{-\boldsymbol{p}_2,R})\ ,\\
&\Gamma_{II,e3}^{AP}(\boldsymbol{p}_1,\boldsymbol{p}_2)\\
\equiv\ &\frac{2\pi}{\hbar}S^2(V_LV_R)^5\int\frac{d^3\boldsymbol{p}_1d^3\boldsymbol{p}_2}{(2\pi)^{12}}|J_{ex}^{-\boldsymbol{p}_1,-\boldsymbol{p}_2}|^2(u_{\boldsymbol{p}_1,L}v_{\boldsymbol{p}_2,R})^2\\
&\times n_B((\epsilon_{\boldsymbol{p}_1,L}-\mu_L)\beta_L)\left(1+n_B((\epsilon_{-\boldsymbol{p}_2,R}-\mu_R)\beta_R)\right)\delta(\epsilon_{\boldsymbol{p}_1,L}-\epsilon_{-\boldsymbol{p}_2,R})\ .
\end{aligned}\tag{4.110}$$

For the tunneling process described by $\mathcal{H}_{C,4}^{AP}$, the transition rates are calculated as in Eq. 4.111, with one case in which the magnon number increase by one for both insulators and the other case with which the magnon number decreases by one for both insulators,

$$\begin{aligned}
&\Gamma_{I,e4}^{AP}(\boldsymbol{p}_1,\boldsymbol{p}_2)\\
\equiv\ &\frac{2\pi}{\hbar}S^2(V_LV_R)^5\int\frac{d^3\boldsymbol{p}_1d^3\boldsymbol{p}_2}{(2\pi)^{12}}|J_{ex}^{\boldsymbol{p}_1,\boldsymbol{p}_2}|^2(v_{\boldsymbol{p}_1,L}v_{\boldsymbol{p}_2,R})^2\\
&\times n_B((\epsilon_{-\boldsymbol{p}_1,L}-\mu_L)\beta_L)n_B((\epsilon_{-\boldsymbol{p}_2,R}-\mu_R)\beta_R)\delta(\epsilon_{-\boldsymbol{p}_1,L}+\epsilon_{-\boldsymbol{p}_2,R})\ ,\\
&\Gamma_{II,e4}^{AP}(\boldsymbol{p}_1,\boldsymbol{p}_2)\\
\equiv\ &\frac{2\pi}{\hbar}S^2(V_LV_R)^5\int\frac{d^3\boldsymbol{p}_1d^3\boldsymbol{p}_2}{(2\pi)^{12}}|J_{ex}^{-\boldsymbol{p}_1,-\boldsymbol{p}_2}|^2(v_{\boldsymbol{p}_1,L}v_{\boldsymbol{p}_2,R})^2\\
&\times\left(1+n_B((\epsilon_{-\boldsymbol{p}_1,L}-\mu_L)\beta_L)\right)\left(1+n_B((\epsilon_{-\boldsymbol{p}_2,R}-\mu_R)\beta_R)\right)\delta(\epsilon_{-\boldsymbol{p}_1,L}+\epsilon_{-\boldsymbol{p}_2,R})\ .
\end{aligned}\tag{4.111}$$

4.B K_z Dependence of the MTC Ratio

We also calculate the MTC ratio as a function of K_z for various damping values, as visualized in Fig. 4.8. For $\alpha = 0$, the MTC ratio has a slight increase when $K_z/(k_BT)$ is taken from 0.2 to 0.6, but is still very close to 1. However, as we introduce Gilbert damping to the system, the MTC ratio starts to deviate from 1.0 dramatically. By taking $\alpha = 0.1$, we obtain the MTC ratio to be 90% for a certain group of parameters, although its dependence on K_z remains very weak in respective of the damping value we choose. Increasing the magnon gap by increasing K_z can decrease the density of states, thus decreasing the magnon tunneling thermal conductance, as shown in the figure. However, we observe that the slopes of curves in this plot are small for the whole parameter range of K_z, which demonstrates that the MTC ratio has a much weaker

dependence on K_z than on Gilbert damping. This indicates that the existence of K_z anisotropy reduces the magnon tunneling current in both parallel and anti-parallel configurations by an approximately equal amount.

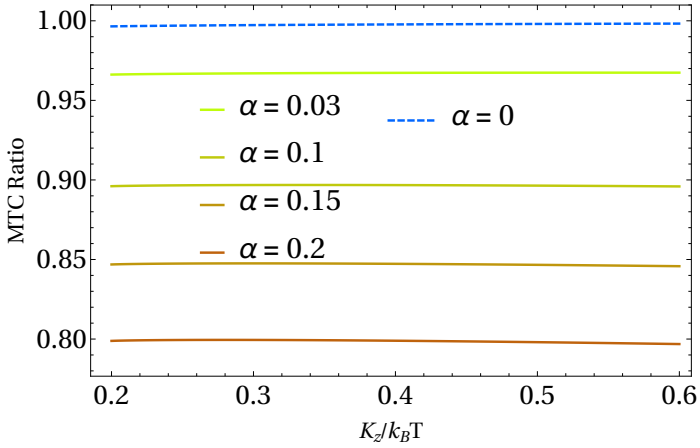

Fig. 4.8: MTC ratio as a function of K_z anisotropy for various Gilbert damping values.

CHAPTER 5

Conclusion and Outlook

As Moore's law of CMOS technology is approaching its physical limit [164], magnon spintronics is gaining more and more attention as a platform to develop the next-generation information processing and storage hardware. The main mission of magnon spintronics is the study of spin and thermal transport mediated by magnons. The flow of spin angular momentum can be used to read and write information, while flow of heat is critical for the thermal management in the design of chip architecture, since the future data centers based on spintronics are still likely to generate huge amounts of heat that need to be managed.

We will first review each chapter and then present an outlook. In Chapter 1, we introduced an overview of magnon spintronics by starting from magnetism and gave an outline of the research projects in the final section of the introduction. Here we remind the reader of one key idea in the recent development of magnon spintronics, which is the electrical generation and detection of magnons, as illustrated in Fig. 5.1.

In Chapter 2, we developed the work on a Green's function formalism to study exchange magnon transport in a normal metal(NM)-ferromagnet insulator(FM)-normal metal(NM) heterostructure. By illustrating the formalism with numerical and analytical calculations, we determined the FM thickness dependence of the magnon spin current. Furthermore, we have shown that the interplay between disorder and Gilbert damping leads to spin-current fluctuations. The developed non-equilibrium Green's function formalism is a natural starting point for numerical studies of magnon transport. So far, the numerical calculations are carried out for a 1D system, its extension to a 2D or 3D system with different form of disorder is natural. Here the numerical calculation was carried out mainly for the case of electrical generation of magnon current, therefore a study on the spin Seebeck effect driven by thermal gradient is lacking but should be straightforward. Moreover, a recent experimental study discovered elec-

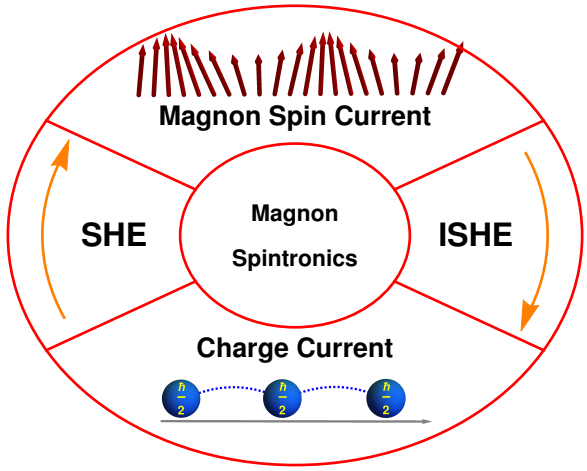

Fig. 5.1: Conversion between charge current and magnon spin current with spin Hall effect (SHE) and inverse spin Hall effect (ISHE).

trical tunable long-distance magnon transport in an antiferromagnetic insulator [30], this gives us extra motivation to generalize this formalism to a heterostructure which contains antiferromagnets (AFM). However, how to incorporate the two sub-lattices of antiferromagnet into this formalism with only one group of magnon operators requires a careful consideration.

In Chapter 3, we presented a stochastic Landau-Lifshitz-Gilbert formalism for magnon drag in a three-dimensional antiferromagnetic metal. By numerical calculations, we demonstrate that tailoring the sign and magnitude of an easy-axis antiferromagnetic metal based Peltier-cooling device is possible by manipulating the external magnetic field, the dissipation parameter β, and its anisotropy. We found that the dissipation parameter β is an essential quantity in the description of the magnon-drag effect in an antiferromagnetic metal. According to the numerical results, the ratio of β over the Gilbert damping parameter α determines the sign of magnon energy current and spin current, although the exact range of β for a typical antiferromagnet is still under debate. Near the spin-flop transition, we also found a strong enhancement of the magnon spin current driven by the electric current through the $s-d$ exchange coupling. Nevertheless, the spin-flop field is typically very large (a few Tesla). Therefore, a search for metallic antiferromagnets with low spin-flop field becomes essential to make this theoretical enhancement not only easier to observe but also useful after its experimental confirmation.

In Chapter 4, we applied Fermi's Golden Rule to study the effect of ellipticity and Gilbert damping on magnon tunneling in a magnon spin valve. Gilbert damping is found to enhance the effect of ellipticity, namely leading to a smaller relative change of magneto-thermal conductance from a parallel configuration to the anti-parallel configuration. However, a formalism to study the magnon tunneling in a general configuration where the alignment between the magnetizations is at an arbitrary angle is lacking and a direction for future work. Ellipticity of the magnetic precession can give

this general configuration a unique angular dependence, which facilitates experiments to determine its existence. In addition, it would be interesting to study the temperature dependence of this relative change in the future. Lastly it is worth performing further numerical calculations on the corresponding magneto-spin conductance and look at its parameter dependence, which can be useful for the design of an efficient magnon-based circuit based on a heterostructure of FM-AFM-FM [165].

In summary, we have presented theoretical progress in the field of magnon spintronics to understand the spin and thermal transport mediated by magnons in ferromagnetic insulators and antiferromagnetic metals, with both analytical and numerical approaches. Nowadays computation hardwares in our information age are mainly relying on a sophisticated manipulation of electrons, which are fundamental particles but unfortunately bring Joule heating to the environment. This limits the power efficiency of information processing devices. The best of magnon spintronics is yet to come, hopefully it will become one of the ultimate technologies in this century to help human beings avoid generating too much entropy per nanosecond on this blue planet.

Bibliography

[1] SO Demokritov, VE Demidov, O Dzyapko, GA Melkov, and AN Slavin. Quantum coherence due to Bose-Einstein condensation of parametrically driven magnons. New Journal of Physics, 10(4):045029, 2008.

[2] L Berger. Emission of spin waves by a magnetic multilayer traversed by a current. Physical Review B, 54(13):9353, 1996.

[3] LJ Cornelissen, J Liu, RA Duine, J Ben Youssef, and BJ Van Wees. Long-distance transport of magnon spin information in a magnetic insulator at room temperature. Nature Physics, 11(12):1022–1026, 2015.

[4] John B Carlson. Lodestone compass: Chinese or Olmec primacy?: Multidisciplinary analysis of an Olmec hematite artifact from San Lorenzo, Veracruz, Mexico. Science, 189(4205):753–760, 1975.

[5] Petrus Peregrinus. The letter of petrus peregrinus on the magnet. AD, Translated by Brothers Arnold, M. Sc., Mc GRAW, New York, 1269, 1904.

[6] MD Simon and AK Geim. Diamagnetic levitation: flying frogs and floating magnets. Journal of applied physics, 87(9):6200–6204, 2000.

[7] Walther Gerlach and Otto Stern. Der experimentelle nachweis der richtungsquantelung im magnetfeld. Zeitschrift für Physik, 9(1):349–352, 1922.

[8] SA Wolf, DD Awschalom, RA Buhrman, JM Daughton, S Von Molnar, ML Roukes, A Yu Chtchelkanova, and DM Treger. Spintronics: a spin-based electronics vision for the future. science, 294(5546):1488–1495, 2001.

[9] Igor Žutić, Jaroslav Fabian, and S Das Sarma. Spintronics: Fundamentals and applications. Reviews of modern physics, 76(2):323, 2004.

[10] JE Hirsch. Spin Hall effect. Physical Review Letters, 83(9):1834, 1999.

[11] Eleftherios N Economou. The Physics of Solids: Essentials and Beyond. Springer Science & Business Media, 2010.

[12] Guang-Yu Guo, Shuichi Murakami, T-W Chen, and Naoto Nagaosa. Intrinsic spin Hall effect in platinum: First-principles calculations. Physical Review Letters, 100(9):096401, 2008.

[13] J-C Rojas-Sánchez, N Reyren, P Laczkowski, W Savero, J-P Attané, C Deranlot, M Jamet, J-M George, L Vila, and H Jaffrès. Spin pumping and inverse spin Hall effect in platinum: the essential role of spin-memory loss at metallic interfaces. Physical Review Letters, 112(10):106602, 2014.

[14] Takeshi Seki, Yu Hasegawa, Seiji Mitani, Saburo Takahashi, Hiroshi Imamura, Sadamichi Maekawa, Junsaku Nitta, and Koki Takanashi. Giant spin Hall effect in perpendicularly spin-polarized FePt/Au devices. Nature Materials, 7(2):125, 2008.

[15] D Qu, SY Huang, Jun Hu, Ruqian Wu, and CL Chien. Intrinsic spin Seebeck effect in Au/YIG. Physical Review Letters, 110(6):067206, 2013.

[16] Walther Meissner and Robert Ochsenfeld. Ein neuer effekt bei eintritt der supraleitfähigkeit. Naturwissenschaften, 21(44):787–788, 1933.

[17] V Arkadiev. A floating magnet. Nature, 160(4062):330, 1947.

[18] John Bardeen, Leon N Cooper, and John Robert Schrieffer. Theory of superconductivity. Physical Review, 108(5):1175, 1957.

[19] Charles Kittel. Introduction to solid state physics. 2005.

[20] FA Buot and JW McClure. Theory of diamagnetism of bismuth. Physical Review B, 6(12):4525, 1972.

[21] JW McClure. Diamagnetism of graphite. Physical Review, 104(3):666, 1956.

[22] Vladimir Cherepanov, Igor Kolokolov, and Victor L'vov. The saga of YIG: spectra, thermodynamics, interaction and relaxation of magnons in a complex magnet. Physics Reports, 229(3):81–144, 1993.

[23] S Dubois, C Marchal, JM Beuken, L Piraux, JL Duvail, A Fert, JM George, and JL Maurice. Perpendicular giant magnetoresistance of NiFe/Cu multilayered nanowires. Applied Physics Letters, 70(3):396–398, 1997.

[24] Masatoshi Imada, Atsushi Fujimori, and Yoshinori Tokura. Metal-insulator transitions. Reviews of Modern Physics, 70(4):1039, 1998.

[25] V Baltz, Aurelien Manchon, M Tsoi, T Moriyama, T Ono, and Y Tserkovnyak. Antiferromagnetic spintronics. Reviews of Modern Physics, 90(1):015005, 2018.

[26] M Louis Néel. Propriétés magnétiques des ferrites; ferrimagnétisme et antiferromagnétisme. In Annales de Physique, volume 12, pages 137–198, 1948.

[27] Hailong Wang, Chunhui Du, P Chris Hammel, and Fengyuan Yang. Antiferromagnonic spin transport from $Y_3Fe_5O_{12}$ into NiO. Physical Review Letters, 113(9):097202, 2014.

[28] Peter Wadley, Bryn Howells, J Železnỳ, Carl Andrews, Victoria Hills, Richard P Campion, Vit Novák, K Olejník, F Maccherozzi, SS Dhesi, et al. Electrical switching of an antiferromagnet. Science, 351(6273):587–590, 2016.

[29] S Yu Bodnar, L Šmejkal, I Turek, T Jungwirth, O Gomonay, J Sinova, AA Sapozhnik, H-J Elmers, M Kläui, and M Jourdan. Writing and reading antiferromagnetic Mn_2Au by Néel spin-orbit torques and large anisotropic magnetoresistance. Nature Communications, 9(1):348, 2018.

[30] R Lebrun, A Ross, SA Bender, A Qaiumzadeh, L Baldrati, J Cramer, A Brataas, RA Duine, and M Kläui. Tunable long-distance spin transport in a crystalline antiferromagnetic iron oxide. Nature, 561(7722):222, 2018.

[31] Wei Yuan, Qiong Zhu, Tang Su, Yunyan Yao, Wenyu Xing, Yangyang Chen, Yang Ma, Xi Lin, Jing Shi, Ryuichi Shindou, et al. Experimental signatures of spin superfluid ground state in canted antiferromagnet Cr_2O_3 via nonlocal spin transport. Science Advances, 4(4):eaat1098, 2018.

[32] PAM Dirac. On the theory of quantum mechanics. Proc. R. Soc. London A, 112:661, 1926.

[33] Yoichiro Nambu. Quasi-particles and gauge invariance in the theory of superconductivity. Physical Review, 117(3):648, 1960.

[34] AV Chumak, VI Vasyuchka, AA Serga, and B Hillebrands. Magnon spintronics. Nature Physics, 11(6):453–461, 2015.

[35] T Tanaka, Hiroshi Kontani, Masayuki Naito, T Naito, Dai S Hirashima, K Yamada, and J Inoue. Intrinsic spin Hall effect and orbital Hall effect in $4d$ and $5d$ transition metals. Physical Review B, 77(16):165117, 2008.

[36] M Morota, Y Niimi, K Ohnishi, DH Wei, T Tanaka, H Kontani, T Kimura, and Y Otani. Indication of intrinsic spin Hall effect in 4 d and 5 d transition metals. Physical Review B, 83(17):174405, 2011.

[37] Laurent Vila, Takashi Kimura, and Yoshi Chika Otani. Evolution of the spin Hall effect in Pt nanowires: size and temperature effects. Physical Review Letters, 99(22):226604, 2007.

[38] Y Niimi, Y Kawanishi, DH Wei, C Deranlot, HX Yang, Mairbek Chshiev, T Valet, A Fert, and Y Otani. Giant spin Hall effect induced by skew scattering from bismuth impurities inside thin film CuBi alloys. Physical Review Letters, 109(15):156602, 2012.

[39] E Saitoh, M Ueda, H Miyajima, and G Tatara. Conversion of spin current into charge current at room temperature: Inverse spin-Hall effect. Applied Physics Letters, 88(18):182509, 2006.

[40] CM Jaworski, J Yang, S Mack, DD Awschalom, JP Heremans, and RC Myers. Observation of the spin-Seebeck effect in a ferromagnetic semiconductor. Nature Materials, 9(11):898–903, 2010.

[41] K Uchida, J Xiao, H Adachi, J-i Ohe, S Takahashi, J Ieda, T Ota, Y Kajiwara, H Umezawa, H Kawai, et al. Spin Seebeck insulator. Nature Materials, 9(11):894, 2010.

[42] Ken-ichi Uchida, Hiroto Adachi, Takeru Ota, Hiroyasu Nakayama, Sadamichi Maekawa, and Eiji Saitoh. Observation of longitudinal spin-Seebeck effect in magnetic insulators. Applied Physics Letters, 97(17):172505, 2010.

[43] Luqiao Liu, Takahiro Moriyama, DC Ralph, and RA Buhrman. Spin-torque ferromagnetic resonance induced by the spin Hall effect. Physical Review Letters, 106(3):036601, 2011.

[44] YL Chen, James G Analytis, J-H Chu, ZK Liu, S-K Mo, Xiao-Liang Qi, HJ Zhang, DH Lu, Xi Dai, Zhong Fang, et al. Experimental realization of a three-dimensional topological insulator, Bi_2Te_3. science, 325(5937):178–181, 2009.

[45] Praveen Deorani, Jaesung Son, Karan Banerjee, Nikesh Koirala, Matthew Brahlek, Seongshik Oh, and Hyunsoo Yang. Observation of inverse spin Hall effect in bismuth selenide. Physical Review B, 90(9):094403, 2014.

[46] Charles Kittel and JK Galt. Ferromagnetic domain theory. In Solid state physics, volume 3, pages 437–564. Elsevier, 1956.

[47] Yaroslav Tserkovnyak, Arne Brataas, and Gerrit EW Bauer. Theory of current-driven magnetization dynamics in inhomogeneous ferromagnets. Journal of Magnetism and Magnetic Materials, 320(7):1282–1292, 2008.

[48] BA Kalinikos and AN Slavin. Theory of dipole-exchange spin wave spectrum for ferromagnetic films with mixed exchange boundary conditions. Journal of Physics C: Solid State Physics, 19(35):7013, 1986.

[49] J Jorzick, SO Demokritov, C Mathieu, B Hillebrands, B Bartenlian, C Chappert, F Rousseaux, and AN Slavin. Brillouin light scattering from quantized spin waves in micron-size magnetic wires. Physical Review B, 60(22):15194, 1999.

[50] Daniel D Stancil and Anil Prabhakar. Spin Waves. Springer, 2009.

[51] Gerrit EW Bauer, Eiji Saitoh, and Bart J Van Wees. Spin caloritronics. Nature Materials, 11(5):391, 2012.

[52] Jiang Xiao, Gerrit EW Bauer, Ken-chi Uchida, Eiji Saitoh, Sadamichi Maekawa, et al. Theory of magnon-driven spin Seebeck effect. Physical Review B, 81(21):214418, 2010.

[53] K Uchida, S Takahashi, K Harii, J Ieda, W Koshibae, Kazuya Ando, S Maekawa, and E Saitoh. Observation of the spin Seebeck effect. Nature, 455(7214):778–781, 2008.

[54] Hyungyu Jin, Stephen R Boona, Zihao Yang, Roberto C Myers, and Joseph P Heremans. Effect of the magnon dispersion on the longitudinal spin Seebeck effect in yttrium iron garnets. Physical Review B, 92(5):054436, 2015.

[55] Akihiro Kirihara, Ken-ichi Uchida, Yosuke Kajiwara, Masahiko Ishida, Yasunobu Nakamura, Takashi Manako, Eiji Saitoh, and Shinichi Yorozu. Spin-current-driven thermoelectric coating. Nature Materials, 11(8):686, 2012.

[56] SM Rezende, RL Rodríguez-Suárez, RO Cunha, AR Rodrigues, FLA Machado, GA Fonseca Guerra, JC Lopez Ortiz, and A Azevedo. Magnon spin-current theory for the longitudinal spin-Seebeck effect. Physical Review B, 89(1):014416, 2014.

[57] J Flipse, FK Dejene, D Wagenaar, GEW Bauer, J Ben Youssef, and BJ Van Wees. Observation of the spin Peltier effect for magnetic insulators. Physical Review Letters, 113(2):027601, 2014.

[58] H Nakayama, Matthias Althammer, Y-T Chen, K Uchida, Y Kajiwara, D Kikuchi, T Ohtani, Stephan Geprägs, M Opel, S Takahashi, et al. Spin Hall magnetoresistance induced by a nonequilibrium proximity effect. Physical Review Letters, 110(20):206601, 2013.

[59] W Zhou, T Seki, T Kubota, GEW Bauer, and K Takanashi. Spin-Hall and anisotropic magnetoresistance in ferrimagnetic Co-Gd/Pt layers. Physical Review Materials, 2(9):094404, 2018.

[60] K Uchida, T Ota, H Adachi, J Xiao, T Nonaka, Y Kajiwara, GEW Bauer, S Maekawa, and E Saitoh. Thermal spin pumping and magnon-phonon-mediated spin-Seebeck effect. Journal of Applied Physics, 111(10):103903, 2012.

[61] Igor Žutić and Hanan Dery. Spintronics: Taming spin currents. Nature Materials, 10(9):647, 2011.

[62] Yaroslav Tserkovnyak, Arne Brataas, and Gerrit EW Bauer. Enhanced Gilbert damping in thin ferromagnetic films. Physical Review Letters, 88(11):117601, 2002.

[63] Yaroslav Tserkovnyak, Arne Brataas, Gerrit EW Bauer, and Bertrand I Halperin. Nonlocal magnetization dynamics in ferromagnetic heterostructures. Reviews of Modern Physics, 77(4):1375, 2005.

[64] HL Wang, CH Du, Y Pu, R Adur, PC Hammel, and FY Yang. Large spin pumping from epitaxial $Y_3Fe_5O_{12}$ thin films to Pt and W layers. Physical Review B, 88(10):100406, 2013.

[65] John C Slonczewski. Current-driven excitation of magnetic multilayers. Journal of Magnetism and Magnetic Materials, 159(1-2):L1–L7, 1996.

[66] Yiming Huai, Frank Albert, Paul Nguyen, Mahendra Pakala, and Thierry Valet. Observation of spin-transfer switching in deep submicron-sized and low-resistance magnetic tunnel junctions. Applied Physics Letters, 84(16):3118–3120, 2004.

[67] GD Fuchs, NC Emley, IN Krivorotov, PM Braganca, EM Ryan, SI Kiselev, JC Sankey, DC Ralph, RA Buhrman, and JA Katine. Spin-transfer effects in nanoscale magnetic tunnel junctions. Applied Physics Letters, 85(7):1205–1207, 2004.

[68] Sabpreet Bhatti, Rachid Sbiaa, Atsufumi Hirohata, Hideo Ohno, Shunsuke Fukami, and SN Piramanayagam. Spintronics based random access memory: a review. Materials Today, 20(9):530–548, 2017.

[69] LJ Cornelissen and BJ Van Wees. Magnetic field dependence of the magnon spin diffusion length in the magnetic insulator yttrium iron garnet. Physical Review B, 93(2):020403, 2016.

[70] Charles Kittel. Theory of antiferromagnetic resonance. Physical Review, 82(4):565, 1951.

[71] H Saglam, W Zhang, MB Jungfleisch, J Sklenar, JE Pearson, JB Ketterson, and A Hoffmann. Spin transport through the metallic antiferromagnet FeMn. Physical Review B, 94(14):140412, 2016.

[72] Lamprini Frangou, Simon Oyarzun, Stephane Auffret, Laurent Vila, Serge Gambarelli, and Vincent Baltz. Enhanced spin pumping efficiency in antiferromagnetic IrMn thin films around the magnetic phase transition. Physical Review Letters, 116(7):077203, 2016.

[73] JBS Mendes, RO Cunha, O Alves Santos, PRT Ribeiro, FLA Machado, RL Rodríguez-Suárez, A Azevedo, and SM Rezende. Large inverse spin Hall effect in the antiferromagnetic metal $Ir_{20}Mn_{80}$. Physical Review B, 89(14):140406, 2014.

[74] Philipp Ross, Michael Schreier, Johannes Lotze, Hans Huebl, Rudolf Gross, and Sebastian TB Goennenwein. Antiferromagentic resonance detected by direct current voltages in MnF_2/Pt bilayers. Journal of Applied Physics, 118(23):233907, 2015.

[75] O Gomonay, T Jungwirth, and J Sinova. Narrow-band tunable Terahertz detector in antiferromagnets via staggered-field and antidamping torques. Physical Review B, 98(10):104430, 2018.

[76] Øyvind Johansen, Hans Skarsvåg, and Arne Brataas. Spin-transfer antiferromagnetic resonance. Physical Review B, 97(5):054423, 2018.

[77] S Seki, T Ideue, M Kubota, Y Kozuka, R Takagi, M Nakamura, Y Kaneko, M Kawasaki, and Y Tokura. Thermal generation of spin current in an antiferromagnet. Physical Review Letters, 115(26):266601, 2015.

[78] G Gitgeatpong, Yang Zhao, P Piyawongwatthana, Yiming Qiu, Leland Weldon Harriger, Nicholas P Butch, TJ Sato, and K Matan. Nonreciprocal magnons and symmetry-breaking in the noncentrosymmetric antiferromagnet. Physical Review Letters, 119(4):047201, 2017.

[79] Y Shiomi, R Takashima, D Okuyama, G Gitgeatpong, P Piyawongwatthana, K Matan, TJ Sato, and E Saitoh. Spin Seebeck effect in the polar antiferromagnet $\alpha - Cu_2V_2O_7$. Physical Review B, 96(18):180414, 2017.

[80] I Dzyaloshinsky. A thermodynamic theory of "weak" ferromagnetism of antiferromagnetics. J. Phys. Chem. Solids, 4:241, 1958.

[81] Toru Moriya. Anisotropic super-exchange interaction and weak ferromagnetism. Phys. Rev., 120:91, 1960.

[82] H Wu, L Huang, C Fang, BS Yang, CH Wan, GQ Yu, JF Feng, HX Wei, and XF Han. Magnon valve effect between two magnetic insulators. Physical Review Letters, 120(9):097205, 2018.

[83] Lev Davidovich Landau and Evgenii Mikhailovich Lifshitz. Statistical Physics. 1958.

[84] Charles Kittel. Introduction to solid state physics, volume 162. John Wiley & Sons, 1966.

[85] T Kasuya and RC LeCraw. Relaxation mechanisms in ferromagnetic resonance. Physical Review Letters, 6(5):223, 1961.

[86] M Sparks. Ferromagnetic resonance in thin films. i. theory of normal-mode frequencies. Physical Review B, 1(9):3831, 1970.

[87] Christian W Sandweg, Yosuke Kajiwara, Andrii V Chumak, Alexander A Serga, Vitaliy I Vasyuchka, Mattias Benjamin Jungfleisch, Eiji Saitoh, and Burkard Hillebrands. Spin pumping by parametrically excited exchange magnons. Physical Review Letters, 106(21):216601, 2011.

[88] Nynke Vlietstra, BJ van Wees, and FK Dejene. Detection of spin pumping from YIG by spin-charge conversion in a $Au/Ni_{80}Fe_{20}$ spin-valve structure. Physical Review B, 94(3):035407, 2016.

[89] A Talalaevskij, M Decker, J Stigloher, A Mitra, HS Körner, O Cespedes, CH Back, and BJ Hickey. Magnetic properties of spin waves in thin yttrium iron garnet films. Physical Review B, 95(6):064409, 2017.

[90] J Holanda, O Alves Santos, RL Rodríguez-Suárez, A Azevedo, and SM Rezende. Simultaneous spin pumping and spin Seebeck experiments with thermal control of the magnetic damping in bilayers of yttrium iron garnet and heavy metals: YIG/Pt and YIG/IrMn. Physical Review B, 95(13):134432, 2017.

[91] XJ Zhou, GY Shi, JH Han, QH Yang, YH Rao, HW Zhang, LL Lang, SM Zhou, F Pan, and C Song. Lateral transport properties of thermally excited magnons in yttrium iron garnet films. Applied Physics Letters, 110(6):062407, 2017.

[92] Er-Jia Guo, Joel Cramer, Andreas Kehlberger, Ciaran A Ferguson, Donald A MacLaren, Gerhard Jakob, and Mathias Kläui. Influence of thickness and interface on the low-temperature enhancement of the spin Seebeck effect in YIG films. Physical Review X, 6(3):031012, 2016.

[93] Ludo J Cornelissen, Kevin JH Peters, GEW Bauer, RA Duine, and Bart J van Wees. Magnon spin transport driven by the magnon chemical potential in a magnetic insulator. Physical Review B, 94(1):014412, 2016.

[94] Benedetta Flebus, SA Bender, Yaroslav Tserkovnyak, and RA Duine. Two-fluid theory for spin superfluidity in magnetic insulators. Physical Review Letters, 116(11):117201, 2016.

[95] Kouki Nakata, Pascal Simon, and Daniel Loss. Wiedemann-Franz law for magnon transport. Physical Review B, 92(13):134425, 2015.

[96] Kouki Nakata, Pascal Simon, and Daniel Loss. Spin currents and magnon dynamics in insulating magnets. Journal of Physics D: Applied Physics, 50(11):114004, 2017.

[97] Baigeng Wang, Jian Wang, Jin Wang, and DY Xing. Spin current carried by magnons. Physical Review B, 69(17):174403, 2004.

[98] Massimiliano Di Ventra. Electrical transport in nanoscale systems, volume 14. Cambridge University Press Cambridge, 2008.

[99] William Fuller Brown Jr. Thermal fluctuations of a single-domain particle. Physical Review, 130(5):1677, 1963.

[100] Silas Hoffman, Koji Sato, and Yaroslav Tserkovnyak. Landau-Lifshitz theory of the longitudinal spin Seebeck effect. Physical Review B, 88(6):064408, 2013.

[101] T Holstein and Hl Primakoff. Field dependence of the intrinsic domain magnetization of a ferromagnet. Physical Review, 58(12):1098, 1940.

[102] Assa Auerbach. Interacting electrons and quantum magnetism. Springer Science & Business Media, 2012.

[103] Scott A Bender, Rembert A Duine, and Yaroslav Tserkovnyak. Electronic pumping of quasiequilibrium Bose-Einstein-condensed magnons. Physical Review Letters, 108(24):246601, 2012.

[104] Y. Ohnuma, M. Matsuo, and S. Maekawa. Theory of spin Peltier effect. ArXiv e-prints, June 2017.

[105] Joseph Maciejko. An introduction to nonequilibrium many-body theory. Lecture Notes, 2007.

[106] Arne Brataas, Yu V Nazarov, and Gerrit EW Bauer. Finite-element theory of transport in ferromagnet-normal metal systems. Physical Review Letters, 84(11):2481, 2000.

[107] Jia, Xingtao, Liu, Kai, Xia, Ke, and Bauer, Gerrit E. W. Spin transfer torque on magnetic insulators. EPL, 96(1):17005, 2011.

[108] P. W. Anderson. Absence of diffusion in certain random lattices. Phys. Rev., 109:1492–1505, Mar 1958.

[109] Martin Evers, Cord A. Müller, and Ulrich Nowak. Spin-wave localization in disordered magnets. Phys. Rev. B, 92:014411, Jul 2015.

[110] I. Yusipov, T. Laptyeva, S. Denisov, and M. Ivanchenko. Localization in open quantum systems. Phys. Rev. Lett., 118:070402, Feb 2017.

[111] M. Evers, C. A. Müller, and U. Nowak. Weak localization of magnons in chiral magnets. ArXiv e-prints, August 2017.

[112] MF Pereira, JP Zubelli, D Winge, Andreas Wacker, AS Rodrigues, V Anfertev, and V Vaks. Theory and measurements of harmonic generation in semiconductor

superlattices with applications in the 100 GHz to 1 THz range. Physical Review B, 96(4):045306, 2017.

[113] Akashdeep Kamra and Wolfgang Belzig. Magnon-mediated spin current noise in ferromagnet| nonmagnetic conductor hybrids. Physical Review B, 94(1):014419, 2016.

[114] Russell. L. Herman. Introduction to partial differential equations. 2015.

[115] TJ Gramila, JP Eisenstein, AH MacDonald, LN Pfeiffer, and KW West. Mutual friction between parallel two-dimensional electron systems. Physical Review Letters, 66(9):1216, 1991.

[116] MB Pogrebinskii. Mutual drag of carriers in a semiconductor-insulator-semiconductor system. Soviet Physics-Semiconductors, 11(4):372–376, 1977.

[117] RV Gorbachev, AK Geim, MI Katsnelson, KS Novoselov, T Tudorovskiy, IV Grigorieva, AH MacDonald, SV Morozov, K Watanabe, T Taniguchi, et al. Strong coulomb drag and broken symmetry in double-layer graphene. Nature Physics, 8(12):896, 2012.

[118] L. Gurevich. J.Phys., 9(477), 1946.

[119] Conyers Herring. Theory of the thermoelectric power of semiconductors. Physical Review, 96(5):1163, 1954.

[120] Hellmut Fritzsche. A general expression for the thermoelectric power. Solid State Communications, 9(21):1813–1815, 1971.

[121] SS Kubakaddi. Phonon-drag thermopower in 3d Dirac semimetals. Journal of Physics: Condensed Matter, 27(45):455801, 2015.

[122] Hiroto Adachi, Ken-ichi Uchida, Eiji Saitoh, Jun-ichiro Ohe, Saburo Takahashi, and Sadamichi Maekawa. Gigantic enhancement of spin Seebeck effect by phonon drag. Applied Physics Letters, 97(25):252506, 2010.

[123] LJ Cornelissen, J Liu, BJ Van Wees, and RA Duine. Spin-current-controlled modulation of the magnon spin conductance in a three-terminal magnon transistor. Physical Review Letters, 120(9):097702, 2018.

[124] H Wu, CH Wan, X Zhang, ZH Yuan, QT Zhang, JY Qin, HX Wei, XF Han, and S Zhang. Observation of magnon-mediated electric current drag at room temperature. Physical Review B, 93(6):060403, 2016.

[125] GN Grannemann and L Berger. Magnon-drag Peltier effect in a Ni-Cu alloy. Physical Review B, 13(5):2072, 1976.

[126] JD Wasscher and C Haas. Contribution of magnon-drag to the thermoelectric power of antiferromagnetic Mn te. Physics Letters, 8(5):302–304, 1964.

[127] Marius V Costache, German Bridoux, Ingmar Neumann, and Sergio O Valenzuela. Magnon-drag thermopile. Nature Materials, 11(3):199, 2012.

[128] Sarah J Watzman, Rembert A Duine, Yaroslav Tserkovnyak, Stephen R Boona, Hyungyu Jin, Arati Prakash, Yuanhua Zheng, and Joseph P Heremans. Magnon-

drag thermopower and Nernst coefficient in Fe, Co, and Ni. Physical Review B, 94(14):144407, 2016.

[129] ME Lucassen, CH Wong, RA Duine, and Y Tserkovnyak. Spin-transfer mechanism for magnon-drag thermopower. Applied Physics Letters, 99(26):262506, 2011.

[130] Benedetta Flebus, Rembert A Duine, and Yaroslav Tserkovnyak. Landau-Lifshitz theory of the magnon-drag thermopower. EPL (Europhysics Letters), 115(5):57004, 2016.

[131] Ran Cheng, Di Xiao, and Arne Brataas. Terahertz antiferromagnetic spin Hall nano-oscillator. Physical Review Letters, 116(20):207603, 2016.

[132] J Železnỳ, H Gao, K Vỳbornỳ, J Zemen, J Mašek, Aurélien Manchon, J Wunderlich, Jairo Sinova, and T Jungwirth. Relativistic Néel-order fields induced by electrical current in antiferromagnets. Physical Review Letters, 113(15):157201, 2014.

[133] Aurelien Manchon, IM Miron, T Jungwirth, J Sinova, J Zeleznỳ, A Thiaville, K Garello, and P Gambardella. Current-induced spin-orbit torques in ferromagnetic and antiferromagnetic systems. arXiv preprint arXiv:1801.09636, 2018.

[134] S Yu Bodnar, L Šmejkal, I Turek, T Jungwirth, O Gomonay, J Sinova, AA Sapozhnik, H-J Elmers, M Kläui, and M Jourdan. Writing and reading antiferromagnetic Mn_2Au by Néel spin-orbit torques and large anisotropic magnetoresistance. Nature Communications, 9(1):348, 2018.

[135] Scott A Bender, Hans Skarsvåg, Arne Brataas, and Rembert A Duine. Enhanced spin conductance of a thin-film insulating antiferromagnet. Physical Review Letters, 119(5):056804, 2017.

[136] Roberto E Troncoso, Camilo Ulloa, Felipe Pesce, and AS Nunez. Antiferromagnetic magnonic crystals. Physical Review B, 92(22):224424, 2015.

[137] DL Mills. Surface spin-flop state in a simple antiferromagnet. Physical Review Letters, 20(1):18, 1968.

[138] AC Swaving and RA Duine. Current-induced torques in continuous antiferromagnetic textures. Physical Review B, 83(5):054428, 2011.

[139] RA Duine. Spin pumping by a field-driven domain wall. Physical Review B, 77(1):014409, 2008.

[140] Paul M Haney, RA Duine, AS Nunez, and AH MacDonald. Current-induced torques in magnetic metals: Beyond spin-transfer. Journal of magnetism and magnetic materials, 320(7):1300–1311, 2008.

[141] Kjetil MD Hals, Yaroslav Tserkovnyak, and Arne Brataas. Phenomenology of current-induced dynamics in antiferromagnets. Physical Review Letters, 106(10):107206, 2011.

[142] William Fuller Brown Jr. Thermal fluctuations of a single-domain particle. Physical Review, 130(5):1677, 1963.

[143] HTC Stoof. Coherent versus incoherent dynamics during Bose-Einstein condensation in atomic gases. Journal of Low Temperature Physics, 114(1-2):11–108, 1999.

[144] Yaroslav Tserkovnyak, Hans Joakim Skadsem, Arne Brataas, and Gerrit EW Bauer. Current-induced magnetization dynamics in disordered itinerant ferromagnets. Physical Review B, 74(14):144405, 2006.

[145] Yaroslav Tserkovnyak, Arne Brataas, and Gerrit EW Bauer. Theory of current-driven magnetization dynamics in inhomogeneous ferromagnets. Journal of Magnetism and Magnetic Materials, 320(7):1282–1292, 2008.

[146] Arati Prakash, Jack Brangham, Sarah J Watzman, Fengyuan Yang, and Joseph P Heremans. Effect of magnons on interfacial phonon drag in YIG/metal systems. arXiv preprint arXiv:1804.07023, 2018.

[147] Mario Norberto Baibich, Jean Marc Broto, Albert Fert, F Nguyen Van Dau, Frédéric Petroff, P Etienne, G Creuzet, A Friederich, and J Chazelas. Giant magnetoresistance of (001) Fe/(001) Cr magnetic superlattices. Physical Review Letters, 61(21):2472, 1988.

[148] B Dieny. Giant magnetoresistance in spin-valve multilayers. Journal of Magnetism and Magnetic Materials, 136(3):335–359, 1994.

[149] Stefan Klingler, Philipp Pirro, Thomas Brächer, Britta Leven, Burkard Hillebrands, and Andrii V Chumak. Spin-wave logic devices based on isotropic forward volume magnetostatic waves. Applied Physics Letters, 106(21):212406, 2015.

[150] Andrii V Chumak, Alexander A Serga, and Burkard Hillebrands. Magnon transistor for all-magnon data processing. Nature communications, 5:4700, 2014.

[151] Jacob Torrejon, Mathieu Riou, Flavio Abreu Araujo, Sumito Tsunegi, Guru Khalsa, Damien Querlioz, Paolo Bortolotti, Vincent Cros, Kay Yakushiji, Akio Fukushima, et al. Neuromorphic computing with nanoscale spintronic oscillators. Nature, 547(7664):428, 2017.

[152] Thomas Brächer and Philipp Pirro. An analog magnon adder for all-magnonic neurons. arXiv preprint arXiv:1806.01389, 2018.

[153] Jie Ren and Jian-Xin Zhu. Theory of asymmetric and negative differential magnon tunneling under temperature bias: Towards a spin Seebeck diode and transistor. Physical Review B, 88(9):094427, 2013.

[154] Miura Diasuke and Sakuma Akimasa. Tunable spin Seebeck diode with magnonic spin tunneling junction. arXiv preprint arXiv:1811.01141v1, 2018.

[155] Ludo J Cornelissen, J Shan, and BJ Van Wees. Temperature dependence of the magnon spin diffusion length and magnon spin conductivity in the magnetic insulator yttrium iron garnet. Physical Review B, 94(18):180402, 2016.

[156] Thomas Langner, Akihiro Kirihara, Alexander A Serga, Burkard Hillebrands, and Vitaliy I Vasyuchka. Damping of parametrically excited magnons in

the presence of the longitudinal spin Seebeck effect. Physical Review B, 95(13):134441, 2017.

[157] Andreas Rückriegel and Peter Kopietz. Rayleigh-Jeans condensation of pumped magnons in thin-film ferromagnets. Physical Review Letters, 115(15):157203, 2015.

[158] Henrik Bruus and Karsten Flensberg. Many-body quantum theory in condensed matter physics: an introduction. Oxford university press, 2004.

[159] Jiwoong Park, Abhay N Pasupathy, Jonas I Goldsmith, Connie Chang, Yuval Yaish, Jason R Petta, Marie Rinkoski, James P Sethna, Héctor D Abruña, Paul L McEuen, et al. Coulomb blockade and the Kondo effect in single-atom transistors. Nature, 417(6890):722, 2002.

[160] A-W de Leeuw, ECI van der Wurff, RA Duine, D van Oosten, and HTC Stoof. Theory for Bose-Einstein condensation of light in nanofabricated semiconductor microcavities. Physical Review A, 94(1):013615, 2016.

[161] Jiansen Zheng, Scott Bender, Jogundas Armaitis, Roberto E Troncoso, and Rembert A Duine. Green's function formalism for spin transport in metal-insulator-metal heterostructures. Physical Review B, 96(17):174422, 2017.

[162] J-M Beaujour, D Ravelosona, I Tudosa, EE Fullerton, and AD Kent. Ferromagnetic resonance linewidth in ultrathin films with perpendicular magnetic anisotropy. Physical Review B, 80(18):180415, 2009.

[163] O d'Allivy Kelly, A Anane, R Bernard, J Ben Youssef, C Hahn, A H Molpeceres, C Carrétéro, E Jacquet, C Deranlot, P Bortolotti, et al. Inverse spin Hall effect in nanometer-thick yttrium iron garnet/Pt system. Applied Physics Letters, 103(8):082408, 2013.

[164] Weisheng Zhao, Erya Deng, Jacques-Olivier Klein, Yuanqing Cheng, Dafiné Ravelosona, Youguang Zhang, Claude Chappert, et al. A radiation hardened hybrid spintronic/CMOS nonvolatile unit using magnetic tunnel junctions. Journal of Physics D: Applied Physics, 47(40):405003, 2014.

[165] CY Guo, CH Wan, X Wang, C Fang, P Tang, WJ Kong, MK Zhao, LN Jiang, BS Tao, GQ Yu, et al. Magnon valves based on YIG/Nio/YIG all-insulating magnon junctions. arXiv preprint arXiv:1810.00380, 2018.

Samenvatting

Terwijl de wet van Moore op het gebied van CMOS-technologie zijn fysieke limiet nadert [164], krijgt magnon spintronica steeds meer aandacht voor de ontwikkeling van de volgende generatie hardware voor informatieverwerking en opslag. Het belangrijkste doel van magnon spintronica is de studie van spin- en thermisch transport door middel van magnonen. De stroom van het spinimpulsmoment kan worden gebruikt om informatie te lezen en te schrijven. Daarnaast is de warmtestroom cruciaal voor het warmtebeheer bij het ontwerp van de chiparchitectuur omdat de toekomstige datacenters op basis van spintronica nog steeds enorme hoeveelheden warmte zullen genereren.

In deze samenvatting bespreken we de hoofdstukken een voor een en tot slot presenteren we een conclusie. In hoofdstuk 1 introduceerden we een overzicht van magnon spintronica vanuit het oogpunt van magnetisme en aan het einde van het hoofdstuk gaven we een overzicht van de verschillende onderzoeksprojecten. We benadrukten één belangrijk idee in de recente ontwikkeling van magnon spintronica: de elektrische opwekking en detectie van magnonen.

In hoofdstuk 2 ontwikkelden we een formalisme op basis van een Greense functie om uitwisseling van magnontransport te bestuderen in een heterostructuur van normaal metaal (NM) - ferromagnetische isolator (FM) - normaal metaal (NM). Door het formalisme te illustreren met numerieke en analytische berekeningen bepaalden we hoe de magnon spinstroom afhankelijk is van de dikte van de FM. Verder hebben we aangetoond dat een samenspel tussen wanorde en Gilbertdemping leidt tot fluctuaties in de spinstroom. Het ontwikkelde niet-evenwicht Greense functieformalisme is een goed uitgangspunt voor numerieke studies van magnontransport. Tot op heden zijn deze numerieke berekeningen uitgevoerd voor een eendimensionaal systeem en de uitbreiding van de berekeningen tot een twee- of driedimensionaal systeem met een andere vorm van wanorde volgt er direct uit. In dit hoofdstuk werd de numerieke berekening voornamelijk uitgevoerd in het geval dat er een elektrische opwekking van de magnonstroom plaatsvond. Daarom ontbreekt een onderzoek naar het spin-Seebeck-effect dat door een thermische gradiënt wordt aangestuurd, maar een uitbreiding naar dit effect op basis van het formalisme zou eenvoudig moeten zijn. Daarnaast realiseerde een recent experiment elektrisch afstembar magnontransport over grote afstanden in een antiferromagnetische (AFM) isolator [30]. Deze ontdekking is een extra motivatie om dit formalisme te generaliseren naar een heterostructuur met een AFM. Het is echter

niet vanzelfsprekend om dit te doen omdat men rekening moet houden met één set van magnonoperatoren in twee subroosters van de AFM.
In hoofdstuk 3 behandelden we een stochastisch Landau-Lifshitz-Gilbertformalisme voor de wrijvingskrachten tussen magnonen en elektronen in een driedimensionaal AFM metaal. Met numerieke berekeningen laten we zien dat het mogelijk is om het teken en de grootte van een Peltier-koelapparaat bestaande uit een AFM metaal met een voorkeursas aan te passen. Dit doen we met manipulatie door het externe magnetische veld, de dissipatieparameter β en de anisotropie. We hebben gevonden dat de dissipatieparameter β essentieel is om het magnon-wrijvingskracht-effect in een AFM metaal aan te sturen. Volgens de numerieke resultaten is de verhouding van β en de Gilbertdempingsparameter α bepalend voor het teken van de energie en spinstroom van de magnonen. Verder vonden we bij de spinflopovergang een sterke verbetering van de magnon spinstroom die werd aangedreven door de elektrische stroom via de $s-d$ wisselwerking. Helaas is het spinflopveld meestal erg groot (een paar Tesla). Daarom is de zoektocht naar een AFM van metaal met een klein spinflopveld belangrijk: niet alleen om deze theoretische verbetering op een makkelijkere manier te observeren, maar ook omdat deze ontdekking een AFM van metaal direct toepasbaar maakt na de experimentele bevestiging.

In hoofdstuk 4 hebben we Fermi's gouden regel gebruikt om het effect van ellipticiteit en Gilbertdemping op magnontunneling in een magnon-transistor te bestuderen. Gilbertdemping blijkt het effect van ellipticiteit te versterken; het leidt namelijk tot een kleinere relatieve verandering van magnetothermische geleiding van een parallelle configuratie naar de antiparallelle configuratie. In dit werk ontbreekt echter een formalisme om magnontunneling in een zeer algemene configuratie te bestuderen waar de uitlijning tussen de magnetisaties in een willekeurige hoek ligt. We beschouwen dit als een nieuwe richting voor toekomstig onderzoek. Het is namelijk mogelijk dat de ellipticiteit van de magnetische precessie in deze algemene configuratie een unieke hoekafhankelijkheid kan hebben en dit kan bepalend zijn voor experimenten om dit gedrag aan te tonen. Daarnaast zou het interessant zijn om de temperatuurafhankelijkheid van deze relatieve verandering te bestuderen in toekomstig onderzoek. Tot slot is het de moeite waard om verdere numerieke berekeningen uit te voeren op de corresponderende magneto-spin geleiding en om te kijken van welke parameters deze geleiding afhangt. De resultaten hiervan kunnen nuttig zijn voor het ontwerp van efficiënte FM-AFM-FM heterostructuur circuits die op magnonen gebaseerd zijn [165].

Kort samengevat hebben we theoretische vooruitgang geboekt op het gebied van magnon spintronica om het spin- en thermisch transport door middel van magnonen te begrijpen in FM isolatoren en AFM metalen. Daartoe hebben we zowel analytische als numerieke methoden gebruikt. Tegenwoordig, in ons informatietijdperk, rekent de computerhardware voornamelijk met een geavanceerde manipulatie van elektronen. Deze elektronen zijn weliswaar fundamentele deeltjes, maar helaas zorgen ze ook voor Joule-opwarming. Dit beperkt de energie-efficiëntie van de huidige informatietechnologie. De beste magnon spintronica moet nog komen en hopelijk wordt het een van de ultieme technologieën in deze eeuw om mensen te helpen voorkomen dat ze te veel entropie per nanoseconde genereren op deze aardbol.

Acknowledgement

Looking back to the past four years, I would like to thank my supervisor Rembert Duine first, for all the advice and support he has given to me during my PhD time here, in both study and daily life. You gave me the opportunity to work with you five years ago and also kindly extended our contract in the end. I have been very lucky to have you, a professor who possesses all the qualities for being a great supervisor, who is patient, brilliant, and resourceful all the time. I have to say, it is amazing that no matter what kind of problem I was faced with, I felt relief immediately to find the way out after each meeting with you during the past years. Furthermore, your humor, optimism, and your devotion to physics research always stimulate me to move forward.

My gratitude also goes to all other professors in the Institute of Theoretical Physics (ITF). Among them, I would to specially thank Henk Stoof, for kindly acting as my PhD promotor, also for the interesting conversations in the coffee room and the occasional guidance when I came to your office. Thank Tomislav for the discussion on a classical theory to financial market, thank Cristiane for her nice character, which inspired me to be positive everyday. Thank the organizer of the DRSTP school, which was really useful and enjoyable. Many thanks to René, Dirk, Lars, Stefan. Also thank Gerrit Bauer in Delft University of Technology for his kindness.

I am grateful to all my scientific collaborators in my three projects. Without their help and thoughtful suggestions, this thesis would not have been done. Special thanks goes to Jogundas Armaitis, Scott Bender, and Andreas Rückriegel for being mentors to me. You three are just incredibly smart and determined in mind, and have really driven me continuously to become a better PhD researcher. Many thanks to the members in Rembert's research group: Etienne, Camilo, Dion, Peter, Ruben. Discussion on physics and sharing what I observed in life with you guys are always fascinating to me. Camilo, thanks for answering me so many naïve physics questions in the past two years.

Furthermore, I would like to thank all other PhD students in the ITF. Many thanks to Leihua (Andy), Lei and Haiqing, for providing me with lots of chances of speaking Mandarin in the university. Thanks to Leihua for all the dinners he invited me to his home for the past 4 years. Thank Erik, Nick, Guido for the interesting conversations during the lunch time from Minnaertgebouw to BBG of the past years. Thank Anton

and Gerwin, for helping a lot in general condensed matter physics. Thank Rick for guiding me how to assemble my Linux desktop at home in the early 2016. Thank Benedikt for being teaching assistant together with me for the course of statistical physics in late 2017. Thank Niklas for the discussion on C++ programming in the middle of 2016. Thank Tatjana, Sonja, Simonas, Chongchuo Li, Cheng Lian, Govert, Willem, Raffaele, Jeroen, Stefano, Domingo, Nava, Sander Kooi, Adriana and Jette for the nice conversations during our coffee breaks. Special thanks goes to Sander Kempkes, who helped me revise the Dutch version of the summary along with Etienne.

To Tara Drwenski, thanks for being my officemate for nearly 30 months. As a non-native English speaker, I came across lots of tiny issues due to language barriers during my daily study, you were always so nice each time when I had to interrupt you during work. Life in BBG has really become much easier with your help and chatting about data science with you has been always so exciting. Also thanks to Misha, I enjoyed the discussion on everything from time series modeling to training a deep learning algorithm with Python. Thank Drian and Kitinan for being another two super nice officemates during my stay in the BBG building.

Thank Joost, Wanda, Olga in the secretary office and other administrative staff, for doing everything from visa applications to preparing the Thursday afternoon snacks. Thank my roommates at Bilthoven and my friends in Wittevrouwen. I am also thankful for the hospitality of Anne-Maria Visuri when visiting her in Geneva during my summer trip of 2017. Thank Juhi Nagori in IMAU for introducing a job opportunity at Rotterdam to me. Furthermore, thanks to my friends who are now living in mainland China, the two trips back to China in 2018 became unforgettable because of them.

Thank my ex-girlfriend, Tian, for proposing the idea in the autumn of 2013 about applying for the CSC scholarship, which made it possible for me to carry out PhD research in Europe. 相濡以沫, 不如相忘于江湖.

Finally, I would like to thank my family, to my sister for her warm welcome in Shanghai during the stay of my supervisor and I, and to my parents, Chunfu Zheng and Xueyu Dai, for bringing me to life and supporting me continuously in the past decades. 最后, 感谢父母近三十年来的养育之恩, 是你们给予了我生命, 使我至少可以在这个宇宙昙花一现.

About the author

Jiansen Zheng (郑建森) was born on September 10th, 1989 in China, where he spent most of his childhood at Wenzhou, which is a city surrounded by mountains in south-eastern Zhejiang province. In June 2007, he completed high school education in Jongjiang Middle School and was enrolled into Donghua University in Shanghai afterwards. Three year later, he graduated with a BSc degree in applied physics. In September 2011, he started his Master's study at Xiamen University in Fujian province. In September 2014, he finished his master thesis project on thermoelectrics with a MSc degree in theoretical physics. From November 2014, he worked as a PhD candidate in the research group of Prof. Rembert A. Duine at the Institute of Theoretical Physics in Utrecht University. This thesis is an account of the research he has done on the magnon spintronics.